Surface-Directed Patterning of Polymer/Nanoparticle Assemblies on Microcontact-Printed Substrates

by

Saman Harirchian-Saei
B.Sc., Amirkabir University of Technology (Tehran Polytechnic), 2004

A Dissertation Submitted in Partial Fulfillment
of the Requirements for the Degree of

DOCTOR OF PHILOSOPHY

in the Department of Chemistry

Supervisory Committee

Surface-Directed Patterning of Polymer/Nanoparticle Assemblies on Microcontact-Printed Substrates

by

Saman Harirchian-Saei
B.Sc., Amirkabir University of Technology (Tehran Polytechnic), 2004

Supervisory Committee

Dr. Matthew G. Moffitt, Department of Chemistry
Supervisor

Dr. Alexandre Brolo, Department of Chemistry
Departmental Member

Dr. Robin Hicks, Department of Chemistry
Departmental Member

Dr. David Sinton, Department of Mechanical Engineering
Outside Member

Abstract

Supervisory Committee
Dr. Matthew G. Moffitt, Department of Chemistry
Supervisor
Dr. Alexandre Brolo, Department of Chemistry
Departmental Member
Dr. Robin Hicks, Department of Chemistry
Departmental Member
Dr. David Sinton, Department of Mechanical Engineering
Outside Member

Two different strategies for producing hierarchical polymer/nanoparticle (NP) patterned structures are presented in this work. The first strategy combines self-assembly of amphiphilic block copolymers at the air-water interface with microscale template assembly of the resulting aggregates on chemically-patterned substrates. Aggregates are formed via interfacial self-assembly of 141k polystyrene-*block*-poly (ethylene oxide) (PS-*b*-PEO, M_w=141 k) or a blend of PS-*b*-PEO (M_w=185 k) and PS-coated CdS (PS-CdS) quantum dots (QDs), to form aggregates of copolymer or copolymer/NP. Using Langmuir-Blodgett (LB) technique, the formed aggregates are then transferred to patterned substrates with alternating hydrophilic/hydrophobic stripes, obtained by microcontact printing (μCP) octadecyltrichlorosilane (OTS) on glass. The effect of different parameters including surface pressure, orientation of the patterned substrate respect to the air-water interface, and withdrawal speed was studied. Successful aggregate transfer to the hydrophilic domains of the patterned hydrophilic/hydrophobic substrate is achieved when patterned stripes are oriented perpendicular to the water surface during LB transfer and when substrates are withdrawn at low speed and low compression pressure.

The second strategy combines the phase-separation of immiscible polymer blends during spin-coating with μCP. We show the surface-directed patterning of a phase-separating polymer blend on optically-transparent (OTS)-patterned glass substrate obtained via μCP. First, morphologies and pattern registration of thin spin-coated films of PS (M_w=131 k)/ poly(methyl methacrylate) (PMMA, Mw= 120 k) blends on patterned glass with alternating hydrophilic/hydrophobic stripes is studied for a range of experimental conditions including polymer concentration, blend composition, solvent, and spin rate. Good registration of polar PMMA to hydrophilic glass surface and non-polar PS to hydrophobic OTS lines is found under conditions, where polymer domain sizes are commensurate with the pattern periodicity. Next, we apply this method to pattern NPs using blends of PMMA and PS-CdS QDs via spin-coating onto OTS-patterned glass. Ultimately the method was extended to simultaneously pattern multi-NP functional assemblies using PS-CdS and a sample of PMMA-coated silver NP (PMMA-Ag). The specific interest in patterns of Ag NPs and CdS QDs is to provide a suitable proof-of-concept system for simultaneous multi-NP patterning. However, this system also has some interesting optical behaviour as a result of QD-surface plasmon interactions that is investigated in details. The challenge in PS-CdS/PMMA-Ag NPs patterning is the gelation as the solvent evaporates during spin-coating that restricts the NPs mobility and constraints their phase-separation. We show that adding homopolymers to the NPs blends prevents the overlap of approaching NP brushes and prevents the resulting gelation. Feature sizes were then fine-tuned by changing solution concentration and spin rate, in order to obtain NPs domains which can be surface-directed on OTS-patterned glass substrates.

Table of Contents

List of Tables

List of Figures

Acknowledgments

I would like to sincerely thank Professor Matthew Moffitt for introducing me to the fascinating field of polymer/nanoparticle assemblies. I am very grateful to him for his constant encouragement, patience and support from the beginning to the end of this work. I am deeply thankful for everything I learned from him; his enthusiasm in science and in delivering it, taught me to become a better scientist and a better teacher.

I would like to express my gratitude to our research collaborators: Professor Byron Gates, for kindly sharing the AFM and for many useful discussions, and Michael Wang, for his patience during long hours of AFM measurement and for his help with operating facilities of the 4D labs at the Simon Fraser University.

I would also like to thank Professor Frank van Veggel for sharing the fluorimetre and Dr. Enrico Bovero for his training and help on the instrument.

In addition, I would like to thank:

My group members; Joe Wang and Yunyong Guo for their support over the years. Former group member, Robert Cheyne, and our post-doctoral fellow, Dr. Celly Izumi, for supplying the PS-CdS sample.

All the Chemistry faculty and staff and fellow graduate students specially people in the Petch lab, for making the five years of my PhD studies, a truly great experience.

Last but not the least I would like to thank my parents and my husband for their endless support and my sister for taking care of my parents during the past five years that I have been away from home.

Dedication

This thesis is dedicated to my parents: my mother Zohreh Rouhfar and my father Iraj Harirchian-Saei, who have always supported me and been on my side as the greatest source of motivation and inspiration. In the last five years that I have been away from home, they went through many difficult stages of their lives and unfortunately I was not physically present with them; I could not be with my mother when she lost her parents and I could not be with my father when he started fighting with cancer but I have always been told by them that my success helps them stay strong even in the hardest situations. They have always made sacrifices to give me the best they could and I can never thank them enough.

Also, this thesis is dedicated to my husband, Enrico Bovero, who has been always there for me; who is the most loving husband and at the same time the most caring best friend. Thank you for all you do and thank you for being YOU, Enrico.

Chapter 1. GENERAL INTRODUCTION

1.1. Introduction

Controlled assemblies of semiconductor and metal nanoparticles (NPs) into ordered structures have applications in micro- and nanoscale devices with specific functions. The self-assembly of polymers provides new paths for controlling the spatial organization of NPs.[1-13] Polymers also offer additional benefits such as providing a matrix with tunable mechanical, optical and electronic properties for the resulting composite structures. Directing NP/polymer self-assemblies externally by using chemical-or topographical features of lithographically-patterned surfaces further improves the ordering and organization of nanostructures, which is the main objective of this work and will be discussed extensively in this thesis.

Quantum dots (QDs) are semiconductor NPs with optical and electronic properties that are intermediate between those of bulk semiconductors and discrete molecules. This is due to quantum effects arising from the confinement of electron-hole pairs, or excitons, in the material.[14-23]An electron-hole pair is bound on a characteristic length scale known as the *Bohr-radius*. When the Bohr radius is comparable to the size of the NP, excitons are confined in all three spatial dimensions, increasing their energy relative to the bulk material and giving rise to size-tunable optical properties (e.g. absorbance and fluorescence). QDs have a wide range of possible applications in the fields of quantum computing,[24]photovoltaics,[25] electronics[26] and biological imaging[27] due to their interesting and size-tunable optical properties.

Metallic nanocrystals are another group of NPs which have interesting optical properties mainly due to their broad and strong absorptions in the visible and near infrared spectral regions associated with surface plasmon (SP) excitations.[28-34] SP

excitations are attributed to coherent oscillations of conduction electrons upon resonant interaction with incident light.[28] The position, width, and intensity of SP bands depend on parameters such as the nature of the metal, the charge, size, geometry and size dispersity of the NPs, as well as the refractive index of the material at the NP surface.[28-34] Since the oscillations occur at the boundary of the metal and the surrounding medium, SPs are very sensitive to any change in the surroundings; for instance, the adsorption of any molecule on the metal surface shifts the position of SP band. This high spectral sensitivity makes metal NPs good candidates for various applications in the fields of sensing.[35-37] Metal NPs also have applications in electronics and optics.[38-44] They have the ability to modify the optical properties of luminescent materials; for example, they can couple with the fluorescent emission of chromophores, such as QDs, and effect either the enhancement or quenching of the emission.[45-55] The relative importance of these effects can be controlled by adjusting the distance between metal NPs and QDs or other chromophores.[56]

An important challenge in the field of nanotechnology is to control the spatial distribution of inorganic NPs and to organize them into specific device-oriented structures. The primary difficulty is that semiconductor QDs and metallic NPs, discussed above, are generally insoluble in organic media such as solvents and polymers, which leads to poor dispersal and uncontrolled phase-separation.[21] Therefore, in order to counter this dispersal problem, organic small molecules[57-60] or polymers[21, 61-74] have been used as ligands on the surfaces of NPs to improve their solubility as well as their stability and processability. The properties of surface-functionalized inorganic colloids depend on the stabilizer that is used on their surfaces; the presence of polymer layers on the surface of

NPs offers the advantage of increasing their compatibility with an external polymeric matrix as well as providing a medium with desirable mechanical properties, which is required for many NP-based devices; appropriate polymer layer can also results in controlled assemblies of NPs due to interactions between surface polymer chains and the surrounding environment.[75-82]

In general, there are two fundamental assembly approaches: bottom-up and top-down. Bottom-up assemblies are naturally driven by intermolecular forces while for top-down assemblies molecules are manipulated by external forces. For polymers, two examples among many bottom-up self-assemblies include polymer/polymer phase-separation or block copolymer microphase-separation. Top-down techniques on the other hand are those for which the assemblies are directed. Examples for top-down method include using chemical-or topographical features of lithographically-patterned surfaces for organizing self-assemblies; this allows fabrication of more complex and engineered structures. The combination of bottom-up and top-down approaches can be utilized to organize assemblies such as the self-assemblies of polymer-stabilized metal and semiconductor NPs[83] into patterned structure, as will be demonstrated in the thesis;[84-86] this provides a high level of spatial controllability because the self-assembled structures are guided by lithographically-defined features on the surface.[84-86]

The main goal in this thesis is to provide new routes for combining these two assembly approaches in order to organize polymers and NPs assemblies in to ordered and device-oriented structures. Self-assembly of block copolymers at the air-water interface[87] and phase-separation of the immiscible polymer blends are the two bottom-up processes, which are combined with a soft lithographic, microcontact printing (μCP), top-down

approach to direct the assemblies of polymers and QDs in the earlier parts of the work (Chapter 3 and 4, respectively). Then in chapter 6 we demonstrate a new methodology to simultaneously pattern multi NP types into patterned structures; this is shown for the blend of QDs and metallic NPs.

The remainder of the present chapter is divided into eight sections. Section 1.2 provides a general introduction to polymers and block copolymers, including a description of polymer-polymer phase-separation, which is a process relevant to Chapter 4-6 of this work. Section 1.3 is devoted to an introduction to semiconductor NPs and Section 1.4 is on metallic NPs. Section 1.5 provides background information on Langmuir-Blodgett (LB) films, including a description of the formation of Langmuir monolayers at the air-water interface and their transfer to solid substrates using the LB technique that is applicable to Chapter 3. In section 1.6, a detailed review of related works on surface-directed assembly of phase-separating polymer blends and block copolymers is presented. Section 1.7 describes important conceptual and technical details on the main instrumental techniques employed in this thesis, including atomic force microscopy (AFM), laser scanning confocal fluorescence microscopy (LSCFM), static and dynamic light scattering (SLS and DLS), and absorption and fluorescence spectroscopies. Finally, section 1.8 provides a summary of the content of the remaining chapters of the thesis.

1.2. General Background to Polymers and Block Copolymers

1.2.1. Polymer Terminology and Definitions

A *polymer* is a large molecule made up of many smaller molecules called *monomers* which are covalently bonded together.[88] Once they are incorporated into a polymer, monomers are generally referred to as *repeat units*, with the size of the polymer being described by the number of repeat units, which is called the *degree of polymerization*. Depending on the bonding arrangement of monomers in the polymer, different polymer architectures, such as linear, branched, or interconnected networks can be achieved. When a polymer is built up from only one type of monomer the product is called a *homopolymer*. If more than one type of monomer is used, then the product is a *copolymer*, which can be further classified based on the relative arrangements of the different types of repeat units.[89] The four main classifications of copolymers are depicted in Figure 1.1, where A and B represent two chemically-different repeat units covalently bonded to neighboring repeat units. A *random copolymer* contains an essentially random, or statistical, distribution of A and B repeat units along the copolymer chain. In an *alternating copolymer*, repeat units A and B are incorporated in an alternating fashion along the chain. When sequences, or blocks, of A repeat units are connected by covalent bond sequences, or blocks, of B repeat units in a linear chain, the resulting copolymer is called a *block copolymer*. Depending on the number of blocks making up the copolymer chains, *diblock* (two blocks), *triblock* (three blocks), *tetrablock* (four blocks) or *polyblock* (many blocks) *copolymers* can be formed. Finally, copolymers in which blocks of one repeat unit are grafted as branches along a backbone of another repeat unit are known as *graft copolymers*.

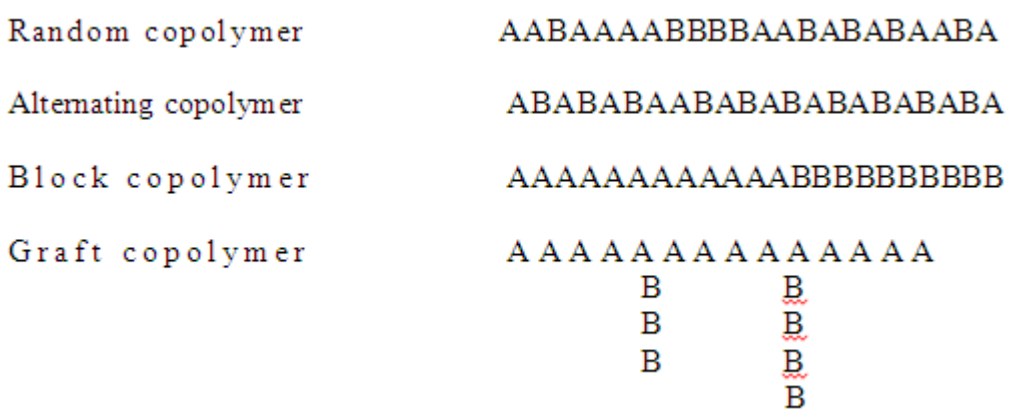

Figure 1.1. Types of copolymers synthesized from monomers A and B.

Unlike small organic molecules, which can be characterized by a single, well-defined molecular weight, the statistical nature of most polymerization reactions leads to a molecular weight distribution for a given sample (Figure 1.2).[90]

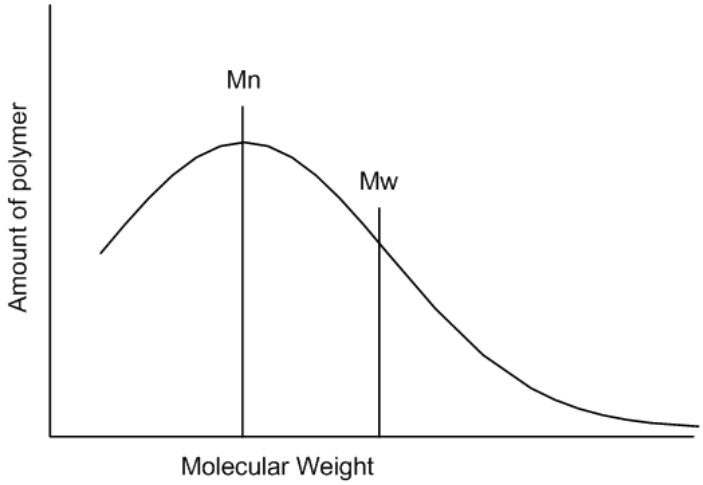

Figure 1.2. An example of a typical molecular weight distribution for a theoretical polymer sample, highlighting the positions of defined molecular weight averages.[90]

For a given molecular weight distribution, different types of molecular weight averages with different numeric values (Fig. 1.2) can be determined, depending on the method of characterization. The *number-average molecular weight*, M_n, is defined as:

$$M_n = \frac{\sum_i N_i M_i}{\sum_i N_i} = \frac{\sum_i w_i}{\sum_i (w_i / M_i)} \qquad (1.1)$$

where N_i is the number of molecules of species i with molecular weight M_i, and w_i is the total weight of all molecules of species i. Based upon this definition, the M_n value is sensitive to the *number of molecules* of each species i present in the system, and M_n is therefore the average value determined by techniques that measure colligative properties of polymer solutions (e.g. osmometry, which measures solution osmotic pressure).

Another quantity which is commonly reported for polymers is the *weight-average molecular weight*, M_w, defined as:

$$M_w = \frac{\sum_i w_i M_i}{\sum_i w_i} = \frac{\sum_i N_i M_i^2}{\sum_i N_i M_i} \qquad (1.2)$$

As expressed in Equation 1.2, M_w is sensitive to the *weight of molecules* of each species i present in the system. The main characterization technique that measures M_w values is static light scattering (SLS), in which the contribution of each molecule or chain to the light scattering intensity increases with its size. As illustrated in Fig. 1.2, M_w is

more strongly weighted toward the higher end of the molecular weight distribution than M_n.

The molecular weight distribution width for a polymer sample can be described using the ratio of M_w to M_n, which is known as the *polydispersity index* (*PI*):

$$PI = \frac{M_w}{M_n} \qquad (1.3)$$

If all chains in a polymer sample are exactly the same molecular weight, then $PI \equiv 1$ and we refer to the sample as being *monodisperse*. However, typical *PI* values for synthetic polymers are closer to 2, with minimum values as low as 1.05 being achievable using specialized "living" polymerization methods such as anionic polymerization.[90]

Dividing the average molecular weight of a polymer sample by the molecular weight of an individual repeat unit, M_0, gives an average number of repeat units per chain, or the *degree of polymerization*. Each of the above molecular weight averages can be used to calculate a degree of polymerization. For example, the number-average degree of polymerization (x_n) is defined as:

$$x_n = \frac{M_n}{M_0} \qquad (1.4)$$

1.2.2. Polymer-Polymer Phase-separation

Immiscible polymer blends have a tendency to phase-separate below a critical temperature in order to minimize the extent of enthalpically-unfavourable contacts.

This is the opposite process of mixing. The tendency of polymers to mix or demix depends on the change in the Gibbs free energy of the mixing process (ΔG_{mix}); a positive ΔG_{mix} leads to spontaneous demixing, as defined by equation 1-5: [91]

$$\Delta G_{mix} = \Delta H_{mix} - T\Delta S_{mix} \qquad (1.5)$$

Where ΔH_{mix} is the change in enthalpy, T is the absolute temperature and ΔS_{mix} is the change in entropy. The sign of ΔG_{mix} is determined by the competition between ΔH_{mix} and ΔS_{mix}. ΔH_{mix} is usually a positive value because there is usually stronger attraction between similar molecules (for example x and x or y and y) than between dissimiliar molecules (x and y). For polymer blends, these two terms can be written based on Flory-Huggins (FH) theory; FH is a mathemathical model describing the thermodynamic of polymer solutions using a lattice model for calculating the entropy change based on statistical calculation of the number of ways that the molecules of polymer and solvent can be arranged on the lattice.[92]

ΔH_{mix} and ΔS_{mix} can be described as equation 1.6 and 1.7, respectively:[91, 92]

$$\Delta S_{mix} = -R\,(\emptyset_1/r_1\, ln\, \emptyset_1 + \emptyset_2/\, r_2\, ln\, \emptyset_2) \qquad (1.6)$$

$$\Delta H_{mix} = RT\, \emptyset_1 \emptyset_2 \chi_{12} \qquad (1.7)$$

where $\emptyset_i$ is the volume fraction of the component i, r_i is the number of segments in polymer i, T is the absolute temperature, R is the gas constant, and χ is the FH parameter which describes the interaction between the two components (a high positive χ indicates

repulsive interactions and a negative χ indicates attractive interactions). By substituting equations 1.6 and 1.7 into 1.5, for polymer blends composed of polymer 1 and 2, ΔG_{mix} (based on FH theory) can be written as below$_x$:

$$\Delta G_{mix} = RT\,(\emptyset_1/r_1\ ln\ \emptyset_1 + \emptyset_2/\ r_2\ ln\ \emptyset_2) + RT\,\emptyset_1\emptyset_2\chi_{12} \qquad (1.8)$$

$$\Delta G_{mix} = RT\,(\emptyset_1/r_1\ ln\ \emptyset_1 + \emptyset_2/\ r_2\ ln\ \emptyset_2 + \emptyset_1\emptyset_2\chi_{12}) \qquad (1.9)$$

χ_{AB} for most polymer pairs is positive indicating unfavorable interaction between dissimilar chains (relative to interaction between similar chains), unless there are specific interactions such as H-bonding between the dissimilar chains; this results in a positive ΔH_{mix}. ΔS_{mix}, which is the combinatorial entropy of mixing for polymer blends, is defined by the number of ways that the chain segments of A and B can be arranged in a lattice model. In a mixing process ΔS_{mix} is increasing; therefore, ΔS_{mix} is a positive value and the term $-T\Delta S_{mix}$ in equation 1.5, is negative; however, for high M_w polymers this contribution is small because ΔS_{mix} for polymers is insignificant compared to that of small molecules solutions as polymers are chains of covalently bonded repeating units; ΔS_{mix} for n small molecules of A or B is $\Delta S_{mix}=2nkln2$ but for polymers composed of x monomers, the number of ways that chains can be arranged on the lattice model is x time (x usually large number) smaller ($\Delta S_{mix}=2xnkln2$) than that of small molecules. As the result, ΔG_{mix} for polymer blends is generally a positive value resulting in demixing of polymer blends.[91, 92]

Plotting ΔG_{mix} against composition (X) for a polymer blend yields in a curve similar to the one shown in Figure 1.3 a. Tangential line to the curve meets the curve at

two points (shown as B) representing the binodal points; the inflection points on the curve (shown as S) are representing the spinodal point. Region between two S points is called spinodal region and two regions between S and B points are called binodal regions. Lowest ΔG_{mix} for compositions in region in between two B points (including both spinodal and bimodal regions) is obtained when the blend decomposes into two phases with composition of B points; therefore, in these regions phase-separation occurs. In spinodal region, the blend is unstable to small fluctuations in composition and decomposes by a mechanism called spinodal decomposition, where first different regions with compositions close to points B are forming and then by further diffusion between the regions the compositions are reaching the B points. In binodal region, the blend is metastable meaning that large fluctuations result in the decomposition, called binodal decomposition, which occurs via nucleation of droplets with composition of one of the points B and then growth of these droplets via diffusion. Binodal and spinodal regions are shown on the phase diagram (plot of temperature against X) in Figure 1.3 b [91]

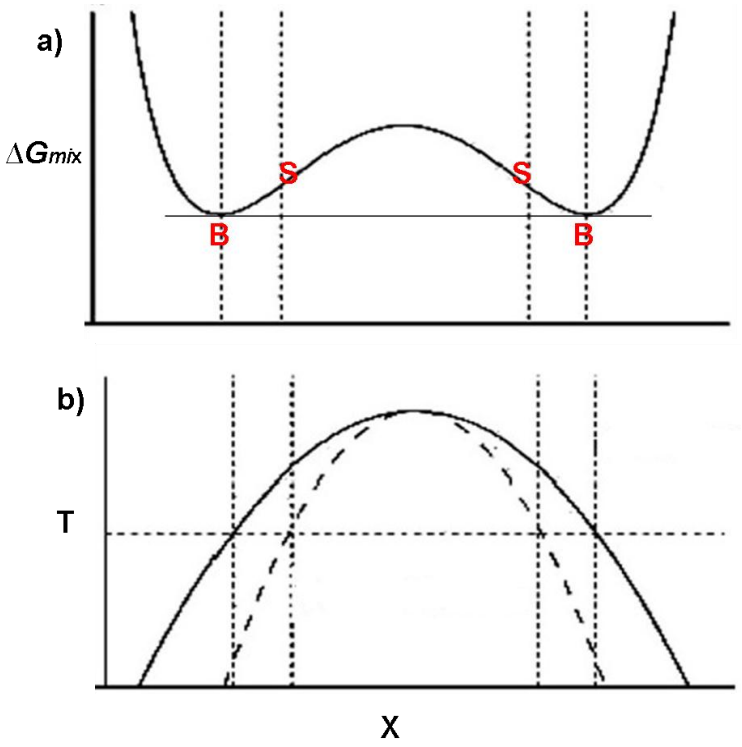

Figure 1.3. Typical (a) ΔG_{mix} against X plot and (b) the phase diagram for polymer blends displaying binodal and spinodal regimes.[91]

1.3. Semiconductor Nanoparticles or Quantum Dots (QDs)

Since the late 1980s, semiconductor nanoparticles, also known as QDs, have attracted significant attention in the field of material science. These NPs, which have diameters in the range of 1 to 10 nm, are a class of materials with behaviour that falls in between that of the molecular and bulk solid. QDs exhibit unique physical properties that give rise to many potential applications in biology, computing, photovoltaic and light emitting devices.[24-27, 93-95] Two fundamental factors, both related to the size of the nanocrystal, are responsible for the unique size-dependent properties of QDs: the first is the large surface-to-volume ratio of the particles compared to bulk materials; the second factor is their different electronic structure due to the quantum confinement effect. Optical and electronic properties of QDs are highly dependent on their size; thissize-

dependence is attributed to the quantum confinement effect, which isdescribed in the following section.

1.3.1. The Quantum Confinement Effect

In bulk semiconductors, energy levels of electronic states are so closely spaced that they form virtually continuous energy bands.[96] Valence bands (formed from filled atomic bands) and conduction bands (formed from unfilled atomic bands) are separated by an energy band gap (E_g), which is characteristic of the material. Given enough energy ($\geq E_g$), an electron in a valence band can be elevated into the conduction band, leaving a positive hole behind; the resulting electron-hole pair is described as an *exciton*. [96]

For nanocrystals because the size of particle is smaller than or comparable to the size of the *Bohr exciton radius*, the delocalized band structure becomes quantized and the energy of the exciton increases. Many theoretical and experimental studies have been carried out to describe this phenomenon.[14-23, 97] Among them is Brus[97] with his particle-in-a-box model, where the exciton is considered the particle which is confined in a box (the spherical nanoparticle). In his model, the infinitely high potential at the surface of the nanoparticle confines the exciton. Using a quantum mechanical solution, Brus calculated the energy of the first exciton (E^*) in this spherical box of radius R to be: [97]

$$E^* \cong E_g + \frac{\eta^2 \pi^2}{2R^2}\left[\frac{1}{m_c} + \frac{1}{m_h}\right] - \frac{1.8e^2}{\varepsilon R} + \ldots \qquad (1.10)$$

where E^* is the energy of the exciton, E_g is the bandgap energy of the bulk semiconductor, R is the radius of the particle, m_e and m_h are the masses of electrons and holes in the lattice, e is the charge of an electron and ε is the permittivity. As the above equation implies, the positive second term, which is the confinement term is inversely proportional to the square of the radius. Hence, a decrease in the particle size increases the confinement term and consequently increases the exciton energy. The negative third term is the Columbic term describing the attractive electron-hole electrostatic interactions. This term is smaller than the confinement term and is proportional to the inverse of the distance between the electron and the hole, and therefore, decreases the energy of exciton for smaller radius sizes. Overall, this model predicts an increase in the energy of the exciton by a decrease in the particle size.[97]

The quantum confinement effect can be seen in the absorption spectra of a series of semiconductor NPs of different mean sizes. As shown in Figure 1.4 for cadmium sulfide (CdS) QDs, the absorption peak blue shifts as the size decreases. For bulk CdS, the exciton Bohr radius is ~ 5.8 nm; therefore, particles much larger than this have electronic and optical properties identical to the bulk material, whereas NPs with smaller sizes exhibit greater exciton energies.[14]

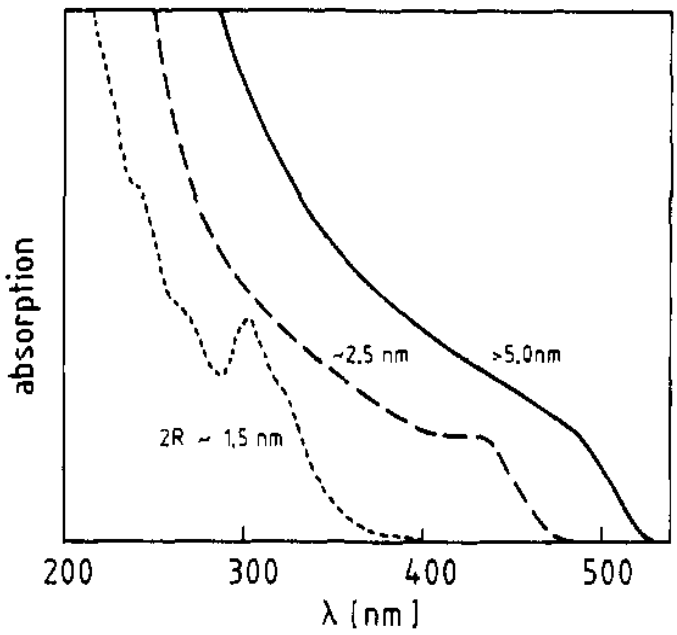

Figure 1.4. UV -Vis absorption spectra of CdS nanoparticles of different average particle sizes.[14]

1.4. Metallic Nanoparticles

Studying noble metal NPs is a fast expanding area due to the various applications of these NPs in the fields of catalysis, biosensing, [35-37] electronics and optics.[38-44] Their optical properties can be attributed to their broad and strong absorption in the visible spectral region associated with the excitation of collective electron oscillations in the metal referred to as surface plasmons (SPs).[28-34]

There are different factors affecting the position, width, and the intensity of SP bands, including the dielectric constant of the surrounding media, the electronic interactions between the stabilizer (ligand attached to the NP cores) and the NP core, the electronic interactions between NPs, particle surface charge, size, geometry and polydispersity.[28-34]

The dielectric constant of the surrounding media affects both the position and the intensity of the SP band;[28] it has been shown [29-30] that by increasing the dielectric constant a red shift occurs. The position and bandwidth of SP bands are also strongly affected by the size of metallic NPs; it has been demonstrated [31] that an increase in the size causes a red shift and broadens the SP band.[32]

There are several methods for the synthesis of metallic NPs including chemical reduction,[98] photochemical reduction,[99] reverse micelle process,[100-102] micelle assisted techniques[103] and electrochemical synthesis.[104-105] Generally the synthesis of a stabilized metal NP starts with the reduction of a metallic salt by a mild reducing agent in the presence of the desired colloidal stabilizer.[98-105]

Metallic NPs have the ability to modify the optical properties of luminescent materials. This has been shown for QDs, quantum wells, semiconductor nanowires and Si nanocrystals.[106-124] Theoretical[125-128] and experimental studies attribute this to the SPs of metallic nanostructures. It has been shown that[106-124, 45-46] localized electric fields near the surface of the metals that are induced by SPs, can couple with the excitation field and intensify the radiation. SPs can also enhance the emission by coupling with the emitted light from the radiative decay of the emitter (energy transfers from the emitter into the dipole mode of SP).[47-48, 116-120] One of the most important parameters affecting the interaction between SP of metals and PL of QDs is the distance: enhancement effect occurs when the separation between the metal and emitter is small because the field induced by SP is highly localized at the metal surface and decays rapidly away from it but putting the molecules too close to each other (reported in the range of 5-10 nm)[126] can result in luminescence quenching due to non-radiative energy transfer between the

excited emitter and metal when the distance is too small; in other word non-radiative dipole-dipole coupling dissipates the energy and quenches the PL.

1.5. Langmuir-Blodgett Transfer (LB)

In Chapter 3, the transfer of polymer/NP assemblies from the air-water interface to chemically-patterned glass substrates using the LB technique is described. Therefore, a brief introduction to the LB method is presented in this section. Some general information is also provided on the behaviour and orientation of amphiphilic molecules at the air-water interface, the formation of Langmuir monolayers, and the characterization of surface pressure-area isotherms.

1.5.1. Amphiphilic Molecules at the Air-Water Interface

Liquids have the tendency to contract their surfaces to a minimal exposed surface area. This property of liquid surfaces is known as surface tension (γ), and is caused by the force imbalance between the molecules in the bulk and at the surface.[130] In bulk, molecules of liquid are pulled equally in every direction by neighboring like molecules which results in a zero net force, whereas at the surface there is an inward non-zero net force on the molecules that creates internal pressure.[130] There are many different methods available to measure the surface tension of liquids.[131-135] Among them is the Wilhelmy plate technique, in which a thin plate is used to measure the equilibrium surface tension at an air-liquid interface.[131] As illustrated in Figure 1.5, the Wilhelmy plate is oriented perpendicular to the interface and is partially immersed in the liquid. The Wilhelmy plate is generally made of glass or platinum which is roughened for

complete wetting and has a width much greater than its thickness. The force exerted on the plate due to γ of the liquid can be measured by a microbalance attached to the plate. The force applied on the Wilhelmy plate (F) is the result of liquid wetting the plate and can be written as equation 1.11:[131]

$$F = 2(w_p + t_p)\gamma\cos\theta \qquad (1.11)$$

Where $2(w_p + t_p)$ is the perimeter of the wetted plate and θ is the contact angle between the liquid and the plate along the three-phase junction (contact line between the liquid subphase, air, and the solid plate). Since liquid fully wets the surface of the Wilhelmy plate, $\theta = 0$ and $\cos\theta = 1$; also, since the thickness of the plate is negligible compared to its width ($t_p << w_p$), we get $F \cong 2w_p\gamma$. This describes the relation between the measured force, the dimensions of the plate and the surface tension of the liquid subphase.

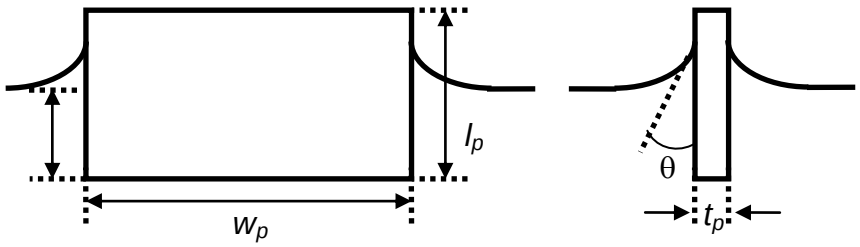

Figure 1.5. Side and front view illustration of a Wilhelmy plate submerged in a liquid subphase.[136]

As described above, surface tension is a property of liquids that is caused by cohesive forces between like molecules. A more general property describing the adhesive force between any two substances is the interfacial tension, where the two

substances may be solids, liquids or gases.[130,131] In fact, one may think of the surface tension of a liquid as a special case of an interfacial tension between the liquid and the air above it. Emulsification and phase-separation in heterogeneous systems are examples of processes caused mainly by the interfacial forces.[131]

Both interfacial and surface forces play an important role in the behaviour of amphiphiles at the air-water interface.[131] Amphiphile is originally a Greek word composed from "amphis" meaning "both" and "philia" meaning "love". It describes the molecules which have both hydrophilic (water-loving) and lipophilic (fat-loving, or hydrophobic) properties. Long chain fatty acids are examples of amphiphilic molecules with an acid-functionalized head and a fatty tail. It is well established that amphiphiles form monolayers at the air-water interface with the hydrophilic head oriented into the water and the hydrophobic tail oriented away from the water toward the air;[137-138] these floating monolayers are known as Langmuir films.

In a Langmuir film when surface molecules are far apart from each other, the surface density (Γ) is small, and molecules move freely at the surface with minimum intermolecular interactions. These films are said to be in a gaseous state, due to the analogy with a three-dimensional (3D) gas.[134] Increasing Γ (for example, by compressing the film using two moveable barriers) brings the molecules closer together, giving rise to the formation of a two-dimensional (2D) liquid state. Further increase in Γ results in the formation of a solid state, where the molecules are tightly packed and their lateral movement at the surface is highly constrained.[134] These three states are depicted in Figure 1.6.

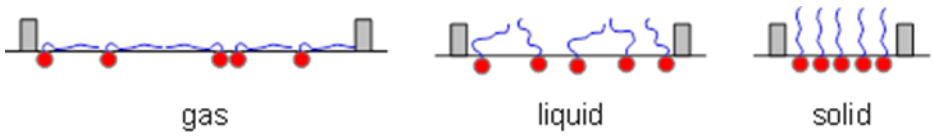

Figure 1.6. Three states of Langmuir films at various Γ.

The presence of amphiphilic molecules on the surface of the liquid disrupts the cohesive energy of the surface liquid molecules and thus lowers the surface tension. The difference between the surface tension of the monolayer film (γ) and that of the air-water interface (γ_0) is referred to as the surface pressure (π):[131]

$$\pi = \gamma_0 - \gamma \qquad (1.12)$$

The surface pressure is usually determined by measuring changes in surface tensions relative to the clean liquid surface, using a Wilhelmy plate as described earlier.[136] Monitoring the surface pressure as a function of the area of the water surface available to each molecule, known as mean molecular surface area (A), during compression of the film at a constant rate and temperature provides insight into conformational changes of the molecules at the interface as they undergo transitions between above-mentioned states upon film compression; the output of such a measurement is a plot called a $\pi - A$ isotherm.[136]

A typical $\pi - A$ isotherm, which illustrates sections corresponding to each state (represented in Fig. 1.6) is shown in Fig. 1.7.[136] At large total surface areas, molecules are in their gaseous state and decreasing the area at this state causes a very little increase in the surface pressure; compression of the monolayer decreases A and brings the

molecules close enough to each other to interact. At *A* corresponding to the beginning of the liquid-gas plateau in Figure 1.7 the liquid-gas transition occurs; after completion of this transition all molecules are in liquid state and as illustrated in Figure 1.7, for this phase there is a stronger increase in π with decreasing the *A* until the second transition (liquid-solid) takes place. In the solid phase, molecules are closely packed and decreasing the *A* increases the π dramatically up to the point that the 2D monolayer collapses into a 3D structure.[136-138]

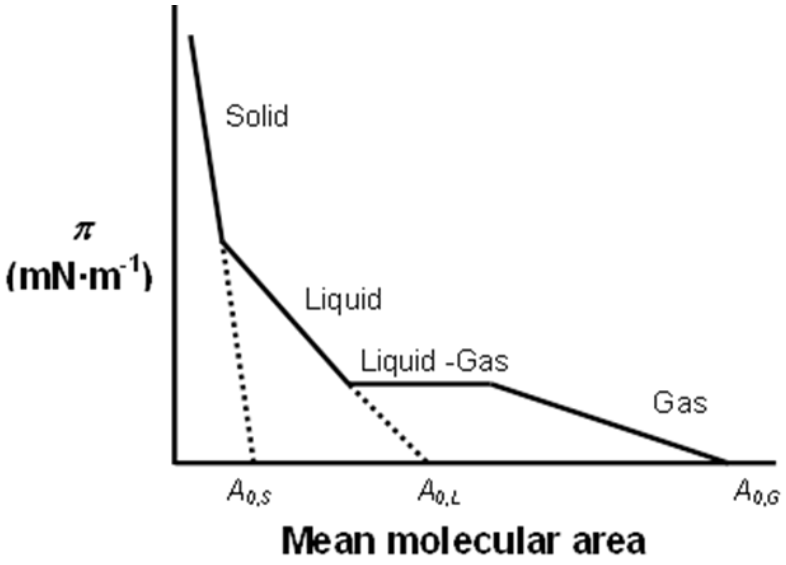

Figure 1.7. Simplified π – *A* isotherm illustrating the gas-, the liquid – gas phase transition plateau, the liquid-, and the solid- like phases. $A_{0,\,L}$ and $A_{0,\,S}$ are the limiting mean molecular areas of the liquid and solid states respectively.

Three important parameters that can be determined from an isotherm for a particular molecule at the water surface are the critical mean molecular area of the gas, liquid and solid ($A_{0,g}$, $A_{0,l}$ *and* $A_{0,s}$, respectively), which can be measured by extrapolating the isotherm to $\pi = 0$, as shown in Figure 1.7.[136, 139-141] The monolayer compressibility (C_m), which depends on intermolecular forces and is a characteristic of the monolayer,

can also be determined from the isotherm; using the same analogy that describes the compressibility of bulk materials in 3D, C_m of a monolayer in 2D can be expressed as the area change relative to a pressure change at a constant temperature.[139]

$$C_m = \frac{-1}{A}\left(\frac{\partial A}{\partial \pi}\right)_T \qquad (1.13)$$

In Chapter 3 of this thesis, Langmuir monolayers of amphiphilic block copolymers are prepared and studied at the air-water interface. Amphiphilic block copolymers have a hydrophilic and a hydrophobic block;[89] their Langmuir films form as a result of the interplay of repulsive interactions between the hydrophobic blocks and water and attractive interactions between the hydrophilic block and water. As a result, hydrophobic chains form nanoscale aggregates of various morphologies at the water surface as a result of spreading and solvent evaporation at zero surface pressure, surrounded by peripheral chains of the hydrophilic block. Depending on the type, composition and concentration of the block copolymer, different aggregate morphologies can be obtained at the air-water interface including dots, spaghettis, continents, ring and chains.[78, 142-144]

1.5.2. Langmuir-Blodgett (LB) Films

Langmuir films formed at the air-water interface can be transferred to a solid substrate to form a LB film by vertical withdrawal of an immersed substrate from the water subphase with a floating Langmuir monolayer at its surface.[145] Transferring the

Langmuir films to a solid substrate is advantageous for characterization, optical, electrical, and biological studies and applications.[145,146] During the course of LB transfer, the surface pressure is held constant at a desired transfer pressure, by two moveable paddles which are electronically controlled through a feedback loop. In order to characterize the efficiency of a transfer process, a term called transfer ratio (*TR*) is used which is the ratio of the monolayer transfer from the interface on to the solid surface. *TR* is defined by equation 1.14 using the change in trough area during transfer (ΔA_T) and the total surface area of the withdrawn substrate (A_S). *TR* should be around 1.0 for an optimized transfer.[136]

$$TR = \frac{\Delta A_T}{A_S} \qquad (1.14)$$

1.6. Surface-Directed Polymer Assemblies on Patterned Surfaces

Patterning polymers is advantageous for the fast growing field of nanomaterials mainly because they open up new paths toward controlling NP organization on a combination of length scales; such patterned structures offer vast potential applications for optical and electronic devices.

As mentioned earlier, there are two general approaches to assemble polymers and other molecular building blocks: 1. “bottom-up” (self-assembly) and 2. “top-down” (directed assembly). Bottom-up assemblies are naturally driven as the result of intermolecular forces while top-down assemblies are externally directed.[84-86] For polymers, as described earlier (in section 1.2), spontaneous polymer-polymer phase-

separation[91] and block copolymer microphase-separation[87] are examples of bottom-up self-assembly. These self- assemblies can be combined with an externally directed approach for example use of lithographically-defined features of a surface for an improved ordering and spatial controllability over the formed structures. [84-86]

A wide range of lithographic techniques have been used to fabricate patterned surfaces by creating topographical or chemical features on the substrates. These pre-patterned surfaces can be used to improve ordering and to direct the placement and orientation of the bottom-up assemblies of phase-separating polymer blends[147-156] or microphase-separating block copolymers.[157-179] Topographically-patterned surfaces promote ordering by imposing a topographic constraint on assembling polymer chains that laterally confines them during self-assembly[156,167-179] Chemically-patterned substrates direct the placement of self-assembled structures by offering regions with different surface energies which direct the placement of selective chemical components of polymer blends or block copolymers based on their preferential wetting.[147-155,157-166] In the remaining part of this section, surface pattern-directed phase-separation of polymers and surface pattern-directed microphase-separation of block copolymers are each discussed individually.

1.6.1. Surface-Directed Phase-separation of Polymer Blends on Patterned Surfaces

On chemically patterned surfaces, which are chemically-heterogeneous with regions of various surface energies, the morphology of demixed polymer domains is influenced by both processes of spinodal decomposition within the film (described in

section 1.2.2) and preferential wetting of demixed components in different regions of the chemically-heterogenous substrate. Therefore, in a blend of two chemically-different polymers, following phase-separation the more polar polymer component will wet the high-surface energy areas of the patterned substrate, while the less polar polymer will be directed to the low-surface energy regions. An example for this is illustrated in Figure 1.8, which shows how demixed polymer domains are addressed to different regions of a chemically-patterned surface based on their preferential wetting to form a patterned polymer film.[154]

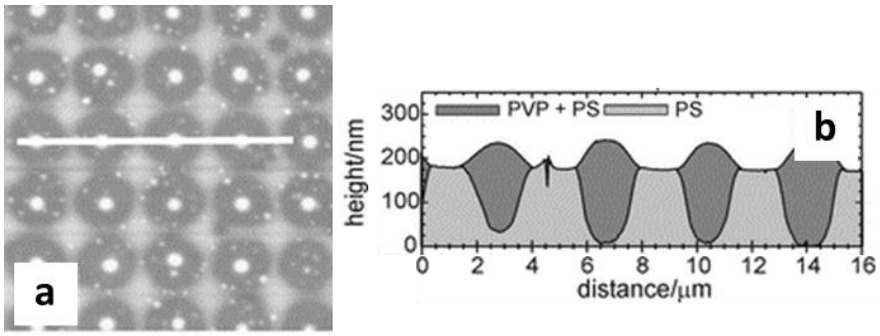

Figure 1.8. Polystyrene (PS)/ Polyvinylpyrrolidone (PVP) polymer blend on a chemically-patterned substrate prepared by μCP 7-octenyltrichlorosilane self-assembled monolayer on to the silicon substrtae with 4 mm period square arrays pattern of 2 mm diameter circles; (a) AFM image and (b) cross-section (along the white line in image a) of the patterned polymers.[154]

Surface pattern replication in polymer films is affected by many parameters, which will be discussed fully in chapter 4, including film thickness[148], composition matching between the blend volume ratio and the area ratio of the patterned surface,[153-154]and length scale matching between the pattern periodicity (λ) and the inherent size of demixed polymer domains (characteristic length scale of phase-separation) (*d*).[148,153-154]*d* can be quantified by fast Fourier transforms (FFT) on morphological features in AFM

images as the correlation lengths of the surface morphologies (Λ_m),determined based on the dominant wave vectors, q_m, (from a Gaussian fit to the main scattering peak) of FFT-AFM power spectra(plots of intensity $I(q)$ vs. scattering vector), as$2\pi/q_m$.[81]

Polymer blend films are commonly prepared using spin-coating technique on a substrate that is rotating at high speed. During spin-coating there are two forces acting on the liquid: centrifugal and viscous forces.[155] Centrifugal forces are directly proportional to the spinning rate (ω) and viscous forces are proportional to the polymer solution concentration (C_p); therefore, film thickness (h) can be adjusted by changing these two parameters: h increases by decreasing ω and increasing C_p. [152, 153, 182] The size of phase-separated domains (d) is also affected by C_p and ω; the empirical scaling law describing this is $d \sim C_p / \omega$ ½ , [148,152, 153, 182] that expresses a direct proportionality between d and C_p, and a inverse proportionality between d and $\omega^{1/2}$; Therefore, R can be adjusted to match the periodicity of the underlying pattern in order to obtain a well ordered patterned morphology on both topographically[156] and chemically[148-155] patterned surfaces.

1.6.2. Surface-Directed Microphase-separation of Block Copolymers on Patterned Surfaces

The difference between the phase-separation of copolymers with that of the polymer blend, discussed in previous section, is that the phase-separation of block copolymers cannot proceed to macroscopic extents, because the immiscible blocks are covalently-bonded; therefore, microphase-separation occurs which leads to the formation of nanoscale domains of various morphologies such as: spherical, lamellae, and cylindrical structures (shown in Figure 1.9).[180-184] These structures are determined by the

volume fraction of polymer segments A and B in the diblock copolymer. When the volume fraction of block A is less than 20% of the total volume of the copolymer, spheres rich in chains of A are formed in the matrix of B. When the volume fraction of A is increased up to 40%, cylinders are formed in a matrix of B. Up to 60% A, lamellae of alternating A and B bilayers are formed. Above that, cylinders are formed in a matrix of A and above 80% A, spheres of B are formed.

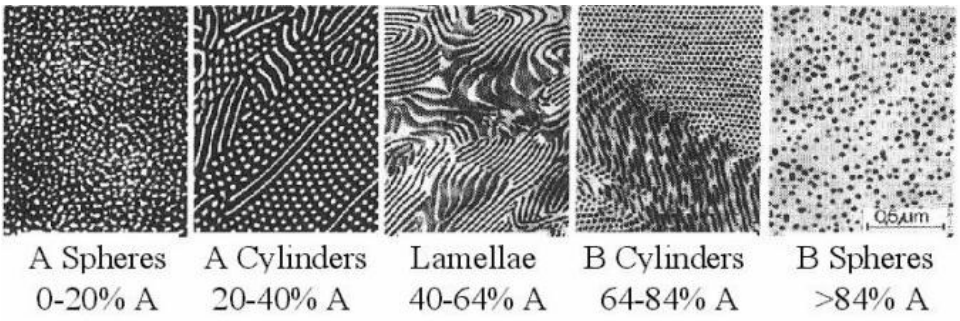

Figure 1.9. TEM images of microphase-separated diblock copolymers at various volume fractions of A.[185]

As mentioned earlier, both topographic[168-173,176-179] and chemical patterns[157-159] have been utilized to guide the placement, orientation and ordering of block copolymer microdomains. For cylindrical microdomains, the orientation of cylinders can be controlled when the block copolymer is allowed to self-assemble on a chemically- or topographically-patterned substrate [168-171] (an example is shown in Figure 1.10 a). Patterning spherical microdomains is also shown to increase the ordering of spheres into hexagonally-packed structures (Figure 1.10 b and c).[170,176-179] It is shown that ordering in block copolymer microdomains is achieved when the periodicity of the

lithographically defined pattern (λ) is in the same order as the natural length scale of the microdomain structure (*L*).[168-170,157-159]

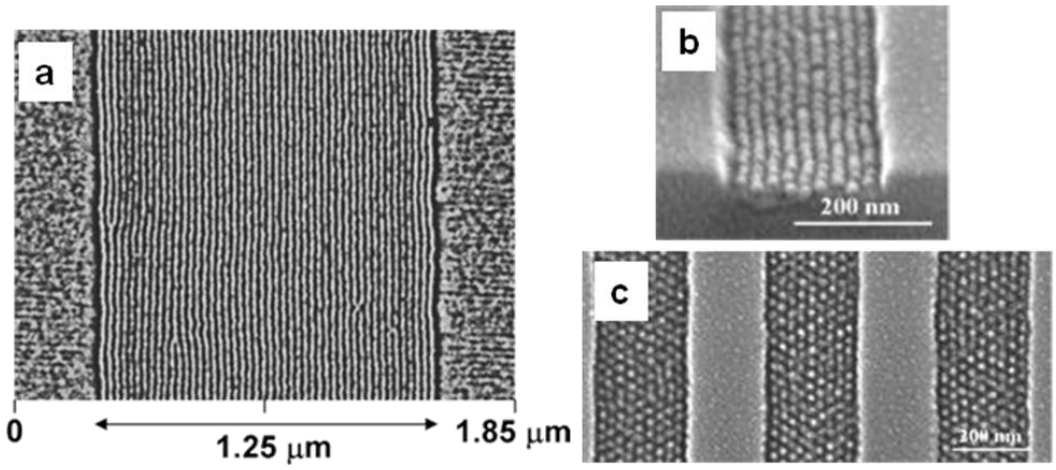

Figure 1.10. Examples for patterned block copolymer microdomains: TEM images of (a) patterned cylindrical polystyrene-*block*-poly (ethylene-*alt*-propylene) (PS-*b*-PEP) diblock copolymers on a topographically-patterned silicon nitride substrate;[169] cylinders align themselves along the edges of the channel , (b) angled-view and (c) top-view of patterned polystyrene-*block*-poly (2-vinylpyridine) (PS-*b*-PVP) spherical microdomains on topographically-patterned grooved silicone wafer.[176]

1.7. Instrumentation

The focus of this thesis is the patterning of polymer/NP assemblies. In order to characterize the patterned films, the primary technique utilized is atomic force microscopy (AFM), which allows topographic imaging of non-conductive samples; this is the case for most of our samples, which consist of non-conductive polymers (PS, PEO, PMMA) on non-conductive substrates (OTS/glass). However, AFM only probes the surface topology of the films whereas for the NP-containing polymer films, an imaging technique that reveals the presence of the embedded NPs within a polymer phase is of

interest. For this matter, laser scanning confocal fluorescence microscopy (LSCFM) was employed which probes embedded QDs. LSCFM is a diffraction-limited technique and thus, does not resolve individual QDs. However, it is useful in probing the distribution of QDs since they are photoluminescent and are localized in micron-scale domains within the films that can be resolved relative to the non-fluorescent background. A brief description of AFM and LSCFM imaging techniques is provided below. Other main characterization techniques employed in this work include laser light scattering (LS) for characterization of the synthesized silver (Ag) NPs (Chapter 5), and absorption and photoluminescence spectroscopies for optical characterization of CdS and Ag NPs blends, for the work presented in chapter 5.

1.7.1. Atomic Force Microscopy (AFM)

Atomic force microscopy (AFM) is a type of scanning probe microscopy (SPM) with resolution in the order of nanometers. In AFM microscopy, similar to other types of SPM techniques, information is collected by scanning the surface with a mechanical probe. AFM can be operated in two primary scanning modes: contact and non-contact (tapping) modes.[186] For most of this work, contact mode imaging was carried out except for chapter 3 in which tapping mode AFM was utilized.

In AFM imaging, the surface of the sample is scanned by a probing tip made of silicon or silicon nitride, which is mounted on a cantilever. When the tip is sufficiently close to the sample surface, interactions between the tip and the sample result in a repulsive net force and consequently cause the cantilever to deflect off from the surface according to Hooke's law. In contact mode imaging, these forces are mechanical due to

the physical contact between the tip and the topographic features of the sample. In contact mode the force between the tip and the sample is maintained constant during the course of imaging by a feedback mechanism which adjusts the tip-to-sample distance. In tapping mode, intermolecular van der Waals forces, and other attractive forces, cause deflection of the oscillating cantilever. In tapping mode imaging, the parameter that is maintained constant via the feedback loop is the amplitude or the frequency of cantilever oscillation.[186]

AFM scans the surface line by line through precisely controlled movements of a cantilever which is controlled by a piezoelectric ceramic scanner. To obtain the topographic micrograph of the sample, the cantilever deflection is measured using a laser spot focused on the tip that reflects from the back of the mirrored cantilever into an array of four-quadrant photodiodes via a second mirror (Figure 1.11). The change in the intensity of the light falling into different quadrants of the photodetector is used for measuring the amount of cantilever deflection. The intensity detected by the detector is then translated into the topographic map of the sample.[186]

AFM is a vibration-sensitive technique and it should be well shielded from outside vibration sources such as air current and sound waves. This is usually done by isolating the instrument in a vibration dampening shield.[186]

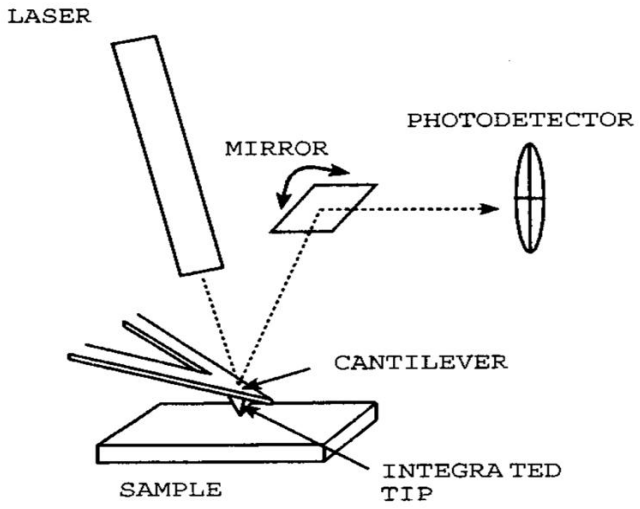

Figure 1.11. Schematic illustration of atomic force microscopy (AFM).[186]

1.7.2. Laser Scanning Confocal Fluorescence Microscopy (LSCFM)

Laser scanning confocal fluorescence microscopy (LSCFM) was employed in this work for detecting fluorescence from QD-containing polymer films. In general, fluorescence microscopy is a type of optical microscopy in which contrast is provided by fluorescence emission from fluorophores localized within a non-fluorescent background of the sample.[187] Similar to all optical microscopies, the resolution is governed by the diffraction limit of visible light, meaning that feature sizes below the 250 nm cannot be resolved due to the optical diffraction. In confocal microscopy, an adjustable pinhole before the detector only permits in-focus light from a thin focal plane to reach the detector resulting in an improved resolution.[187-188] By adjusting the focus to different focal planes and compiling the resulting set of data (called a z-stack) a three-dimensional (3D) image of the sample can be generated.[187]

LSCFM combines fluorescence microscopy with the 3D imaging capabilities of confocal optics and point-by-point scanning of the laser.[187] A typical diagram of an LSCFM is shown in Figure 1.12. To image the specimen, a laser beam is directed to the sample through an objective lens; this excites the photoluminescent species (e.g. an organic dye or a QD) within the sample. The fluorescent light emitted from the sample together with the reflected or scattered laser light are then focused back through the objective lens and pinhole aperture to the detector; a beam splitter then separates different wavelength components, and blocks the light at the original excitation wavelength while allowing the emitted fluorescent wavelengths to pass through to a photo detector, usually a photomultiplier tube (PMT). The point-by-point signals then are reconstructed into an image by a computer.[187]

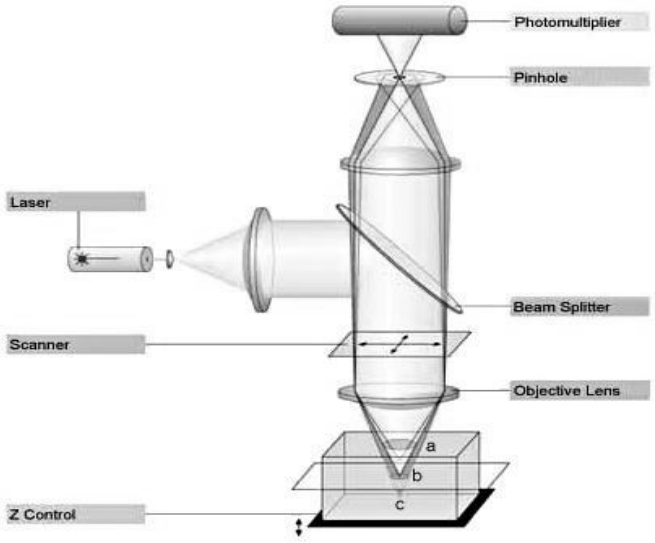

Figure 1.12. A typical diagram of LSCFM.[189]

1.7.3. Laser Light Scattering (LS)

LS is a common technique used to determine the size and molecular weight of polymers and colloidal particles dispersed in solution. In laser light scattering, a high intensity laser is passed through the solution and causes scattering from the particles. The scattered light is then collected by a detector at a single or multiple angles (angle between the detector and incident laser beam). Two main types of light scattering techniques are static light scattering (SLS) and dynamic light scattering (DLS), which are described below in more detail.

1.7.3.1. Dynamic Light Scattering (DLS)

DLS measures dynamic properties of a polymer or colloidal particles by measuring the scattering light at a single angle and recording the autocorrelation of the scattered intensity during the experiment. DLS characterizes fluctuations in the intensity of scattered light which are due to the brownian motion of the particles. These movements change the interparticle distances and consequently the intensity of the scattered light; because smaller particles move more rapidly, the intensity changes can be related to the size of the particles;[190] DLS measures the diffusion coefficient (D) of particles to determine the hydrodynamic radius (R_h) from the Stokes-Einstein relation, as below:

$$R_h = kT/6\pi\eta D_0 \qquad (1.15)$$

where R_h is the effective size of a particle in a solution including any solvent molecules that surround the particle, k is the Boltzmann constant, T is the temperature and η is the viscosity of the solvent and D_0 is diffusion coefficient at infinite dilution.[190]

1.7.3.2. Static Light Scattering (SLS)

SLS measures the intensity of the scattered light to obtain three useful physical values including the weight average molecular weight (M_w), the radius of gyration (R_g), which is the root mean square distance of the atoms of a particle, a micelle, or a polymer chain from its center of gravity, and also the second virial coefficient (A_2), which is a thermodynamic term describing the characteristic of the interaction between species in the system.[193] SLS measurement is usually performed for multiple angles and solution concentrations by measuring the scattering intensity for different solution concentrations and at different angles between the incident beam and the detector. Measured data can be plotted as Kc/R_θ versus $Sin^2\theta/2 + k'c$, which results in a grid-like plot, called Zimm plot. that is based on Zimm equation, as below: [191]

$$Kc/R_\theta = 1/M_w\,[1 + (16\pi^2\,Sin^2(\theta/2)\,s^{-2}) / \ 3\lambda^2] \qquad (1.16)$$

where k' is a system constant, c is the concentration, θ is the measurement angle, $\langle s^{-2}\rangle^{1/2}$ is the R_g, λ is the particle size, and R_θ is the Rayleigh ratio, which describes the reduced intensity of the scattered light respect to the incident beam at θ angle .

A typical Zimm plot is shown in Figure 1.13; M_w can be determined by double extrapolating the plot to zero angle and zero concentration, as illustrated in Figure 1.13.

For double extrapolation a straight line is passed through equal concentration points and then extrapolated to zero angle. Another straight line is then drawn through all points measured at the same angle and then extrapolated to zero concentration. Joining the extrapolated points, results in $\theta=0$ and $c=0$ lines, which are then extrapolated to the axis, where they intersect at a point corresponding to $1/M_w$. A_2 and R_g are determined from the slope of $\theta=0$, and the slope of $c=0$ lines, respectively.[191-193]

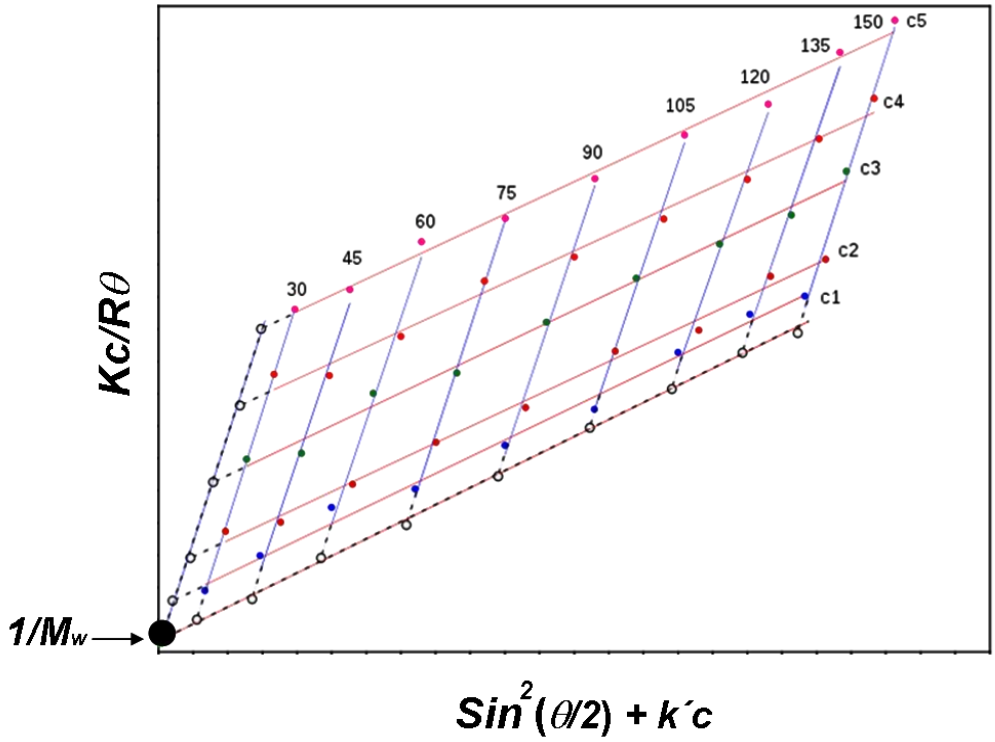

Figure 1.13. Typical Zimm plot, $1/M_w$ point is shown on the plot, where θ=0 and c=0 lines intersect on the axis.[194]

1.7.4. Absorption and Photoluminescence (PL) Spectroscopy

Absorption and PL spectroscopy are powerful techniques used to characterize the optical properties of a material.[195]The type of spectroscopy utilized is determined by the

energy corresponding to the involved transition. In our case we concentrated on the electronic states of our materials with energies in UV-visible portion of the electromagnetic spectrum (300 - 700 nm). Absorption and photoluminescence measurements were performed to determine the energy level structures and PL lifetimes.

1.7.4.1. Absorption Spectroscopy

Absorption spectroscopy measures the change in the intensity of the radiation passing through the sample; the intensity is generally decreasing compared with a reference due to the absorption of the sample. This is expressed as the absorbance or molar extinction coefficient described by equation 1.15. [195,196] This equation expresses the absorbance (A) as the ratio between the intensity of the beam after going through the sample (I) and the intensity of the incident beam (I_0).

$$A = - \log I/I_0 \qquad (1.17)$$

1.7.4.2. Photoluminescence (PL) Spectroscopy

PL spectroscopy measures the radiation emission generated through a transition from an initial high energy to a lower energy state. Photoluminescence spectroscopy in general can be divided in two categories: fluorescence and phosphorescence.[196] Fluorescence denotes transitions between two singlet states, while in phosphorescence the excited electron undergoes an intersystem crossing to a triplet state. Phosphorescence is characterized by longer lifetimes.[196]

The fluorescence process is illustrated in the Jablonski diagram shown in Figure 1.14; the vertical axis of this diagram is the energy and the horizontal axis is the nuclear coordinate. The electron in the excited state decays through the vibrational states to the bottom of the excited electronic states (via vibrational relaxation) and then it decays to the ground state emitting a photon via fluorescence emission.

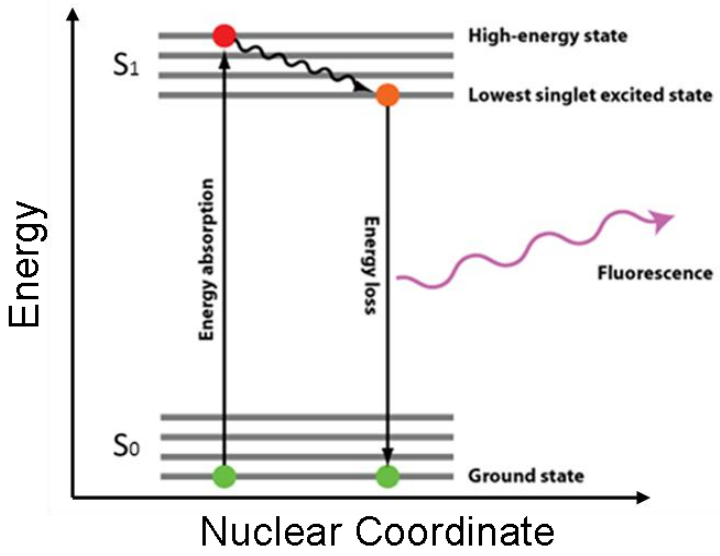

Figure 1.14. Simple Jablonski diagram illustrating absorption and fluorescence emission.[197]

In this work, PL from QDs is measured using PL spectroscopy. For QDs, band-edge emission is usually a sharp band corresponds to the recombination from band-edge or near band-edge states. [14-23] The presence of stabilizing molecules on the surface of QDs often generates traps states, causing another emission band at lower energy known as trap state emission.

Two types of static PL experiments can be carried out: emission and excitation spectroscopies. For an emission spectrum, samples are excited at a fixed excitation wavelength while the emission range is scanned. For excitation spectra the detector

measures photon counts at a fixed emission wavelength as the excitation wavelength is scanned. This identifies the structure of the excited states that are leading to a particular emission transition.

Dynamics of PL can be investigated by measuring the lifetime of the excited states using pulsed excitation source, allowing the system to decay, and single photon counting; in single photon counting the detector counts the number of photons collected per unit of time. The intensity which is given by the instrument as an output is normally determined by the current generated in the photomultiplier and is expressed in counts per second; this is proportional to the number of photons detected in a second. Output of lifetime measurement is a decay profile which is fitted to a suitable multi-exponential model to determine life time of the excited states.

1.8. Content of the Thesis

The remainder of this thesis consists of five chapters; the content of these five chapters is as follows: Chapter 2 focuses on the μCP technique to chemically pattern glass substrates by printing octadecyltrichlorosilane (OTS) using an elastomeric stamp with a patterned topology consist of microscale stripes. The challenge in this patterning is the sensitivity of the process to the ambient condition, due to high reactivity of OTS with water vapor; therefore, the exposure of OTS to humid air has to be minimized during the course of patterning; hence, the OTS solution is prepared and dried under N_2 gas and immediately used for patterning. Different experimental parameters, which influence the patterning, are studied to develop a protocol for preparing OTS patterned films on glass surfaces.

In Chapter 3 the top-down technique of μCP, optimized in Chapter 2, is combined with the bottom-up assemblies of polystyrene-*block*-polyethylene oxide (PS-*b*-PEO) copolymers at the air-water interface. This is a new methodology that we develop for patterning copolymer monolayers by transferring their Langmuir films to a patterned surface. We also demonstrate that this method can be used for patterning NPs; for this, a Langmuir film of a blend of PS-*b*-PEO and PS-stabilized CdS QDs (PS-CdS) prepared and transferred to an OTS-patterned glass substrate to form patterned structures of polymers/NPs.

Chapter 4 demonstrates another example for combining the top-down and bottom-up assemblies. In this part, OTS-patterned substrates were used to direct a different self-assembly process: polymer/polymer phase-separation. First, surface-directed phase-separation of PS and poly (methyl methacrylate) (PMMA) homopolymers are obtained on patterned surfaces based on their different surface energies. The methodology is then extended to patterning polymer/NPs by replacing the PS homopolymer of the blend with a PS-coated NP. Spin-coating a blend of PS-CdS and PMMA on an OTS-patterned glass substrate result in the formation of photoluminescent array of QDs.

Final chapter of this thesis is devoted to develop a methodology for simultaneous patterning of two types of NPs via their surface energies. Our strategy to do this is to use NPs which are polymer-coated by the same polymers studied in Chapter 4 to behave similarly to the PS/PMMA blend. For this study, PS-CdS QDs and a sample of PMMA-coated silver NPs (PMMA-Ag) are used. The reason for choosing such blend is the interesting optical interactions between metallic NPs and QDs, which may result in the PL enhancement of QDs. Chapter 5 is entirely devoted to optical characterization of NPs

blend films and in this part we report a strong enhancement in PL of QDs for the closely interacting blends.

In chapter 6 the morphology of phase-separating "PS-like" QDs and "PMMA-like" Ag NPs are studied. Gelation is occurring in the NPs blend films as they get concentrated by solvent evaporation that is preventing the phase-separation. Chapter 6 focuses on overcoming this challenge in order to obtain domain morphologies, which can be patterned using OTS-patterned substrates.

1.9. References

(1) Tang, Z.; Kotov, N. A. *Adv. Mater*. **2005**, 17, 951.

(2) Sear, R. P.; Chung, S.-W.; Markovich, G.; Gelbart, W. M.; *Heath, J. R. Phys. Rev. E*. **1999**, 59, 6255.

(3) Hassenkam, T.; Nørgaard, K.; Iversen, L.; Kiely, C. J.; Brust, M.; Bjørnholm, T. *Adv. Mater*. **2002**, 14, 1126.

(4) Reuter, T.; Vidoni, O.; Torma, V.; Schmid, G.; Nan, L.; Gleiche, M.; Chi, L.; Fuchs, H. *Nano Lett.***2002**, 2, 709.

(5) Fahmi, A. W.; Oertel, U.; Steinert, V.; Froeck, C.; Stamm, M. *Macromol. Rapid Commun.***2003**, 24, 625.

(6) Rabani, E.; Reichman, D. R.; Geissler, P. L.; Brus, L. E. *Nature* **2003**, 426, 271.

(7) Maillard, M.; Motte, L.; Ngo, A. T.; Pileni, M. P. *J. Phys. Chem. B.* **2000**, 104, 11871.

(8) Shah, P. S.; Sigman, M. B., Jr.; Stowell, C. A.; Lim, K. T.; Johnston, K. P.; Korgel, B. A. *Adv. Mater*. **2003**, 15, 971.

(9) Zhang, L.; Gaponik, N.; Mu¨ ller, J.; Plate, U.; Weller, H.; Erker, G.; Fuchs, H.; Rogach, A. L.; Chi, L. *Small* **2005**, 1, 524.

(10) Lin, Y.; Bo¨ker, A.; He, J.; Sill, K.; Xiang, H.; Abetz, C.; Li, X.; Wang, J.; Emrick, T.; Long, S.; Wang, Q.; Balazs, A.; Russell, T. P. *Nature***2005**, 434, 55.

(11) Chiu, J. J.; Kim, B. J.; Kramer, E. J.; Pine, D. J. *J. Am. Chem.Soc.* **2005**, 127, 5036.

(12) Bockstaller, M. R.; Lapetnikov, Y.; Margel, S.; Thomas, E. L. *J. Am. Chem. Soc.***2003**, 125, 5276.

(13) Lopes, W. A.; Jaeger, H. M. *Nature***2001**, 414, 735.

(14) Henglein, A. *Chem. Rev.* **1989,***89,* 1861.

(15) Steigerwald, M. L.; Brus, L. E. *Acc. Chem. Res.* **1990,***23,* 183.

(16) Weller, H. *Angew. Chem., Int. Ed. Engl.* **1993,***32,* 41.

(17) Alivisatos, A. P. *Science* **1996,***271,* 933.

(18) Collier, C. P.; Vossmeyer, T.; Heath, J. R. *Annu. Rev. Phys. Chem.* **1998,***49,* 371.

(19) Murray, C. B.; Kagan, C. R.; Bawendi, M. G. *Annu. Rev. Mater. Sci.* **2000,***30,* 545.

(20) El-Sayed, M. A. *Acc. Chem. Res.* **2001,***34,* 257.

(21) Wang, C.-W.; Moffitt, M. G. *Langmuir* **2004,***20,* 11784.

(22) Spatz, J. P.; Herzog, T.; Moumer, S.; Ziemann, P.; Moller, M. *Adv. Mater.***1999**, *11*, 149.

(23) Moffitt, M.; McMahon, L.; Pessel, V.; Eisenberg, A. *Chem. Mater.***1995**, *7*, 1185.

(24) Loss, D.; DiVincenzo, D. P., *Phys. Rev. A,***1998**, *57*, 120.

(25) Koleilat, G. I.; Levina L.; Shukla, H.; Myrskog, S. H.; Hinds, S.; Pattantyus-Abraham, A. G.; Sargent, E. H., *ACS Nano*, **2008**, *2*, 833.

(26) Klein, D. L.; Roth, R.; Rim, A. K. L.; Alivisatos, A. P.; McEuen, P. L., *Nature*, **1997**, *389*, 699.

(27) Michalet,X.; Pinaud, F. F.; Bentolila, A.; Tsay,J. M.; Doose, J. J.; Sundaresan,G.; Gambhir, A.M.S.S.; Weiss, W., *Science*,**2005**, *307*, 538.

(28) Moores, A.; Goettmann, F., *New Journal of Chemistry* **2006,** 30, (8), 1121-1132.

(29) Liz-MarzÃ¡n, L. M.; Giersig, M.; Mulvaney, P., *Langmuir* **1996,** 12, (18), 4329-4335.

(30) Maye, M. M.; Lim, I. I. S.; Luo, J.; Rab, Z.; Rabinovich, D.; Liu, T.; Zhong, C.-J., *Journal of the American Chemical Society* **2005,** 127, (5), 1519-1529.

(31) Tiggesbäumker, J.; Köller, L.; Lutz, H. O.; Meiwes-Broer, K. H., *Chemical Physics Letters* **1992,** 190, (1-2), 42-47.

(32) Link, S.; El-Sayed, M. A., *The Journal of Physical Chemistry B* **1999,** 103, (21), 4212.

(33) Chapman, R.; Mulvaney, P., *Chemical Physics Letters* **2001,** 349, (5-6), 358.

(34) Lica, G. C.; Zelakiewicz, B. S.; Constantinescu, M.; Tong, *The Journal of Physical Chemistry B* **2004,** 108, (52), 19896.

(35) Haick, H., *J. Phys. D: Appl. Phys.***2007**, 40, 7173.

(36) McFarland, A. D.; Van Duyne, R. P., *Nano Letters***2003**, 3 (8), 1057.

(37) Lee, K. S.; El-Sayed, M. A., *J. Phys. Chem. B***2006**, 110, 19220.

(38) Lal, S.; Link, S.; Halas, N. J., *Nature Photonics***2007**, 1, 641.

(39) Haes, A.; Van Duyne, R. P. A., *Anal. Bioanal.Chem.***2004**, 379, 920.

(40) Taton, T. A.; Mirkin, C. A.; Letsinger, R. L., *Science***2000**, 289, 1757.

(41) Jeanmaire, D. L.; Van Duyne, R. P., *J. Electroanal. Chem.***1977**, 84, 1.

(42) Albrecht, M. G.; Creighton, J. A., *J. Am. Chem. Soc.***1977**, 99, 5215.

(43) Kneipp, K.; Wang, Y.; Kneipp, H.; Perelman, L. T.; Itzkan, I.; Dasari, R. R.; Feld, M. S., *Phys. Rev. Lett*. **1997**, 78, 1667.

(44) Nie, S.; Emory, S. R., *Science***1997**, 275, 1102.

(45) Kuhn, S.; Akanson U. H.; Rogobete, L.; Sandoghdar, V., *Phys. Rev. Lett.***2006**, 97, 017402.

(46) Kulakovich, O.; Strekal, N.; Yaroshevich, A.; Maskevich, S.; Gaponenko, S.; Nabiev, I.; Woggon, U.; Artemyev, M., *Nano Lett.***2002**, 2, 1449.

(47) Neogi, A.; Lee, C. W.; Everitt, H. O.; Kuroda, T.; Tackeuchi, A.; Yablonovitch, *E. Phys. Rev. B* **2002**, 66, 153305.

(48) Okamoto, K.; Niki, I.; Shvartser, A.; Narukawa, Y.; Mukai, T.; Scherer, A., *Nature. Mater.***2004**, 3, 601.

(49) Shimizu, K. T.; Woo, W. K.; Fisher, B. R.; Eisler, H. J.; Bawendi, M. G., *Phys. Rev. Lett.***2002**, 89, 117404.

(50) Pompa, P. P.; Martiradonna, L.; Della Torre, A.; Della Sala, F.; Manna, L.; ; De Vittorio, M.; Calabi, F.; Cingolani, R.; Rinaldi, R., *Nature Nano.***2006**, 1, 126.

(51) Jin, Y.; Gao, X., *Nature Nano.***2009**, 4, 571.

(52) Song, J. H.; Atay, T.; Shi, S. F.; Urabe, H.; Nurmikko, A. V., *Nano Lett.***2005**, 5, 1557.

(53) Chen, C. J.; Osgood, R. M., *Phys. Rev. Lett*. **1983**, 50, 1705.

(54) Link, S.; El-Sayed, M.A., *Int. Rev. Phys. Chem*. **2000**, 19, 409.

(55) Tam, F.; Goodrich, G.P.; Johnson, B. R.; Halas, N. J., *Nano Letters***2007**, 7, 496.

(56) Khurgin, J. B.; Sun, G.; Soref, R. A., *Appl. Phys. Lett.***2009**, 94, 071103.

(57) Kim, S.; Bawendi, M. G. *J. Am. Chem. Soc.* **2003,***125*, 14652.

(58) Puzder, A.; Williamson, A. J.; Zaitseva, N.; Galli, G., *Nano Lett*., **2004**, 4, 2361.

(59) Wong, M.; Hoertz, P. G.; Liang, C. J.; Shi, B.-M.; Meyer, G. J.; Searson, P. C., *Langmuir* **2001**, 17, 8362.

(60) Zhang, H.; Yang, D.; Ma, X.; Ji, Y.; Li, S. Z.; Que, D., *Mater. Chem. Phys*.**2005**, 93, 65.

(61) Moffitt, M.; Vali, H.; Eisenberg, A. *Chem. Mater*. **1998,***10*, 1021.

(62) Qi, L.; Cölfen, H.; Antonietti, M., *Nano Lett.***2001**, 1, 61.

(63) Corbierre, M. K.; Cameron, N. S.; Sutton, M.; Mochrie, S. G. J.; Lurio, L. B.; Rühm, A.; Lennox, R. B., *J. Am. Chem. Soc*. **2001**, 123, 10411.

(65) Cummins, C. C.; Schrock, R. R.; Cohen, R. E. *Chem. Mater*. **1992**, 4, 27.

(66) Moffitt, M.; McMahon, L.; Pessel, V.; Eisenberg, *A. Chem. Mater.***1995**, 7, 1185.

(67) Forster, S.; Antonietti, M. *Adv. Mater*. **1998**, 10, 195.

(68) Spatz, J. P.; Herzog, T.; Mossmer, S.; Ziemann, P.; Moller, M. *Adv.Mater.***1999**, 11, 149.

(69) Zhang, M.; Drechsler, M.; Muller, A. H. E. *Chem. Mater*. **2004**, 16, 537.

(70) Bennett, R. D.; Miller, A. C.; Kohen, N. T.; Hammond, P. T.; Irvine, D. J.; Cohen, R. E. *Macromolecules***2005**, 38, 10728.

(71) Kang, Y.; Taton, T. A. *J. Am. Chem. Soc.***2003**, 125, 5650.

(72) Kang, Y.; Taton, T. A. *Angew. Chem. Int. Ed.***2005**, 44, 409.

(73) Kang, Y.; Taton, T. A. *Macromolecules* **2005**, 38, 6115.

(74) Filali, M.; Meier, M. A. R.; Schubert, U. S.; Gohy, J.-F. *Langmuir***2005**, 21, 7995.

(75) Murray, C. B.; Norris, D. J.; Bawendi, M. G. *J. Am. Chem. Soc.***1993**, *115*, 8706

(76) Ni, T.; Nagesha, D. K.; Robles, J.; Materer, N. F.; Mussig, S.; Kotov, N. A. *J. Am. Chem. Soc.***2002**, *124*, 3980.

(77) Grohn, F.; Gu, X.; Grull, H.; Meredith, J. C.; Nisato, G.; Bauer, B. J.; Karim, A.; Amis, E. J. *Macromolecules***2002**, 35, 4852.

(78) Cheyne R. B.; Moffitt, M. G. *Langmuir* **2005**, 21, 10297.

(79) Yusuf, H.; Kim, W.-G.; Lee, D. H.; Guo, Y.; Moffitt , M. G. *Langmuir***2007**, 23, 868.

(80) Yusuf, H.; Kim, W.-G.; Lee, D. H.; Aloshyna, M.; Brolo, A. G.; Moffitt, M. G. *Langmuir***2007**, 23, 5251.

(81) Guo, Y.; Moffitt, M. G. *Macromolecules***2007**, 40, 5868.

(82) Wang, C.-W.; Moffit, M. G. *Chem. Mater*. **2005**, 17, 3871.

(83) Ozin, G. A. *Adv. Mater.* **1992,***4*, 612.

(84) Kramer, S.; Fuierer, R. R.; Gorman, C. B. *Chem. Rev.* **2003,**103, 4367.

(85) Maury, P.; Escalante, M.; Reinhoudt, D.N.; Huskens, J., *Adv. Mater*. **2005,** 17, 2718.

(86) Hua, F.; Shi, J.; Lvov, Y.; Cui, T., *Nano Letters*, **2002**, 2, 1219.

(87) Harirchian-Saei, S.; Wang, M. C. P.; Gates, B. D.; Moffitt, M. G. *Langmuir*, **2010**, 26, 5998.

(88) Bower, D. I., *An introduction to polymer physics*, University press, Cambridge, 2002, pg.1.

(89) Bower, D. I., *An introduction to polymer physics*, University press, Cambridge, 2002, pg.8.

(90) Bower, D. I., *An introduction to polymer physics*, University press, Cambridge, 2002, pg.63.

(91) Bower, D. I., *An introduction to polymer physics*, University press, Cambridge, 2002, pg.344.

(92) Cowie, J. M. G., Ed. *Polymers: Chemistry & Physics of Modern Materials*, 2nd ed.; Chapman & Hall: New York, 1973, pg. 130.

(93) Michalet, X.; Pinaud, F. F.; Bentolila, L. A.; Tsay, J. M.; Doose, S.; Li, J. J.; Sundaresan, G.; Wu, A. M.; Gambhir, S. S.; Weiss, S. *Science***2005**, 307, 538.

(94) Jamieson, T.; Bakhshi, R.; Petrova, D.; Pocock, R.; Imani, M.;Seifalian, A. M.*Biomaterials***2007,** 28, 4717.

(95) Loss, D.; DiVincenzo, D. P. *Phys. Rev. A***1998**, 57, 120.

(96) Shriver, D.; Atkins, P. *Inorganic Chemistry*, 3 ed.; Oxford University Press: New York, 1999.

(97) Brus, L. *J. Phys. Chem.***1986**, *90*, 2555.

(98) Li, X.; Zhang, J.; Xu, W.; Jia, H.; Wang, X.; Yang, B.; Zhao, B.; Li, B.; Ozaki, Y., *Langmuir* **2003,** 19, 4285.

(99) Jia, H.; Zeng, J.; Song, W.; An, J.; Zhao, B., *Thin Solid Films* **2006,** 496, (2), 281.

(100) Xie, Y.; Ye, R.; Liu, H., *Colloids and Surfaces A: Physicochemical and Engineering Aspects* **2006,** 279, 175.

(101) Maillard, M.; Giorgio, S.; Pileni, M. P., *Advanced Materials* **2002,** 14, (15), 1084.

(102) Lei, Z.; Zhang, L.; Wei, X., *Journal of Colloid and Interface Science* **2008,** 324, 216.

(103) Chaudhari, V. R.; Haram, S. K.; Kulshreshtha, S. K.; Bellare, J. R.; Hassan, P. A., *Colloids and Surfaces A: Physicochemical and Engineering Aspects* **2007,** 301, (1-3), 475.

(104) Zhu, J.J.; Liao, X.H.; Zhao, X.N.; Chen, H.Y., *Materials Letters* **2001,** 49, (2), 91.

(105) Liu, S.; Huang, W.; Chen, S.; Avivi, S.; Gedanken, A., *Journal of Non-Crystalline Solids* **2001,** 283, 231.

(106) Schuck, P. J.; Fromm, D. P.; Sundaramurthy, A.; Kino, G. S.; Moerner, W. E., *Phys. Rev. Lett.***2005,** 94, 017402.

(107) Carminati, R.; Greffet, J.J.; Henkel, C.; Vigoureux, J.M., *Opt. Commun.***2006**, 261, 368.

(108) Rogobete, L.; Schniepp, H.; Sandoghdar, V.; Henkel, C., *Opt. Lett.***2003**, 28, 1736.

(109) Girard, C.; Martin, O. J. F.; Dereux, A., *Phys. Rev. Lett.***1995**, 75, 3098.

(110) Novotny, L., *Appl. Phys. Lett.***1996**, 69, 3806.

(111) Thomas, M.; Greffet, J.J.; Carminati, R.; Arias-Gonzalez, J. R., *Appl.Phys.Lett.***2004**, 85, 3863.

(112) Baffou, G.; Girard, C.; Dujardin, E.; des Francs, G. C.; Martin, O. J. F., *Phys. Rev. B* **2008**, 77, 121101(R).

(113) des Francs, G. C.; Girard, C.; Laroche, T.; Leveque, G.; Martin, O. J. F., *J. Chem. Phys.***2007**, 127, 034701.

(114) Yeh, D. M.; Huang, C. F.; Lu, Y. C.; Yang, C. C., *Appl. Phys. Lett.***2008**, 92, 091112.

(115) Tang, J.; Birkedal, H.; McFarland, E. W.; Stucky, G. D., *Chem. Commun.* **2003**, 2278-2279.

(116) Neogi, A.; Morkoc, H., *Nanotechnology* **2004**, *15*, 1252.

(117) Gontijo, I.; Boroditsky, M.; Yablonovitch, E.; Keller, S.; Mishra, U. K.; DenBaars, S. P., *Phys. Rev. B* **1999**, *60*, 11564.

(118) Kamat, P. V.; Shanghavi, B. *J., Phys. Chem. B* **1997**, *101*, 7675.

(119) Gryczynski, I.; Malicka, J.; Jiang, W.; Fischer, H.; Chan, W. C. W.; Gryczynski, Z.; Grudzinski, W.; Lakowicz, J. R. *J., Phys. Chem. B* **2005**, *109*, 1088.

(120) Lee, J.; Govorov, A. O.; Dulka, J.; Kotov, N. A., *Nano Lett.* **2004**, *4*, 2323.

(121) Gueroui, Z.; Libchaber, A. *Phys. Re*V. *Lett.* **2004**, *93*, 166104.

(122) Hecker, N. E.; Hopfel, R. A.; Sawaki, N.; Maier, T.; Strasser, G., *Appl. Phys. Lett.* **1999**, *75*, 1577.

(123) Biteen, J. S.; Pacifici, D.; Lewis, N. S.; Atwater, H. A., *Nano Lett.* **2005**, *5*, 1768.

(124) Nien, S. Y.; Chiu, N. F.; Ho, Y. H.; Lee, J. H.; Lin, C. W.; Wu, K. C.; Lee, C. K.; Lin, J. R.; Wei, M. K.; Chiu, T. L., *Appl. Phys. Lett.***2009**, 94, 103304.

(125) Sun, G.; Khurgin, J. B.; Soref, R. A., *J. Opt. Soc. Amer. B* **2008**, 25, 1748.

(126) Khurgin, J. B.; Sun, G.; Soref, R. A., *Appl. Phys. Lett.***2009**, 94, 071103.

(127) Sun, G.; Khurgin, J. B.; Soref, R.A., *Appl. Phys. Lett.***2009**, vol. 94, 101103.

(128) Sun, G.; Khurgin, J. B. Yang, C. C., *Appl. Phys. Lett.***2009**, vol. 95, 171103.

(129) Hutter, E.; Fendler, J. H., *Adv. Mater*.**2004**, 16, 1685.

(130) McMurry, J.; Fay, R. C., *Chemistry*, 2nd ed., Prentice Hall, 1998.

(131) Hiemenz, P. C., *Principles of Colloid and Surface Chemistry*., Marcel Dekker Inc., 1977.

(132) van Olphen, H.; Mysels, K. J., *Physical Chemistry: Enriching Topics From Colloid and Surface Science*, Theorex, 1975.

(133) MacRitchie, F., *Chemistry at Interfaces*., Academic Press Inc., 1990.

(134) Gaines, G. L., *Insoluble Monolayers at Liquid-Gas Interfaces*., Wiley and Interscience Publishers, 1966.

(135) Ulman, A., *An Introdiction to Ultrathin Organic Films: From Langmuir-Blodgett to Self-Assembly*., Academic Press, 1991.

(136) *KSV 3000 Instruction Manual*, KSV Instruments Ltd., 2001.

(137) Gelbart, W. M.; Ben-Shaul, A.; Roux, D., *Micelles, Membranes Microemulsions and Monolayers*., Springer-Verlag, Inc., 1994.

(138) Jones, M. N.; Chapman, D., *Micelles, Monolayers and Biomembranes*., John Wiley & Sons, Inc., 1995.

(139) MacRitchie, F., *Chemistry at Interfaces*., Academic Press Inc., 1990.

(140) Gaines, G. L., *Insoluble Monolayers at Liquid-Gas Interfaces*., Wiley and Interscience Publishers, 1966.

(141) Ulman, A., *An Introdiction to Ultrathin Organic Films: From Langmuir-Blodgett to Self-Assembly*., Academic Press, 1991.

(142) Baker, S. M.; Leach, K. A.; Devereaux, C. E.; Gragson, D. E. *Macromolecules* **2000**, *33*, 5432.

(143) Devereaux, C. A.; Baker, S. M. *Macromolecules* **2002**, *35*, 1921.

(144) Cox, J. K.; Yu, K.; Constantine, B.; Eisenberg, A.; Lennox, R. B. *Langmuir* **1999**, *15*, 7714.

(145) Blodgett, K. A.; Langmuir, I. *Phys. Rev.* **1937,***51*, 964.

(146) Langmuir, I.; V.J., S. *J. Am. Chem. Soc.* **1938,***60*, 1351.

(147) Krausch, G.; Kramer E. J.; *Appl. Phys. Lett.***1994**, 64, 2655.

(148) Kielhorn, L.; Muthukumar M., *J. Chem. Phys.***1999**, 111, 2259.

(149) Rockford, L.; Liu, Y.; Mansky, P.; Russell, T.P., *Phys. Rev. Lett*., **1999**, 82, 2602.

(150) Fukunaga, K.; Elbs H.; Krausch, G., *Langmuir* **2000**, 16, 3474.

(151) Sprenger, M.; Walheim, S.; Schafle, C.; Steiner, U., *Adv. Mater*. **2003**, 15, 703.

(152) Cyganik, P.; Budkowski, A.; Steiner, U.; Rysz, J.; Bernasik, A.; Walheim, S.; Postawa, Z.; Raczkowska, J., *Europhysics Letters*, **2003**, 62,855.

(153) Raczkowska, J.; Cyganik, P.; Budkowski, A.; Bernasik, A.; Rsz, J.; Raptis, I.; Czuba, P.; Kowalski, K., *Macromolecules,***2005**, 38, 8486.

(154) Andrew, P.; Huck, W. T. S., *Soft Matter*, **2007**, 3, 230.

(155) Jaczewska, J.; Budkowski, A.; Bernasik, A.; Raptis, I.; Moons, E.; Goustouridis, D.; Haberko, J.; Rysz, J., *Soft Matter*, **2009**, 5, 234.

(156) Newby, B.M.Z.; Composto, R. J., *Macromolecules*, **2000**, 33, 3274.

(157) Rockford, L.; Liu, Y.; Mansky, P.; Russell, T. P., *Phys. Rev. Lett* ,**1999**, 82:2602.

(158) Rockford, L.; Mochrie, S. G. J.; Russell, T. P., *Macromolecules*, **2001**, 34:1487.

(159) Yang, X. M.; Peters, R. D.; Nealey, P. F.; Solak, H. H.; Cerrina, F., M*acromolecules*,**2000**, 33:9575.

(160) Cheng, J. Y.; Rettner, C. T.; Sanders, D. P.; Kim, H. C.; Hinsberg, W. D., *Adv. Mater.*,**2008**, 20:3155.

(161) Edwards, E. W.; Stoykovich, M. P.; Solak, H. H.; Nealey, P. F., *Macromolecules,* **2006**, 39:3598.

(162) Edwards, E. W.; Montague, M. F.; Solak, H. H.; Hawker, C. J.; Nealey, P. F., *Adv. Mater***., 2004**, 16:1315.

(163) Kim, S.O.; Solak, H. H.; Stoykovich, M. P.; Ferrier, N. J.; De Pablo, J. J.; Nealey P. F., *Nature* ,**2003**, 424:411.

(164) Edwards, E. W.; Muller M.; Stoykovich, M. P.; Solak, H. H.; Depablo, J. J.; Nealey, P. F., *Macromolecules,***2007**, 40:90.

(165) Stoykovich, M. P.; Muller, M.; Kim, S. O.; Solar, H. H.; Edwards, E. W.; De Pablo, J. J.; Nealey, P. F., *Science,* **2005**, 308:1442.

(166) Ji, S.; Nagpal, U.; Liao, W.; Liu, C.-C.; de Pablo, J. J.; Nealey, P. E. *Adv. Mater.*2011, 23, 3692.

(167) Cheng, J. Y.; Ross, C. A.; Smith, H. I.; Thomas, E. L., *Adv. Mater.*,**2006**, 18:2505.

(168) Sundrani, D.; Darling, S. B.; Sibener, S. J., *Langmuir*, **2004**, 20:5091.

(169) Sundrani, D.; Darling, S. B.; Sibener, S. J., *Nano. Lett,* **2004**, 4:273.

(170) Segalman, R. A.; Hexemer, A.; Kramer, E. J., *Macromolecules*, **2003**, 36:6831.

(171) Chai, J.; Buriak, J. M., *ACS Nano*, 2008, 2:489.

(171) Sundrani, D.; Sibener, S. J., *Macromolecules,***2002**, 35:8531.

(173) Black, C. T.; Bezencenet, O., *IEEE Trans. Nano. Technol.***2004**, 3:412.

(174) Neogi, P.; *Diffusion in polymers*, Marcel Dekker Inc. 1996, pg. 1996.

(175) Ruiz, R.; Sandstrom, R. L.; Black, C. T., *Adv.Mater,* **2007**, 19:587.

(176) Cheng, J. Y.; Ross, C. A.; Thomas, E. L., *Appl. Phys. Lett.*, **2002**, 81:3657.

(177) Cheng, J. Y.; Ross, C. A.; Thomas, E. L.; Smith, H. I.; Julius Vansco, G., Adv. *Mater,***2003**, 15:1599.

(178) Cheng, J. Y.; Zhang, F.; Smith, H. I.; Julius Vansco, G.; Ross, C. A., *Adv. Mater.***2006**, 18:597.

(179) Segalman, R. A.; Yokoyama, H.; Kramer, E. J., *Adv. Mater,* **2001**, 13:1152.

(180) Leiber, L., *Macromolecules* **1980**, 13, 1602.

(181) Chakrabarti, A.; Toral, R.; Gunton, J. D. *Phys. Rev. Lett*.**1989**, 63, 2661.

(182) Bates, F. S.; Fredrickson, G. H., *Annu. Rev. Phys. Chem*., 41: 525, 1990.

(183) Bates, F. S; Fredrickson, G. H., *Physics Today*, 1999, 32.

(184) Hadjichristidis, N.; Pispas, S.; Floudas, G. A., *Block Copolymers, Wiley – Interscience,* New Jersey, 2003, pg. 257.

(185) http://www.psrc.usm.edu/mauritz/block.html.

(186) Marek, T. *Explorer^{TM} Instrument Operation Manual*; ThermoMicroscopes Corporation: CA, 2001.

(187) Pawley, J.B., *Handbook of Biological Confocal Microscopy,* 3rd ed., Berlin, Springer, 2006.

(188) Ploem, J. S. *Applied optics***1987**, 26, 3226.

(189) http://www.lbb.ethz.ch/Equipment/CLSM.

(190) Sperling, L. H. *Introduction to Physical Polymer Science*, 4th ed., New York, Wiley, 2006, pg. 102.

(191) Zimm, B. H. *J. Chem. Phys*. **1948**, 16, 1099.

(192) Sperling, L. H. *Introduction to Physical Polymer Science*, 4th ed., New York, Wiley, 2006, pg. 92.

(193) Cowie, J. M. G.; Arrighi, V. *Polymers: Chemistry and Physics of Modern Materials*, 3rd ed., CRC Press, 2008, pg. 234.

(194) http://en.wikipedia.org/wiki/Static_light_scattering#Zimm_plot.

(195) Atkins, P.W.; Friedman, R.S., *Molecular Quantum Mechanics*, 3rd Ed., Oxford University Press, 1997.

(196) Lakowicz, J. R., *Principles of Fluorescence Spectroscopy*, 2nd Ed., Springer, 1999.

(197) http://www.scienceinyoureyes.com/uploads/pics/jablonski_eng.gif.

Chapter 2. MICROCONTACT PRINTING PATTERNED ALKYLSILANE FILMS ON GLASS SURFACES

2.1. Introduction

Many new and innovative fields in nanotechnology require materials with specific micro- and nanoscale patterned structures. A variety of patterning techniques have been used for fabrication of such structures. Optical lithography is a method that has been widely utilized for patterning;[1] an example is the fabrication of integrated circuits.[2] However, optical methods are diffraction limited meaning that feature sizes below the 250 nm barrier cannot be obtained due to the optical diffraction. This limit is slightly improved in some advanced optical lithographic techniques such as deep ultraviolet (DUV) lithography,[3,4] excimer laser lithography[5] and soft X-ray lithography.[6] Some non-optical methods such as electron beam lithography,[7,8] focused ion beam (FIB) writing[9,10] and scanning probe lithography[11] are also developed for the fabrication of patterned features on the order of a few nanometers; however these techniques are quite expensive in both cost and time to use. An alternative patterning technique is soft-lithography which is a non-optical method developed by Whitesides and coworkers.[12,13]

Soft lithographic techniques are fast and efficient patterning methods that can be used for patterning a wide variety of materials such as polymers, colloids, metals and semiconductor NPs.[14-19] All soft lithographic techniques have the use of a patterned elastomer in common; either as a stamp, mold or mask. Poly (dimethylsiloxane) (PDMS) elastomer is the most common elastomer used in soft lithography; it has a low glass transition temperature (T_g) and therefore, is usually liquid at room temperature and readily solidifies by cross-linking.[20]

Although there are multiple different soft lithographic patterning techniques,[19, 21-26] microcontact printing (μCP) is the soft lithography technique exploited in this work. In

this technique, a topological relief pattern on the surface of a PDMS stamp is used to transfer self-assembled monolayer (SAM)-forming molecules (the "ink") onto various surfaces selectively in regions where the stamp makes contact with the surface. There are many parameters influencing the fidelity and the quality of the patterns obtained by μCP; among those, the parameters that influence the mass transport during printing such as concentration of the "ink" solution and the printing time (PDMS-glass contact time) are shown to be the most important.[12,13,19,32] It has been previously demonstrated that the quality of the transferred SAM improves (in terms of packing and chain orientation) by increasing the printing time[32] and it starts to decrease above a certain time due to the diffusion and/or transport of the "ink" to non-contact regions.[12, 32] The effect of the "ink" solution has been also investigated; Jeon et al.[32] showed that increasing the concentration results in an increase in the thickness of the film and also in increased defects due to increased diffusion rates between contact and non-contact regions (for the same reasons provided above).

μCP has been widely used to pattern alkanethiol SAMs on gold,[13,27-29] silver[30] and copper[31] surfaces. It has also been utilized for patterning alkylsilane monolayers on hydroxyl-terminated surfaces such as Al/Al_2O_3, glass, mica, and plasma-treated polymers and mainly Si/SiO_2.[32-40] It has been shown that [32,33,37-40] patterning alkylsilanes SAMs on glass and silicone substrates is highly sensitive to the reaction conditions and is a very moisture-sensitive process due to high reactivity of silane molecules, thus the patterning has to be performed with minimal air exposure. Patterning alkylsilanes SAMs is less common compared with alkanethiols due to the high sensitivity of the process to many experimental conditions and also because of the lack in ordering of SAMs. However,

fabricating patterned films on Si/SiO_2 or glass surfaces is advantageous for many applications since Si/SiO_2 has applications in semiconducting industry and glass surfaces have applications in optical devices due to their transparency.[37-40] Works reported on this are mainly focused on patterning octadecyltrichlorosilane (OTS) on Si;[37-40] patterning docosyltrichlorosilane (DTS) on Si has been also reported.[38]

In this chapter, different procedures for μCP OTS on glass surfaces are investigated; high sensitivity of the process to many experimental parameters makes it difficult to find optimal conditions from the literature and therefore, the parameters have to be optimized by individuals working on the experiment in a given lab. Specifically, we investigate the effects of OTS concentration and printing time on the coverage and uniformity of the pattern as well as on the chemical heterogeneity of the films. To produce the topological pattern of the PDMS elastomeric stamp, the relief pattern of a commercial compact disc (CD) was used as the master. The stamp was then utilized to transfer OTS to piranha-treated hydrophilic glass surfaces (Figure 2.1) to form alternating micron scale stripes of hydroxyl-terminated hydrophilic regions and hydrophobic areas. Hydrophobicity of alternating stripes is the result of the chemical reaction between OTS molecules and hydroxyl functional groups of the piranha-treated glass, as demonstrated in Figure 2.2.

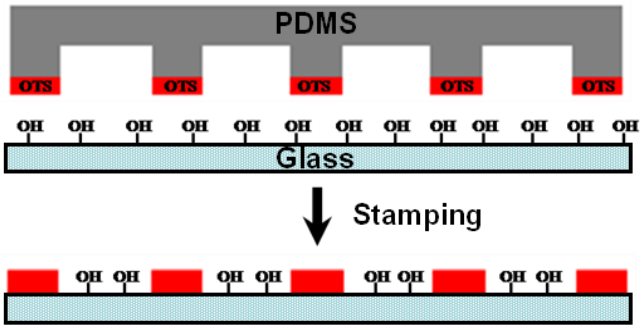

Figure 2.1. Microcontact printing OTS on hydrophilic glass substrate and resulted chemically heterogeneous substrate.

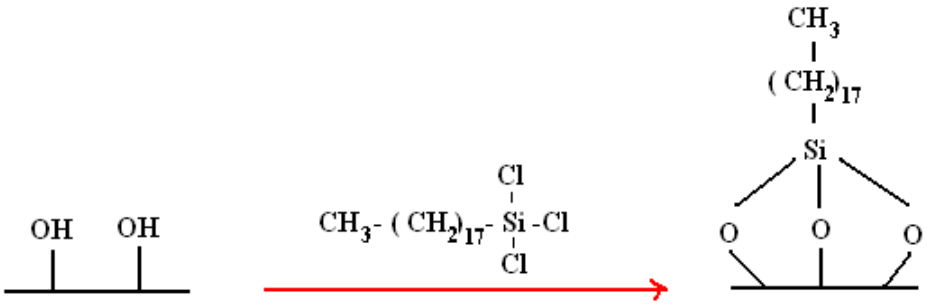

Figure 2.2. Piranha-treated hydrophilic surface of glass transforms to hydrophobic surface by the chemical reaction between hydroxyl groups with OTS.

Patterned OTS surfaces will be used in following parts of this thesis to direct SAMs of block copolymers formed at the air-water interface in Chapter 3, and the phase evolution of phase-separating polymer blend films in Chapter 4. In Chapter 6, they are used to simultaneously direct two types of polymer-stabilized nanoparticles into patterned polymer/nanoparticle films with structural hierarchy.

2.2. Experimental

2.2.1. Preparation of Polydimethylsiloxane (PDMS) Stamps for Microcontact Printing

Masters with microscale periodic stripe patterns were obtained using commercial compact discs (CDs). A CD consists of a 120 mm-diameter, 2 mm-thick disk of polycarbonate (PC) with spiral grooves with the depth of approximately 150 nm that starts at 46 mm from the center of the disc to the edge. Layers on top of the PC include a reflective metal layer, a clear lacquer coating and finally the label.[34]After removing all three top layers, the exposed PC pattern containing micron scale feature sizes can be used as the master for μCP. To remove the top layers, first the protective layer of a CD was removed by scoring with a scalpel and vigorously rinsing with deionized (DI) water. Then, the metallic layer and thin lacquer coat were removed via a quick rinse with methanol and subsequent sonication in a 1 : 4 (v : v) methanol/DI water solution for 2 h, followed by a final methanol rinse, revealing the underlying PC layer with the desired topographic features. The PC was cut into square pieces ~ 2 cm x 2 cm. Prepolymer and curing agent for PDMS (Dow Corning: Sylgard 184 DC-184 A and DC 184-B) were mixed in a 10 : 1 (v : v) ratio, then poured over a polycarbonate master, followed by 4 h curing at 80˚C. The PDMS was then carefully peeled from the master in the direction of the CD grooves, at a steady rate of ~ 1 cm/s. The topology of the resulting PDMS stamps consisted of periodic raised stripes corresponding to the troughs of the PC masters; topographic AFM images of the master and the stamp are provided in Figure 2.4. The PDMS stamps were sonicated in a 1 : 2 (v : v) solution of ethanol/DI water immediately prior to use, in order to remove possible dust or unpolymerized PDMS, followed by

drying with a stream of ultra-high purity (UHP) N_2 (g). To avoid build-up of siloxane deposits from OTS "ink", PDMS stamps were used only once.

2.2.2. Microcontact Printing Glass Substrates with Octadecyltrichlorosilane (OTS)

Glass cover slips (VWR scientific, 18 x 18 mm) were cleaned by sonication for 10 min in 95% ethanol, followed by 10 min sonication in DI water. To introduce a layer of hydroxyl groups on the glass surface, the cover slips were submerged in a piranha solution at 70˚C for 30 min. Piranha solution consists of a 3 : 1 (v : v) mixture of concentrated H_2SO_4 and 30% H_2O_2. Treated, hydrophilic slides were then rinsed with DI water followed by methanol. The resulting hydrophilic glass substrates were dried with a UHP N_2 (g) stream and used immediately for microcontact printing (μCP). One of these piranaha treated substrates was used as a uniformly hydrophilic control slide. The ink for μCP was prepared by dissolving OTS (Aldrich) in anhydrous hexane (≥ 99%, Aldrich) under UHP N_2 (g) to obtain 5, 10 and 20 mM solutions. The uniformly hydrophobic control for the μCP process was obtained by immersing the clean piranaha-treated glass in OTS solution under UHP N_2 for 30 min,resulting in a substrate completely functionalized with reacted OTS. To form patterned films with alternating micron-scale hydrophilic/hydrophobic stripes, PDMS stamps were inked by first depositing a single drop of OTS solution from a pasteur pipette onto the centre of a 2 x 2 cm^2 piece of lens paper; a stamp was then brought into contact with the inked paper for 10 s. To carry out μCP, an inked PDMS stamp was then immediately brought into contact with a

hydrophilic glass cover slip for either 30 or 60s (the printing time) under a 200 g weight. The resulting substrates were characterized to determine the quality and uniformity of the pattern.

2.2.3. Characterizing the films

Patterned films were all characterized using optical microscopy (OM) with and without DI water (details provided in the following sections), atomic force microscopy (AFM) and contact angle measurement.

2.2.3.1. Optical microscopy

Optical microscopy of patterned OTS films on glass was performed in order to determine the coverage and uniformity of the pattern. To demonstrate the microscale patterning of surface energies on the resulting surface, we deposited a large drop of DI water on the substrate and monitored the evaporation of water over time by OM. For this, a 60 μl drop of DI water was placed on the centre of a patterned film and allowed to evaporate in a covered petri dish on the bench top for 40 min at room temperature. Images of drying water droplets after various evaporation times were collected using a CCD camera attached to the OM.

2.2.3.2. Atomic force microscopy (AFM)

Contact mode AFM was performed using a ThermoMicroscope Explorer (Veeco Instruments) equipped with a Veeco silicon nitride tip (MLCT-EXMT-A). Each sample was imaged several times at different locations on the substrate to assess the OTS pattern over the entire film. For each film, a total of at least 80 features (stripes) were measured to determine the mean dimensions, with reported errors representing a single standard deviation unit.

2.2.3.3. Contact angle measurement

A drop of DI water (~ 10 μl) was deposited on the horizontal substrate using a Hamilton microsyringe. Side view images of the drop on the substrate were taken by a fixed focal length telescope (VZM 1000i imaging lens) with the lens positioned at the level of the glass slide. Advancing contact angles were measured on these images at both sides of each drop for four drops at four different regions of the film. A mean contact angle and standard deviation were thus determined from the resulting measurements.

2.3. Results and Discussion

2.3.1. Fabrication and Characterization of PDMS Stamps

In μCP, a stamp with striped topology was used to selectively transfer OTS to hydrophilic glass in areas of contact between the stamp and the substrate; a chemical reaction between OTS and hydroxyl groups on the piranha-treated glass surface resulted

in a chemically-heterogeneous surface with an alternating pattern of hydrophilic/hydrophobic stripes with microscale periodicity.

One technical challenge in this technique is the distortion of the elastomeric stamp during printing. This occurs when the aspect ratio (*h/w*) of the features on the PDMS stamp is too high or too low. Specifically, when the height of the features (*h*) is much greater than the width (*w*) (*h* » *w*), they collapse during printing, and pairing between the neighboring features occurs, as depicted in Figure 2.3 a. For the case of *w* » *h*, sagging of the flat areas of the stamp in between the raised features (Figure 2.3 b) causes defects. It has been experimentally shown by Whitesides and coworkers[12] showed when the dimension of the stamp features are such that the aspect ratio *(h/w)* is in the range of 0.1-0.4, no stamp distortion takes place during printing. This is confirmed theoretically by Kenneth et al.[41] and Hui et al.[42] in their studies on the mechanical properties of PDMS stamps.

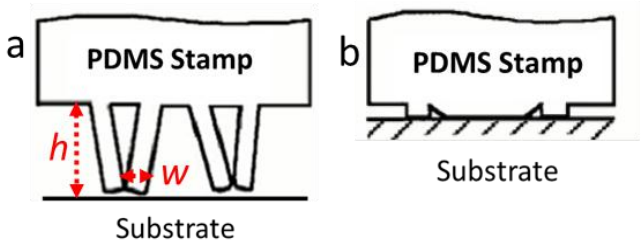

Figure 2.3. Stamp distortion when feature aspect ratio (*h/w)* is (a) too high or (b) too low. The first type of distortion is known as pairing between neighboring features and the second type is called sagging.

An AFM image of the PC master obtained from a commercial CD is illustrated in Figure 2.4 a, which shows the microscale striped topology (small portion of the spiral pattern appear as parallel stripes). From topology data in several regions of the substrate,

the PC trenches have a mean FWHM of 0.5 ± 0.1 μm, a centre-to-centre distance of 1.5 ± 0.2 μm, and a depth of 178 ± 8 nm. A sample height profile is provided in Figure 2.4 b. The PDMS stamp prepared using this master contains the negative topology of the master, with raised stripes that correspond to trenches in the master. This is shown in AFM image of the resulting PDMS stamp (Figure 2.4 c). Mean dimensions of PDMS raised stripe features are: FWHM width, w = 0.6 ± 0.1 μm, centre-to-centre distance between adjacent stripes (periodicity), λ = 1.4 ± 0.3 μm, and height, h = 182 ± 6 nm. The lateral topology of the stamp is illustrated in Figure 2.4 d. The aspect ratio of these PDMS features (h/w = 0.3) fit in the recommended range provided by Whitesides and coworkers[12] (described above), and no evidence of stamp distortion was observed in our patterned OTS films.

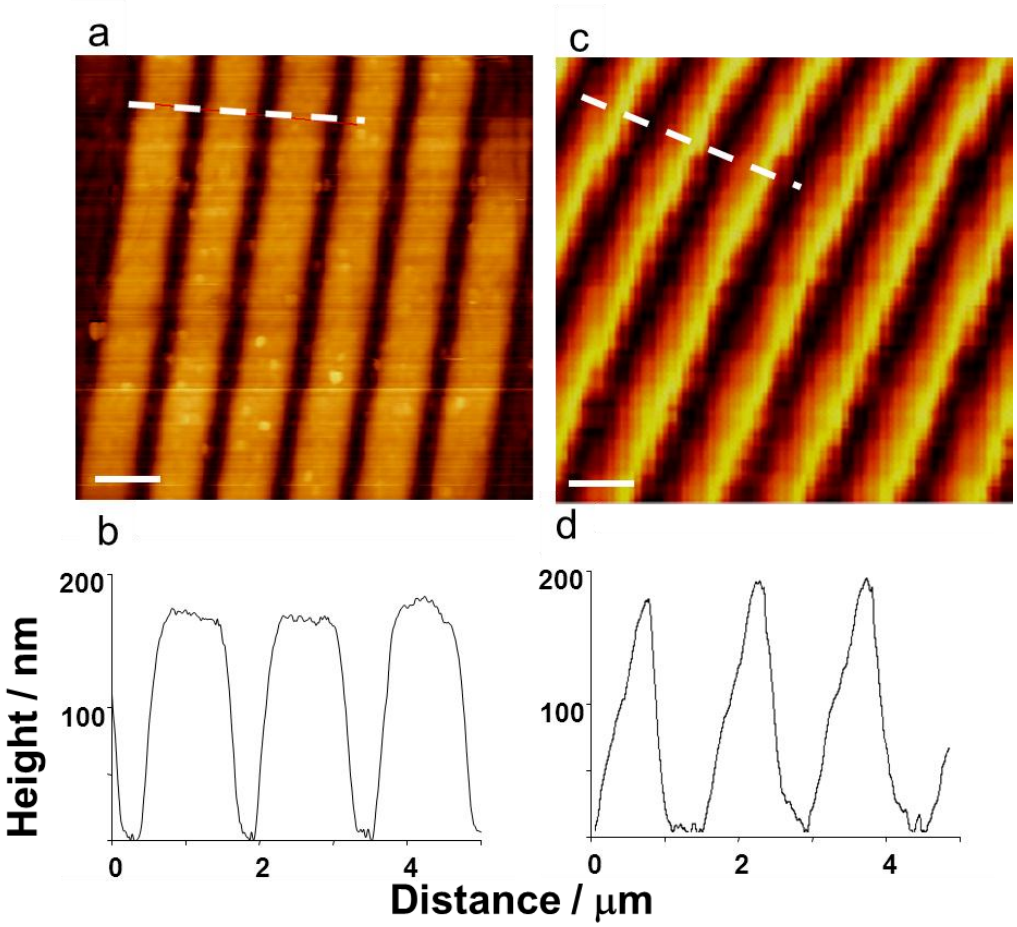

Figure 2.4. (a, c) AFM images and (b, d) height profiles along the dashed white lines on AFM micrographs for (a, b) the PC master and (c, d) the PDMS stamp.

2.3.2. Optical Microscopy Characterization of OTS Patterned Films on Glass Substrates

The PDMS stamps described in the previous section were employed to transfer a striped pattern of hydrophobic OTS onto the hydrophilic glass substrates. Two important parameters affecting the patterning were investigated here: the concentration of the OTS "ink" solution and the printing time. Three different OTS concentrations of 5, 10 and 20 mM and two different printing times of 30 s and 60 s were investigated.

First, optical microscopy (OM) imaging was employed for characterization of the resulting patterned OTS films (Figure 2.5). OM images show the stripe pattern for all cases; the contrast is increasing for higher contact time (60 s) for all three cases of 5, 10 and 20 mM OTS-patterned films suggesting the formation of thicker films. Effect of concentration is more evident for films prepared via longer printing time (Figure 2.5 b, d, f) and less so in films prepared via shorter printing time (Figure 2.5 a, c, e). For films prepared using high concentration of OTS, clusters are forming above the striped pattern that are observed as superimposed features in OM images (Figure 2.5 d and f); this suggests the possibility of OTS clustering. Similar observation has been previously reported by Jeon et al.[32] and can be attributed to the large amount of transferred OTS and consequent diffusion of molecules from printed stripes to non-printed glass regions forming a layer of OTS with no pattern. Another possibility is that concentrated OTS fills the trenches in the stamp and therefore, is transferred uniformly on glass.

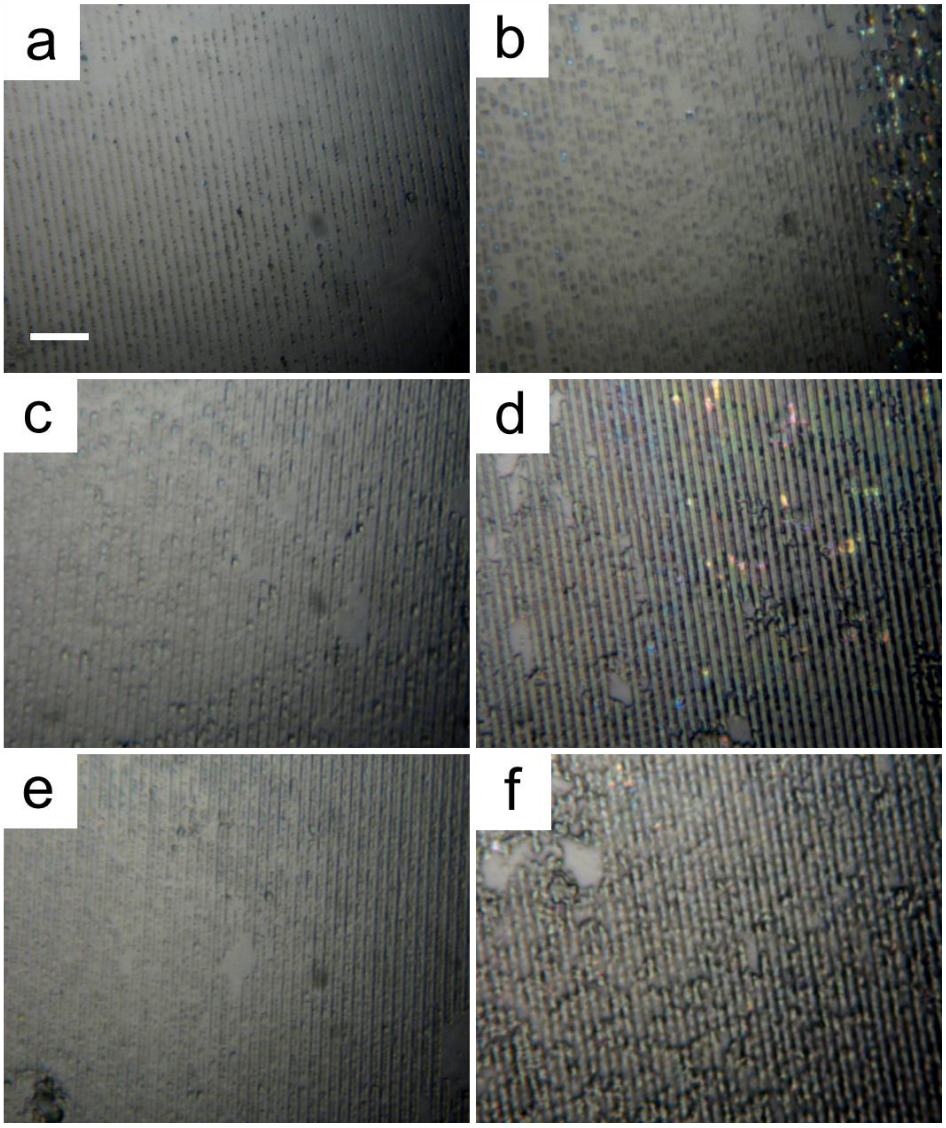

Figure 2.5. OM images of the 5 mM (a, b), 10 mM (c, d) and 20 mM (e, f) OTS patterned films prepared at 30 s (a, c, e), and 60 s (b, d, f) printing times (scale bar shows 10 μm).

To demonstrate the patterning of surface energies, OM was also used to monitor the drying process of an evaporating DI water drop on the patterned OTS surfaces. Representative OM images of the various OTS films with evaporating water droplets are shown in Figure 2.6. As water evaporates during drying process, the drop breaks into droplets via dewetting from hydrophobic regions that occurs due to Rayleigh instabilities

of the liquid film[44, 45] resulting in rupture and the formation of droplets. OM images of the patterned films at an intermediate stage of drying/dewetting reveal that DI water droplets are oriented along parallel stripes on the micron scale, confirming the localized hydrophilicity of these regions. The size of the formed patches is increasing with increasing the OTS concentration because on more hydrophobic substrates with higher water contact angle, which will be discussed in the consequent section, destabilization and dewetting occurs earlier and before the film gets thin.

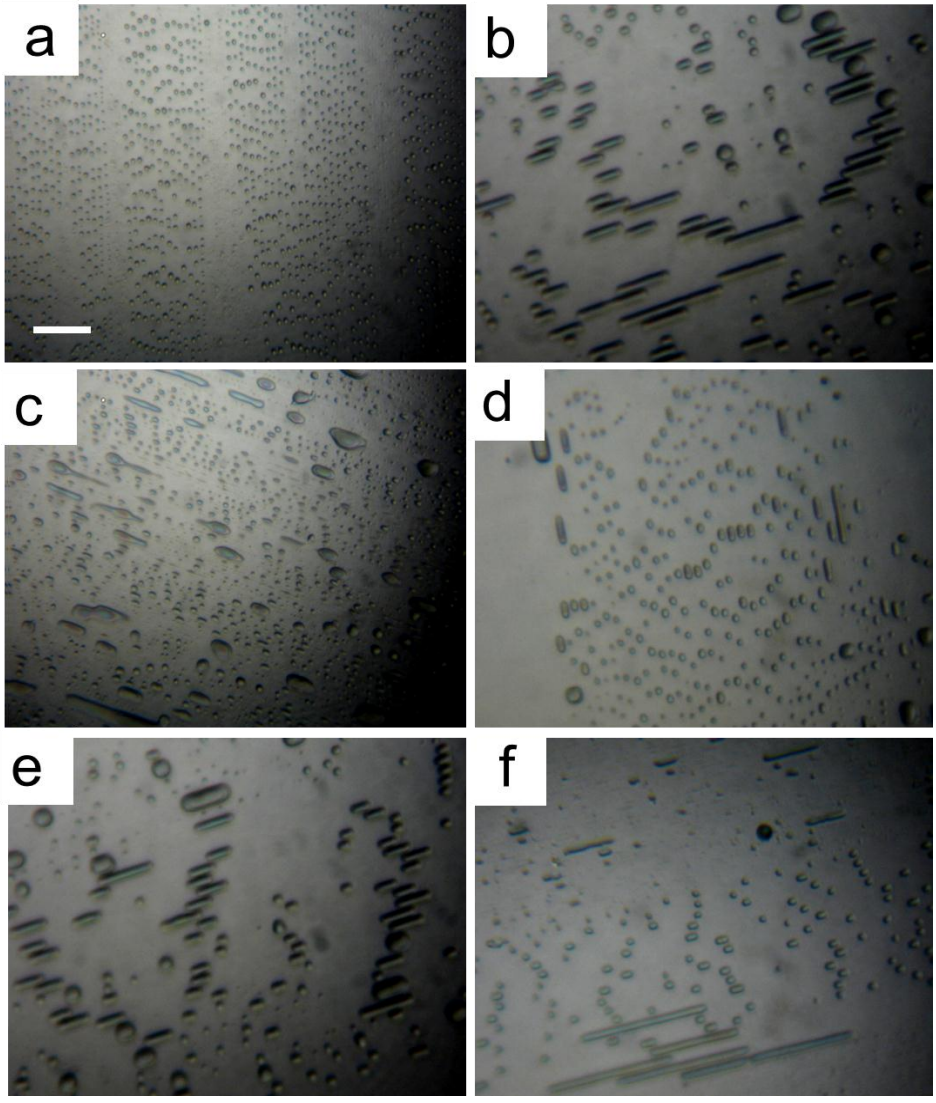

Figure 2.6. OM images of evaporating DI water droplets on the 5 mM (a, b), 10 mM (c, d) and 20 mM (e, f) OTS patterned films prepared at 30 s (a, c, e), and 60 s (b, d, f) printing times (scale bar shows 10 mm).

2.3.3. Contact Angle Measurements

In order to investigate the average surface energies of the patterned OTS films, water contact angle measurements were performed. The contact angle is defined as the angle between the liquid/gas interface and the solid/liquid interface when three phases are in equilibrium (portrayed on Figure 2.7 a).[46] Young's equation describes this angle based on interfacial tensions between three phases of liquid, solid, and gas, as below:[46]

$$\gamma_{SG} = \gamma_{LS} + \gamma_{GL} Cos\theta \qquad (2.1)$$

where θ is the equilibrium contact angle on a flat surface, γ_{SG}, γ_{LS}, and γ_{GL} are the solid-gas, liquid-solid, and gas-liquid interfacial energies, respectively. If the liquid is strongly attracted to the solid surface droplet spreads out and wets the surface ($\theta \sim 0°$); an example for this is a water drop on a hydrophilic surface. As the surface energy decreases, water does not wet the solid and contact angles increase.

There are different measured contact angles: advancing (the angle measure when drop is advancing), and receding (the angle measure when drop is receding); neither are the same as the thermodynamically defined contact angle.[46] However, comparison between different surfaces can be made by comparing advancing contact angles, obtainable by imaging the droplet as it advances over the surface (i.e. as a water drop is pushed onto the surface via a syringe). Telescopic images of a DI water drop, which

were used to measure advancing contact angles, on patterned and non-patterned OTS films are shown in figure 2.7-2.9.

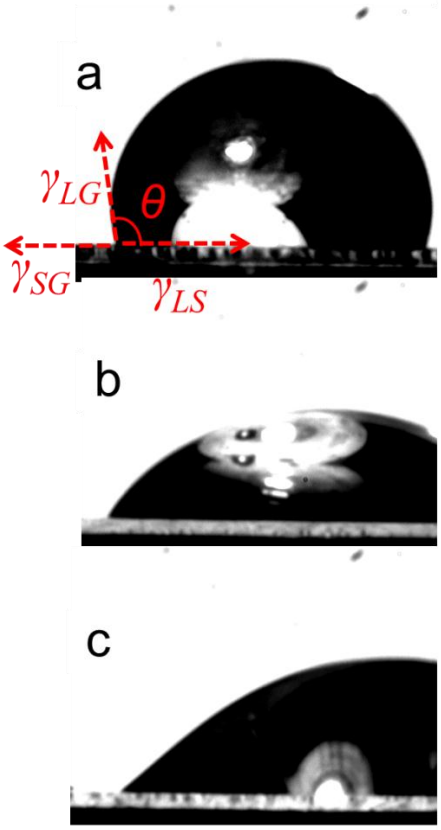

Figure 2.7. Single droplet of DI water on (a) 5 mM OTS non-patterned glass substrate, on 5 mM OTS patterned prepared by (b) 30 s, and (c) 60 s printing time. Interfacial energies between three phases and the contact angle are displayed on a.

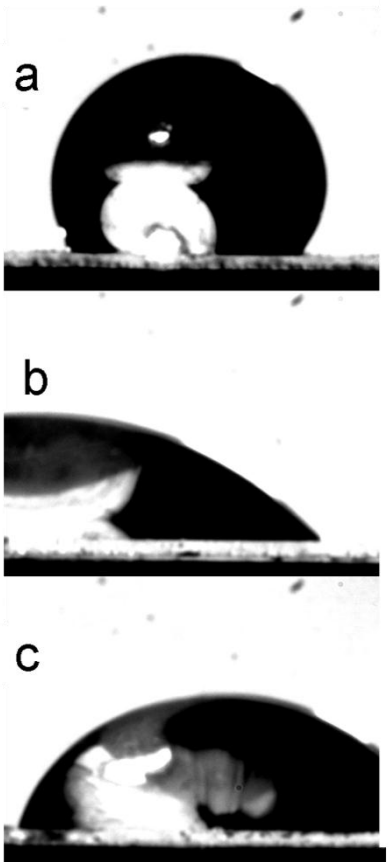

Figure 2.8. Single droplet of DI water on (a) 10 mM OTS non-patterned glass substrate, on 10 mM OTS patterned prepared by (b) 30 s, and (c) 60 s printing time.

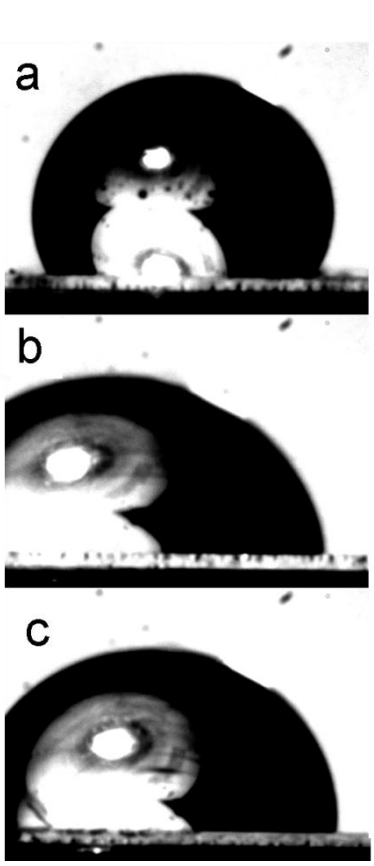

Figure 2.9. Single droplet of DI water on (a) 20 mM OTS non-patterned glass substrate, on 20 mM OTS patterned prepared by (b) 30 s, and (c) 60 s printing time.

The values for advancing water contact angles are listed in Table 2.1. The contact angle for the hydrophilic control film, which is uniformly treated with piranha solution, is close to zero (images not shown here). For the hydrophobic control films, contact angles are greater than 100˚ for all three different concentrations of OTS, as listed in Table 2.1. For patterned films, the contact angles are in between those of uniform hydrophilic (~ 0˚) and uniform hydrophobic substrates (around 120˚); for instance the contact angle for both 10 mM OTS patterned film is ~ 60º, which is in between the value for the uniform hydrophilic control (~ 0º) and the uniform hydrophobic film prepared using the same OTS concentration (~ 120º). Intermediate contact angles for patterned films are

explained by the existence of both microscale hydrophilic and hydrophobic stripes on each surface. In addition, the contact angles increase as the concentration of OTS solution and the printing time increases. This is due to the formed clusters shown in Figure 2.5 d and f that increases the surface roughness of the film and consequently increases the contact angle. The increasing trend in contact angle can be also attributed to more extensive surface coverage (fewer regions with no transferred OTS) when films are prepared using high concentration of OTS.

Table 2.1. Results of advancing water contact angle measurement

	5 mM OTS Solution	10 mM OTS Solution	20 mM OTS Solution
Uniform OTS Film	$\theta = 115 \pm 6^{\circ}$	$120 \pm 20^{\circ}$	$120 \pm 14^{\circ}$
30 s contact time	$\theta = 48 \pm 4^{\circ}$	$60 \pm 20^{\circ}$	$70 \pm 18^{\circ}$
60 s contact time	$\theta = 50 \pm 9^{\circ}$	$70 \pm 18^{\circ}$	$80 \pm 13^{\circ}$

2.3.4. AFM Characterization of OTS Patterned Films on Glass Substrates

AFM imaging reveals the topology of the patterned OTS films; dimensions of the features including *w*, λ and *h* of OTS stripes were determined by height analysis on AFM micrographs. AFM images, which were obtained for patterned OTS films at 5, 10 and 20 mM OTS solution concentration and 30 s, 60 s contact time are shown in Figure 2.10.

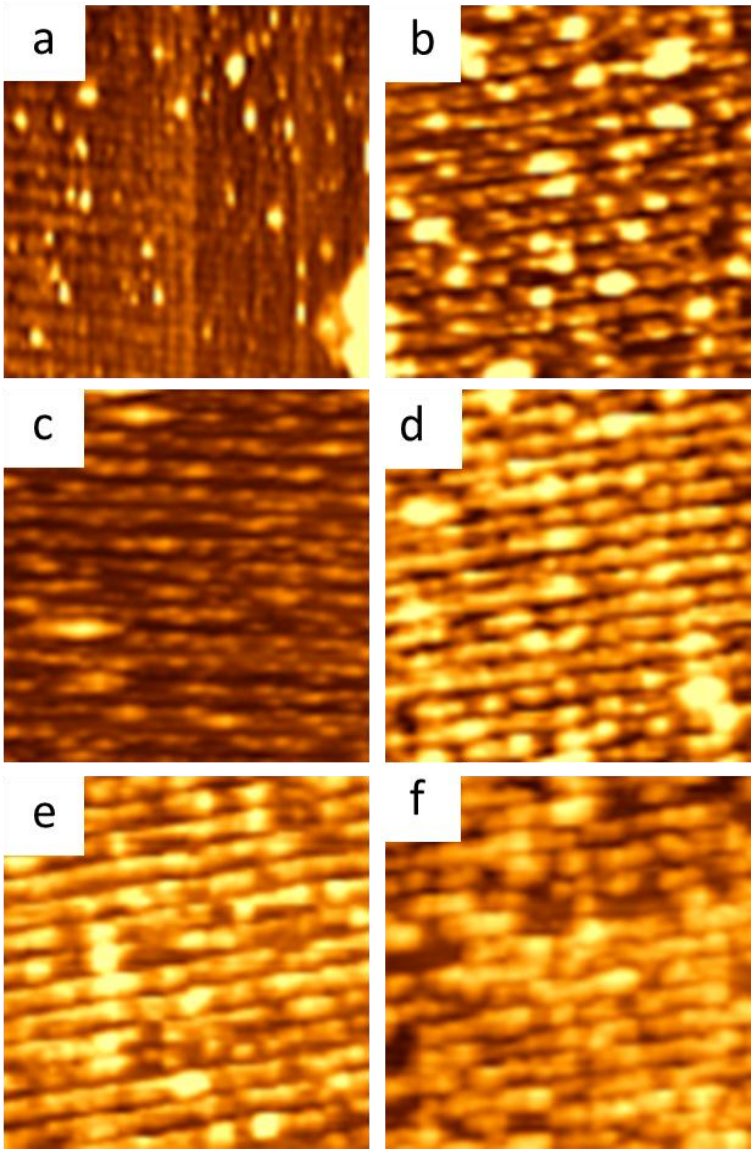

Figure 2.10. 20-20 μm AFM images of the 5 mM (a, b), 10 mM (c, d) and 20 mM (e, f) OTS patterned films prepared at 30 s (a, c, e) and 60 s (b, d, f) printing times.

Height analysis on AFM images provides information on the height of OTS lines, which demonstrates that the *h* of the patterned OTS film is increasing by increasing the solution concentration and printing time. Height analysis shows that in films prepared using 5 mM OTS, mean OTS stripe dimensions are $w = 1.2 \pm 0.2$ μm with $\lambda = 1.6 \pm 0.1$ μm, and $h = 64 \pm 8$ nm. At increased OTS concentration of 10 mM, dimensions

are: w = 1.2 ± 0.4 μm, λ = 1.8 ± 0.3 μm, and h = 180 ± 18 nm. Finally for the most concentrated OTS solution (20 mM), mean dimensions are w = 0.9 ± 0.4 μm, λ = 2.0 ± 0.2 μm, and h = 220 ± 10 nm. Results demonstrate a dramatic change in the height of OTS stripes and a relatively small change in the width and the periodicity by increasing the solution concentration. Height of the transferred OTS, even for the lowest OTS concentration, is larger than the theoretical molecular length of OTS which is 2.65 nm;[41] this indicates the transfer of OTS multilayers during printing. However, there is a good surface energy contrast between the adjacent stripes (based on OM studies with water and contact angle measurements), which is the main requirement for our work since these patterned surfaces will be used in next chapters to direct polymers and polymers/NPs self-assemblies based on their preferential wettings at different regions of the patterned substrate.

2.4. Conclusion

In order to fabricate chemically patterned surfaces, μCP method was employed to transfer OTS to piranha-treated hydrophilic glass substrate. A general experimental protocol for this was developed in this chapter and the effect of parameters such as OTS solution concentration and printing time, were studied. It was shown that the amount of transferred OTS molecules during printing increases by an increase in the OTS solution concentration and the printing time. Types of non-uniformity defects observed in patterned films as the result of low and high transferred OTS were demonstrated in OM and AFM studies.

Contact angle and OM monitoring of a drying DI water droplet confirmed the chemical heterogeneity of such patterned films. These films with alternating micron scale hydrophilic/hydrophobic stripes will be used in the next parts of the work to direct the bottom-up assemblies of polymers and nanoparticles into patterned structures. In Chapter 3, the 5 mM OTS solution concentration and 30 s ptinting time are used for patterned OTS film preparation because these conditions resulted in more uniform patterned film with less clustering defects. However, following the development of a general procedure for μCP OTS on glass in this chapter, the specific experimental details were modified somewhat throughout the thesis to accommodate specific self-assembly applications in the various chapters. For example, we observed that an excess of piranha solution remaining on patterned surfaces adversely affected Langmuir-Blodgett transfer due to apparent chemical reaction with the transferred polymer layers. Therefore, in chapter 3, extra sonicating and washing steps were applied. In later chapters, the uniformity of the patterned OTS films became an additional consideration, requiring a further experimental modification in chapters 4, 5 and 6 to avoid transfer of excess OTS. The specific details for these various experimental protocols for μCP OTS on glass are decribed in the respective chapters.

2.5. References

(1) Mack, C. *Fundamental Principles of Optical Lithography*, Wiley, Chichester, **2007**.

(2) Brambley, D.; Martin, B.; Prewett, P.D., *Adv. Mater. Opt. Electron*, **1994**, 4, 55.

(3) Stulen, R. H.; Sweeney, D. W., *IEEE Journal of Quantum Electronics,***1999**, 35, 694.

(4) Goodberlet, J. C., Appl. Phys. Lett. 2000, 76, 667.

(5) Jain, K., *Excimer Laser Lithography*, SPIE Society of Photo-Optical instrumentation Engineers, Bellingham, **1990**.

(6) Feder, R.; Spiller, E.; Topalian, J., *Polym. Eng. Sci.***1977**, 17, 385.

(7) Kazuaki, S., *Journal of the Institute of Electrical Engineers of Japan***2000**, 120, 348.

(8) Vieu, C.; Carcenac, F.; Pepin, A.; Chen, Y.; Mejias, C. M.; Lebib, A.; Manin-Ferlazzo, L.; Couraud, L.; Launois, H. *Appl. Surf. Sci*. **2000**, 164, 111.

(9) Melngailis, J., *Nuclear Instruments and Methods in Physics Research***1993**, 81, 1271.

(10) Huh, J. S.; Shepard, M. I.; Melngailis, J. *J. Vac. Sci. Tech. B.* **1991**, 9, 173.

(11) Soh, H. T.; Guarini, K. W.; Quate, C. F., *Scanning Probe Lithography*, Kluwer Academic Publishers, Massachausetts, **2001**.

(12) Y. Xia, G. M. Whitesides, *Annu. Rev. Mater. Sci*., **1998**, 28, 153.

(13) Y. Xia, G. M. Whitesides, *Angew. Int. Ed*., **1998**, 37, 550.

(14) Hidber, P. C.; Helbig, W.; Kim, E.; Whitesides, G.M., *Langmuir*, **1996**, 12, 1375.

(15) Zhao, X.M.; Xia, Y.; Whitesides, G.M., *J. Mater. Chem.,***1997**, 7, 1069**.**

(16) Jeon, N. L.; Choi, I. S.; Whitesides, G. M.; Kim, N.Y.; Laibinis, P.E.; Harada, Y.; Finnie, K. R.; Girolami, G. S.; Nuzzo, R.G., *Appl. Phys. Lett.,***1999**,75, 4201.

(17) Zhong, Z.; Gates, B.; Xia, Y.; Qin, D., *Langmuimr*,**2000**, 16, 10369.

(18) Yu, M.; Lin, J.; Wang, Z.; Fu, J.; Wang, S.; Zhang, H. J.; Han, Y. C. *Chem. Mater*.,**2002**, 14, 2224.

(19) Kumar, A.; Whitesides GM. 1993. *Appl.Phys. Lett.*, **2002**, 4, 63.

(20) Clarson, S.J.; Semlyen, J.A., *Siloxane Polymers.* Englewood Cliffs, NJ, Prentice Hall, **1993.**

(21) Xia, Y.; Kim, E.; Zhao, X.M.; Rogers, J.A.; Prentiss, M.; Whitesides, G.M., *Science,***1996,** 273, 347.

(22) Zhao, X.M.; Xia, Y.; Whitesides, G.M., *Adv. Mater,***1996**,8, 837.

(23) Kim, E.; Xia, Y., Whitesides GM., *Nature,* **1995**, 376, 581.

(24) Kim, E.; Xia, Y.; Zhao, X.M.; Whitesides, G.M., *Adv. Mater.,* **1997**,9,651.

(25) Masuda, H.; Fukuda, K.; *Science,* **1995**, 268, 1446.

(26) Huber, T.E.; Luo, L.; *Appl. Phys. Lett.,* **1977**,70, 2502.

(27) Wilbur, J.L.; Kumar, A.; Kim, E.; Whitesides, G.M., *Adv. Mater.*, **1994**, 6, 600.

(28) Delamarche, E.; Michel, B.; Biebuyck, H.A.; Gerber, C., *Adv. Mater.,* **1996**, 8, 719.

(29) Boltau, M.; Walheim, S.; Mlynek, J.; Krausch, G.; Steiner, U.,*Nature,* **1998**, 391, 877.

(30) Fenter, P.; Eisenberger, P.; Li, J.; Camillone, N.; Bernasek, S., *Langmuir,* **1991**, 7,2013.

(31) Xia, Y.; Kim, E.; Mrksich, M.; Whitesides, G.M., *Chem. Mater.*, **1996**, 8, 601.

(32) Jeon, N.L.; Nuzzo, R.G.; Xia, Y.; Mrksich, M.; Whitesides, G.M., *Langmuir*, **1995**, 11, 3024.

(33) Xia, Y.; Mrksich, M.; Kim, E.; Whitesides, G.M.,*J. Am. Chem. Soc.*, **1995**, 117, 9576.

(34) Allara, D.L., Parikh, A.N.; Rondelez, F., *Langmuir*, **1995**, 11, 2357.

(35) Wirth, M.J.; Fairbank, R.W.P.; Fatunmbi, H.O., *Science*, **1997**,275, 44.

(36) Huang, Z.; Wang, P.C.; MacDiarmid, A.G.; Xia, Y.; Whitesides, G.M., *Langmuir*, **1997**, 13, 6480.

(37) Cui, L.; Zhang, Z.; Li, X.; Han, Y., *Polymer Bulletin*, **2005**, 55, 131.

(38) Finnie, K.R.; Haasch, R.; Nuzzo, R.G.; *Langmuir*, **2000**, 16, 6968.

(39) Pompe, T.; Fery, A.; Herminghaus, S.; Kriele, A.; Lorenz, H.; Kotthaus, J.P.,*Langmuir* 15, 2398-2401 (1999)

(40) Jeon, N.L.; Finnie, K.; Branshaw, K.; Nuzzo, R.G.,*Langmuir,* **1997**,13, 3382.

(41) Kenneth, G. S.; Blackman, G. S.; Glassmaker, N. J.; Jagota, A.; Hui, C.-Y. *Langmuir***2004**, 20, 6430.

(42) Hui, C. Y.; Jagota, A.; Lin, Y. Y., Kramer, E. J. *Langmuir* **2002**, 18, 1394.

(43) Jung, M.-H.; Choi, S.-H. *Korean J. Chem. Eng*. **2009**, 26, 1778.

(44) Sharma, A.; Reiter, G. *Journal of Colloids and interface science* **1996**, 178, 383.

(45) Reiter, G. *Phys. Rev. Lett.* **1991**, 68, 75.

(46) Gast; A. P.; Adamson, A.W., *Physical Chemistry of Surfaces*, 6th ed., Wiley, New York, 1997.

Chapter 3. PATTERNING BLOCK COPOLYMER AGGREGATES VIA LANGMUIR-BLODGETT TRANSFER TO MICROCONTACT-PRINTED SUBSTRATES

3.1. Introduction

The self-assembly of polymers provides many important routes for controlling the spatial organization of organic and inorganic functional elements on surfaces.[1-16] For example, the incorporation of metal and semiconductor nanoparticles into microphase-separated diblock copolymers,[1-13] or phase-separated blends of homopolymers,[14-16] results in controlled arrangement of nanoparticles via selective incorporation within specific polymer phases. Increased complexity and improved long-range order for the self-assembly of block copolymers[17-23] and polymer blends[24-27] has been achieved on chemically- or topographically-patterned substrates produced via various lithographic techniques. This combination of top-down lithography with bottom-up self-assembly offers new opportunities for the fast and efficient organization of nanoparticles into device-oriented structures.[28]

A widely-studied strategy for obtaining nanopatterned polymer surfaces is the self-assembly of amphiphilic block copolymers at the air-water interface, which gives rise to tunable nanoscale aggregates that can be transferred to solid substrates via the Langmuir-Blodgett (LB) method.[29-43]A large number of tunable aggregate morphologies, including dots, strands (spaghetti-like), networks of strands, continents, chains, and rings, have been observed by varying several experimental parameters, including the block copolymer composition,[29-31] the spreading concentration,[39-41] and the surface pressure.[34] For example, aggregate formation on the surface of water has been investigated for polystyrene-*block*-poly(ethylene oxide) (PS-*b*-PEO) copolymers consisting of hydrophobic PS and hydrophilic PEO blocks.[36-41] More recently,[42, 43] PS-*b*-PEO self-assembly has been used to direct the organization of PS-coated cadmium sulfide (CdS)

nanoparticles into strands, rings and cables at the air-water interface; in that work, nanoparticle ordering occurred via preferential interactions between PS blocks of PS-*b*-PEO and the external PS layer of the polymer-coated CdS nanoparticles (designated PS-CdS).[42, 43] Despite demonstrated tunability of block copolymer aggregate morphologies via self-assembly at the air-water interface, the ability to control the spatial distribution and ordering of the aggregates upon LB transfer to solid substrates is extremely limited. Although circular aggregates have been shown to form well-ordered hexagonal arrays upon compression at the water surface,[32, 36, 37] other interesting aggregate morphologies, including strands, are generally highly disordered and randomly distributed within LB films.[34, 39-41]

Several recent examples of nonlithographic patterning of LB films have highlighted the importance of substrate surface energies for controlling monolayer transfer from the air-water interface.[44-46] For example, Yang and coworkers have shown that LB transfer of nanoparticles to highly wettable (i.e. hydrophilic) substrates will form continuous monolayer films; however, the addition of polymer to the subphase induces fingering instabilities, which template nanoparticle stripes perpendicular to the contact line.[45] On the other hand, the same group has found that for LB transfer to partially wettable (i.e. hydrophobic) substrates, wetting instabilities induce a "stick and slip" motion of the retreating meniscus, forming regular arrays of nanoparticle lines parallel to the contact line.[46] In addition to such non-lithographic approaches, LB transfer to topographically-patterned substrates has recently been applied to direct the placement of colloidal crystals on surfaces.[47] As well, several research efforts have applied chemically-patterned substrates with microscopically-heterogeneous surface energies to control two-

dimensional organization within liquid and colloid films via selective dewetting processes.[48-52]

In this work, we combine the concepts LB patterning and selective dewetting to control the spatial distribution of block copolymer aggregates formed at the air-water interface on substrates with chemically-patterned heterogeneities in surface energy. Specifically, we first use microcontact printing to produce hydrophilic/hydrophobic arrays with microscale periodicities, consisting of octadecyltrichlorosilane (OTS) stripes patterned onto glass surfaces. Strand-like aggregates of a PS-*b*-PEO block copolymer formed via self-assembly at the air-water interface are then transferred to these patterned substrates via the LB method. We show that under specific conditions of surface pressure, withdrawal speed, and substrate orientation, the transferred aggregates are selectively positioned within the hydrophilic stripes due to selective dewetting along the three-phase contact line. We also apply this method to control the transfer of self-assembled PS-*b*-PEO strands with incorporated CdS nanoparticles, producing microscale photoluminescent nanoparticle/polymer stripes with an internal strand-like structure. To our knowledge, the current work represents the first use of microscopically-patterned surface energies to control the patterning of LB films on solid substrates. These results highlight the immense potential of combining facile top-down patterning with efficient bottom-up self-assembly, in order to increase the regularity, complexity, and functionality of hierarchical polymer and polymer-nanoparticle architectures.

3.2. Experimental

3.2.1. Materials

The two different PS-*b*-PEO copolymers used in this work were obtained from Polymer Source Ltd. Both copolymers have PS blocks much longer than their respective PEO blocks. The first copolymer, designated 141k, has a number-average molecular weight of M_n = 141 k and a PEO content of 11.4 wt%; the second copolymer, designated 185k, has a number-average molecular weight of M_n = 185 k and a PEO content of 18.9 wt%. Both copolymers were stored at -9 °C to prevent decomposition of the PEO block.[53] The block copolymer-stabilized CdS nanoparticles used in this study (PS-CdS) were synthesized via templated growth of CdS in the cores of reverse micelles consisting of the polystyrene-*block*-polyacrylic acid copolymer PS(130)-*b*-PAA(20), where numbers in brackets indicate number-average degrees of polymerization for each block. The detailed characterization of the PS-CdS sample employed here are described in refs 42 and 43. In summary, each PS-CdS unit consists of a core of a ~4 nm CdS nanoparticle (determined from UV-vis and using Henglein's empirical relationship),[54, 55] with a poly(cadmium acrylate) (PACd) layer at the CdS surface, covalently-attached to a solubilized external PS brush layer. Based on DLS results in chloroform, the overall hydrodynamic diameter of PS-CdS is ~28 nm.[42,43] Further details on the synthesis of PS-CdS can be found in references 55 and 56.

3.2.2. Preparation of Polydimethylsiloxane (PDMS) Stamps for Microcontact Printing

Masters with microscale periodic stripe patterns were obtained using commercial compact discs (CDs). First, the protective layer of a CD was removed by scoring with a scalpel and vigorously rinsing with deionized (DI) water. Then, the metallic layer and thin lacquer coat were removed via a quick rinse with methanol and subsequent sonication in a 1 : 4 (v : v) methanol/DI water solution for 2 h, followed by a final methanol rinse, revealing the underlying polycarbonate layer with the desired topographic features. The polycarbonate was cut into square pieces ~2 cm x 2 cm. Prepolymer and curing agent for polydimethylsiloxane (PDMS) (Dow Corning: Sylgard 184 DC-184 A and DC 184-B) were mixed in a 10:1 (v:v) ratio, then poured over a polycarbonate master, followed by 4 h curing at 80˚C. The PDMS was then carefully peeled from the master in the direction tangential to the CD grooves, at a steady rate of ~1 cm/s. The topology of the resulting PDMS stamps consisted of periodic raised stripes corresponding to the troughs of the polycarbonate masters. The PDMS stamps were sonicated in a 1 : 2 (v : v) solution of ethanol/DI water immediately prior to use, in order to remove possible dust or unpolymerized PDMS, followed by drying with a stream of ultra-high purity (UHP) N_2 (g). To avoid build-up of siloxane deposits, PDMS stamps were used only once.

3.2.3. Microcontact Printing Glass Substrates with Octadecyltrichlorosilane (OTS)

Glass cover slips (VWR scientific, 18 x 18 mm) were cleaned by sonication for 10 min in 95% ethanol, followed by 10 min sonication in DI water. To introduce a layer of hydroxyl groups on the glass surface, the cover slips were submerged in a piranha solution at 70˚C for 30 min. Piranha solution consists of a 3 : 1 (v : v) mixture of concentrated H_2SO_4 and 30% H_2O_2. Following piranha treatment, the cover slips were sonicated in DI water for 10 min then rinsed with methanol, followed by two further repetitions of the sonication/rinsing process. The resulting hydrophilic glass substrates were dried with a UHP N_2 (g) stream and used immediately for microcontact printing (μCP). The ink for μCP was prepared by dissolving octadecytrichlorosilane (OTS, Aldrich) in anhydrous hexane (≥99%, Aldrich) under UHP N_2 (g) to obtain a 5 mM solution. PDMS stamps were inked by first depositing a single drop of the resulting OTS solution from a Pasteur pipette on the centre of a 2 cm x 2 cm piece of lens paper; a stamp was then brought into contact with the inked paper for 10 s. To carry out μCP, an inked PDMS stamp was brought into contact with one half of a hydrophilic glass cover slip for 30 s under a 200-g weight, such that the OTS stripe pattern was transferred to half of the coverslip, with the remaining unpatterned hydrophilic half serving as the control. The resulting substrates were used for LB experiments by submersion in the aqueous subphase of the LB trough immediately following μCP. In order to characterize the structure of chemically-patterned substrates without LB deposition, microcontact-printed substrates were submerged immediately in the aqueous subphase of the LB trough without polymer deposition for 65 min (equivalent to the substrate submersion time for

LB deposition), followed by vertical withdrawal at a rate of 1 mm/min and air-drying in an identical manner to LB film experiments. To confirm that the transferred patterns were due to reacted OTS, and not due to dust or unpolymerized PDMS, an identical inking and stamping process was also carried out using pure anhydrous hexane as the inking solution.

3.2.4. Contact Angle Measurements

For contact angle measurements, microcontact-printed substrates were immersed in DI water for 65 min immediately after μCP (equivalent to the substrate submersion time for LB deposition). Immediately following removal of the OTS-patterned glass from water, a drop of DI water (~10μl) was deposited on the horizontal substrate using a microsyringe. Images of the drop on the substrate were taken by a fixed focal length telescope (VZM 1000i imaging lens) with the lens positioned at the level of glass slide. Advancing contact angles were measured for drops in three different regions of the slide and using both sides of each drop. A mean contact angle and standard deviation were thus determined from the resulting 6 measurements.

3.2.5. Preparation of PS-b-PEO (141 k) and PS-CdS/PS-b-PEO (185 k) Solutions

Both 141k and 185k copolymers were dried overnight in a dark vacuum oven at room temperature prior to use. To prepare the 141k copolymer solution, the copolymer was dissolved in spectroscopic grade chloroform (≥99.8%, Aldrich) to a concentration of

2.0 mg/mL; the stock solution was allowed to equilibrate overnight, then diluted to 1.0 mg/mL by addition of chloroform followed by 4 h stirring. To prepare the PS-CdS/185k blend solution, 2.0 mg/mL solutions of both PS-CdS and 185k copolymer were first prepared separately in spectroscopic grade chloroform and allowed to equilibrate overnight. Both stock solutions were then diluted to 1.0 mg/mL by addition of chloroform followed by 4 h stirring. Finally, the diluted PS-CdS and 185k solutions were mixed to give a blend solution with blend composition *f* (weight PS-CdS / total polymer weight) = 0.75 and a total polymer concentration of 1.0 mg/mL. The blended solution was stirred for at least 4 h prior to use.

3.2.6. Surface Pressure-Area Compression Isotherms of 141k and PS-CdS/185k Langmuir Films

Surface pressure versus area (π-A) isotherms and LB films transfer were performed with a KSV 3000 Langmuir trough (KSV Instruments Ltd.) secured in a dust shield. The water subphase in the trough has a 150 x 515 mm^2 surface area and ~ 1L volume. For isotherm experiments, 0.10 mg solid was deposited on the water surface from 1.0 mg/mL spreading solutions in chloroform; 100 μL solution (~ 10 drops) was added drop-wise and symmetrically (~5 drops on each side) to the subphase surface using a Hamilton microsyringe. After a 30 min period for solvent evaporation, compression isotherms were obtained via controlled symmetric movement of two computer-controlled hydrophobic paddles at 10 mm/min toward the centre of the trough; accompanying changes in surface pressure were simultaneously monitored using a roughened platinum

Wilhelmy plate. DI water (Barnstead NANOpure Diamond, 18.2 mΩ/cm) was used as the subphase and was maintained at 21 ± 0.5 °C for all experiments. Trough and paddles were cleaned three times with ethanol and DI water prior to use. Prior to compression experiments, the surface of the subphase was cleaned by aspirating off any debris, such that the surface pressure remained < 0.20 mN/m over a full compression.

3.2.7. Langmuir-Blodgett Film Transfer to Patterned and Unpatterned Substrates

The initial steps for preparing LB films were analogous to those used for preparing Langmuir films for isotherm measurements; however, for LB experiments, only 0.05 mg of solid (half the mass used to obtain isotherms) was deposited at the air-water interface. After 30 min solvent evaporation, the film was compressed at a rate of 10 mm/min until the target surface pressure (π = 5 or 10 mN/m) was reached. This π was maintained for another 30 min before transfer of the LB film. Following this equilibration time, the LB films were transferred to the half-patterned glass by a vertical withdraw of the submerged cover slips, generally at a rate of 1 mm/min and with the hydrophilic/hydrophobic stripes oriented perpendicular to the air-water interface, unless otherwise stated in the text. The resulting films were dried vertically under ambient conditions for at least 12 h before imaging. All LB experiments resulted in transfer ratios close to one (0.8-1.0) unless otherwise noted.

3.2.8. Atomic Force Microscopy (AFM)

AFM in tapping mode was performed on a MFP-3D atomic force microscope from Asylum Research with 300 kHz-resonance frequency Si tips (spring constants 40 to 70 N/m) from Vistaprobe. Contact mode AFM was performed using a ThermoMicroscope Explorer (Veeco Instruments) equipped with a Veeco silicon nitride tip (MLCT-EXMT-A). Each sample was imaged several times at different locations on the substrate to determine the regularity of the film structure. All images presented in this chapter were scanned over a 10 μm x 10 μm area at a scan rate of 0.5 Hz and represent typical images of each LB film. For each LB film, statistical analysis of feature widths and heights were carried out from three 10 μm x 10 μm images obtained in three different regions of the film; a total of at least 80 features were measured to determine mean dimensions, with reported errors representing a single standard deviation unit.

3.2.9. Photoluminescence Spectroscopy of PS-CdS

Photoluminescence measurements of PS-CdS in chloroform were recorded with an Edinburg Instruments FLS 920 fluorimeter. The excitation source was a 450 W Xe arc lamp, the detector employed was an R928P Hamamatsu PMT, and the spectral resolution was 1 nm. An excitation spectrum was recorded by setting λ_{em} = 610 nm and an emission spectrum was recorded by setting λ_{ex} = 300 nm. Both excitation and emission spectra were collected without using a filter. Reported spectra were obtained by subtracting a solvent background from the raw data.

3.2.10. Laser Scanning Confocal Fluorescence Microscopy (LSCFM)

LSCFM measurements of photoluminescent PS-CdS/185k LB films were carried out on a Zeiss LSM 410 with Ar/Kr laser. Films were excited at λ_{ex} = 488 nm, using a band pass 485 ± 20 nm line selection filter and a FT 510 dichroic beam splitter. A long-pass 610 nm emission filter only allowed light above 610 nm to reach the PMT detector. A Zeiss Plane-Aprochromat 63x oil-immersion objective lens was used for imaging. The pinhole diameter was set to 1.2 Airy units. To prepare samples for LSCFM measurements, an LB-containing glass coverslip was taped to a glass microscope slide, such that the film was sandwiched between the slide and coverslip. Zeiss Immersionsoel 518 C oil was deposited between the objective and the coverslip in order to provide a constant-refractive index media between the objective and the glass. Both halves of the glass substrate (OTS-patterned and unpatterned) were scanned for comparison. As a control, one of the 141k LB films, without CdS nanoparticles, was also scanned under the same conditions, resulting in no observed signal; this confirmed that the observed bright regions in the LSCFM images of PS-CdS/185k films were due to photoluminescence from CdS nanoparticles.

3.3. Results and Discussion

The general strategy for the controlled transfer of block copolymer aggregates from the air-water interface to chemically-patterned substrates combines well-established procedures for μCP[57-59] and interfacial block copolymer self-assembly,[36-43] as illustrated in Figure 3.1. First (Figure 3.1a), a PDMS stamp with striped topology was employed to

selectively transfer OTS to piranha-treated glass in areas of contact between the stamp and the substrate; chemical reaction between OTS and hydroxyl groups on the glass surface resulted in a chemically-heterogeneous surface with an alternating pattern of hydrophilic/hydrophobic stripes with microscale periodicity. Next (Figure 3.1b), a solution 141k PS-*b*-PEO block copolymer (or blend of 185k PS-*b*-PEO block copolymer and PS-CdS nanoparticles) in chloroform was spread on the water surface of an LB trough; subsequent solvent evaporation induced block copolymer self-assembly at the air-water interface due to the interplay of attractive PEO-water interactions and repulsive PS-water and PS-PEO interactions.[36-43] As portrayed in Figure 3.1b, the resulting low-density aggregates of PS-*b*-PEO consist of hydrophobic PS cores surrounded by peripheral PEO chains in a 2D pancake conformation at the air-water interface;[36-43] Cox et al. have further suggested that additional PEO chains form a buffer layer between the PS cores and the water surface.[37] Finally (Figure 3.1c), following compression of the aggregates to a specified surface pressure (π), the chemically-patterned substrate (with a non-patterned hydrophilic half serving as a control) was lifted vertically at constant π through the air-water interface, effecting transfer of the aggregates to the substrate. As illustrated in Figure 3.1c, the substrate stripe pattern was typically oriented perpendicular to the air-water interface during LB transfer, although LB transfer with parallel pattern orientation was also investigated, as described in the text; other experimental variables for LB transfer were the surface pressure (π = 5 and 10 mN/m) and withdrawal speed (1 and 5 mm/min).

The chemically-patterned substrates without LB film deposition were first characterized following μCP, submersion in deionized water for 65 min, vertical

withdrawal at 1 mm/min, and air drying. The water submersion, vertical withdrawal, and air-drying steps were carried out to match corresponding LB experiments and to account for any effects of OTS swelling by water on the morphology and surface properties of the OTS film. An optical microscopy (OM) image of the resulting patterned surface (Figure 3.2a) shows the periodic stripe pattern of OTS on glass imposed by the topology of the PDMS stamp used for μCP. From OM, the periodicity of the dark OTS stripes is 1.4 μm ± 0.1, consistent with the periodicity of peaks on the PDMS stamps, as measured by AFM (1.4 μm ± 0.3). To demonstrate the microscale patterning of surface energies on the resulting surface, we deposited a large drop of water on the substrate shown in Figure 3.2a, and monitored the evaporation of water over time by OM. As evaporating water droplets decreased to sizes on the order of the pattern periodicity, they were found to segregate in the hydrophilic regions between the OTS stripes, forming oriented water patches with an approximately rectangular shape. In the inset to Figure 3.2a, four such water patches (outlined with white dotted lines) can be seen, each localized within a hydrophilic domain between the periodic OTS lines (highlighted with black dotted lines). The drying behavior of water droplets thus confirms the microscale surface energy heterogeneities on the patterned substrates, which consist of arrays of alternating hydrophilic/hydrophobic stripes. Advancing water contact angle measurements of the heterogeneous surface gave a mean value of $40^{o} \pm 10^{o}$, compared to a near-zero contact angle determined for the hydrophilic glass surface used as a control substrate in this study.

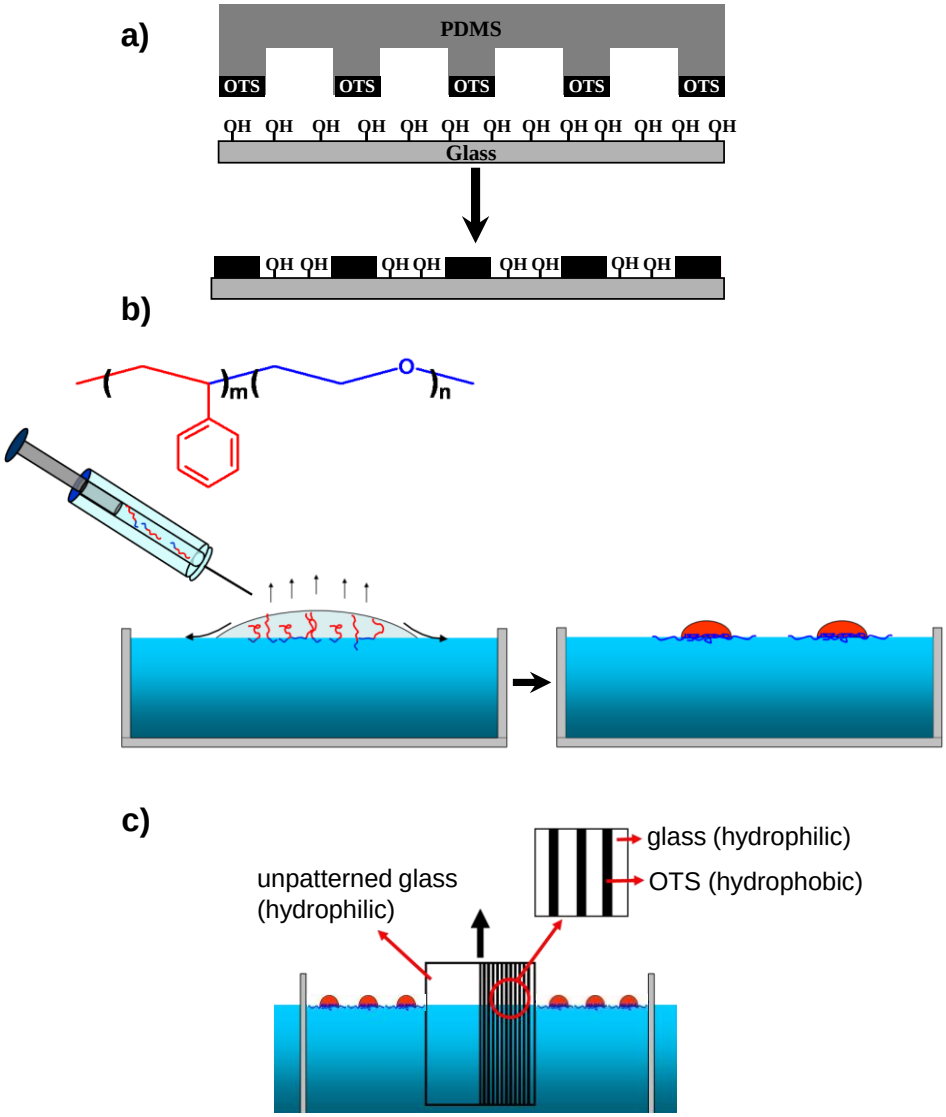

Figure 3.1. Schematic illustrations (not to scale) of the various steps applied in the current method: a) microcontact printing of OTS on hydrophilic glass to obtain substrates with a hydrophilic/hydrophobic stripe pattern; b) self-assembly of PS-*b*-PEO copolymer at the air-water interface via solution spreading and chloroform evaporation; c) LB transfer of copolymer aggregates from the air-water interface to OTS substrates consisting of a patterned hydrophilic/hydrophobic region and a hydrophilic control region.

Further structural details of the patterned OTS-glass surfaces were determined by AFM and accompanying topology profiles (Figure 3.2b). Control AFM images of glass

slides produced using PDMS stamps inked with pure anhydrous hexane (no OTS) showed no stripe pattern transferred to the glass, confirming that the observed raised regions in Figure 3.2b are chemically-bonded OTS (Supporting Information). The observed double-stripe topology in Figure 3.2b indicates that each OTS domain is thicker at the outside edges than in the middle. This observed topology is probably a manifestation of the well-known "coffee ring" effect,[60] in which evaporation-driven flow within drying patches of transferred ink gives rise to a higher concentration of OTS at the periphery of the hydrophobic domains. From AFM, the periodicity of the stripe pattern is 1.4 ± 0.1 μm, consistent with OM results, and the widths of the hydrophobic OTS and hydrophilic glass domains are 0.4 ± 0.1 μm and 1.0 ± 0.1 μm, respectively. The mean OTS film height determined at the raised edges of the OTS domains is 4 ± 1 nm, which is slightly greater than previously-determined OTS monolayer heights of ~2.5 nm,[61] suggesting some cross-polymerization in these concentrated regions.

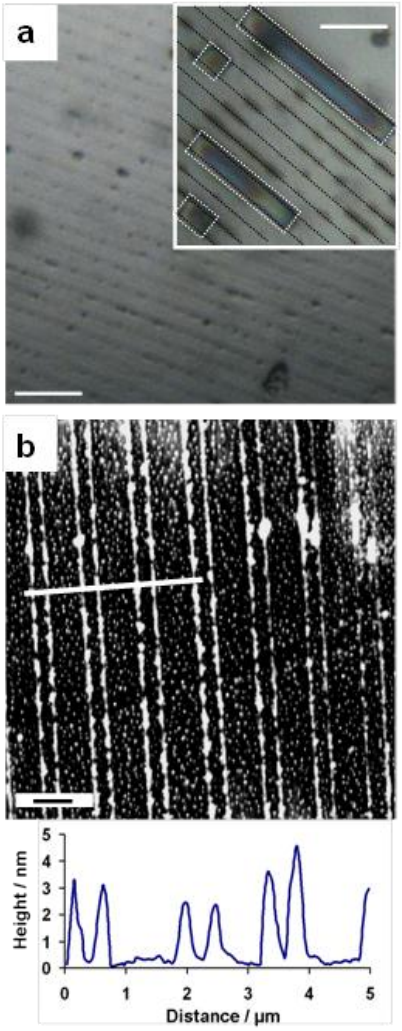

Figure 3.2. (a) OM and b) AFM images of the patterned substrate consisting of OTS stripes transferred to glass. Following µCP, the substrate was immersed in water for 65 min (without copolymer deposition at the water surface) then withdrawn vertically at 1 mm/min, in order to replicate the conditions of LB transfer experiments. The inset to a) shows localization of drying water patches (outlined with white dotted lines) within hydrophilic domains between the periodic OTS stripes (highlighted with black dotted lines), confirming the microscale patterning of surface energies on the substrate. The white line in b) indicates region in which accompanying height profile (b, below) was taken. Scale bars in a) and inset indicate 5 µm and scale bar in b) indicates 1 µm.

Before their transfer to chemically-patterned substrates, the behaviors of the self-assembled copolymer and blend films were compared at the air-water interface via Langmuir compression isotherms (Figure 3.3). The obtained π-*A* isotherm for the pure 141k copolymer (red curve) is typical of PS-*b*-PEO aggregates at the air-water interface upon compression, showing an initial gradual increase in π accompanied by a fast decrease in *A* (liquid expanded state), followed by sharp increase in π beginning at ~10 mN/m (condensed state). The transition between these two compression regions is generally correlated with the submersion of peripherial PEO chains into the aqueous subphase (pancake-to-brush transition) resulting in close-packing of aggregate cores.[39-41, 62-67] In contrast, the PS-CdS/185k isotherm (blue curve) does not show the initial soft compression region with accompanying fast decrease in *A*. Instead, π increases (and *A* decreases) steadily from the beginning of the compression. The isothermal behavior of the blend therefore suggests a decreased contribution from the overlap and conformational transition of PEO chains surrounding the aggregate cores, due to the increased PS content of the blend, as we have reported previously.[4]

Consistent with our previous studies of this copolymer at the same spreading concentration,[40-43,68] the LB film of pure 141k transferred to non-patterned hydrophilic glass at π = 5 mN/m reveals mainly strandlike branched and interconnected aggregates (Figure 3.4a). AFM scans in other regions of the same LB film also show the presence of occasional small circular aggregates (dots). Topology profiles of the strands reveal a mean width of ~100 nm and a mean height of 11 ± 2 nm, consistent with a monolayer of PS-*b*-PEO chains.[40] We observed a generally uniform distribution of aggregates across the non-patterned glass. As well, it was found that the strandlike aggregates were

randomly oriented, as indicated in Figure 3.4a. This indicates that transfer of the aggregates from the air-water interface to the non-patterned glass has minimal influence on the lateral placement and orientation of the aggregates in the final LB film.

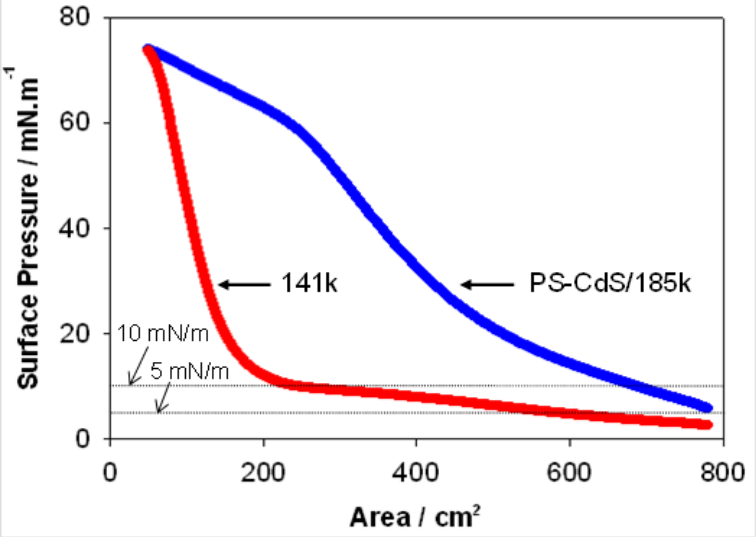

Figure 3.3. Compression isotherms obtained for pure 141k copolymer (red curve) and the PS-CdS/185k blend (blue curve). The two different surface pressures used for LB transfer experiments, π = 5 mN/m and π = 10 mN/m, are indicated with dotted lines.

In contrast, Figure 3.4b shows the LB film of the 141k copolymer transferred at π = 5 mN/m to the chemically-patterned substrate, with the hydrophilic/hydrophobic stripes oriented along the direction of vertical withdrawal, perpendicular to the air-water interface. The resulting film clearly matches the underlying pattern of the substrate, showing a stripe array with periodicity 1.3 ± 0.1 μm, nearly identical to that determined for the OTS pattern described in Figure 3.2 (1.4 ± 0.1 μm). The mean widths of the raised and lower regions of the LB film, 1.0 ± 0.1 μm and 0.4 ± 0.1 μm, respectively,

correspond to the widths of the hydrophilic glass and hydrophobic OTS regions on the chemically-patterned substrate. The film structure therefore indicates that LB deposition under these conditions resulted in selective positioning of copolymer aggregates within the hydrophilic regions of the substrate. Within most regions of the stripes, the overlap of multiple aggregates made it impossible to resolve individual dots or strands from the topographic images. However, near the top of the LB films, where the film thickness was thinner than the average value, contact mode AFM of individual stripes revealed an internal structure of dots and strands (Figure 3.4b, inset) with lateral dimensions consistent with those of the aggregates observed on the non-patterned substrate. This result indicates that the aggregates retained their structural integrity upon transfer to the patterned substrate, and suggests that the film in Figure 3.4b contains a similar mixture of dots and strandlike aggregates as the film in Figure 3.4a, only with a different surface density and spatial distribution. The resilience of aggregate morphologies during LB patterning is not unexpected, considering that the PS cores will be below their glass transition temperature following evaporation of the spreading solvent.[36,37,40-43] These results suggest a building up of structural hierarchy via nanoscale self-assembly at the air-water interface followed by substrate-directed organization into microscale arrays. From AFM topographic profiles, the mean height of the aggregate-containing regions (Figure 3.4b) is 32 ± 6 nm, approximately 3x the height of individual aggregates transferred to non-patterned glass (Figure 3.4a), indicating a stacking of aggregates in most of the hydrophilic regions of the structured surface.

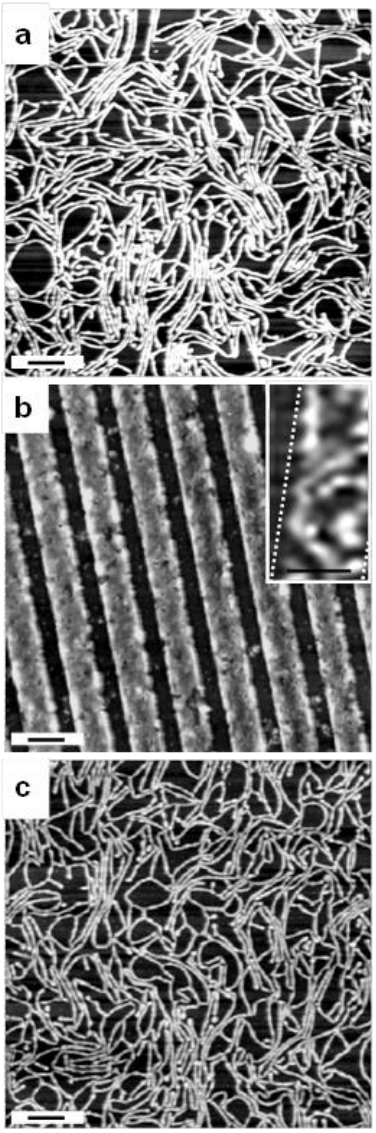

Figure 3.4. AFM images of LB films obtained by transfer of pure 141k copolymer from the air-water interface to non-patterned hydrophilic glass (a), and to patterned OTS substrates (b, c) with hydrophilic/hydrophobic stripes oriented perpendicular (b) or parallel (c) to the water surface during vertical withdrawal. In all cases, LB transfer was carried out at a surface pressure of π = 5 mN/m and using a withdrawal speed of 1 mm/min. The inset to b) shows a contact mode AFM image of strandlike aggregates assembled within a single hydrophilic stripe, with dotted lines indicating the boundaries of the hydrophilic domain. All scale bars indicate 1 μm.

The LB patterning of aggregates observed in Figure 3.4b is explained by surface-directed selective dewetting along the water-substrate contact line as the substrate is

withdrawn with hydrophilic/hydrophobic stripes perpendicular to the air-water interface (Figure 3.5a,b). First, copolymer aggregates deposit on the patterned substrate along the contact line (Figure 3.5a). Then, the drying of the deposited thin film induces a selective dewetting process, directed by the microscale heterogeneities in surface energies along the drying front. As a result, the drying water film accumulates in the hydrophilic stripes, effecting rearrangement of the monolayer as copolymer aggregates are carried with the water due to surface tension. As the patterned substrate is pulled through the air-water interface, continuation of this process results in the templated assembly of nanoscale aggregates into microscale stripes registered with the underlying hydrophilic regions (Figure 3.5b). In a related previous study,[45] nonlithographic LB patterning of nanoparticle stripes oriented perpendicular to the air-water interface was achieved via dewetting-induced segregation along the contact line; however, in that case, particle segregation was due to "fingering instabilities" of the drying front rather than underlying surface heterogeneities, resulting in stripe periodicities an order of magnitude longer than that shown in Figure 3.4b. Therefore, the current strategy of LB patterning via surface-directed dewetting offers a complimentary approach in which the length scale and organization of LB films can be controlled for specific applications using simple and well-established μCP methods.

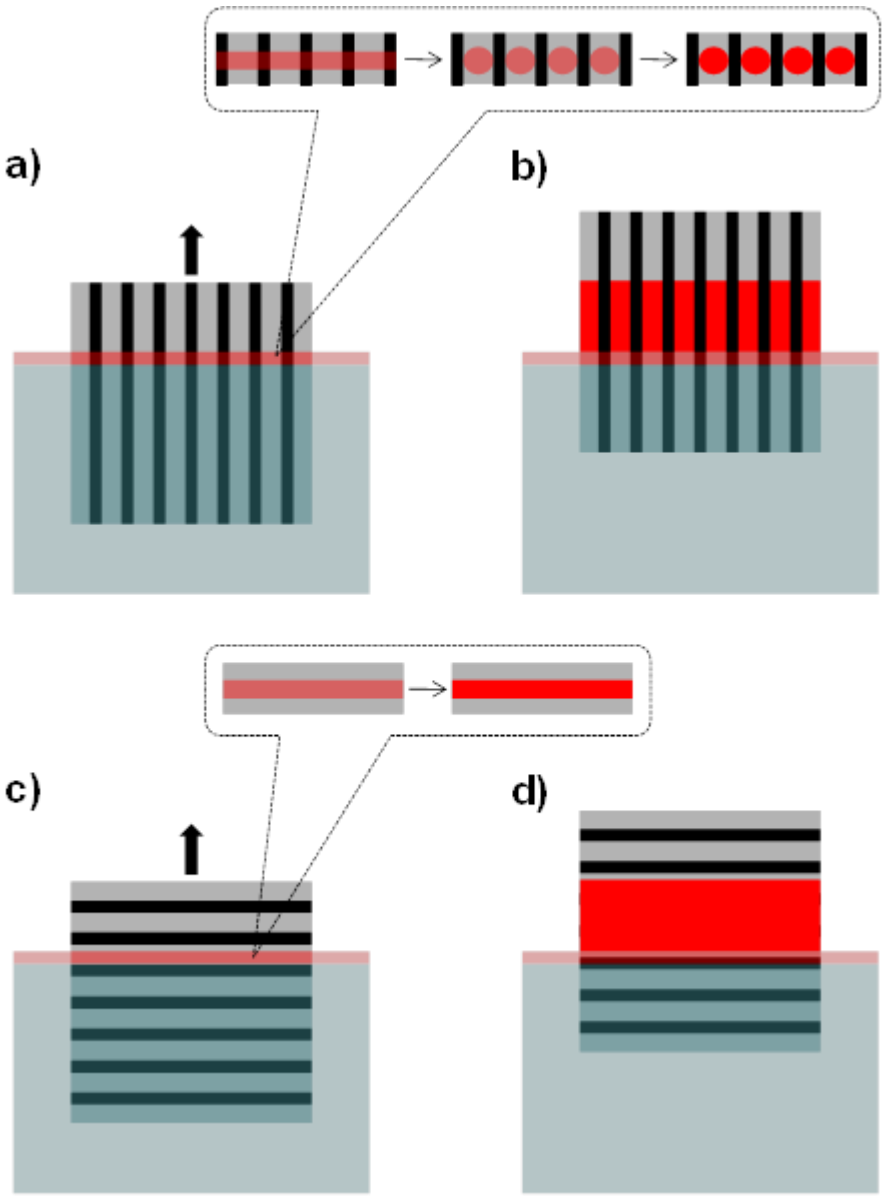

Figure 3.5. Schematic illustration of the principle of templated aggregate assembly during LB transfer to microscale stripes of alternating surface energies. For stripes oriented perpendicular to the water surface (a, b), copolymer aggregates first deposit wet at the contact line (a); then, film drying induces a selective dewetting process, directed by the alternating surface energies along the drying front, resulting in segregation of aggregates in the hydrophilic stripes (a, inset). As the patterned substrate is pulled through the air-water interface (b), continuation of this process forms microscale stripes of aggregates registered with the underlying hydrophilic regions. In contrast, for stripes oriented parallel to the water surface (c, d), a wet film of aggregates deposited along the contact line experiences the same underlying surface energy along its entire length (c), such

that the film dries without dewetting-induced segregation of aggregates (c, inset); therefore substrate withdrawal (d) results in a uniform monolayer with no registration to the underlying surface pattern.

According to the above mechanism, the presence of heterogeneities in surface energy along the contact line is of critical importance for surface-directed LB patterning. This was confirmed by carrying out LB transfer at the same surface pressure and withdrawal speed and using an identical patterned substrate, but with the hydrophilic/hydrophobic stripes oriented parallel to the air-water interface. The result of this experiment (Figure 3.4c) shows a monolayer of aggregates very similar to that found on the unpatterned substrate (Figure 3.4a), exhibiting no effect of the underlying surface pattern on the spatial distribution of aggregates. This situation is described in Figure 3.5c,d. Here, for a given position of the substrate, the contact line experiences the same underlying surface energy along its entire length (Figure 3.5c). Therefore, no dewetting-induced segregation of the water subphase occurs at the moving drying front, resulting in uniform monolayer transfer as the substrate is pulled through the air-water interface (Figure 3.5d). It is expected that as the parallel stripes of alternating wettabilities move through the air-water interface, the meniscus height will fluctuate over time, due to periodic changes in the surface energy at the contact line. However, these time-dependent fluctuations do not appear to strongly influence the transfer of the aggregate monolayers, as evinced by the similarity between Figure 3.4c and the non-patterned substrate case (Figure 3.4a).

Next, we investigated the effect of surface pressure on the transfer of PS-*b*-PEO aggregates to the patterned substrate. Figure 3.6 shows AFM images of the 141k

copolymer transferred to non-patterned (Figure 3.6a,b) and patterned (Figure 3.6c,d) substrates, at two different surface pressures: π = 5 mN/m (Figure 3.6a,c) and π = 10 mN/m (Figure 3.6b,d). The LB film transferred at π = 5 mN/m to the non-patterned substrate (Figure 3.6a) shows a monolayer consisting of both dots and strandlike aggregates, as discussed previously. When the surface pressure is increased to π = 10 mN/m for transfer to the non-patterned substrate (Figure 3.6b), a similar mixture of aggregate morphologies is observed, although the surface density of the monolayer has increased markedly compared to the lower-π case. In contrast to Figure 3.6a, the denser packing of aggregates in Figure 3.6b results in close contact between most of the neighboring PS cores; this is consistent with the sharp increase in surface pressure beginning at ~10 mN/m in the compression isotherm of the monolayer (Figure 3.3, red curve), associated with the overlap of relatively incompressible PS blocks. Interestingly, the two different surface pressures result in significantly different transfer behavior to the patterned substrates. As shown previously, transfer to the patterned substrate at π = 5 mN/m results in templated assembly of aggregates within the hydrophilic regions, forming a stripe pattern registered with the chemical pattern of the solid surface (Figure 3.6c). In contrast, transfer of aggregates to the patterned surface at increased surface pressure (π = 10 mN/m) results in a monolayer of aggregates with no selective positioning relative to the underlying stripes (Figure 3.6d).

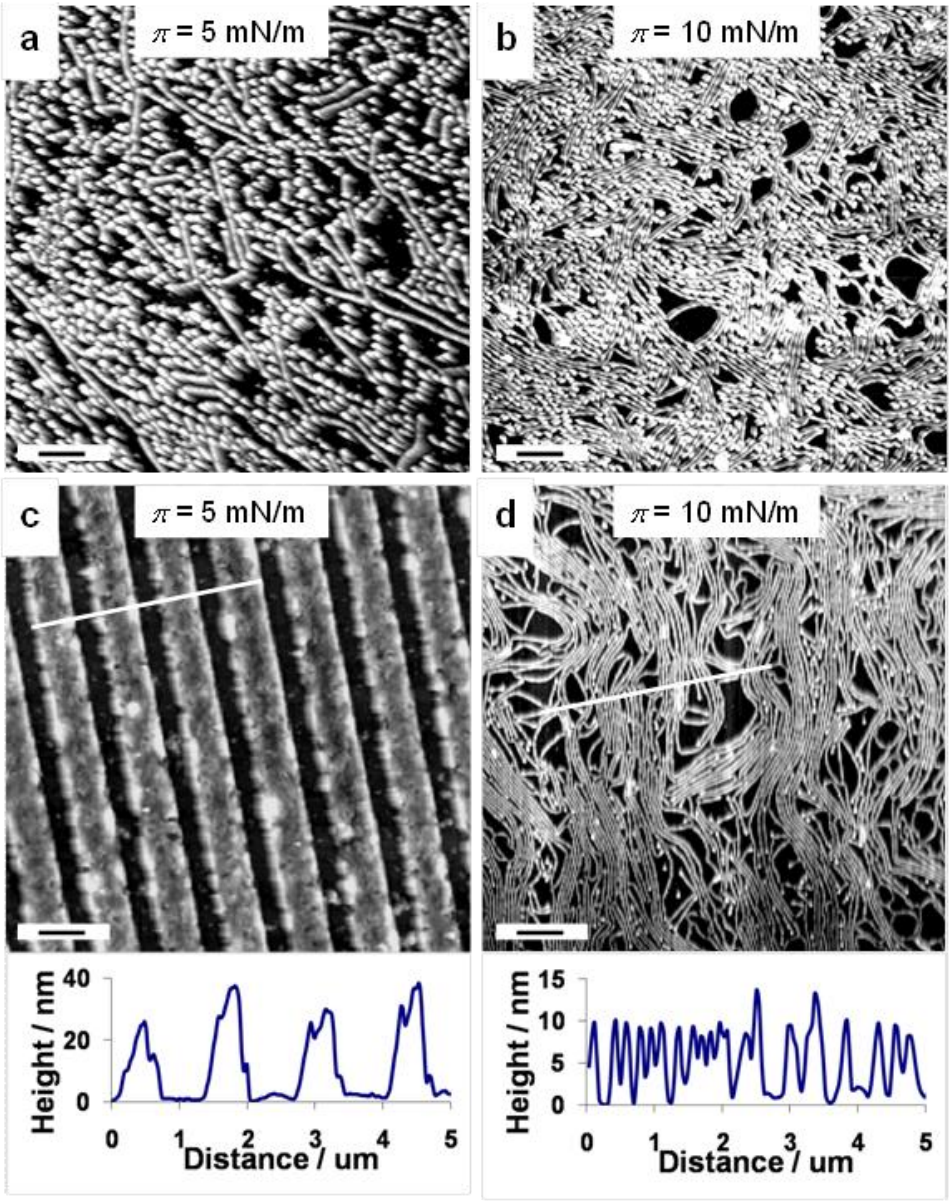

Figure 3.6. Effect of surface pressure on LB transfer of pure 141k copolymer to non-patterned hydrophilic glass (a, b) and to patterned OTS substrates (c, d). AFM images show LB films obtained by transfer at surface pressures of π = 5 mN/m (a, c) and π = 10 mN/m (c, d) using a withdrawal speed of 1 mm/min. For the LB films transferred to patterned substrates (c, d), the hydrophilic/hydrophobic stripes were oriented perpendicular to the water surface during vertical withdrawal (the orientation of both images with respect to the underlying stripes is the same); the white lines in c) and d) indicate regions in which accompanying height profiles (c, d, below) were taken. All scale bars indicate 1 µm.

The observed dependence of surface pressure on LB transfer to patterned substrates can be understood in terms of the effect of compression on the packing of copolymer aggregates at the air-water interface. As represented in Figure 3.7a (top), at π = 5 mN/m, the aggregates exist in the liquid expanded state at the water surface, with PEO chains in the pancake conformation between neighboring cores. In this low-density state, the aggregates possess a relatively large degree of freedom at the air-water interface, allowing them to rearrange upon transfer to the patterned substrate by accumulating with the water in the hydrophilic domains (Figure 3.7a, bottom). However, when the aggregates are compressed to π = 10 mN/m, a dramatic increase in the aggregate density occurs, as evinced by the large decrease in surface area in the compression isotherm (Figure 3.3, red curve). In the resulting high-density state (Figure 3.7b, top), the intervening PEO chains have submerged into the water, and the cores have become close-packed, introducing significant constraints on their translational motion. Therefore, the aggregates do not possess sufficient translational freedom to accumulate in the hydrophilic stripes when the underlying water dewets from the substrate. As a result, the LB film is transferred as a cohesive monolayer across both the hydrophobic and hydrophilic stripes (Figure 3.7b, bottom).

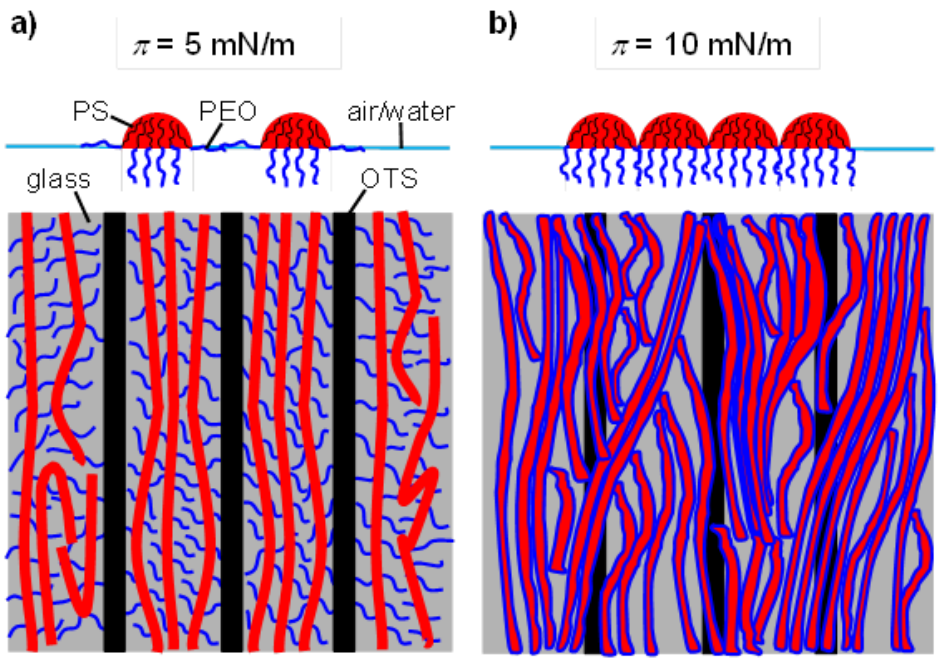

Figure 3.7. Schematic illustrations (not to scale) showing the effect of surface pressure on the transfer of strandlike aggregates of 141k to patterned OTS substrates. At π = 5 mN/m, the aggregates exist in the liquid expanded at the water surface (a, top). In this state, the aggregates possess sufficient translational freedom to rearrange and accumulate in the hydrophilic domains upon transfer to the patterned substrate (a, bottom). In contrast, at π = 10 mN/m, the aggregates exist in a condensed state the water surface (b, top). As a result of packing constraints on translational motion, the aggregates cannot segregate within the hydrophilic stripes upon transfer to the patterned substrate (b, bottom).

Next, we used this methodology to pattern copolymer aggregates containing photoluminescent CdS nanoparticles on solid surfaces, introducing optical functionality and another length scale of organization within the resulting hierarchical arrays. As demonstrated in our previous work,[42,43] when a blend of polystyrene-functionalized CdS nanoparticles (PS-CdS) and PS-*b*-PEO copolymer is spread in chloroform solution at the air-water interface, evaporation-induced self-assembly gives rise to strandlike aggregates with the nanoparticles distributed within the PS cores (Figure 3.8a). The excitation and

emission spectra of the constituent PS-CdS nanoparticles dispersed in chloroform solution are shown in Figure 3.8b, demonstrating their photoluminescent properties. The emission spectrum shows two peaks: an intrinsic bandedge emission peak centered at ~450 nm and a broad trap-state emission peak centered at ~610 nm.

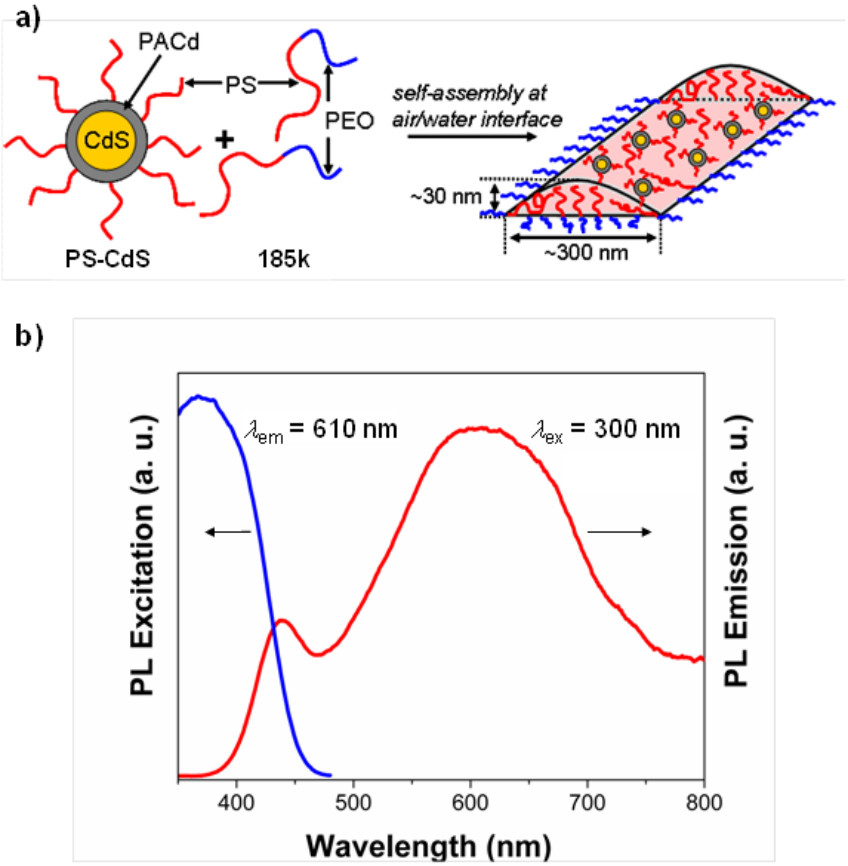

Figure 3.8. (a) Schematic showing the formation of strandlike copolymer-nanoparticle aggregates via self-assembly of the PS-CdS/185k blend at the air-water interface, as described previously in references 42 and 43. b) Photoluminescence properties of the PS-CdS nanoparticles dispersed in chloroform, showing excitation (blue curve) and emission (red curve) spectra. Both excitation and emission spectra were collected without using a filter. Reported spectra were obtained by subtracting a solvent background.

Figure 3.9 shows AFM images of the blend PS-CdS/185k transferred to non-patterned (Figure 3.9a,b) and patterned (Figure 3.9c,d) substrates at surface pressures of π = 5 mN/m (Figure 3.9a,c) and π = 10 mN/m (Figure 3.9b,d). The LB films transferred at π = 5 mN/m and π = 10 mN/m to unpatterned substrates (Figure 3.9a,b) both show highly branched, strandlike aggregates with heights ~30 nm and widths ~300 nm that are taller and wider than the strands formed from the pure 141k copolymer. We note that the difference in the surface densities of aggregates at the two different surface pressures, based on comparison of the AFM images in Figure 3.9a and 9b, is much less significant than that found in the pure 141k case (Figure 3.6a and 6b). Thus, we find a less efficient packing of aggregates at the higher surface pressure for the blend (Figure 3.9b) compared to pure 141k (Figure 3.6b). These AFM results are consistent with the compression isotherms, which show only a small decrease in surface area (and increase in density) for the blend upon compression from π = 5 mN/m to π = 10 mN/m (Figure 3.3, blue curve), compared to a dramatic decrease in area (and increase in density) for pure 141k (Figure 3.3, red curve).

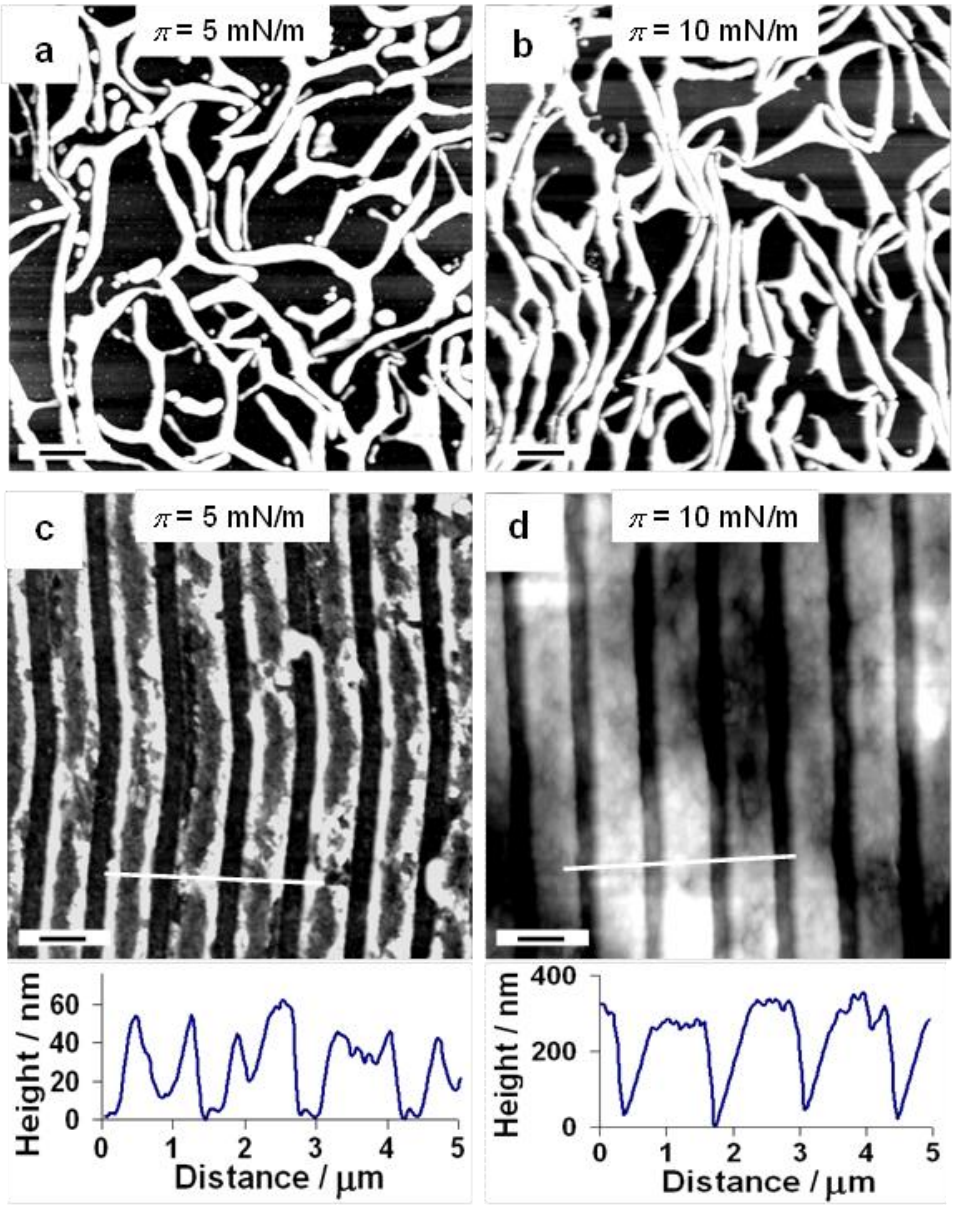

Figure 3.9. Effect of surface pressure on LB transfer of the PS-CdS/185k blend to non-patterned hydrophilic glass (a, b) and to patterned OTS substrates (c, d). AFM images show LB films obtained by transfer at surface pressures of π = 5 mN/m (a, c) and π = 10 mN/m (c, d) using a withdrawal speed of 1 mm/min. For the LB films transferred to patterned substrates (c, d), the hydrophilic/hydrophobic stripes were oriented perpendicular to the water surface during vertical withdrawal; the white lines in c) and d) indicate regions in which accompanying height profiles (c, d, below) were taken. All scale bars indicate 1 µm.

The relatively low packing density of the blend aggregates at π = 10 mN/m compared to the pure 141k copolymer means that they are not subject to the same constraints in translational motion. Therefore, unlike the 141k case, we find that templated assembly of blend aggregates on the patterned substrates occurs at both the higher and lower surface pressures (Figure 3.9c and 9d, respectively); however, the resulting film thicknesses depend strongly on the transfer surface pressure. For transfer at π = 5 mN/m, AFM and accompanying topology profiles (Figure 3.9c) reveal a mean film height of 60 ± 10 nm in the hydrophilic regions. Also, the LB film is found to be significantly thicker at the edges of the hydrophilic stripes, likely due to convective flow of aggregates during drying of localized water patches; in general, the elevated regions at the stripe edges show widths consistent with individual strandlike aggregates, suggesting a tendency for strands to orient along the stripe direction. When the surface pressure is increased to π = 10 mN/m, transfer of blend aggregates to the stripe pattern results in a more uniform filling of the hydrophilic domains compared to the π = 5 mN/m case, with the topology profile revealing uniform heights (mean height = 340 ± 50 nm) across the elevated stripes (Figure 3.9d).

To demonstrate the photoluminescence of the patterned and non-patterned strands due to the embedded CdS nanoparticles, laser scanning confocal fluorescence microscopy (LSCFM) imaging was also carried out for blend films transferred at π = 10 mN/m, with excitation and emission filters selected according to the photoluminescence properties of PS-CdS (Figure 3.8b). In Figure 3.10a we see the result for the non-patterned substrate: submicron strandlike photoluminescent aggregates uniformly distributed over the entire surface, consistent with AFM results. Figure 3.10b shows localized CdS emission from

the microscale photoluminescent stripe array, formed via transfer of the strandlike aggregates to the chemically-patterned surface.

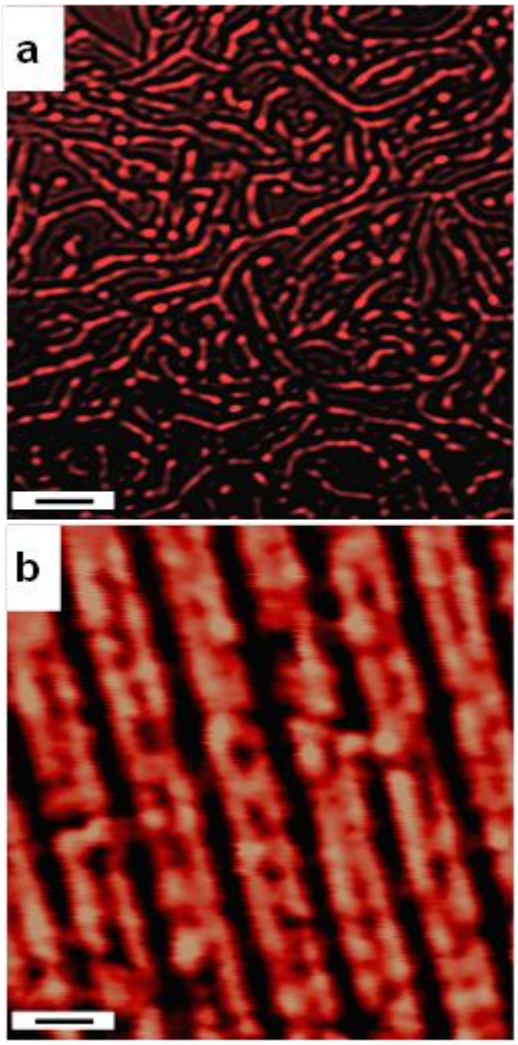

Figure 3.10. LSCFM images showing photoluminescence of PS-CdS/185k aggregates transferred to non-patterned hydrophilic glass (a) and to the patterned OTS substrate (b) at a surface pressure π = 10 mN/m and using a withdrawal speed of 1 mm/min. For the LB film transferred to the patterned substrate (b), the hydrophilic/hydrophobic stripes were oriented perpendicular to the water surface during vertical withdrawal. Both scale bars indicate 1 μm.

Finally, it was of interest to investigate the effect of increasing the substrate withdrawal speed on LB deposition to chemically-patterned surfaces, since the slow rate of LB film transfer is generally viewed as a critical limitation for its application to device fabrication. For this experiment, a withdrawal speed of 5 mm/min was applied to transfer blend aggregates at π = 10 mN/m to the half-patterned cover slip, and comparison was made with the analogous experiment at 1 mm/min described in Figure 3.9b and 9d. The resulting transfer ratio of 0.410 was less than half the value (~1) obtained at the slower withdrawal speed. The unpatterned half of the cover slip (Figure 3.11a) possessed a monolayer of strandlike aggregates indistinguishable from the analogous film prepared at 1 mm/min (Figure 3.9b). However, the patterned surface following LB deposition (Figure 3.11b) resembled a patterned OTS film without copolymer transfer (Figure 3.2b). This combination of AFM and transfer ratio data indicates that, at a withdrawal speed of 5 mm/min, efficient transfer of aggregates to the unpatterned half of the cover slip was achieved, whereas no detectable aggregates were transferred to the patterned surface, compared to their efficient transfer and patterning at the slower withdrawal speed of 1 mm/min. The lack of aggregate transfer to the patterned region at the faster withdrawal speed may be attributed to insufficient drying time. Another possible contribution is the presence of downward viscous drag forces imposed by the transferred subphase film, which have been shown to increase with increasing withdrawal speed.[47] The large difference in the transfer efficiencies to unpatterned and patterned surfaces at the faster withdrawal speed is probably a result of the difference in contact angles between the unpatterned hydrophilic glass (~0º) and the patterned OTS surface (~40º).[69,70] Clearly, the present method of transfer and selective positioning of aggregates relies on the complex

interplay of several time-dependent processes, including substrate pulling, copolymer and water transfer to the substrate, water evaporation, and dewetting, imposing the operational requirement of a sufficiently slow substrate withdrawal.

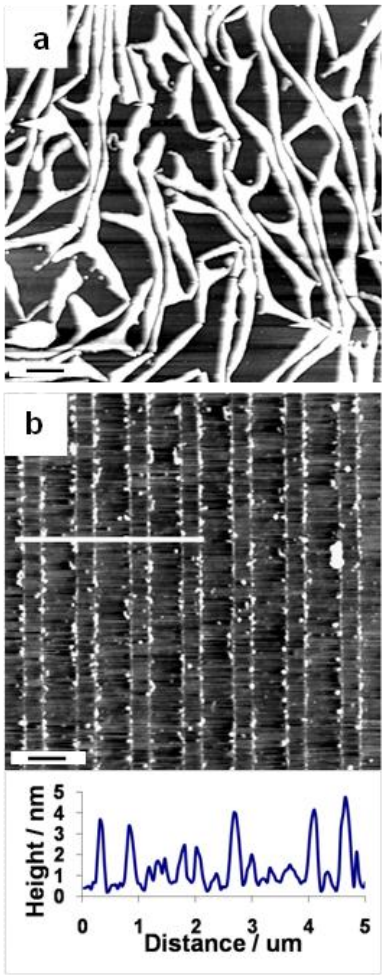

Figure 3.11. Effect of increased substrate withdrawal speed on LB transfer of the PS-CdS/185k blend to unpatterned hydrophilic glass (a) and to the patterned OTS substrate (b). AFM images show LB films obtained by transfer at a surface pressure of π = 10 mN/m using a withdrawal speed of 5 mm/min. For the LB film transferred to the patterned substrate (b), the hydrophilic/hydrophobic stripes were oriented perpendicular to the water surface during vertical withdrawal. The white line in b) indicates region in which accompanying height profiles (b, below) was taken. Both scale bars indicate 1 μm.

3.4. Conclusions

A methodology has been developed which combines nanoscale self-assembly of amphiphilic block copolymers at the air-water interface with microscale templated assembly of the resulting aggregates via LB transfer to chemically-patterned surfaces. The selective positioning of copolymer aggregates within the hydrophilic stripes of a hydrophilic/hydrophobic stripe pattern of OTS on glass is the result of surface-directed dewetting of the subphase during the slow vertical withdrawal of the substrate through the water surface. The LB patterning of aggregates depends on surface energy heterogeneities along the subphase-substrate contact line: this was confirmed by comparing LB transfer of aggregates with hydrophilic/hydrophobic stripes oriented perpendicular and parallel to the air-water interface, which resulted in selective positioning of aggregates only in the former case. The effect of surface pressure on LB patterning was also studied, revealing that packing constraints imposed by compression of aggregates to high surface densities prevents the formation of patterned LB films. The method was also extended to include patterning of hierarchical photoluminescent strands formed via self-assembly of polymer-coated CdS nanoparticles and an amphiphilic block copolymer at the air-water interface. We believe this combination of μCP with block copolymer self-assembly at the air-water interface provides a versatile approach for fabricating hierarchical polymer and polymer-nanoparticle architectures with a broad range of potential functionality.

3.5. References

(1) Haryono, A.; Binder, W. H. *Small* **2006**, *2*, 600.

(2) Tsutsumi, K.; Funaki, Y.; Hirokawa, Y.; Hashimoto, T. *Langmuir* **1999**, *15*, 5200.

(3) Lopes, W. A.; Jaeger, H. M. *Nature* **2001**, *414*, 735.

(4) Bockstaller, M. R.; Lapetnikov, Y.; Margel, S.; Thomas, E. L. *J. Am. Chem. Soc.* **2003**, *125*, 5276.

(5) Sohn, B.-H.; Choi, J.-M.; Yoo, S. I.; Yun, S.-H.; Zin, W.-C.; Jung, J. C.; Kanehara, M.; Hirata, T.; Teranishi, T. *J. Am. Chem. Soc.* **2003**, *125*, 6368.

(6) Weng, C. C.; Wei, K. H. *Chem. Mater.* **2003**, *15*, 2936.

(7) Lin, Y.; Boker, A.; He, J. B.; Sill, K.; Xiang, H. Q.; Abetz, C.; Li, X. F.; Wang, J.; Emrick, T.; Long, S.; Wang, Q.; Balazs, A.; Russell, T. P. *Nature* **2005**, *434*, 55.

(8) Chiu, J. J.; Kim, B. J.; Kramer, E. J.; Pine, D. J. *J. Am. Chem. Soc.* **2005**, *127*, 5036.

(9) Meli, L.; Li, Y.; Lim, K. T.; Johnston, K. P.; Green, P. F. *Macromolecules* **2007**, 40, 6713.

(10) Huang, C. M.; Wei, K. H. *Macromolecules* **2008**, *41*, 6876.

(11) Chang, J. J.; Kwon, J. H.; Yoo, S. I.; Park, C.; Sohn, B. H. *J. Mater. Chem.* **2009**, *19*, 1621.

(12) Xu, C.; Ohno, K.; Ladmiral, V.; Milkie, D. E.; Kikkawa, J. M.; Composto, R. J. *Macromolecules* **2009,** *42*, 1219.

(13) Akasaka, S.; Mori, H.; Osaka, T.; Mareau, V. H.; Hasegawa, H. *Macromolecules* **2009**, *42*, 1194.

(14) Minelli, C.; Geissbuehler, I.; Eckert, R.; Vogel, H.; Heinzelmann, H.; Liley, M. *Coll. Polym. Sci.* **2004**, *282*, 1274.

(15) Wang, C.-W.; Moffitt, M. G. *Chem. Mater.* **2005**, *17*, 3871.

(16) Guo, Y.; Moffitt, M. G. *Chem. Mater.* **2007**, *19*, 6581.

(17) Rockford, L.; Mochrie, S. G. J.; Russell, T. P. *Macromolecules* **2001**, *34*, 1487.

(18) Kim, S. O.; Solak, H. H.; Stoykovich, M. P.; Ferrier, N. J.; de Pablo, J. J.; Nealey, P. F. *Nature* **2003**, *424*, 411.

(19) Segalman, R. A.; Hexemer, A.; Kramer, E. J. *Macromolecules* **2003**, *36*, 6831.

(20) Sundrani, D.; Darling, S. B.; Sibener, S. J. *Langmuir* **2004**, *20*, 5091.

(21) Stoykovich, M. P.; Muller, M.; Kim, S. O.; Solak, H. H.; Edwards, E. W.; de Pablo, J. J.; Nealey, P. F. *Science* **2005**, *308*, 1442.

(22) Edwards, E. W.; Muller, M.; Stoykovich, M. P.; Solak, H. H.; de Pablo, J. J.; Nealey, P. F. *Macromolecules* **2007**, *40*, 90.

(23) Cheng, J. Y.; Rettner, C. T.; Sanders, D. P.; Kim, H. C.; Hinsberg, W. D. *Adv. Mater.* **2008**, *20*, 3155.

(24) Boltau, M.; Walheim, S.; Mlynek, J.; Krausch, G.; Steiner, U. *Nature* **1998**, *391*, 877.

(25) Raczkowska, J.; Cyganik, P.; Budkowski, A.; Bernasik, A.; Rysz, J.; Raptis, I.; Czuba, P.; Kowalski, K. *Macromolecules* **2005**, *38*, 8486.

(26) Park, L. Y.; Munro, A. M.; Ginger, D. S. *J. Am. Chem. Soc.* **2008**, *130*, 15916.

(27) Jaczewska, J.; Budkowski, A.; Bernasik, A.; Raptis, I.; Moons, E.; Goustouridis, D.; Haberko, J.; Rysz, J. *Soft Matter* **2009**, *5*, 234.

(28) Chai, J.; Buriak, J. M. *ACS Nano* **2008**, *2*, 489.

(29) Zhu, J.; Eisenberg, A.; Lennox, R. B. *J. Am. Chem. Soc.* **1991**, *113*, 5583.

(30) Zhu, J.; Eisenberg, A.; Lennox, R. B. *J. Phys. Chem.* **1992**, *96*, 4727.

(31) Zhu, J.; Eisenberg, A.; Lennox, R. B., *Macromolecules* **1992,** *25*, 6547.

(32) Li, Z.; Zhao, W.; Quinn, J.; Rafailovich, M. H.; Sokolov, J.; Lennox, R. B.; Eisenberg, A.; Wu, X. Z.; Kim, M. W.; Sinha, S. K.; Tolan, M. *Langmuir* **1995**, *11*, 4785.

(33) Seo, Y.-S.; Kim, K. S.; Galambos, A.; Lammertink, R. G. H.; Vancso, G. J.; Sokolov, J.; Rafailovich, M. *Nano Lett.* **2004**, *4*, 483.

(34) Lu, Q.; Bazuin, C. G. *Nano Lett.* **2005**, *5*, 1309.

(35) Lopes, S. I. C.; Gonçalves da Silva, A. M. P. S.; Brogueira, P.; Picarra, S.; Martinho, J. M. G., *Langmuir* **2007**, *23*, 9310.

(36) Cox, J. K.; Yu, K.; Constantine, B.; Eisenberg, A.; Lennox, R. B. *Langmuir* **1999**, *15*, 7714.

(37) Cox, J. K.; Yu, K.; Eisenberg, A.; Lennox, R. B. *Phys. Chem. Chem. Phys.* **1999**, *1*, 4417.

(38) Baker, S. M.; Leach, K. A.; Devereaux, C. E.; Gragson, D. E. *Macromolecules* **2000**, *33*, 5432.

(39) Devereaux, C. A.; Baker, S. M. *Macromolecules* **2002**, *35*, 1921.

(40) Cheyne, R. B.; Moffitt, M. G. *Langmuir* **2005**, *21*, 5453.

(41) Cheyne, R. B.; Moffitt, M. G. *Langmuir* **2006**, *22*, 8387.

(42) Cheyne, R. B.; Moffitt, M. G. *Langmuir* **2005**, *21*, 10297.

(43) Cheyne, R. B.; Moffitt, M. G. *Macromolecules* **2007**, *40*, 2046.

(44) Gleiche, M.; Chi, L. F.; Fuchs, H. *Nature* **2000**, *403*, 173.

(45) Huang, J.; Kim, F.; Tao, A. R.; Connor, S.; Yang, P. *Nature Mater.* **2005**, *4*, 896.

(46) Huang, J.; Tao, A. R.; Connor, S.; He, R. R.; Yang, P. *Nano Lett.* **2006**, *6*, 524.

(47) Hur, J.; Won, Y.-Y. *Soft Matter* **2008**, *4*, 1261.

(48) Gau, H.; Herminghaus, S.; Lenz, P.; Lipowsky, R. *Science* **1999**, *283*, 46.

(49) Xia, Y.; Qin, D.; Yin, Y. *Curr. Opin. Coll. Inter. Sci.* **2001**, *6*, 54.

(50) Fustin, C. A.; Glasser, G.; Spiess, H. W.; Jonas, U. *Adv. Mater.* **2003**, *15*, 1025.

(51) Lu, N.; Chen, X.; Molenda, D.; Naber, A.; Fuchs, H.; Talapin, D. V.; Weller, H.; Muller, J.; Lupton, J. M.; Feldmann, J.; Rogach, A. L.; Chi, L. *Nano Lett.* **2004**, *4*, 885.

(52) Benor, A.; Hoppe, A.; Wagner, V.; Knipp, D. *Thin Solid Films* **2007**, *515*, 7679.

(53) Bailey, F. E.; Koleske, J. V. *Poly(ethylene oxide)*; Academic Press: New York, 1976.

(54) Henglein, A. *Chem. Rev.* **1989**, *89*, 1861.

(55) Moffitt, M.; McMahon, L.; Pessel, V.; Eisenberg, A. *Chem. Mater.* **1995**, *7*, 1185.

(56) Wang, C.-W.; Moffitt, M. G. *Langmuir* **2004**, *20*, 11784.

(57) Xia, Y.; Whitesides, G. M. *Annu. Rev. Mater. Sci.* **1998**, *28*, 153.

(58) Xia, Y.; Whitesides, G. M. *Angew. Chem. Int. Ed.* **1998**, *37*, 550.

(59) Kumar, A.; Biebuyck, H. A.; Whitesides, G. M. *Langmuir* **2002**, *10*, 1498.

(60) Deegan, R. D. *Phys. Rev. E* **2000**, *61*, 475.

(61) Wang, M.; Liechti, K. M.; Wang, Q.; White, J. M. *Langmuir* **2005**, *21*, 1848.

(62) Sauer, B. B.; Yu, H.; Tien, C. F.; Hager, D. F. *Macromolecules* **1987**, *20*, 393.

(63) Charron, J. R.; Tilton, R. D. *Langmuir* **1997**, *13*, 5524.

(64) Dewhurst, P. F.; Lovell, M. R.; Jones, J. L.; Richards, R. W.; Webster, J. R. P. *Macromolecules* **1998**, *31*, 7851.

(65) Gonçalves da Silva, A. M.; Simoes Gamboa, A. L.; Martinho, J. M. G. *Langmuir* **1998**, *14*, 5327.

(66) Xu, Z.; Holland, N. B.; Marchant, R. E., *Langmuir* **2001**, *17*, 377.

(67) Bijsterbosch, H. D.; de Haan, V. O.; de Graaf, A. W.; Mellema, M.; Leermakers, F. A. M.; Cohen Stuart, M. A.; van Well, A. A. *Langmuir* **2002**, *11*, 4467.

(68) Price, E. W.; Guo, Y. Y.; Wang, C. W.; Moffitt, M. G. *Langmuir* **2009**, *25*, 6398.

(69) Evans, S. D.; Sanassy, P.; Ulman, A. *Thin Solid Films* **1994**, *243*, 325.

(70) Cerro, R. L. *J. Coll. Interf. Sci.* **2003**, *257*, 276.

Chapter 4. PATTERNING PHASE-SEPARATED POLYMER/POLYMER BLENDS ON MICROCONTACT-PRINTED GLASS SUBSTRATES

4.1. Introduction

Bottom-up self-assembly of polymers has been an area of intensive research over the past several decades mainly because of the routes it provides for organizing organic and inorganic functional elements on surfaces.[1-17] It has been shown that controlled arrangement of nanoparticles (NPs) can be obtained by their incorporation into a specific polymer phase of a phase-separated blend of immiscible homopolymers[15-17] or a microphase-separated diblock copolymer.[1-14] Bottom-up self-assemblies can be combined with a top-down lithographic technique to obtain complex device-oriented structures with improved long-range structural ordering. This has been demonstrated for block copolymers,[18-30] polymer blends,[31-43] and polymer/NP blends,[15,26,44]where assemblies are directed on chemically- or topographically-patterned substrates. Various lithographic techniques can be used to generate such patterns on surfaces.[45-46] For instance, microcontact printing is a fast and efficient soft lithographic[47-54] method for making chemically-patterned substrates with micro- or nanoscale heterogeneous surface energies.[47-48]

Phase-separation of immiscible polymer blends by spin-coating from a common solvent is a well-established method for obtaining microscale structures of polymer domains on surfaces.[55-60] Structured blend films have a variety of applications in electronics and optoelectronic devices;[61-66] for example, high-efficiency polymeric photovoltaic devices,[61,63] and organic light emitting diodes (OLEDs)[63-65] utilize the structures obtained by blends of conjugated polymers. The morphology of polymer structures, the size and orientation of the domains, affects the operation and efficiency of such devices.[61-66]

The phase-separation in spin-coated polymer blend films has been experimentally investigated[67-72]and theoretically modeled.[43] Among polymer blends, polystyrene/poly (methyl methacrylate) (PS/PMMA) polymer blends have been a system of particular interest in fundamental studies; the phase-separation for this blend has been widely studied both in bulk[73] and in thin films[67-72]. Heriot et al[67] used time-resolved small-angle light scattering to monitor the evolution of PS and PMMA domains in real time during spin-coating; they showed that the early stage of the phase-separation process is described by the development of a two-layer film with a PS-rich layer with lower surface energy on top and a PMMA-rich layer weting the glass surface. As the solvent further evaporates, an instability of the PS/PMMA interface caused by solvent concentration gradients generates capillary waves that disrupt the stratified film structure. The amplitude of the wave increases leading to the formation of the phase-separated structures observed in spin-coated films.

The morphology of polymer domains is influenced by both spinodal decomposition and by preferential wetting of the blend components at the boundary surfaces. Therefore, spin-coating polymer blends onto chemically heterogeneous pre-patterned substrates, possessing regions of various surface energies, can deliver polymer patterns to the films. This method was originally demonstrated by Boltau et al.[31] for a blend of PS and polyvinylpyridine (PVP) on a gold surface patterned by self-assembled monolayers of alkanethiols. Since then the methodology has been applied for patterning variety of polymer blends into different pattern types.[15,31-34,37, 39-41] However, to the best of our knowledge our work is the first report on patterning PS/PMMA blend on OTS-patterned glass surfaces.

It has been shown[34, 37, 39, 41] that surface-directed patterning of polymer blends can be obtained on such pre-patterned surfaces when the characteristic length scale of the phase-separation is on the order of the pattern periodicity of the substrate; this size matching is commonly referred to as length scale commensuration.[34, 37, 41, 43] Matching between the area fractions of the patterned surface and the volume fraction of the blend composition, known as composition commensuration,[32, 39] as well as the film thickness[34, 37, 41, 43] are also shown to influence the patterning of polymer blend films.

In this work, we apply polymer/polymer phase-separation on pre-patterned substrates for patterning PS/PMMA blends on OTS-patterned glass. For this purpose, first microcontact printing (μCP) is employed using the procedure developed in chapter 2, to produce a microscale pattern of hydrophilic and hydrophobic arrays, corresponding to octadecyltrichlorosilane (OTS) stripes and piranaha-treated glass, respectively. We study the effect of spin-coating rate, polymer solution concentration, composition, and solvent on the structure of the resulting films in order to determine the conditions in which polymer domains are directed by the underlying pattern. We also apply this method to pattern the phase-separating blend of PMMA and PS-stabilized cadmium sulfide (PS-CdS) quantum dots (QDs), producing microscale photoluminescent nanoparticle/polymer stripes. These results demonstrate a successful example for combining facile top-down patterning with efficient bottom-up self-assembly, in order to increase the complexity and ordering of hierarchical polymer and polymer-NP architectures.

4.2. Experimental

4.2.1. Material

The polystyrene (PS) homopolymer employed in this chapter with M_w=131 000 g/mol was previously synthesized in our group by anionic polymerization. Poly (methyl methacrylate) (PMMA) homopolymer with M_w=120 000 g/mol was purchased from Aldrich.

4.2.2. Preparation of Polydimethylsiloxane (PDMS) Stamps for Microcontact Printing

Masters with microscale periodic stripe patterns were obtained using commercial compact discs (CDs). First, the protective layer of a CD was removed by scoring with a scalpel and vigorously rinsing with deionized (DI) water. Then, the metallic layer and thin lacquer coat were removed via a quick rinse with methanol and subsequent sonication in a 1 : 4 (v : v) methanol/deionized water solution for 2 h, followed by a final methanol rinse, revealing the underlying polycarbonate layer with the desired topographic features. The polycarbonate was cut into square pieces ~2 cm x 2 cm. Prepolymer and curing agent for polydimethylsiloxane (PDMS) (Dow Corning: Sylgard 184 DC-184 A and DC 184-B) were mixed in a 10 : 1 (v : v) ratio, then poured over a polycarbonate master, followed by 4 h curing at 80˚C. The PDMS was then carefully peeled from the master in the direction tangential to the CD grooves, at a steady rate of ~ 1 cm/s. PDMS stamps consist of periodic raised stripes corresponding to the troughs of the polycarbonate masters; topographic micrographs of the master and the stamp are

illustrated in chapter 2 (Figure 2.4). Stamps were sonicated in a 1 : 2 (v : v) solution of ethanol/deionized water immediately prior to use, followed by drying with a stream of ultra-high purity (UHP) N_2 (g). More detailed description of the procedure is provided in section 2.2.1.

4.2.3. Microcontact Printing (μCP) Glass Substrates with Octadecyltrichlorosilane (OTS)

Glass cover slips (VWR scientific, 18 x 18 mm) were cleaned by sonication for 10 min in 95% ethanol, followed by 10 min sonication in DI water. To introduce a layer of hydroxyl groups on the glass surface, the cover slips were submerged in a piranha solution at 70˚C for 30 min. Piranha solution consists of a 3 : 1 (v : v) mixture of concentrated H_2SO_4 and 30% H_2O_2. Following piranha treatment, the cover slips were sonicated in DI water for 10 min then rinsed with methanol, followed by two further repetitions of the sonication/rinsing process. The resulting hydrophilic glass substrates were dried with a UHP N_2 (g) stream and used immediately for μCP. The ink for μCP was prepared by dissolving octadecytrichlorosilane (OTS, Aldrich) in anhydrous hexane (≥ 99%, Aldrich) under UHP N_2 (g) to obtain a 5 mM solution.

For inking the PDMS stamp, a non-patterned smooth block of PDMS was used as ink pad (instead of using an inked paper, which was used for chapter 2 and 3, as described in section 2.2.1). One drop of the ink solution was spin-coated on the pad at 3000 rpm for 30 s followed by 20 s drying by UHP N_2 (g). A PDMS stamp was then brought into contact with the inked pad for 10 s. The inked PDMS stamp was brought into contact with a hydrophilic glass cover slip for 30 s under a 200-g weight so that the

OTS stripe pattern was transferred to the coverslip. Microcontact-printed substrates were then used immediately as substrates for spin-coating PS/PMMA or PS-CdS/PMMA blend films. The method of using a rubber pad, spin-coating the ink on the pad, and drying the inked stamp before printing yields in a more uniform pattern of double-stripe OTS lines. In previous technique, which was employed in Chapters 2 and 3, both OTS double-stripe and single-stripes are observed in different regions of the patterned film. For this work, the uniformity is an essential and therefore, we modified the technique as above to transfer less OTS to the glass surface via printing in order to obtain double-stripe OTS pattern uniformly throughout the film.

4.2.4. Preparation of PS/PMMA Blend Solutions

Appropriate quantities of PS and PMMA components were each dissolved individually in spectroscopic grade of toluene, THF or MEK (Aldrich) to a polymer concentration of 2.0 wt%. The solutions were stirred for 4 h and allowed to equilibrate overnight in the dark. 20/80, 30/70 and 50/50 (w/w) PS/PMMA solutions were prepared by mixing appropriate amount of each solution followed by stirring for 4 h. The resulting blend solutions were then allowed to equilibrate overnight in the dark. Finally, blend solutions of the various PS/PMMA compositions were diluted gravimetrically with filtered solvent to prepare blend solutions with 0.5 and 1.0 wt% total polymer

4.2.5. Preparation of PS/PMMA Blend Films

The blend films were prepared by spin-coating one drop of each blend solution onto clean 18 x 18 mm glass coverslips at 9000 rpm spinning rate for 60s. The drop was applied after the substrate reached a rate of 9000 rpm and it was deposited onto the centre of the spinning substrate using a microsyringe. Spin-coated film looks uniformly clear and it was dried overnight under vacuum prior to characterization

4.2.6. Preparation of PS-CdS/PMMA Blend Films

The polystyrene-stabilized cadmium sulfide (PS-CdS) QDs used in this study were previously synthesized in our group via templated growth of CdS in the cores of reverse micelles consisting of the poly (styrene)-*block*-poly (acrylic acid) copolymer PS(226)-b-PAA(22), where numbers in brackets indicate number-average degrees of polymerization for each block. The detailed characterization of the PS-CdS sample employed here, which is the same sample used in chapter 3, is described in reference 14. In summary, each PS-CdS unit consists of a core of a ~ 5 nm CdS NP (determined from UV-Vis and using Henglein's empirical relationship),[14] with a poly (cadmium acrylate) (PACd) layer at the CdS surface, covalently-attached to external PS brush layer[14](schematic shown in chapter 3, Figure 3.8a). The fluorescence characterization of the PS-CdS sample is presented in chapter 3 (Figure 3.8 b); the emission spectrum shows two peaks: an intrinsic bandedge emission peak centered at ~ 450 nm and a broad trap-state emission peak centered at ~ 610 nm.

Appropriate quantities of PS-CdS and PMMA were each dissolved individually in spectroscopic grade of toluene (Aldrich) to a polymer concentration of 1.0 wt%. The

solutions were stirred for 4 h and allowed to equilibrate overnight in the dark. A blend solution of 30/70 (w/w) PS-CdS/PMMA with total polymer concentration of 1.0 wt % was prepared by mixing appropriate amounts of each solution and was stirred for 4 h. Solution was allowed to equilibrate overnight in the dark and then spin-coated onto clean (non-patterned) and onto OTS-patterned 18 x 18 mm glass coverslips at 9000 rpm spinning rate for 60s.

4.2.7. Selective Removal of Components of the Blend Films

In order to investigate the lateral distribution of polymer phases within the blend film, selective etching of the components by their selective solvents was performed. PMMA removal was carried out by placing the films in a petri dish containing acetic acid (glacial grade from Aldrich), which is a good solvent for PMMA and a poor solvent for PS, with a stir bar and stirring for 20 min. The films were then removed and further rinsed with fresh acetic acid followed by 4 h air drying and then further drying under active vacuum at room temperature overnight. For selective etching of PS domains, cyclohexane (anhydrous grade from Aldrich), a good solvent for PS and a poor solvent for PMMA, was used as the selective solvent and the same etching and drying procedure as above was applied to the films.

4.2.8. Atomic Force Microscopy (AFM)

AFM in contact mode was performed on a MFP-3D atomic force microscope from Asylum Research with non-conductive silicon nitride cantilevers from Veeco

(model: NP-10). The cantilevers are 0.4 - 0.7 μm thick and their resonance frequency ranges from 12-75 kHz with spring constants ranging from 0.06-0.58 N/m. Each sample was imaged several times at different locations on the substrate to determine the regularity of the film structure. All images presented in this paper were scanned over a 10 μm x 10 μm area at a scan rate of 0.5 Hz and represent typical images of each film. Statistical analysis of feature dimensions was carried out on the AFM images of spin-coated and selectively-etched films. A total of at least 60 features were measured to determine mean dimensions with reported errors.

4.2.9. Laser Scanning Confocal Fluorescence Microscopy (LSCFM)

LSCFM measurements of 30/70 (w/w) PS-CdS/PMMA blend films on non-patterned and on OTS-patterned glass substrates were carried out on a Zeiss LSM 700 with a diode laser. Films were excited at λ_{ex} = 405 nm and the emitted light was directed to the photomultiplier tubes (PMT) detector by a variable dichroic filter. A Zeiss 63x oil-immersion objective lens (NA=1.3) was used for imaging. The pinhole diameter was set to 2.4 Airy units; multiple sections at different depths of the films were obtained for constructing the image. To prepare samples for LSCFM measurements, a blend film-containing glass coverslip was taped to a glass microscope slide, such that the film was sandwiched between the slide and coverslip. Zeiss Immersionsoel 518 C oil was deposited between the objective and the coverslip in order to provide a constant-refractive index media between the objective and the glass.

4.3. Result and Discussion

The general strategy utilized in this work for the surface-directed patterning of the polymer blends onto chemically-patterned substrates combines the well-established procedure for μCP[47-48] with the phenomenon of polymer phase-separation.[67-72] As illustrated in Figure 4.1a, a PDMS stamp with a striped pattern was employed to selectively transfer OTS to piranha-treated glass in areas of contact between the stamp and the substrate (similar to Chapter 2 and 3); the resulting drying process and chemical reaction between OTS and hydroxyl groups on the piranaha-treated glass substrate results in a chemically-heterogeneous surface with a double-stripe pattern of OTS. From AFM of the resulting patterns (Figure 4.1b), the average height of the OTS lines is 3 ± 1 nm and the periodicity (λ) is 1.4 ± 0.1 μm (indicated in Figure 4.1b). Figure 4.1b shows the double-striped pattern due to solution drying; within each double-stripe repeat unit, the average short and long distances (w_s and w_l, respectively) between OTS lines are 0.4 ± 0.1 μm and 1.0 ± 0.1 μm, respectively (illustrated in Figure 4.1c). These patterned OTS films were used to direct the phase-separation of spin-coated PS/PMMA blends.

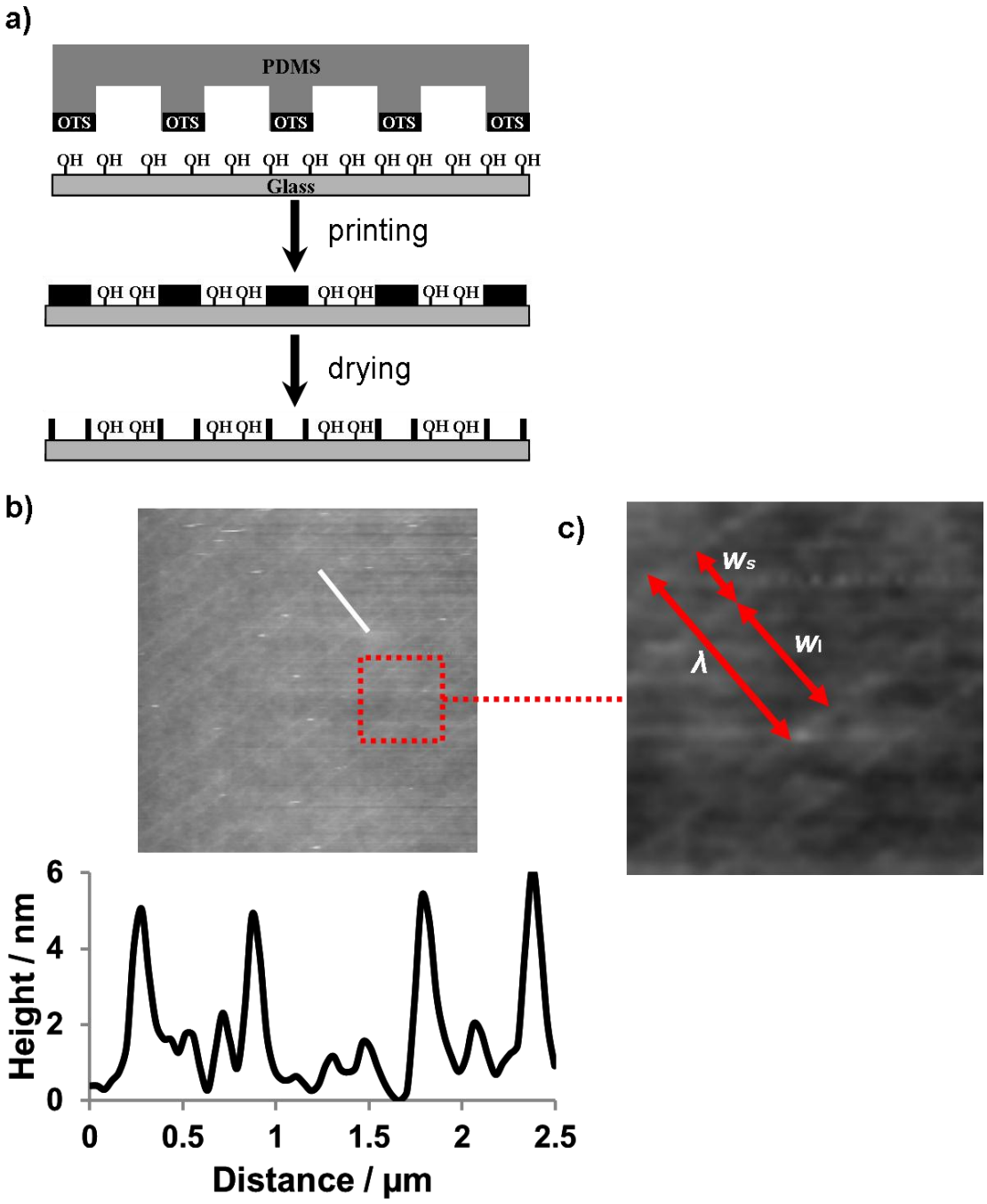

Figure 4.1. (a) µCP OTS on a hydrophilic (hydroxyl-terminated) glass surface by a PDMS stamp generating alternating striped pattern on the surface; drying accumulates OTS at the edges and results in a double stripe pattern, (b) 10-10 µm AFM image of the OTS patterned film, (c) height profile along the white line on the AFM image (c) zooming into a region of the AFM image to illustrateo λ, w_s and w_l.

Before studying the morphology of phase-separated PS/PMMA domains on patterned surfaces, the morphologies obtained by spin-coating on clean, non-patterned glass were investigated. For this, a 1.0 wt% blend solution of 30/70 PS/PMMA was spin-coated onto glass surface and characterized by contact-mode AFM, which reveals the topology of the PS- and PMMA- rich phases. A difference in the relative heights of PS and PMMA in phase-separated films has been observed previously as a result of the difference in the relative solubilities of the two polymers in the casting solvent.[59-60, 67-68] Toluene is a better solvent for PS than for PMMA; therefore, the PMMA phase will contain less solvent than the PS phase during spin-coating such that it solidifies at an earlier stage of the solvent evaporation. Further evaporation eventually leads to collapse of the solvent-swollen PS below the level of the already solidified PMMA domains. Hence, the elevated islands observed in the AFM image of this blend (shown in Figure 4.2a) are expected to be the PMMA-rich domains. However, AFM images do not provide us with direct information on the identity of the polymer phases; therefore, selective removal of the domains using selective solvents was performed: PS domains were removed by cyclohexane and PMMA by acetic acid. Results shown in Figure 4.2b and c, confirm the distribution proposed above: PS removal etches the matrix away and leaves behind discrete domains of PMMA (Figure 4.2b). PMMA removal takes away the elevated islands leaving holes behind in the PS film (Figure 4.2c).

As pointed out earlier, beside polymer/polymer interactions which cause the phase-separation, the other parameter affecting the morphology of the phase-separated films is polymer/substrate interaction.[59-62] For example if one of the polymer components has preferential affinity to the surface (due to attractive intermolecular forces), it

accumulates at the surface and forms a wetting layer. In the control film shown in Figure 4.2, both polymers appear to exhibit similar affinity to the glass surface, since no wetting layer is formed and both laterally-separated PS and PMMA domains extend down to the glass surface. This is also concluded from the selective etching experiments because both phases can be removed independent of the other (Figure 4.2 b and c). FFT analysis of PMMA domains after PS etching was carried out that is illustrated as the inset of Figure 4.2 b, resulting in d_{FFT} value of 0.2 ± 0.1 μm. d_{FFT} is determined from AFM images converted to receprical space (refer to 1.6.1). Structures of polymer blend films on non-patterned substrates, as shown in Figure 4.2, are generally isotropic; however, non-isotropic structures can be obtained on chemically-patterned surfaces, where the blend components have preferential affinity to different regions of the patterned substrate.[31-43] Therefore, for a blend of two chemically-different polymers, such as PS/PMMA blend, on a patterned substrate the more polar polymer (PMMA) is expected to wet the high-surface energy glass while the less-polar polymer (PS) is expected to wet the low-surface energy OTS lines.

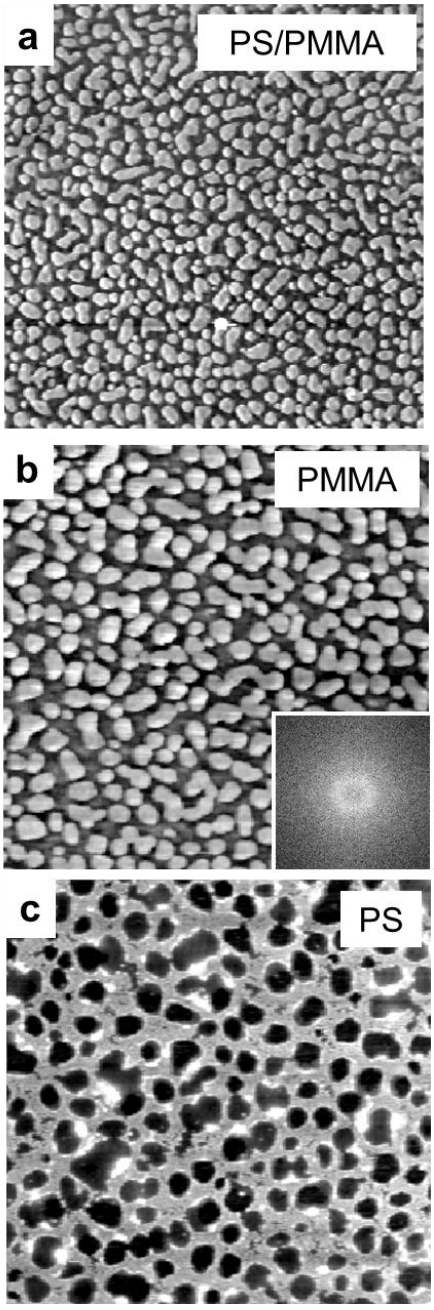

Figure 4.2. 10-10 μm AFM images of c_p = 1.0 wt% 30/70 PS/PMMA film (a) as spin-coated, (b) after PS-removal, and (c) after PMMA-removal. FFT analysis of PMMA features are shown as the inset of b.

The replication of the pattern of underlying substrate to the phase-separated polymer film is affected by many parameters, including the composition matching[32,39] between the blend volume ratio and the area ratio of the patterned surface, film

thickness,[34,37,41,43] and length scale matching between the pattern periodicity (λ) and the characteristic length scale of the phase-separation (*d*).[34,37,39,41,43]As described in section 1.2.2, *d* will be determined by the extent of domain coarsening arising from spinodal decomposition and will vary for spin-coated films depending on the polymer solution concentration (c_p) and the spinning rate (ω).[32-35] The empirical scaling law describing this is:

$$d \sim c_p/\omega^{1/2} \qquad (5.1)$$

Equation 5.1 expresses a direct proportionality between *d* and c_p, and an inverse proportionality between *d* and $\omega^{1/2}$; therefore, *d* can be tuned by adjusting c_p and ω to match λ, in order to obtain a patterned morphology of polymers on chemically-patterned surfaces. [32-34,37, 39-43] *h* is also influenced by these two parameters (c_p and ω) because the two forces defining the *h* of the spin-coated films are the viscous and centrifugal forces,[32,74-75] that are influenced by c_p and ω, respectively. Centrifugal forces are directly proportional to ω and viscous forces are directly proportional to c_p; therefore, *h* can also be adjusted by changing these two parameters: *h* increases by decreasing ω and increasing c_p.[32] It has been shown that[34,37,41,43] pattern replication in polymer blend films occurs when the films are thin (*h* in the same order as *d*). Hence, a high ω (= 9000 rpm) was utilized for spin-coating our polymer blends. *h* and *d* are related as for thick films (large *h*), solvent evaporation takes longer giving rise to a more extensive coarsening and therefore a large *d*.

4.3.1. Effect of the Polymer Blend Solution Concentration on Pattern Replication

To investigate the effect of c_p, blend solutions of 30/70 PS/PMMA at three different concentrations of 0.5, 1.0 and 2.0 wt% were spin-coated onto OTS-patterned glass substrates at 9000 rpm. AFM images of the blend films on patterned substrates are shown in Figure 4.3 a, b, and c for 0.5, 1.0 and 2.0 wt% concentrations. For the 0.5 wt% blend film (Figure 4.3a), the film is composed of elevated regions with internal height fluctuations of small PS/PMMA domains in between trenches corresponding to OTS lines. For the 1.0 wt% case on the other hand, the phase-separated domains are registered more closely with the underlying stripe pattern, resulting in an approximately alternating PS/PMMA stripe pattern (Figure 4.3b). However, for the 2.0 wt% solution concentration, the morphology resembles the morphology of the blend film on a non-patterned substrate (Figure 4.2 a). FFT analysis performed on AFM images as described in section 1.6.1, for c_p = 0.5, 1.0 and 2.0 wt% films was carried out resulting in d_{FFT} values of 0.1 ± 0.1 μm, 0.4 ± 0.1 μm, and 0.6 ± 0.2 μm, respectively. For c_p = 1.0 wt% FFT analysis result in an oval shape pattern due to non-isotropic nature of the stripes, which are oriented in one direction. For c_p = 0.5 wt%, FFT analysis was performed on a cropped section in between OTS lines that contains isotropic features and not the stripes (inset of Figure 4.3 a). d_{FFT} of cp = 1.0 wt% matches well with w_s of the underlying OTS pattern and therefore, the domains of cp = 1.0 wt% film are very well elongated in short distance regions of the substrate.

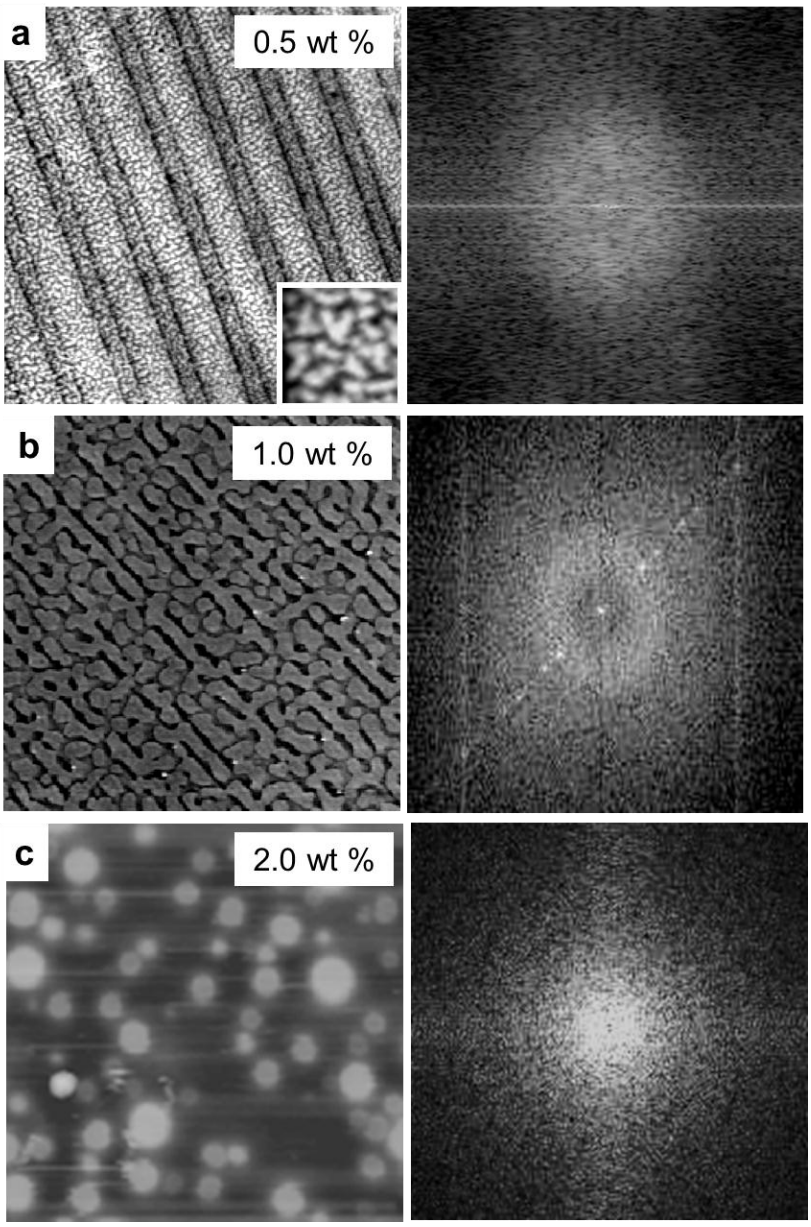

Figure 4.3. 10-10 μm AFM images of 30/70 PS/PMMA blend of c_p = (a) 0.5 wt% ($d<\lambda$), (b) 1.0 wt% ($d \sim \lambda$), and (c) 2.0 wt% ($d>\lambda$) solution concentrations on OTS-patterned glass substrates. Corresponding FFT analysis are shown on the right side of the images: for (a) the FFT is from the 1-1 μm cropped portion of the image (inset), for (b) and (c) FFT is from the corresponding 10-10 μm AFM images.

To confirm the lateral organization of polymer domains and to probe the location of PS and PMMA in relation to the underlying pattern, selective removal of both PS and

PMMA was performed on the spin-coated films in Figure 4.3; AFM images and sample height profiles before and after selected etching for polymer blend films prepared from 0.5 wt% and 1.0 wt% spin-coating solutions are showin in Figures 4.4 and 4.5, respectively.

For the 0.5 wt% film before selective etching (Figure 4.4a), elevated domains with small height fluctuations are observed in regions in between deep trenches that correspond to the underlying OTS lines; the average depth of the trenches is 2.3 ± 0.4 nm (a sample height profile is provided in Figure 4.4b). After selective PS etching, the morphology of PMMA domains (Figure 4.4c) is identical to the morphology of the spin-coated film but with an increased vertical contrast suggesting the removal of PS from the trenches and also from regions in between small PMMA domains; after PS removal, the average trench depth above the OTS lines increases to 6 ± 1 nm (Figure 4.4d). After PMMA removal (Figure 4.4e), the blend regions in between the trenches, including both small PS and PMMA domains, are completely removed, suggesting a PMMA wetting layer at the substrate in these regions. What is left behind are PS lines 5 ± l nm tall that correspond to the OTS lines (Figure 4.4f); their height is significantly greater than the average height of bare OTS lines suggesting the presence of a thin layer of PS above the OTS. The presence of PS above OTS lines is confirmed by another PS etching after PMMA etching, which results in bare OTS-patterned film.

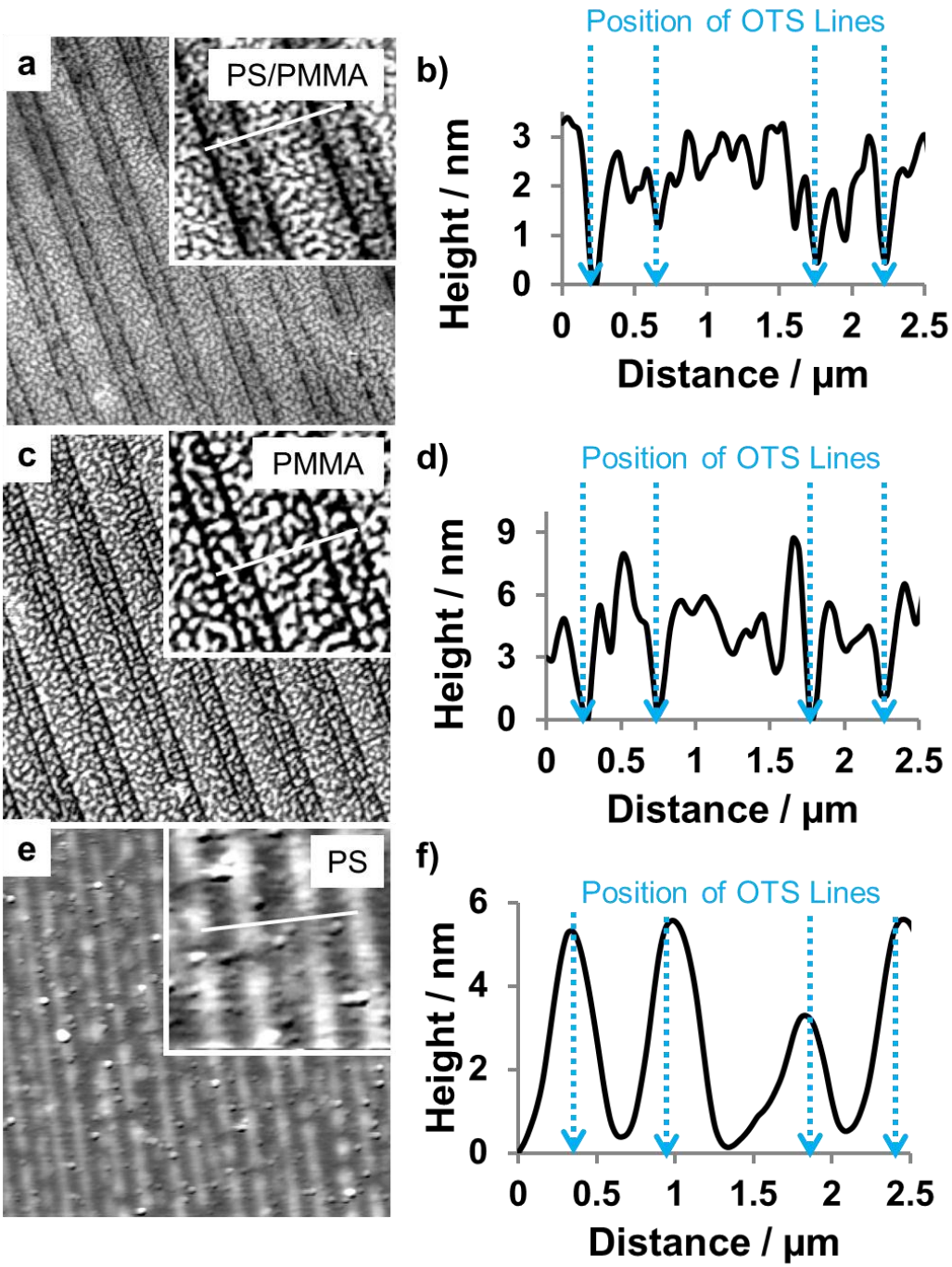

Figure 4.4. 10-10 µm AFM images (a, c, e) and corresponding height profiles along the white lines shown on the insets of the AFM images (b, d, f) of c_p =0.5 wt% 30/70 PS/PMMA blend films (a, b) as spin-coated, (c, d) after PS-removal, (e, f) after PMMA-removal. Estimated positions of the underlying OTS lines are pointed out by blue dashed arrows on the height profiles.

Based on the selective etching results shown in Figure 4.4, we propose a phase structure for the 30/70 PS/PMMA blend spin-coated from 0.5 wt% solution onto OTS-patterned glass as depicted in Figure 4.6a. Close to the substrate, PS accumulates locally on hydrophobic OTS bands and PMMA, which is the more polar component (with higher affinity to the hydrophilic areas), wets the glass surface forming a wetting layer, above which further phase-separation results in the formation of raised PMMA and lower PS domains, as observed in Figure 4.4a.

For the c_p = 1.0 wt% blend, the spin-coated film without etching (Figure 4.5a) displays a pattern of elevated domains oriented along the direction of the underlying stripes and localized in the regions in between the OTS lines. Many of these domains are elongated in shape along the direction of the underlying lines, while some exist as irregular droplets with a general arrangement along the pattern direction. The average height of these features is 4 ± 1 nm (Figure 4.5b). PS removal (Figure 4.5c) leaves behind the raised domains from Figure 4.5a indicating that they consist of PMMA; however, the average height of these domains is increased to 10 ± 1 nm after PS removal (Figure 4.5d) suggesting that the gaps in between the elevated PMMA domains contained a PS film ~6 nm thick. Selective removal of PMMA from the spin-coated blend film confirms that PS is mainly localized along the underlying OTS stripes (Figure 4.5e), with a periodicity close to that of the underlying OTS array; the average height of the PS lines is 6 ± 1 nm (Figure 4.5f), in agreement with the PS layer thickness inferred from the difference between the non-etched and PS-etched films.

Based on the images and height analysis shown in Figure 4.5, the lateral phase distribution for c_p =1.0 wt% 30/70 PS/PMMA blend film is proposed as the morphology

portrayed in Figure 4.6b. Close to the substrate a similar phase distribution to the one observed for 0.5 wt% case (Figure 4.6a) occurs: PS selectively wets the hydrophobic OTS lines and PMMA wets the glass surface, above which the PMMA domains grow and extend to the top of the film (air interface).

The film morphologies of Figure 4.4 and 4.5 both demonstrate surface-directed phase-separation of polymer phases. For c_p = 0.5 wt% film because $d < \lambda$, selective wetting occurs in a thin layer close to the substrate; in this layer PS is segregated to the OTS lines and PMMA is directed to hydrophilic regions, where it forms a wetting layer. Above this layer, further phase-separation between PS and PMMA occurs that results in the final structure. For c_p = 1.0 wt% blend, since d is in the same order as λ, surface-directed patterning of PS/PMMA is observed in the final structure and a patterned morphology of lower PS domains on OTS stripes and raised PMMA domains in regions between the OTS lines is obtained. In the region with w_s since the sizes match *(w_s* and *d)*, PMMA fills the space while in regions with w_l because the width is slightly larger than d there is more volume to fill and therefore, some PS exist in these regions in between the raised PMMA domains. structures observed for both c_p = 0.5, and 1.0 wt% are therefore, superficially the same and are the result of phase-separation, followed by selective wetting of the blend components at the substrate and a further phase-separation in regions between OTS lines. The difference between films prepared using these two c_p is only in the size of domains which is larger for 1.0 wt%.

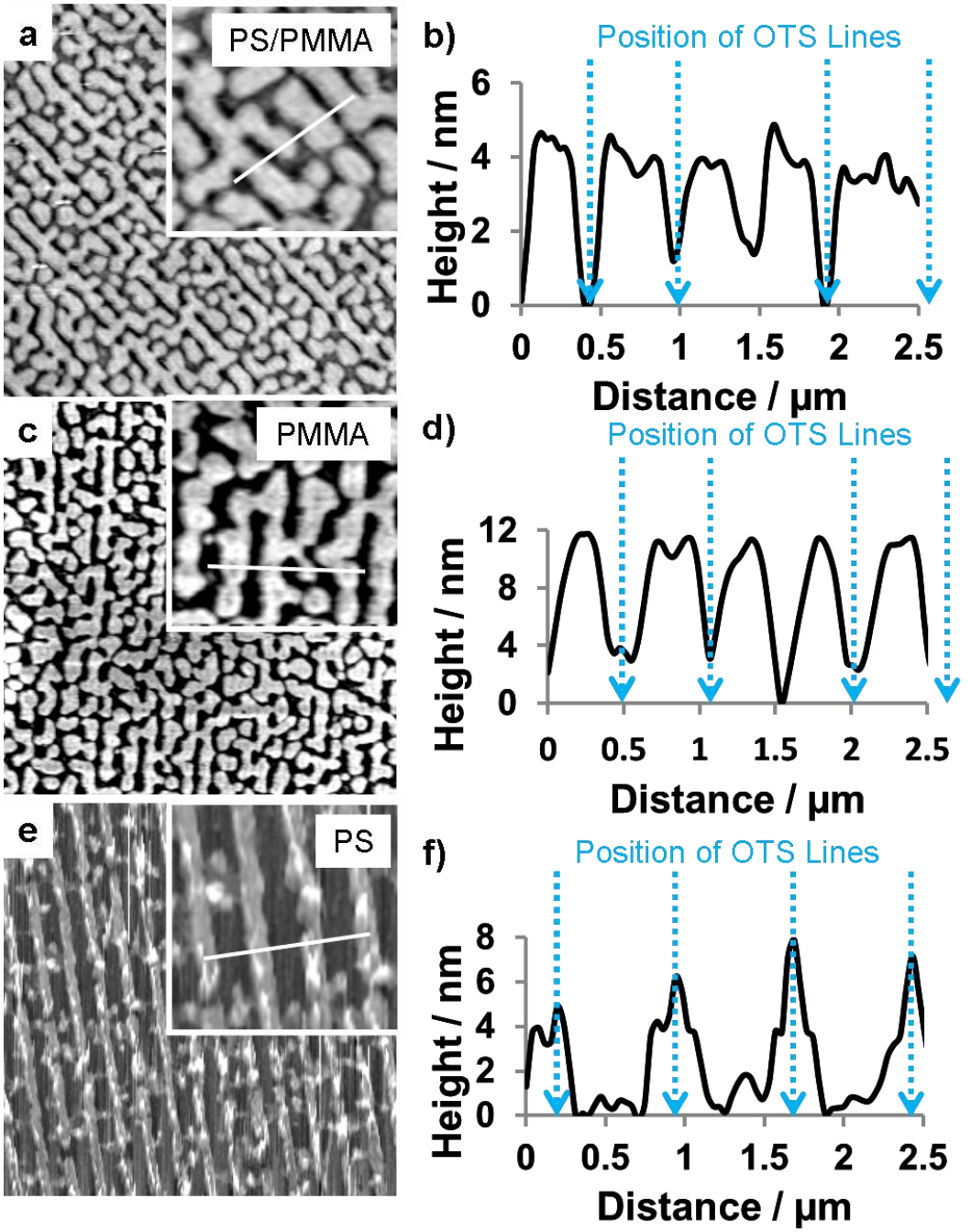

Figure 4.5. 10-10 μm AFM images (a, c, e) and corresponding height profiles along the white lines shown on the insets of the AFM images (b, d, f) of c_p =1.0 wt% 30/70 PS/PMMA blend films (a, b) as spin-coated, (c, d) after PS-removal, (e, f) after PMMA-removal. Estimated positions of the underlying OTS lines are pointed out by blue dashed arrows on the height profiles.

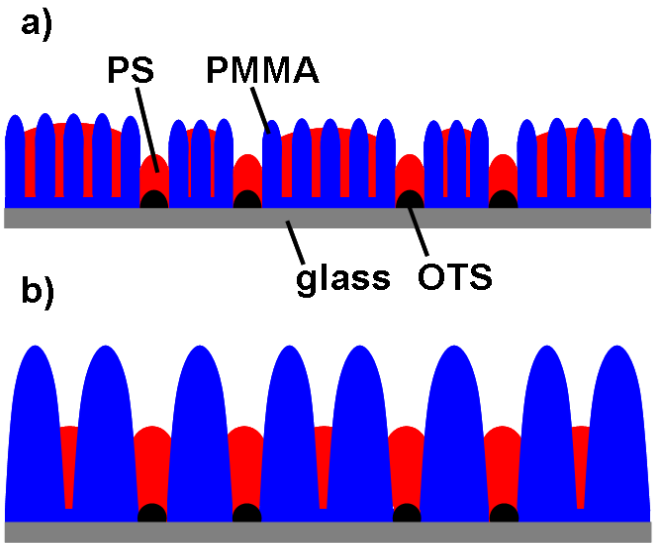

Figure 4.6. Lateral distribution of (a) c_p =0.5 wt% and (b) 1.0 wt% 30/70 PS/PMMA blend films on OTS-patterned glass substrates.

4.3.2. Effect of the Polymer Blend Solution Composition on Pattern Replication

The effect of blend composition on the pattern replication was also investigated.[32,39] For the OTS-patterned film prepared by μCP for this work, the OTS lines have an areal fraction of ~ 0.28 ± 0.04; this value was determined from the measurement of area for OTS lines on several printed AFM images. To investigate the effect of blend composition, two blends of 20/80 and 50/50 (w/w) PS/PMMA (both spin-coated at c_p = 1 wt % concentration) in addition to the 30/70 blend presented above, were studied, and the resulting domain morphologies are shown in Figure 4.7.

For both films, localization of PS on OTS lines and PMMA in regions in between the lines occurs although the relative composition has a strong influence on the degree of mismatch between the location of PS and PMMA with the underlying nonpolar and polar

regions, respectively. This is explained by the importance of matching the area of the underlying domains with the film area of the respective polymer components within the blend (approximately equivalent to the volume fraction assuming films of uniform height). For example, in the 20/80 blend film, possessing an excess of PMMA relative to the underlying pattern, the raised PMMA domains are connected by multiple bridges that span the OTS lines of the underlying substrate (Figure 4.7a), while very little PS appears to wet the OTS lines (Figure 4.7c). Conversely, in the 50/50 blend film, possessing an excess of PS relative to the underlying pattern, the raised PMMA domain shapes are mostly irregular droplets surrounded by significant PS, with very little elongation along the pattern direction (Figure 4.7b), while the PS domains localized over the OTS lines are connected by multiple bridges that span the relatively polar substrate regions (Figure 4.7d). AFM images for 20/80 and 30/70 PS/PMMA blends before and after etching together with corresponding height profiles are illustrated in Figure 4.8 and 4.9, respectively. Compared to both of these cases, the match between polymer domains and the underlying substrate regions is clearly much better in the case of the 30/70 blend, although the lack of perfect matching even in this case may be correlated to the difference between the areal and volume fraction of blend films with PS and PMMA domain sizes of different heights. Average height of the features observed in the blend films before and after etching are listed in Table 4.1 for 20/80, 30/70, and 50/50 PS/PMMA blends with c_p = 1.0 wt% for comparison.

Table 4.1. Average height of features observed in AFM images of c_p = 1.0 wt% at three different compositions.

	20/80 PS/PMMA	**30/70 PS/PMMA**	**50/50 PS/PMMA**
Spin-coated Film	6 ± 2 μm	4 ± 1 μm	8 ± 1 μm
PS-etched Film	8 ± 3 μm	10 ± 1 μm	16 ± 1 μm
PMMA-etched Film	2 ± 1 μm	6 ± 1 μm	10 ± 2 μm

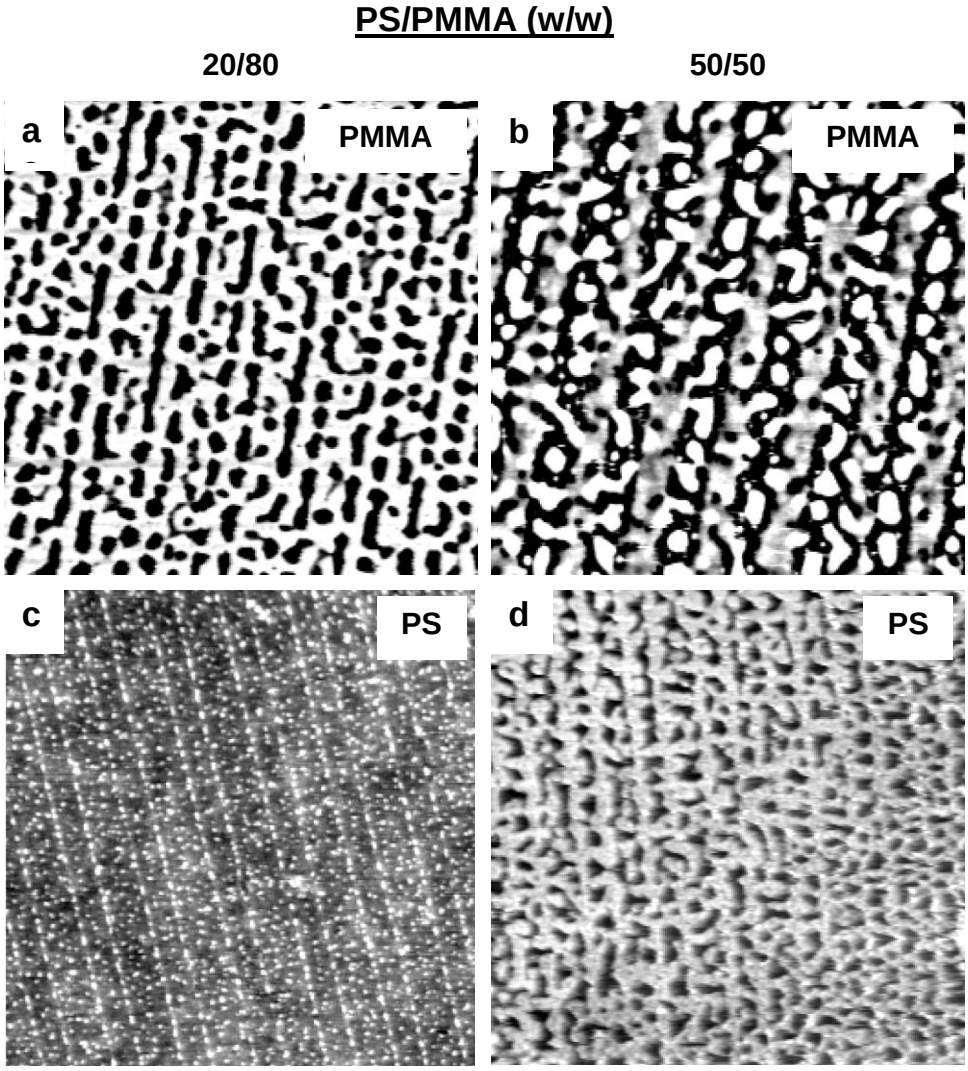

Figure 4.7. 10-10 μm AFM images of c_p = 1.0 wt% 20/80 (a, c) and 50/50 (b, d) PS/PMMA polymer blend films after PS-removal (a, b) and after PMMA removal (c, d).

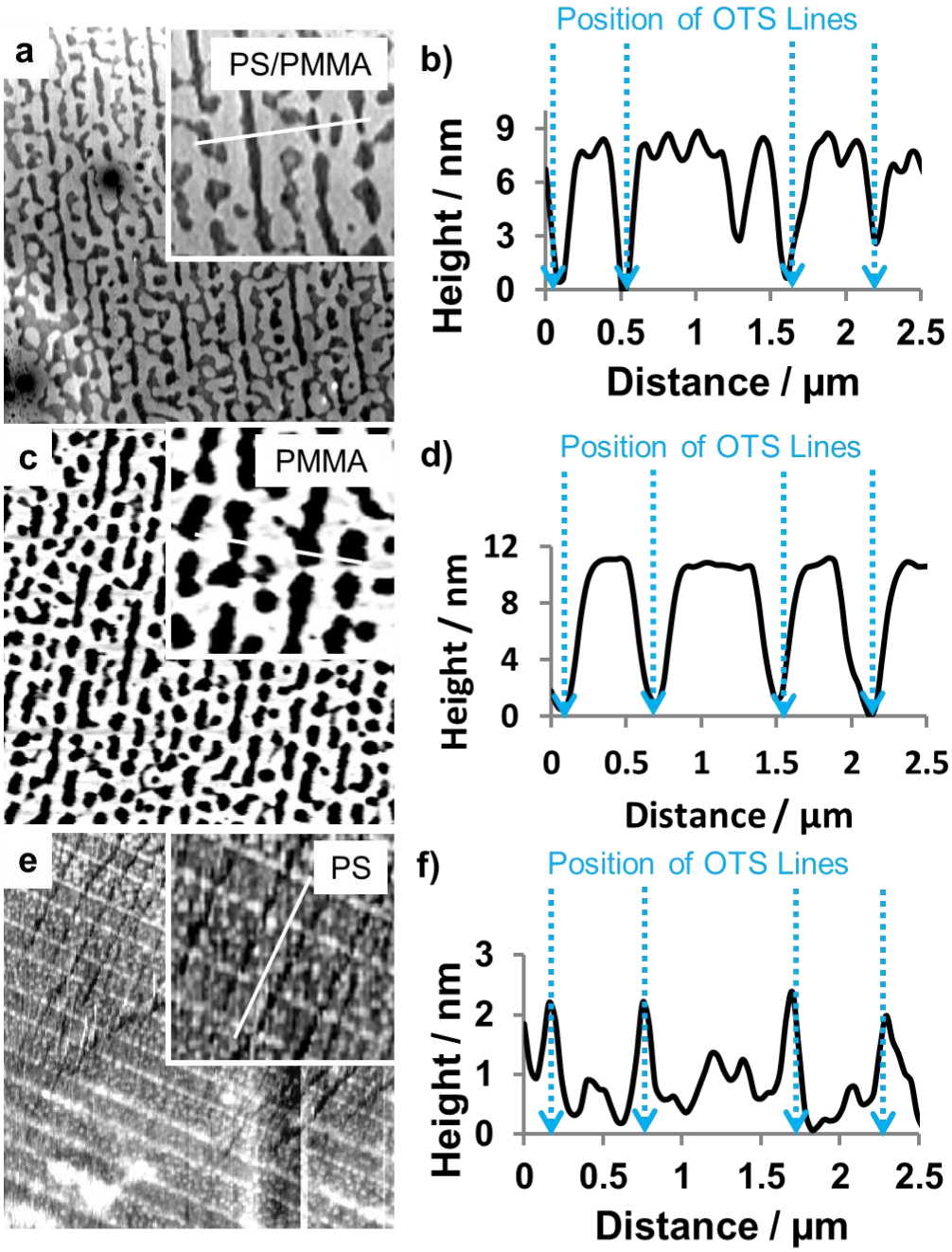

Figure 4.8. 10-10 μm AFM images (a, c, e) and corresponding height profiles along the white lines shown on the insets of the AFM images (b, d, f) of c_p = 1.0 wt% 20/80 PS/PMMA blend films (a, b) as spin-coated, (c, d) after PS-removal, (e, f) after PMMA-removal. Estimated positions of the underlying OTS lines are pointed out by blue dashed arrows on the height profiles.

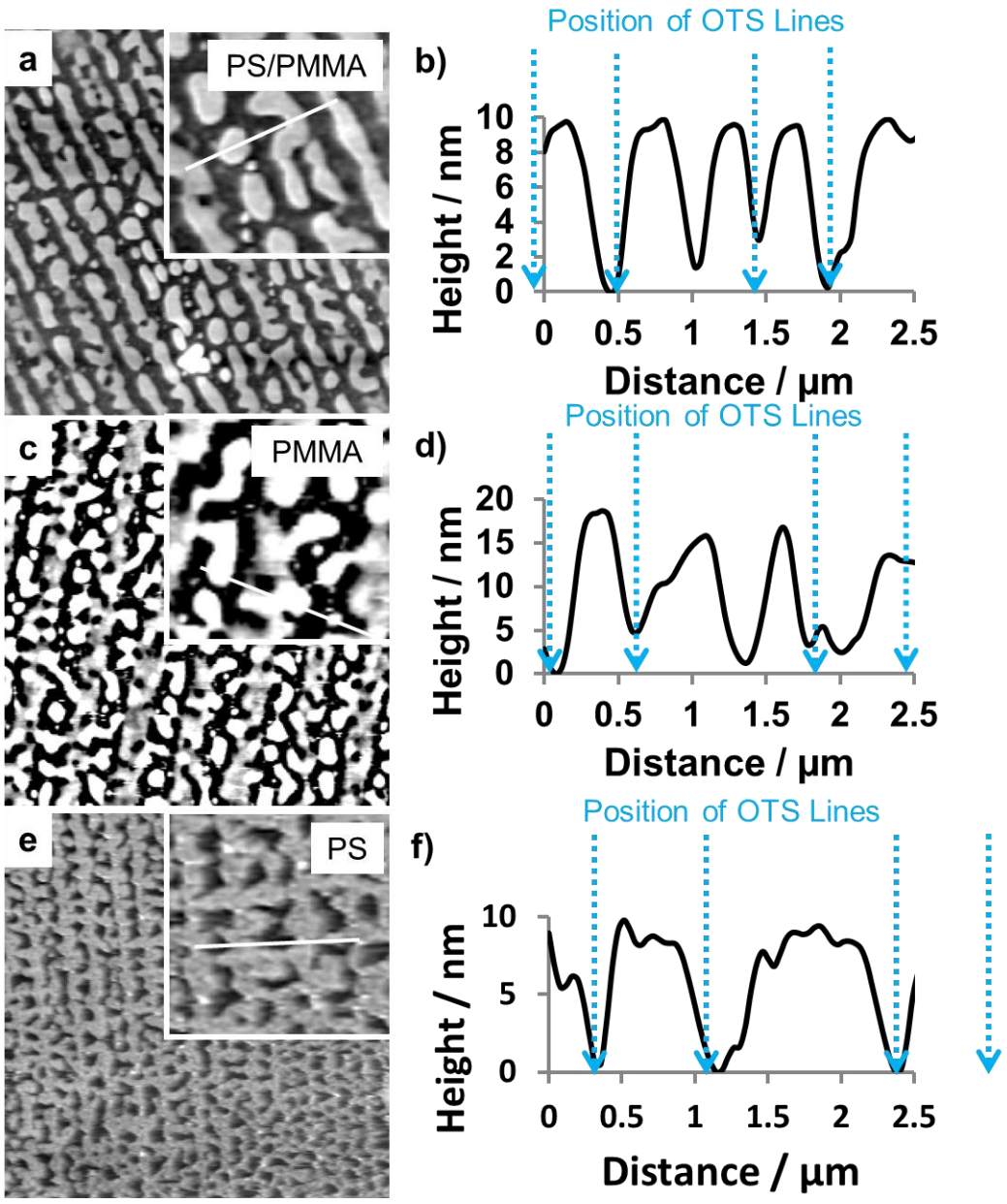

Figure 4.9. 10-10 μm AFM images (a, c, e) and corresponding height profiles along the white lines shown on the insets of the AFM images (b, d, f) of c_p =1.0 wt% 50/50 PS/PMMA blend films (a, b) as spin-coated, (c, d) after PS-removal, (e, f) after PMMA-removal. Estimated positions of the underlying OTS lines are pointed out by blue dashed arrows on the height profiles.

4.3.3. Effect of the Solvent of the Polymer Blend Solution on Pattern Replication

The effect of solvent is studied for three different solutions of c_p = 1.0 wt%, 30/70 PS/PMMA in toluene, MEK and THF. The vapour pressures for these solvents are 5.4, 10.5 and 17.0 KPa at 20°C, respectively, indicating an order of volatility of THF > MEK > toluene.[76]. The morphology of the resulting blend films spin-coated on OTS-patterned glass substrates is illustrated in Figure 4.10, showing that the underlying pattern was replicated by the polymer blend structure only in the toluene case. The THF and MEK blends both show approximately circular raised domains isotropically dispersed over the entire film with no observed orientation or elongation of the blend features. These results can be attributed to the relatively fast evaporation rates of MEK and THF compared to toluene during spin-coating, which leads to a rapid depletion of the solvent and polymer vitrification before the blend structure can significantly develop. In other words, the fast rate of solvent evaporation during spin-coating does not give the polymers enough time to segregate into energetically matching regions of the underlying pattern. Therefore, it appears that low-volatility solvents, such as toluene, are optimal for the type of patterning applications developed in this work.

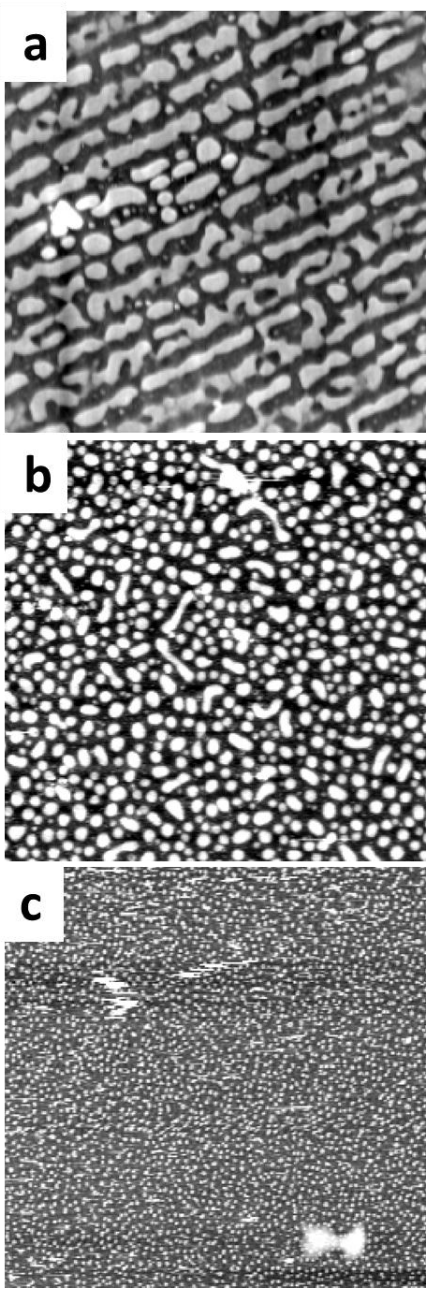

Figure 4.10. 10-10 μm AFM images of c_p = 1.0 wt% 30/70 PS/PMMA spin-coated from (a) toluene, (b) MEK, and (c) THF onto OTS-patterned glass substrates.

4.3.4. Patterning PS-CdS QDs via Surface-Directed Polymer Phase-separation Technique

The methodology which we developed for patterning polymer blends was also employed to pattern blends containing photoluminescent CdS QDs, introducing optical functionality and another length scale of organization within the resultant hierarchical pattern. As demonstrated in previous work from our group,[16] spin-coating a blend of polystyrene-stabilized CdS nanoparticles (PS-CdS) and PMMA results in organization of QDs in microscale (due to the polymer phase-separation) and nanoscale (due to the steric interactions between polymer brushes of QDs within the PS-CdS domains); however, domains in such films are randomly distributed and there is no control over their placement on the substrate. Our technique for directing the phase-separation on chemically-patterned surfaces brings controllability and long-range order to the QDs-containing structures. For this, a blend of c_p =1.0 wt% 30/70 PS-CdS/PMMA was spin-coated on glass substrate from toluene and characterized both by AFM and LSCFM. AFM image (Figure 4.11 a) displays a similar morphology to that of c_p =1.0 wt% 30/70 PS/PMMA blend. To demonstrate the photoluminescence of the patterned blend due to the embedded QDs, LSCFM imaging was performed; the excitation and emission filters for that were selected according to the photoluminescence properties of the constituent PS-CdS QDs that are shown in chapter 3 of this thesis (Figure 3.8b). LSCFM image of the film (Figure 4.11 b) shows localized CdS emission from the photoluminescent striped pattern, formed via surface-directed patterning of the “PS-like” QDs on a chemically-patterned surface.

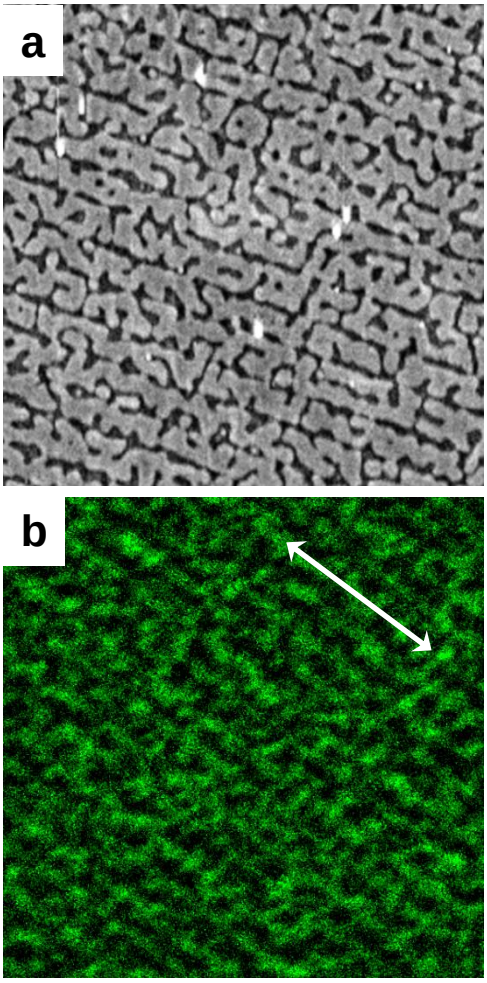

Figure 4.11.10-10 μm (a) AFM and (b) LSCFM images of c_p = 1.0 wt% 30/70 PS-CdS/PMMA blend on OTS-patterned glass substrate. Arrow on the LSCFM image shows the direction of pattern lines.

4.4. Conclusion

This work describes combination of the bottom-up process of polymer phase-separation during spin-coating, and top-down approach of μCP. We demonstrate the directed phase-separation of PS/PMMA polymer blends on chemically-patterned surfaces possessing regions of various surface energies: alternating low surface energy OTS

stripes and high energy glass; these surfaces laterally arrange the phase-separated polymer domains based on their preferential wettings. Analysis on the morphologies for different polymer blend solution concentration demonstrates that pattern replication occurs when d is in the same order as λ (c_p = 1.0 wt%). When $d > \lambda$ no pattern is observed in polymer film (c_p = 2.0 wt%), and when $d < \lambda$ (c_p = 0.5 wt%) the small phase-separated domains are forming in regions in between OTS lines (Figure 4.3). Studying the blend films of different composition demonstrates that when the composition does not match the area fraction of the underlying patterned surface, the composition mismatch increases the extent of defects such as bridging between the raised domains in the patterned film (Figure 4.7-4.9). The effect of solvent is also considered and it is shown that when solvent has high vapour pressure, the high rate of evaporation does not give the polymers enough time to segregate into energetically matching regions of the underlying pattern (Figure 4.10).

The approach of directing the phase-separation of polymers was also employed to organize polymer domains of PS-stabilized photoluminescent CdS QDs and PMMA into striped pattern. LSCFM imaging displays the luminescent arrays of such films due to the embedded QDs, which are addressed to underlying OTS stripes because of the preferential wetting of PS at those regions (Figure 4.11). This achievement motivated us to prepare another type of NPs (for the next part of the work), which are PMMA-stabilized in order to employ the same methodology of PS/PMMA patterning to simultaneously pattern two types of NPs: PS-stabilized QDs/PMMA-stabilized NPs on to our patterned surfaces; this topic will be discussed in chapter 6 in more details.

4.5. References

(1) Haryono, A.; Binder, W. H. *Small***2006**, 2, 600.

(2) Tsutsumi, K.; Funaki, Y.; Hirokawa, Y.; Hashimoto, T. *Langmuir***1999**, 15, 5200.

(3) Lopes, W. A.; Jaeger, H. M. *Nature***2001**, 414, 735.

(4) Bockstaller, M. R.; Lapetnikov, Y.; Margel, S.; Thomas, E. L. *J. Am. Chem. Soc*. **2003**, 125, 5276.

(5) Sohn, B.-H.; Choi, J.-M.; Yoo, S. I.; Yun, S.-H.; Zin, W.-C.; Jung, J. C.; Kanehara, M.; Hirata, T.; Teranishi, T. *J. Am. Chem. Soc*. **2003**, 125, 6368.

(6) Weng, C. C.; Wei, K. H. *Chem. Mater*. **2003**, 15, 2936.

(7) Lin, Y.; Boker, A.; He, J. B.; Sill, K.; Xiang, H. Q.; Abetz, C.; Li, X. F.; Wang, J.; Emrick, T.; Long, S.; Wang, Q.; Balazs, A.; Russell, T. P. *Nature* **2005**, 434, 55.

(8) Chiu, J. J.; Kim, B. J.; Kramer, E. J.; Pine, D. J. *J. Am. Chem. Soc*. **2005**, 127, 5036.

(9) Meli, L.; Li, Y.; Lim, K. T.; Johnston, K. P.; Green, P. F. *Macromolecules* **2007**, 40, 6713.

(10) Huang, C. M.; Wei, K. H. *Macromolecules***2008**, 41, 6876.

(11) Chang, J. J.; Kwon, J. H.; Yoo, S. I.; Park, C.; Sohn, B. H. *J. Mater. Chem*. **2009**, 19, 1621.

(12) Xu, C.; Ohno, K.; Ladmiral, V.; Milkie, D. E.; Kikkawa, J. M.; Composto, R. J. *Macromolecules***2009**, 42, 1219.

(13) Akasaka, S.; Mori, H.; Osaka, T.; Mareau, V. H.; Hasegawa, H. *Macromolecules***2009**, 42, 1194.

(14) Cheyne, R. B.; Moffitt, M. G., Langmuir 2005, 21, 10297.

(15) Minelli, C.; Geissbuehler, I.; Eckert, R.; Vogel, H.; Heinzelmann, H.; Liley, M. *Coll. Polym.Sci.***2004**, 282, 1274.

(16) Wang, C.-W.; Moffitt, M. G. *Chem. Mater*. **2005**, 17, 3871.

(17) Guo, Y.; Moffitt, M. G. *Chem. Mater*. **2007**, 19, 6581.

(18) Rockford, L.; Mochrie, S. G. J.; Russell, T. P. *Macromolecules* **2001**, 34, 1487.

(19) Kim, S. O.; Solak, H. H.; Stoykovich, M. P.; Ferrier, N. J.; de Pablo, J. J.; Nealey, P. F. *Nature***2003**, 424, 411.

(20) Segalman, R. A.; Hexemer, A.; Kramer, E. J. *Macromolecules***2003**, 36, 6831.

(21) Sundrani, D.; Darling, S. B.; Sibener, S. J. *Langmuir***2004**, 20, 5091.

(22) Stoykovich, M. P.; Muller, M.; Kim, S. O.; Solak, H. H.; Edwards, E. W.; de Pablo, J. J.; Nealey, P. F. *Science***2005**, 308, 1442.

(23) Edwards, E. W.; Muller, M.; Stoykovich, M. P.; Solak, H. H.; de Pablo, J. J.; Nealey, P. F. *Macromolecules***2007**, 40, 90.

(24) Cheng, J. Y.; Rettner, C. T.; Sanders, D. P.; Kim, H. C.; Hinsberg, W. D. *Adv. Mater*. **2008**, 20, 3155.

(25) Sundrani, D.; Darling, S. B.; Sibener, S. J., *Nano. Lett*., **2004**, 4:273.

(26) Chai, J.; Buriak, J. M., *ACS Nano*, **2008**, 2:489.

(27) Sundrani, D.; Sibener, S. J., *Macromolecules*, **2002**, 35:8531.

(28) Black, C. T.; Bezencenet, O., *IEEE Trans. Nano. Technol*. **2004**, 3:412.

(29) Cheng, J. Y.; Ross, C. A.; Thomas, E. L., *Appl. Phys. Lett*., **2002**, 81:3657.

(30) Cheng, J. Y.; Zhang, F.; Smith, H. I.; Julius Vansco, G.; Ross, C. A., *Adv. Mater*. **2006**, 18:597.

(31) Boltau, M.; Walheim, S.; Mlynek, J.; Krausch, G.; Steiner, U. *Nature***1998**, 391, 877.

(32) Raczkowska, J.; Cyganik, P.; Budkowski, A.; Bernasik, A.; Rysz, J.; Raptis, I.; Czuba, P.; Kowalski, K. *Macromolecules***2005**, 38, 8486.

(33) Park, L. Y.; Munro, A. M.; Ginger, D. S. *J. Am. Chem. Soc*.**2008**, 130, 15916.

(34) Jaczewska, J.; Budkowski, A.; Bernasik, A.; Raptis, I.; Moons, E.; Goustouridis, D.; Haberko, J.; Rysz, J. *Soft Matter***2009**, 5, 234.

(35) Cyganik, P.; Budkowski, A.; Steiner, U.; Rysz, J.; Bernasik, A.; Walheim, S.; Postawa, Z.; Raczkowska, J., *Europhysics Letters*, **2003**, 62,855.

(36) Newby, B.M.Z.; Composto, R. J., Macromolecules, 2000, 33, 3274.

(37) Sehgal, A.; Ferreiro, V.; Douglas, J. F.; Amis, E. J.; Karim, A. *Langmuir* **2002**, 18, 7041.

(38) Sprenger, M.; Walheim, S.; Schafle, C.; Steiner, U., *Adv. Mater*. **2003**, 15, 703.

(39) Andrew, P.; Huck, W. T. S., *Soft Matter*, **2007**, 3, 230.

(40) Fukunaga, K.; Elbs H.; Krausch, G., *Langmuir***2000**, 16, 3474.

(41) Rockford, L.; Liu, Y.; Mansky, P.; Russell, T. P., Phys. Rev. Lett ,1999, 82:2602.

(42) Krausch, G.; Kramer, E. J.; Bates, F. S., *Phys. Rev. Lett*. **1993**, 71, 3669.

(43) kielhorn, L.; Muthukumar M., *J. Chem. Phys*. **1999**, 111, 2259.

(44) Harirchian-Saei, S.; Wang, M. C. P.; Gates, B. D.; Moffitt, M. G. *Langmuir*, **2010**, 26, 5998.

(45) Cui, Z., *Nanofabrication: principles, capabilities and limits*, Springer, **2008**, New York.

(46) Taylor, J. C., *Advanced lithographic patterning technologies: Materials and processes*, The University of Texas, **2007,** Texas.

(47) Y. Xia, G. M. Whitesides, Annu. Rev. Mater. Sci., 1998, 28, 153.

(48) Y. Xia, G. M. Whitesides, Angew. Int. Ed., 1998, 37, 550.

(49) Hidber, P. C.; Helbig, W.; Kim, E.; Whitesides, G.M., Langmuir, 1996, 12, 1375.

(50) Zhao, X.M.; Xia, Y.; Whitesides, G.M., J. Mater. Chem.,1997, 7, 1069.

(51) Jeon, N. L.; Choi, I. S.; Whitesides, G. M.; Kim, N.Y.; Laibinis, P.E.; Harada, Y.; Finnie, K. R.; Girolami, G. S.; Nuzzo, R.G., Appl. Phys. Lett., 1999,75, 4201.

(52) Zhong, Z.; Gates, B.; Xia, Y.; Qin, D., Langmuimr, 2000, 16, 10369.

(53) Yu, M.; Lin, J.; Wang, Z.; Fu, J.; Wang, S.; Zhang, H. J.; Han, Y. C. Chem. Mater., 2002, 14, 2224.

(54) Kumar, A.; Whitesides GM. 1993. Appl.Phys. Lett., 2002, 4, 63.

(55) Tanaka, K.; Takahara, A.; Kajiyama, T. *Macromolecules***1996**, 29, 3232.

(56) Walhein, S.; Bo¨ltau, M.; Mlynek, J.; Krausch, G.; Steiner, U. *Macromolecules***1997**, 30, 4995.

(57) Ton-That, C.; Shard, A. G.; Daley, R.; Bradley, R. H. *Macromolecules* **2000**, 33, 8453.

(58) Harris, M.; Appel, G.; Ade, H. *Macromolecules***2003**, 36, 3307.

(59) Walheim, S.; Ramstein, M.; Steiner, U. *Langmuir***1999**, 15, 4828.

(60) Zong, Q.; Li, Z.; Xie, X., *Macromolecular Chemistry and Physics***2004**, 205, (8), 1116.

(61) Li, G.; Shrotriya, V.; Huang, J.; Yao, Y.; Moriarty, T.; Emery, K.; YANG, Y. *Nature Materials* **2005**, 4, 864.

(62) Coakley, K. M.; McGehee, M. D.*Chem. Mater*.**2004**, *16* (23), 4533.

(63) Kim, J. S.; Park, Y.; Lee, D. Y.; Lee, J. H.; Park, J. H.; Kim, J. K.; Cho, K. *Adv. Mater*. **2010**, 20, 540.

(64) Halls, J. J. M.; Arias, A. C.; MacKenzie, J. D.; Wu, W.; Inbasekaran, M.; Woo, E. P.; Friend, R. H. *Adv. Mater*.**2000**, 12, 498.

(65) Chappell, J.; LidzeyD. G. *Journal of Microscopy* **2003**,209, 188.

(66) Chen, L.-M.; Hong, Z.; Li, G.; Yang, Y. *Adv. Mater*. **2009**, 21, 1434.

(67) Heriot, S. Y.; Jones, R. A. L., *Nat. Mater.***2005**, 4, (10), 782-786.

(68) Walheim, S.; Boltau, M.; Mlynek, J.; Krausch, G.; Steiner, U. *Macromolecules***1997**, 30, 4995.

(69) Tanaka, K.; Takahara, A.; Kajiyama, T. *Macromolecules***1996**, *29*, 3232.

(70) Jukes, P. C.; Heriot, S. Y.; Sharp, J. S.; Jones, R. A. L. *Macromolecules* **2005,** *38,* 2030.

(71) Dalnoki-Veress, K.; Forrest, J.A.; Stevens, J.R.; Dutcher, J.R. *Physica A,***1997**, 87, 239.

(72) Kim, J.-S.; Ho, P. K. H.; Murphy, C. E.; Friend, R. H.*Macromolecules***2004**, *37* (8), 2861.

(73) Kessler, J.; Higashida, N.; Shimomai, K.; Inoue, T.; Ougizawa, T. *Macromolecules* **1994**, *27*, 2448.

(74) Ribbe, A. E.; Hashimoto, T. *Macromolecules* 1997, 30, 3999.

(75) Schubert, D. W.; Dunkel, T., *Spin-coating from a molecular point of view: its concentration regimes, influence of molar mass and distribution;* Materials Research Innovations Vol. 7, p. 314, Springer, **2003**.

(76) Lide, D. R. *CRC Handbook of chemistry and physics,* 90th ed., Taylor and Francis, **2009.**

Chapter 5: PHOTOLUMINESCENCE CHARACTERIZATION OF SEMICONDUCTOR QUANTUM DOT/METAL NANOPARTICLE ASSEMBLIES FORMED VIA POLYMER/POLYMER PHASE-SEPARATION

5.1. Introduction

Metallic nanostructures have been the subject of intensive research in recent years, partly due to their ability to modify the optical properties of luminescent materials, such as quantum dots (QDs), quantum wells (QWs), semiconductor nanowires and Si nanocrystals;[1-24] this have been demonstrated theoretically[25-29] and experimentally to be associated with photo excited free-electron oscillations in the metals called surface plasmons (SPs), which support localized electric fields near the surface of the metals.[30-32] For instance, it has been shown that metallic nanostructures can considerably improve the efficiency of light emitting devices due to interactions between surface-loacalized SP fields and emitters.[33, 34] Emission properties of semiconductor QDs[12,20,40-42] can also be improved in the presence of plasmonic nanostructures (embedded within a metallic film,[12, 20, 41] or encapsulated in a metallic shell[42]). In addition, metallic nanostructures can also enhance raman signals dramatically; this enhancement is reported[35, 36 to be as] as high as 10^{14}-10^{15} and is the basis for surface-enhanced raman scattering (SERS).[35-39]

In general, the interaction between photoluminescent materials and SPs of metallic nanostructures can enhance the photoluminescence (PL) by either increasing the rate of radiative emission[13-19] and/or by increasing the excitation field near the emitter.[2, 12, 43-45] In the first case, the emission enhancement occurs when the excited emitter relaxes by releasing a photon, which couples with the SP of metal, in other word this mechanism is based on the coupling between the emitted photon and SP.[13-19] In the second case, the emission enhancement is the result of coupling between the electromagnetic excitation field and the dipole mode of SP field around the metal; in other words, metals amplify the incident light improving the efficiency of light

absorption for emitters within the surface-localized electric flied of the metal. [2, 12, 43-45] Therefore, the separation between the metal and the emitter is one of the most important parameters affecting the enhancement effect; in general, the largest enhancement can be obtained when this distance is small because the SP is highly localized at the metal surface and decays rapidly away from it;[46,48] however, below a certain minimum distance (reported in the range of 5-10 nm)[12]luminescence quenching will occur. The reason is the non-radiative energy transfer between the excited emitter and metal when the distance is too small; in other word non-radiative dipole-dipole coupling dissipates the energy and quenches the PL.[12, 25-30]

Among metallic nanostructures, nanoparticles (NPs) have received the most attention due to the various applications that they have in the fields of catalysis, biosensing, electronics and optics; details of these applications are provided in the review report by Moores and Goettmann[46] and also listed in section 1.4 of this thesis; as pointed out, many of their applications are due to the SPs. For metal NPs the position, width, and intensity of SP bands is affected by many factors including the dielectric constant of the surrounding media, the electronic interactions between the stabilizing layer and the NP core, the interparticle interactions between NPs, the NP electronic structure, as well as the charge, size, geometry, and polydispersity of NPs.[46-52]

There are several methods for the synthesis of colloidal metal NPs;[53-60] In general the process starts with the reduction of a metallic salt by a mild reducing agent in the presence of a desired colloidal stabilizer, which controls coagulation and the rate of growth relative to rate of nucleation. In this work, we synthesize polymer-stabilized silver (Ag) NPs; the synthesis utilizes the microphase-separated templates of block

copolymers; in the organic solvents amphiphilic block copolymers form micelles with insoluble cores of the block that contains the metal ion. The metal ions are then reduced into metal NPs inside the spherical core of the micelle.[61,62] This method has the advantage of size control for NPs due to the spatial confinement created by micelles. Also polymers are very efficient steric stabilizers (when they are grafted to NPs surface to form a spherical brush) and they can be used as a tool to control the assemblies of NPs due to interactions between surface polymer chains and the surrounding environment; they also offer a medium with desirable mechanical properties that is required for many NP-based devices.[61,62]

Patterning of polystyrene-stabilized cadmium sulfide (PS-CdS) quantum dots (QDs) was demonstrated in previous chapter; here our interest is in patterning different NP types addressed to different regions of a chemically-patterned substrate. Therefore, a NP with core of different optical properties and shell of different polymer, which results in a different surface energy is required. In this chapter, we choose PMMA-stabilized silver (PMMA-Ag) NP. Ag NP was chosen based on the interesting optical interactions between metal NPs and QDs. PMMA was selected as the stabilizer of Ag NP because the behaviour of phase-separating PS/PMMA blends was extensively studies in our work in Chapter 4.

PMMA-Ag NP is synthesized by micellization of Poly (methyl methacrylate)-*block*-poly (acrylic acid) (PMMA)-*b*-(PAA) amphiphilic block copolymer in a selective solvent followed by introduction of silver acetate to the micelle core and the reduction of Ag ion by adding a reducing agent. Detailed synthesis and characterization of PMMA-Ag NPs is described in this chapter followed by optical studies on the blends of these NPs

with PS-CdS QDs to investigate the interactions between SP of Ag NPs with the PL of QDs in thin films. Phase-separation between "PS-like" CdS and "PMMA-like" Ag, gives rise to the formation of NP domains. These phase-separated structures are optically studied in this chapter and are used in the next chapter for the demonstration of simultaneous patterning of two NP types by surface-directed patterning on a chemically-patterned substrate

5.2. Experimental

5.2.1. PMMA-Ag Synthesis

5.2.1.1. Materials

Poly (methyl methacrylate)-*block*-poly (acrylic acid) copolymer, PMMA(170)-*b*-PAA(28), where numbers in brackets indicate number-average degrees of polymerization for each block, was purchased from Polymer source Inc. Silver Acetate 99.99%, Sodium borohydride ($NaBH_4$) andmethanol were purchased from Aldrich.Reagent grade THF was purchased from Anachemia.

5.2.1.2. PMMA-Coated Silver Nanoparticle (PMMA-Ag) Synthesis

In order to prepare PMMA-Ag NPs, first a 2 wt% solution of PMMA (170)-*b*-PAA (28) was prepared in reagent grade THF and stirred for 3 h. In the mean time a 0.25 M suspension of silver acetate in deionized (DI) water was prepared and a stoichiometric amount of that was added to the copolymer solution with constant stirring. The reason

for adding silver acetate from a suspension is that we are trying to keep the amount of water in the reaction solution at a minimum, in order to avoid precipitation of copolymer from the THF solution. The reaction solution turned from clear and colourless to turbid bluish indicating the formation of micelles. After 1 h stirring, the reducing agent, which is 0.50 M aqueous solution of $NaBH_4$, was added to the solution in variable excess amounts relative to the molar amount of added silver acetate. Reduction of Ag^+ to Ag results in a color change to dark yellow. The solution was stirred overnight and then precipitated into cold methanol followed by washing with methanol for several times and then drying overnight under vacuum; the procedure is illustrated in Figure 5.1.

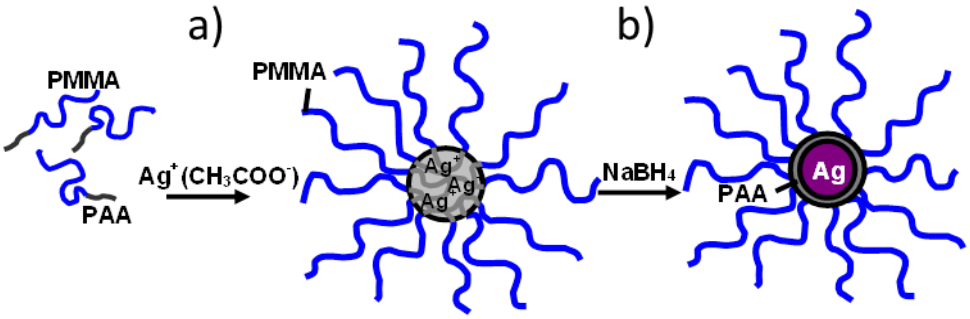

Figure 5.1. Synthesis of PMMA-Ag NPs: (a) micelle formation by the addition of silver acetate to the solution of PMMA-*b*-PAA in THF with soluble PMMA brush layer and insoluble Ag^+-containing PAA core (b) Ag NPs formation by reduction of Ag^+ in the core to Ag^0 using $NaBH_4$ as the reducing agent.

5.2.2. PMMA-Ag Characterization

5.2.2.1. UV-Vis Spectroscopy

UV-Vis measurements were performed on a CARY 5 UV-Vis-NIR spectrophotometer.

5.2.2.2. X-Ray Diffraction (XRD)

XRD measurements of Ag NPs was carried out using a Rigaku miniflex diffractometer operating with a Cr anode (Cr Kα1 λ=2.228970 Å) at 30 kV accelerating voltage and 15 mA electric current. 2θ value changes between 50° to 110° with a rate of 0.5°/min. Dry crystals were ground and placed on a glass sample holder for the measurement.

5.2.2.3. Static Light Scattering (SLS) and Dynamic Light Scattering (DLS)

SLS and DLS measurements were performed on a Brookhaven Instruments photon correlation spectrometer with a BI-200SM goniometer, a BI-9000AT digital autocorrelator, and a Melles Griot He-Ne Laser (632.8 nm) with a maximum power output of 75 mW. Samples for both SLS and DLS measurements were prepared with extra care to avoid dust in the samples (dust scatter the light and result in imprecise measurement). 5 mg/mL stock solutions of PMMA-Ag was prepared in spectroscopic grade toluene which was filtered through two membrane filters with 0.45 μm nominal

pore size connected in series. The solution was then equilibrated overnight. To remove dust, the solution was filtered again through two membrane filters connected in series. Successive dilutions of the solution were carried out by adding known quantities of the filtered solvent.

SLS measurement of PMMA-Ag was carried out in a concentration range from 0.2 to 1 mg/mL. For each concentration, angles of detection from 15° to 155° were measured with 5° increments between angles. Ten repeat measurements of scattered light intensity were taken at each angle and each concentration to obtain Zimm plots. All SLS measurements were conducted at 23 °C.

DLS measurement of PMMA-Ag in toluene was conducted at a 90° scattering angle and at concentrations of 0.05 mg/mL. Three repeated measurements of the autocorrelation function were obtained and all DLS measurements were conducted at 23 °C.

5.2.2.4. Transmission Electron Microscopy (TEM)

TEM was carried out on a JEOL JEM-1400 electron microscope, operating at an electron accelerating voltage of 80 kV. Drop-cast samples were prepared by depositing a drop of 0.5 mg/mL PMMA-Ag solution in Toluene on a copper grid (300 mesh) coated with an amorphous carbon film; the grids were then dried at room temperature overnight before imaging. TEM images were collected at different magnifications and the particle size analysis was carried out on the samples at various regions of the TEM grid for a minimum of 90 particles.

5.2.2.5. Fourier Transform Infrared Spectroscopy (FTIR)

A Perkin Elmer spectrum 1000 FTIR spectrometer was used in absorption mode for FTIR measurements.

5.2.3. PS-CdS/PMMA-Ag Blend Films Preparation

5.2.3.1. PS-CdS Preparation

The polystyrene-stabilized cadmium sulfide (PS-CdS) QDs used in this study were synthesized via templated growth of CdS in the cores of reverse micelles consisting of the poly (styrene)-block-poly (acrylic acid) copolymer PS(226)-b-PAA(22), where numbers in brackets indicate number-average degrees of polymerization for each block. The synthesis of the PS-CdS sample employed here is similar to one described in previous works from our group;[61, 62](synthesis was performed by our former post-doctorate fellow; Celly Izumi). In summary, each PS-CdS unit consists of a core of a ~ 5 nm CdS nanoparticle (determined from UV-Vis and using Henglein's empirical relationship), with a poly(cadmium acrylate) (PACd) layer at the CdS surface, covalently-attached to external PS brush layer. Hydrodynamic radius (r_h) measured from DLS is 28.7 nm and aggregation number, which is calculated from the molecular weight (M_w= 27892 g mol^{-1}), is 485.

5.2.3.2. NPs Blend Solutions Preparation

PMMA-Ag NPs, prepared as described in 5.2.1, were blended together with PS-CdS QDs. First, solutions of 0.5, 1, 2 and 4 wt% in spectro grade toluene (Aldrich) were separately prepared and stirred for 4 h then sat overnight to equilibrate. The 30/70 and 50/50 (w/w) PS-CdS/PMMA-Ag blend solutions were made by mixing the appropriate amounts of the two solutions into a clean vial. The blend solutions were then stirred for 4 h then sat overnight to equilibrate.

5.2.3.3. Spin coating the NPs blend films

One drop of the NPs blend solution was spin coated on a non-patterned glass cover slip (18mm x 18mm, VWR) or quartz microscopic slide (25 mm x 25 mm, chemglass) for 60 s at different spinning rates of 3000, 6000 and 9000 rpm. For each condition three copies were prepared for complete characterization. Samples were dried in a vacuum oven for 12 h before characterization, and stored in dark. Glass and quartz slides were cleaned prior to spin coating by sonication in methanol, chloroform, toluene and acetone, each for 10 min followed by vacuum drying overnight.

5.2.4. PS-CdS/PMMA-Ag Blend Film Characterization

5.2.4.1. UV-Vis Spectroscopy

A Perkin Elmer PE Lambda 1050 Spectrophotometer was employed for obtaining absorption spectra of blend films.

5.2.4.2. Photoluminescence (PL) Spectroscopy

Photoluminescence measurements of the control and the blend films or solutions were collected on a FL 900 Edinburg Instrument fluorimeter, using a 450 W Xe arc lamp to excite samples at 420 and 450 nm. A 435 nm high band pass filter was used initially on the emission side to eliminate the excitation wavelength scattered by the sample. Since this filter itself showed an emission peak at around 600 nm, which is the area of interest for our QDs, the filter was later replaced by a longpass filter with cut-on wavelength of 450 nm (FEL450 from Thorlabs). Front face illumination of the samples was detected at a 30° angle (with respect to the surface of the sample) by a Hammamatsu R928P visible PMT detector. All spectra shown in this work are collected using the 450 nm longpass filter with spectral resolution of 0.5 nm step size and they all are the result of an average over three measurements. Excitation spectra were recorded by setting the emission wavelentgth at ~ 620 nm with the same geometry and set up as above.

5.2.4.3. Photoluminescence Lifetime Measurement

This was also carried out on a F900 Edinburgh instrument Fluorimeter. The samples were excited at 420, 435 and 450 nm for three different series of measurements. A Vibrant OPO laser generating 5 ns pulses was utilized to excite the samples. Emission at 620 nm was detected by a Hamamatzu R928P visible photomultiplier (PMT). All decay curves were collected up to a maximum intensity of 10000 photon counts. Decay profiles were fitted to multi-exponential model using a tail-fit algorithm. Three separate measurements of decay profiles were carried out in order to determine the errors on reported lifetime.

5.2.4.4. Film Thickness Measurements

To determine the thickness of the spin coated films, three scratches at three different positions were made on the films by scalpel. The depth of the scratch which is the thickness of the film was then measured by AFM at three different points along the scratch. AFM in contact mode was performed on a MFP-3D atomic force microscope from Asylum Research with non-conductive silicon nitride cantilevers from Veeco (model: NP-10). The cantilevers are 0.4 - 0.7 μm thick and their resonance frequency ranges from 12-75 kHz and spring constants ranging from 0.06-0.58 N/m.

5.3. Results and Discussion

5.3.1. Synthesis and Characterization of PMMA-*b*-PAA$^-$Ag$^+$ Reverse Micelles

PMMA-*b*-PAA$^-$Ag$^+$ micelles preparation is the first step in the synthesis of PMMA-Ag NPs synthesis before the reducing stage that reduces the metal ions to the metal NP. Hydrodynamic radius *(R_h)* of the micelles was measured by DLS; the average value between three runs resulted in R_h = 35.8 nm. SLS was also performed on the micelle sample resulting in M_w = (1.02 ± 0.09) 10^6 g/mol. Obtained Zimm-plot is provided in Figure 5.2.

M_w of the micelle was then used to calculate the aggregation number of PMMA-Ag NPs because direct SLS measurement on NPs resulted in M_w of (1.63 ± 0.18) 10^9 g/mol, which is two orders of magnitude greater than what expected due to the large extent of scattering by metal NPs. Since R_h value determined from DLS for micelle sample (35.8 nm) is in good agreement with NPs (35.4) it can be assumed that the size of

NPs does not change much during reduction. Therefore, the aggregation number of NPs can be calculated from the M_w of the micelle sample by dividing this value by the M_w of a PMMA-*b*-PAA chain (22800 g/mol); this results in the aggregation number of 44.9 for PMMA-Ag NPs.

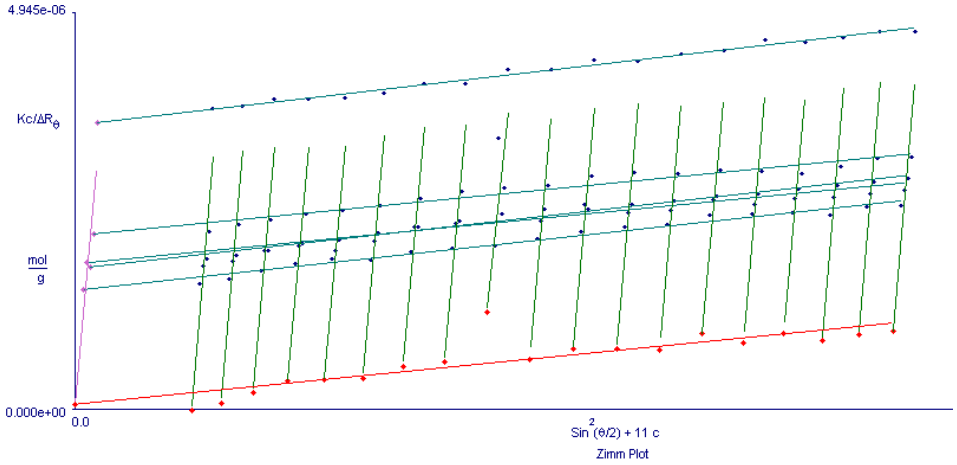

Figure 5.2. Zimm-plot of PMMA-b-PAA$^-$Ag$^+$ micelles.

5.3.2. Synthesis and Characterization of PMMA-Ag Nanoparticles

The synthesis of PMMA-stabilized Ag NPs results in the formation of NPs with size and properties that are dependent on the experimental parameters. An important factor that strongly affects the properties of the resultant NPs is the amount of the reducing agent relative to the number of metal ions.[63] In this work, the reduction of Ag^+ metallic ions into NPs was performed using $NaBH_4$, which is a versatile reducing agent and is commonly used for Ag NP synthesis;[53-55] To ensure that $NaBH_4$ does not affect the polymeric stabilizer of the NPs, in other word in does not reduce -COO- group in methacrylate to -COH-, FTIR spectra were collected for PMMA-*b*-PAA$^-$Ag$^+$ micelle sample before adding the reducing agent and for PMMA-Ag and also after the reduction

by 10x excess amount of the reducing agent. Identical carbonyl stretching absorption peaks were observed for both spectra (Figure 5.3a and b); this proves that the polymer attached to the NPs remain undisturbed during reduction.

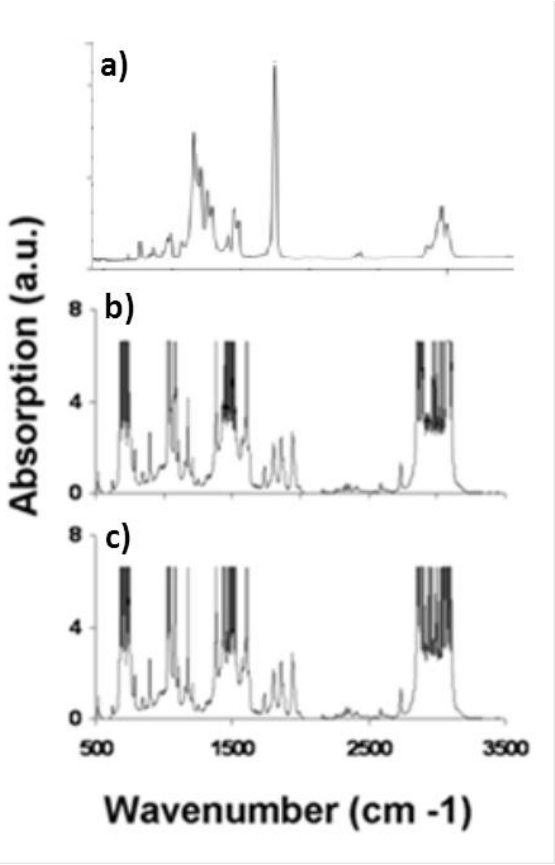

Figure 5.3. FTIR spectra of (a) PMMA-*b*-PAA, (b) PMMA-*b*-PAA$^-$Ag$^+$ micelles sample and (c) PMMA-Ag NPs sample after reduction with 10x excess $NaBH_4$.

To investigate the effect of the amount of the reducing agent on the properties of the synthesized NPs, three different samples were prepared using three different amounts of $NaBH_4$. PMMA-Ag prepared with 5x, 8x and 10x excess reducing agent relative to the molar amount of Ag^+ were prepared and characterized for this study; these samples

are designated PMMA-Ag1, PMMA-Ag2, PMMA-Ag3, respectively. Characterization data for all three samples are shown below.

First, the crystal structures of the Ag cores for PMMA-Ag1, PMMA-Ag2, and PMMA-Ag3 was characterized using XRD; the diffraction patterns are illustrated in Figure 5.4. For all three samples, the observed peaks match the *silver-3c syn* crystal structure (pink traces shown on XRD patterns).[64,65] This structure has been reported as a common structure for stable Ag NPs and is a face centre cubic structure with diffraction peaks at 2θ = 58°, 68° and 105° corresponding to the (111), (200) and (220) planes.[64, 65] XRD patterns also show peaks at 2θ = 65° and 83° in addition to the *silver-3c syn* structural lines due to the formation of silver oxides. These two impurity peaks appeared much weaker for PMMA-Ag3 (prepared using the largest relative amount of reducing agent).

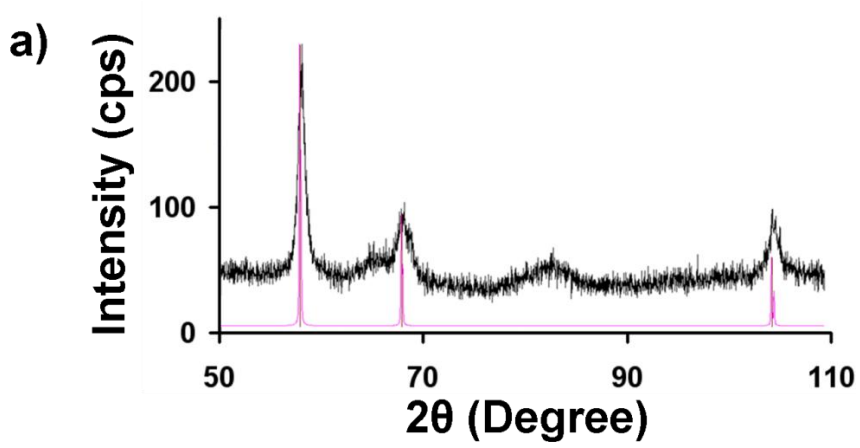

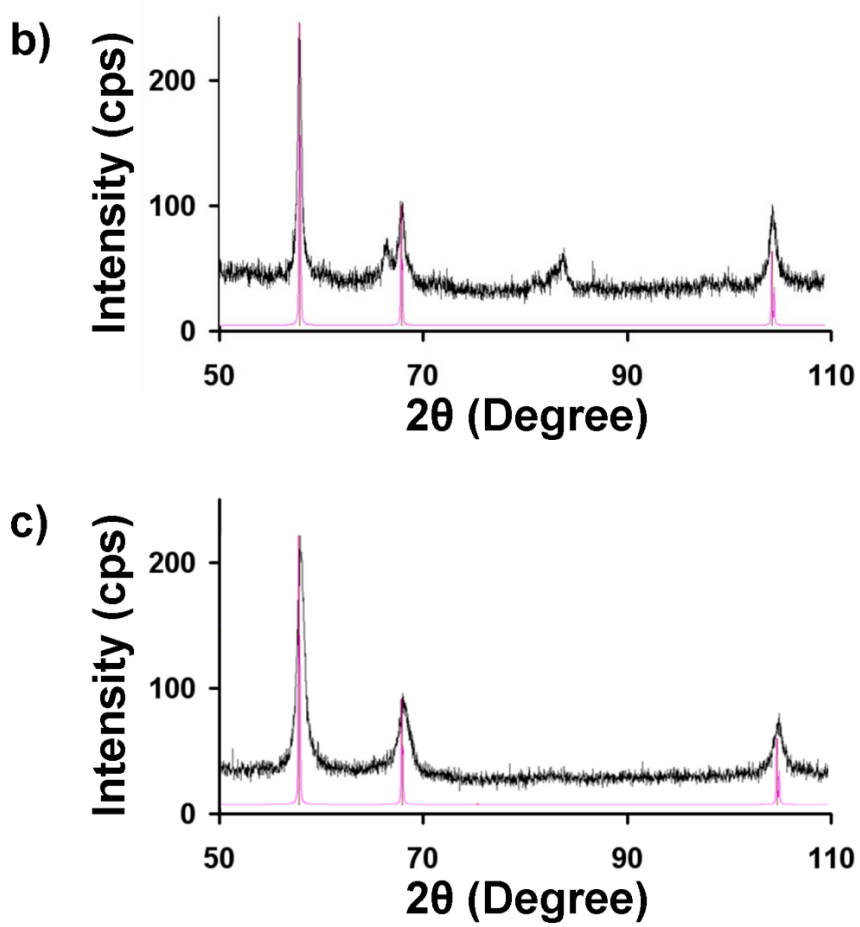

Figure 5.4. XRD pattern of (a) PMMA-Ag1, (b) PMMA-Ag1, and (c) PMMA-Ag1. Pink traces illustrate the crystalline pattern of *silver 3c-syn* structure.

Hydrodynamic radii (R_h) of PMMA-Ag1, PMMA-Ag2, and PMMA-Ag3 were determined by DLS measurements; average R_h values, calculated from three repeat DLS runs for each sample are: R_h = 41.7, 60.6 and 35.4 nm for samples prepared using 5, 8, and 10x excess reducing agent, respectively.

The shape and size distribution of the NPs can be determined by TEM imaging and statistical analysis on TEM images. Representative images of features observed for each of the samples is provided in Figure 5.5.

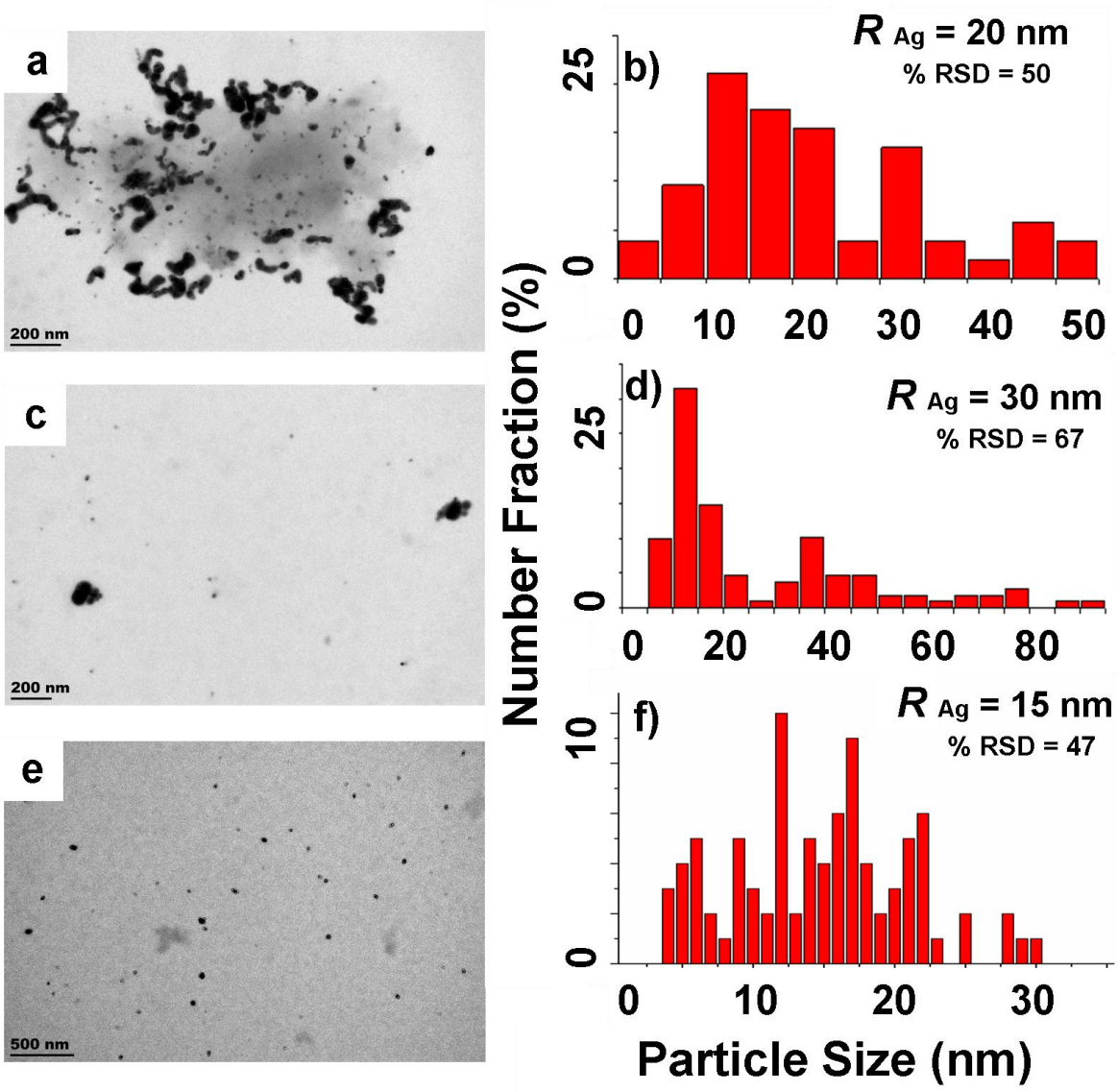

Figure 5.5. Representative TEM images (a, c, e) and the size distributions (b, d, f) of (a, b) PMMA-Ag1, (c, d) PMMA-Ag2 and (e, f) PMMA-Ag1. Average size of NPs (R_{Ag} and % RSD are shown.

TEM images (Figure 5.5a, c, e) show a distribution of Ag NP cores. Statistical particles size measurement results in size distributions for different amounts of reducing agent as shown in Figure 5.5b, d, f. Average size of PMMA-Ag1, PMMA-Ag2, and

PMMA-Ag3 NPs are R_{Ag} = 20, 30, and 15 nm, respectively. %RSD is the highest for the PMMA-Ag2 and the lowest for PMMA-Ag3.

DLS and TEM results both demonstrate that increasing the amount of reducing agent is causing an increase in the size of NPs followed by a decrease. The size analysis also shows that the lowest polydispersity of NPs is obtained for the sample prepared using the largest amount of reducing agent (PMMA-Ag3).

Another difference between the three PMMA-Ag NPs is in their core morphologies; for NPs within block copolymer micelles reduction with smaller amount of reducing agent typically results in NPs with exclusively "cherry-like" (one NP per micelle)[63] morphology, as shown in Figure 5.6 b.[63] In contrast, reduction in the presence of the highest amount of reducing agent (10 x excess) forms about 8% cores with "raspberry-like" morphology (many small NPs per micelle), [63] as displayed in Figure 5.6a. This difference can be understood based on the high rate of nucleation in PMMA-Ag3 due to the high amount of reducing agent resulting in multiple nucleation sites per core.[63]

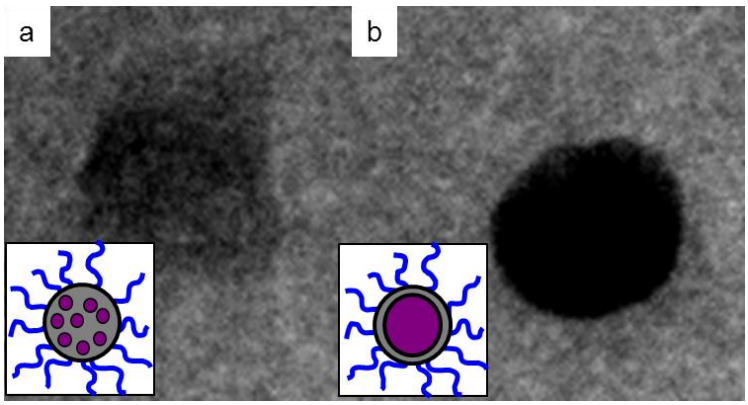

Figure 5.6. Demonstration of both (a) "raspberry-like" and (b) "cherry-like" NPs morphologies on a TEM image of the PMMA-Ag3; cartoons demonstrate the difference between these two morphologies.

UV-Vis absorption spectra were also collected for these samples that reveal the shape and the position of SP bands for PMMA-Ag NPs samples (illustrated in Figure 5.7). For the NPs prepared with the least amount of reducing agent (PMMA-Ag1), a broad shouldered SP band is observed at 407 nm. Increasing the amount of reducing agent to 8x (PMMA-Ag2) shifts the peak to 417 nm and alters it to a sharper band. The sharpest SP peak was observed for the sample prepared using 10x excess $NaBH_4$ (PMMA-Ag3) positioned at 419 nm. There is also a shoulder observed at ~ 350 nm that becomes weaker by increasing the amount of reducing agent.

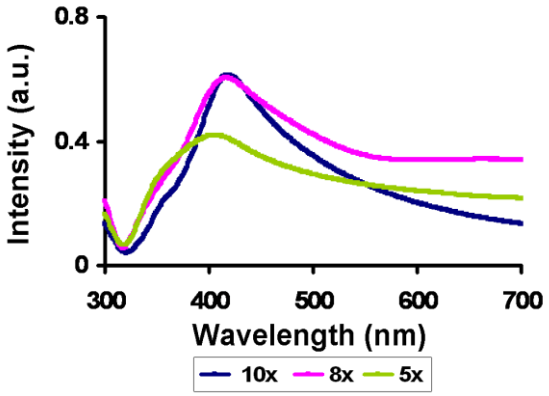

Figure 5.7. UV-Vis absorption spectra of PMMA-Ag NPs (dispersed in toluene); three samples were prepared using 5x (PMMA-Ag1), 8x (PMMA-Ag2), and 10x (PMMA-Ag3) excess $NaBH_4$.

Considering all parameters such as the quality of the crystal based on the impurity peaks observed in the XRD diffraction patterns of PMMA-Ag NPs, the sharpness of the SP peak, and the polydispersity of the particles we chose to use the sample prepared using 10x excess reducing agent (PMMA-Ag3) for all further experiments in the current and the following chapter because it shows the weakest impurity peaks in the XRD pattern, it has the sharpest SP band and it has the smallest polydispersity among the three samples.

5.3.3. Optical Studies of PS-CdS/PMMA-Ag NPs Blend Films

To understand the optical behaviour of blend films of PS-CdS and PMMA-Ag NPs, the first step is to characterize the components of the blend individually. To do so, emission and absorption of PS-CdS and PMMA-Ag NPs dispersed in toluene were measured. Absorption spectra which are shown in Figure 5.8 demonstrate the SP absorption band of individual PMMA-Ag NPs centered at 419 nm and the absorption shoulder for individual PS-CdS QDs with the absorption threshold at 488 nm. The

absorption spectra of PS-CdS and PMMA-Ag films spin-coated at 9000 rpm are also shown together with the absorption spectra of the blend films for comparison. Absorption spectra of the blend films resemble the absorption spectrum of PMMA-Ag with only small contribution from PS-CdS QDs, which appears as a small shoulder at around 520 nm; this is due to the higher extinction coefficient of Ag NPs compared to CdS QDs.

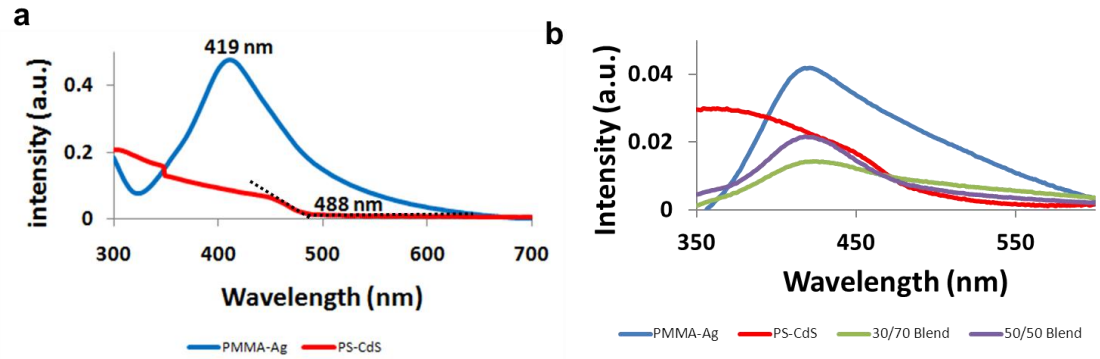

Figure 5.8. Absorption spectra of (a) PMMA-Ag and PS-CdS dispersed in toluene, (b) Absorption spectra of control PMMA-Ag, PS-CdS and blend films all spin-coated at 9000 rpm.

PL spectrum of PS-CdS QDs usually (similar to the PL spectrum showed for previous PS-CdS sample used in Chapter3, Figure 3.8 b) exhibits two emission peaks: one corresponding to the band edge emission at 471 nm and the other to the trap state (states localized at the QD surface) emission at 621 nm.[61, 62] Therefore, the 450 to 700 nm range is of our interest; however, in all our PL measurements (of both the blends and the individual components) a peak of unknown origin was present at ~ 480 nm wavelength, which interferes with the band edge emission peak of QDs. The nature of this peak and the source that generates it are not completely clear to us but most likely the peak is a raman peak due to an unknown species present in the chamber; our evidence for

suggesting this, is the shift in its position by changing the excitation wavelengths. Since we could not avoid this peak, all emission spectra that we present in this work are shown in the 500 to 800 nm wavelength range.

Figure 5.9 illustrates the PL spectra of PMMA-Ag and PS-CdS dispersed in toluene by exciting at λ_{ex} = 420 nm. The emission band of QDs is centered at 621 nm and no emission was observed for Ag NPs in this range, as expected.

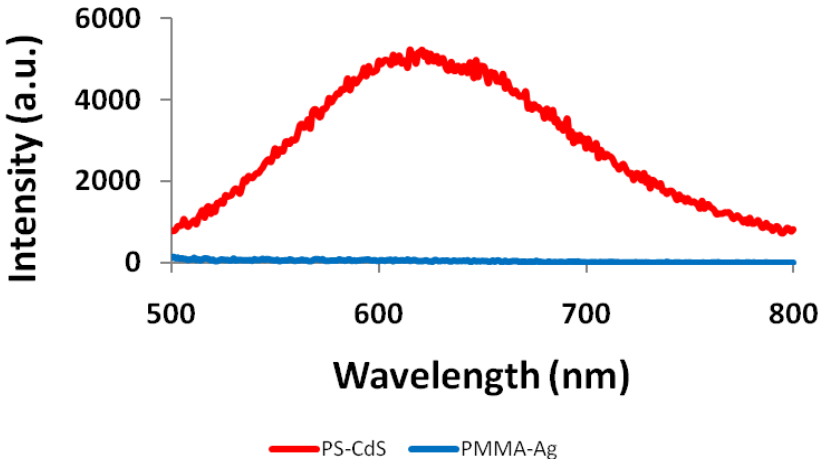

Figure 5.9. Emission spectra of PMMA-Ag and PS-CdS dispersed in toluene.

To investigate the optical properties of the PS-CdS/PMMA-Ag NPs blends, two compositions of 30/70 (w/w) and 50/50 (w/w) PS-CdS/PMMA-Ag were considered. A series of spin coating solution concentrations in range of c_p = 0.5 - 4.0 wt% were examined for these blends in order to optimize the preparation conditions. It was observed that for c_p lower than 4.0 wt% no PL signals were observed from the films due to low film thickness value leading to very few emitters being excited within the path length of the beam; therefore, all further experiments described in this chapter were carried out using c_p = 4.0 wt%. For each blend composition, three different spin rates of 3000, 6000, and 9000 rpm were investigated. The motivation for studying different PS-

CdS/PMMA-Ag blend compositions is to investigate the effect of the relative amount of interacting NPs and the reason that different spin rates were considered is to investigate the effect of the characteristic correlation length of the phase-separated domains (*d*), which is influenced by spin rate.

Figure 5.10 shows the PL intensities of the films prepared at 3000 rpm spin rate. fluorescence intensities of the 50/50 and 30/70 blends are both ~30% of the intensity of the control PS-CdS film (reported percentages are determined from values of peak intensities at the maxima); there is also a blue shift observed for the emission peak of the blend films relative to the PS-CdS control film: the peak position of the 50/50 blend shifts by 5 nm and the 30/70 blend shifts by 9 nm.

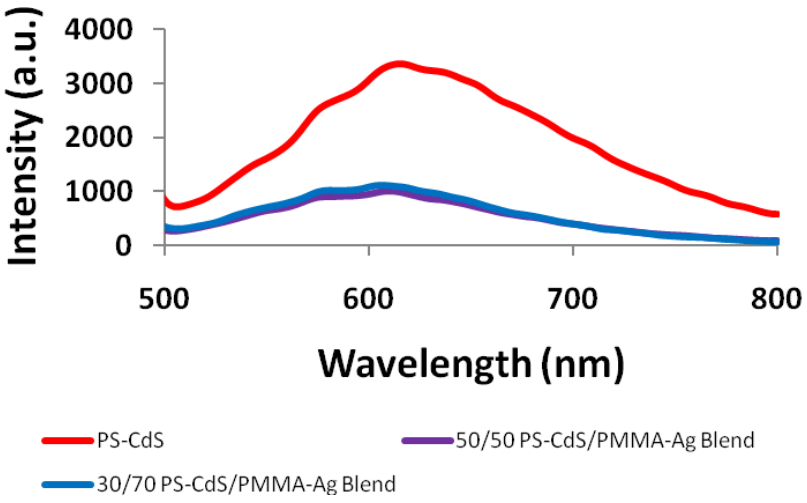

Figure 5.10. PL spectra 30/70 and 50/50 PS-CdS/PMMA-Ag NPs blend films together with PS-CdS control film, all three films spin coated at 3000 rpm.

For 6000 rpm (Figure 5.11) the fluorescence intensities of the 50/50 and 30/70 blends are 30% and 16% of the intensity of the pure PS-CdS control film (ratio of the peak intensities at the maxima), respectively. The position of peak maximum for the

50/50 blend blue shifted from that of the PS-CdS control film by 5 nm and for the 30/70 blend blue shifted by 8 nm.

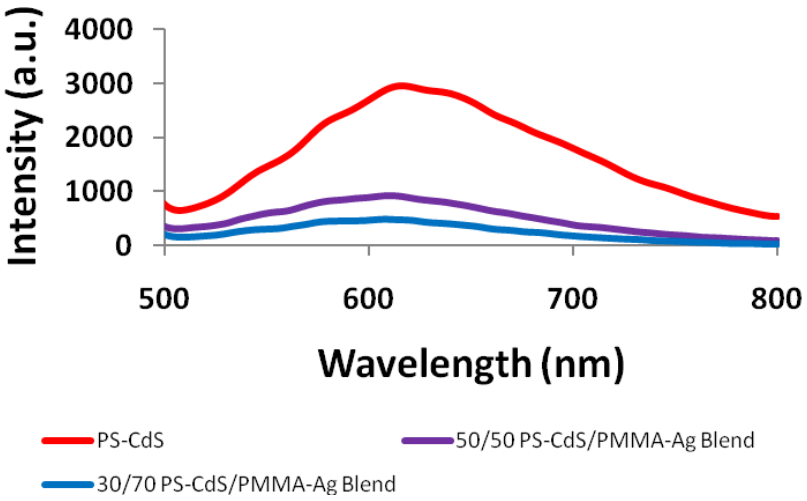

Figure 5.11. PL spectra 30/70 and 50/50 PS-CdS/PMMA-Ag NPs blend films together with PS-CdS control film, all three films spin coated at 6000 rpm.

For the 9000 rpm spin rate (Figure 5.12), the fluorescence intensities of the blend films are closer to the intensity of the control film: for the 50/50 and the 30/70 blends, peak intensities are 78% and 47% of the control film (ratio of the peak intensities at the maxima), respectively. This demonstrates the PL enhancement for the 9000 rpm blend films relative to the 3000 and 6000 rpm cases (Figure 5.10 and 5.11). Similar to previous cases, peaks of the blend films are blue shifted; the shift is 5 nm for the 50/50 blend and 6 nm for the 30/70 blend. A similar blue shift effect has been reported previously by Lee et al.[18] for a system of CdTe NWs in vicinity of gold NPs; the effect is attributed to the interactions between emitting NWs and SP resonance of the NPs.

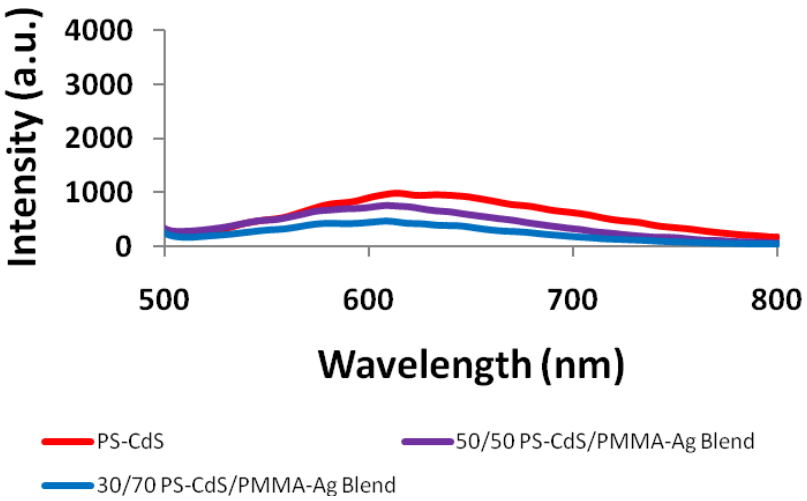

Figure 5.12. PL spectra 30/70 and 50/50 PS-CdS/PMMA-Ag NPs blend films together with PS-CdS control film, all three films spin coated at 9000 rpm.

The reason that in all three series shown in Figure 5.10-5.12, the fluorescence intensities of the PS-CdS/PMMA-Ag blend films are lower than the intensity of the PS-CdS control film can be attributed to the lower concentration of QDs in the blends compared to the control film. Additionally, there is also a possible film thickness differences due to the difference in viscosity of the blends.

The PL spectra (same data presented in Figure 5.10 to 5.12) can also be plotted as shown in Figure 5.13, which shows the PL from the films with the same composition prepared at different spin rates. Figure 5.13 demonstrates a decreasing trend in fluorescence intensities by increasing the spin rate.

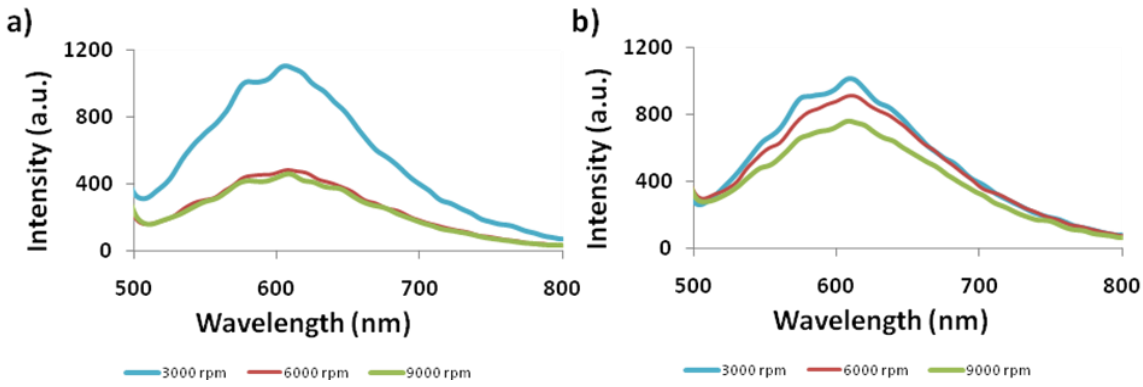

Figure 5.13. PL spectra of (a) 30/70 and (b) 50/50 PS-CdS/PMMA-Ag blend films spin coated at different spin rates.

This can be attributed to the film thickness which is decreasing as the spin rate is increasing as the result of higher centrifugal forces. Therefore, the film thickness differences are affecting the PL intensities and should be taken into account when comparing the PL spectra of the films.

In order to compare the relative intensities of PL spectra from films of different thicknesses, two different methods were used to quantify the film thicknesses. First, film thicknesses were measured by making a scratch on the film down to the substrate and then scanning over the scratch by AFM to determine the depth of the scratch, which is the absolute thickness of the film. Second, the relative thicknesses were determined from the ratios of SP absorption peaks (Figure 5.14 a and b). The second method is based on the Beer-Lambert law,[70] which describes the absorption as equation 5.2:

$$A = \varepsilon . C . l \qquad (5.2)$$

where ε is the extinction coefficient, C is the concentration and l is the path length. For blend films with the same concentration and composition, C and ε are similar; therefore A is proportional to l which is the film thickness.

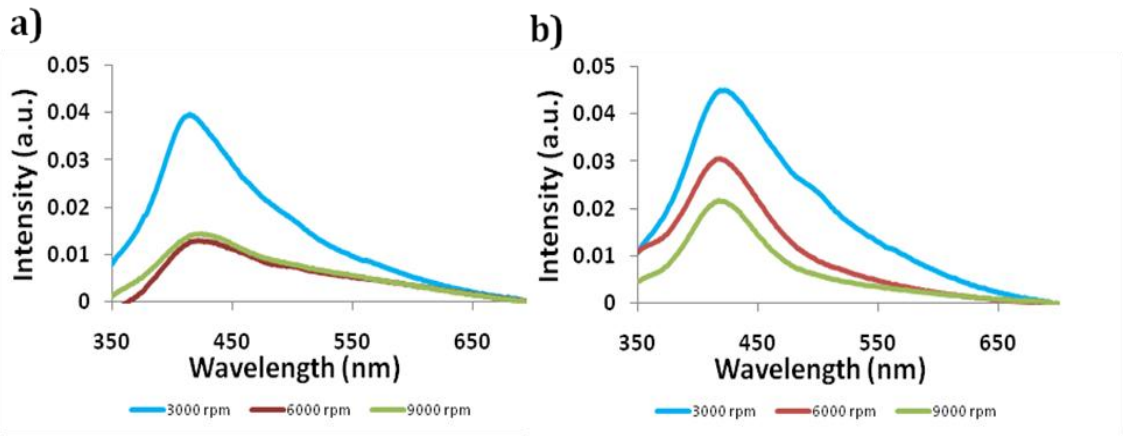

Figure 5.14. Absorption spectra of (a) 30/70 and (b) 50/50 PS-CdS/PMMA-Ag blend films at different spin rates.

Both methods result in comparable relative film thickness values, as listed in Table 5.1; however, it was not possible to determine relative thicknesses for PS-CdS control films using the second method because their absorption spectra did not contain the SP band; therefore, we chose to use the thickness values, determined from the scratch experiment, to correct the PL spectra of those films.

Table 5.1. Relative film thicknesses determined from the values determined by the scratch experiment and the ratios of the absorption intensities.

Blend	spin rate ratio of compared films	Thickness ratio from SP absorption intensities*	Thickness ratio from AFM
30/70	3000/6000	*2.75*	*2.13*
	3000/9000	*3.07*	*2.43*
50/50	3000/6000	*1.47*	*2.11*
	3000/9000	*2.07*	*1.90*

***** Figure 5.14 a and b

Figure 5.13 a and b show PL from 30/70 and 50/50 PS-CdS/PMMA-Ag blend series before any corrections, respectively. For both series, the PL intensity decreases by increasing the spinning rate. However, as pointed out earlier, this trend might be due to the thickness differences between the films; therefore, the effect of NPs interactions on PL cannot be assessed and the thickness differences have to be corrected. To do the corrections, the ratios determined above by the direct method, listed in Table 5.1, were used. The thickness-corrected PL spectra are illustrated in Figure 5.15.

Figure 5.15 reveals an opposite trend in PL intensities: after corrections, PL is increasing by increasing the spin rate. the Plotting the data as in Figure 5.15, makes the comparison between the intensities easier because all the three films that are plotted together have similar amounts of CdS QDs. The difference between their thicknesses is also corrected; thus, the only variation between them is in the extent of interaction

between NPs which is causing the observed enhancement for high spin rates in both 50/50 and 30/70 blend films. PL of 9000 and 6000 rpm 50/50 spin-coated blend films are 1.6 and 1.3 times more intense than that of the 3000 rpm film, respectively. For 30/70 blends the intensity ratios (ratio between maximum intensities) are 1.3 and 1.2, respectively. The enhancement is slightly larger for 50/50 than for 30/70 blend films possibly due to the nanoscale structure of the blends, which we could not resolve because of imaging limitations which will be discussed in Chapter 6.

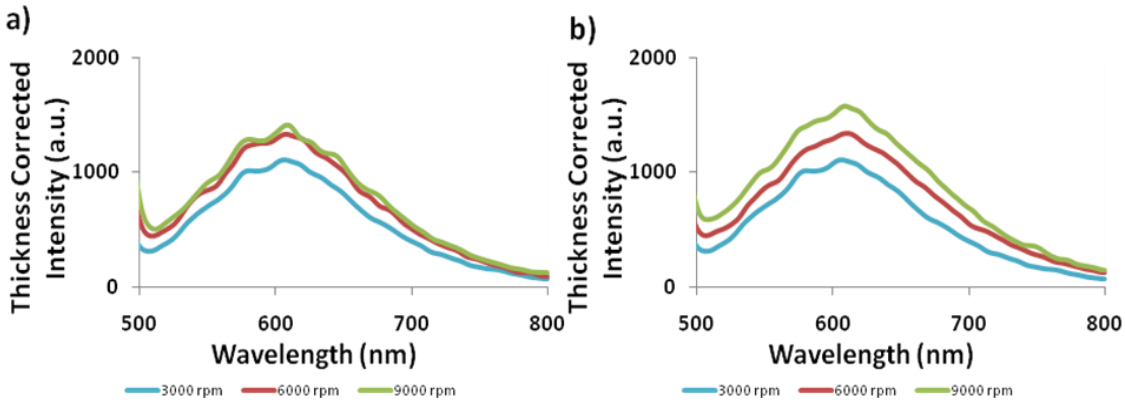

Figure 5.15. Thickness-corrected PL spectra of (a) 30/70 and (b) 50/50 PS-CdS/PMMA-Ag blend films spin coated at different spin rates.

In order to demonstrate the effect of the Ag NPs on the PL of QDs and to quantify the enhancement factors PL spectra of the two compositions should be plotted together with the spectrum of the PS-CdS control film in order to compare films containing and not-containing Ag NPs. An additional correction can be applied here for the difference between the relative amounts of QDs in the films. Relative number concentration of QDs per unit volume in the blends were obtained as shown in equations 5.3 and 5.4 for the

50/50 and the 30/70 blends using densities[74] of PS = 1.05 g/cm^3 and PMMA = 1.20 g/cm^3, and the composition of the blends.

$$X_{CdS} = (30 / 1.05) / ((30 / 1.05) + (70 / 1.20)) \quad (5.3)$$

$$X_{CdS} = (50 / 1.05) / ((50 / 1.05) + (50 / 1.20)) \quad (5.4)$$

The equations above give X_{CdS} = 0.33 and 0.53 for the 30/70 and the 50/50 blends, respectively; this fraction is by definition 1 for PS-CdS control films.

Before applying the corrections, the strongest PL was observed for the control film, which contains the largest amount of photoluminescent QDs (Figure 5.10-5.12) and the intensity is decreasing as the mole fraction of QDs is decreasing. After the corrections (for difference in thicknesses and QDs contents), the opposite trend was observed: the corrected PL of the blend films appeared more intense than that of the control film; PL spectra illustrated in Figure 5.16 a-c for 3000, 6000 and 9000 rpm films, respectively. This confirms the enhancement in PL of QDs in vicinity of Ag NPs .

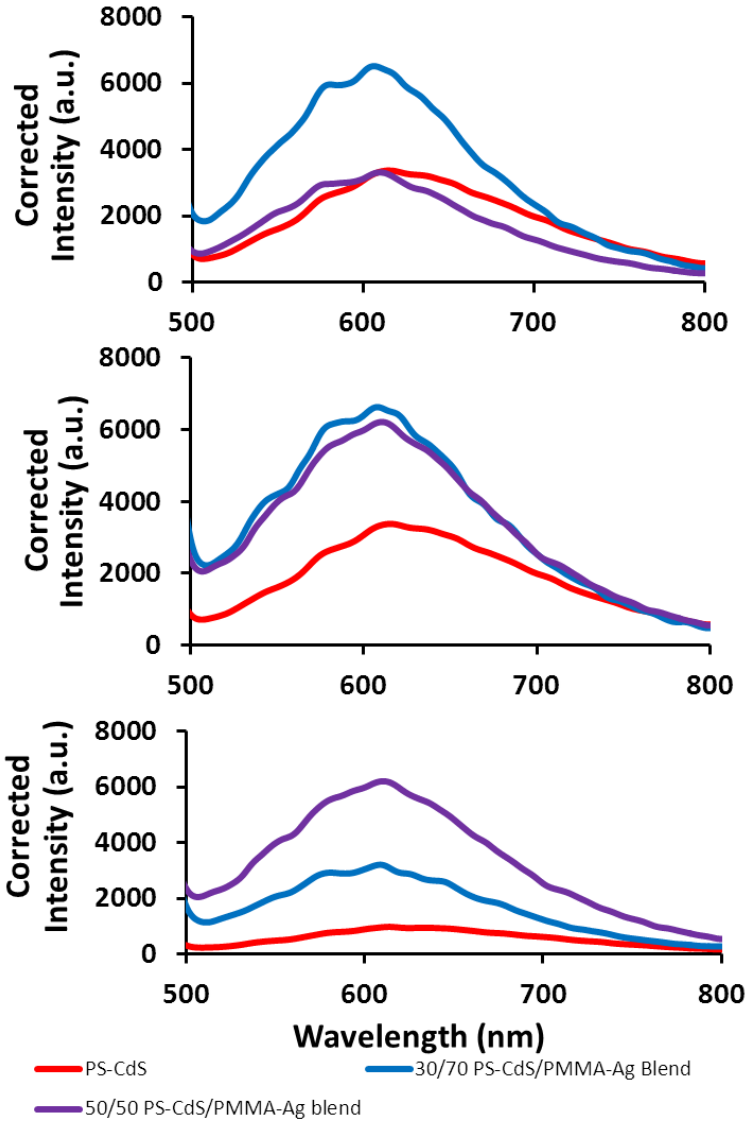

Figure 5.16. Emission spectra double corrected (for the PS-CdS content and the film thickness difference) spin coated at (a) 3000 (b) 6000 and (c) 9000 rpm.

Table 5.2. Enhancement Factors

Blend Films		Enhancement Factor
3000 rpm	50/50 PS-CdS/PMMA-Ag	0.98
	30/70 PS-CdS/PMMA-Ag	1.92
6000 rpm	50/50 PS-CdS/PMMA-Ag	2.10
	30/70 PS-CdS/PMMA-Ag	2.25
9000 rpm	50/50 PS-CdS/PMMA-Ag	2.13
	30/70 PS-CdS/PMMA-Ag	3.28

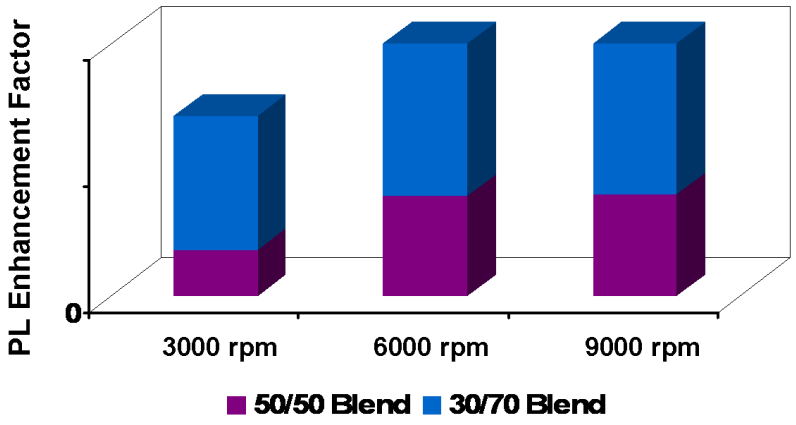

Figure 5.17. Enhancement factors in PL of blends respect to the control films.

To determine the net enhancement effect the enhancement factors were calculated from the ratio of the fluorescence intensities (at the maxima) of the blend to that of the respective PS-CdS control film. For the 3000 rpm series, enhancement factors are 0.98 and 1.92 for 50/50 and 30/70 blends, respectively. For 6000 rpm films these values are

2.10 and 2.25, and finally for 9000 rpm blends they increase to 2.13 and 3.28. Table 5.2 and Figure 5.17 display the enhancement factors; for all three series the enhancement is stronger for the 30/70 blend, this can be attributed to higher Ag NPs content. It is also observed that the enhancement effect is increasing for higher spin rates.

It has been shown[66-69] that in the spin coated films the characteristic length of a spinodal pattern (d), that is determined from the extent of coarsening during the spinodal decomposition (described in section 1.2.2), changes with the solution concentration (c_p) and the spinning rate (ω) (more details provided in section 1.6.1). The empirical scaling law describing this is:

$$d \sim c_p/\omega^{1/2} \qquad (5.1)$$

This law demonstrates the inverse proportionality between d and ω; therefore, it implies that at high spin rates domains are small. Expected phase-separation of the NPs based upon the different polymers at their surfaces give rise to the formation of Ag-rich and QDs-rich domains that are in contact with each other along the domain boundaries. When d is small, there is larger area of contact (larger interfacial area) between NPs domains to interact with each other, and they are also in closer proximity to each other. It has been shown[12,20,41,42] that interactions between metal and QDs occur over a short distance (10-20 nm) because the electromagnetic SP field of metal NPs is highly localized at the NP surface and decays rapidly away from the surface; therefore, when d is small there are more particles within the operative length scale of interaction from each other (within the electromagnetic field of the SP). This consequently increases the coupling between the SP of Ag NPs and PL of QDs and causes a stronger enhancement effect.

There are two possible mechanisms for the PL enhancement in these systems: enhancement of the incident electromagnetic (excitation) field due to plasmon excitation, and enhancement of the rate of the radiative emission due to coupling between the SP and photon emitted by a radiate decay. To realize the mechanism operative here we continue with the optical characterization of the blend films.

The excitation spectra of the PS-CdS/PMMA-Ag NPs blend films were also obtained for the emission wavelength corresponding to the emission peak maximum for each sample (~ 620 nm) and scanning the range of excitation wavelengths. These spectra are presented in Fig. 5.18 together with the excitation spectra of PS-CdS control films.

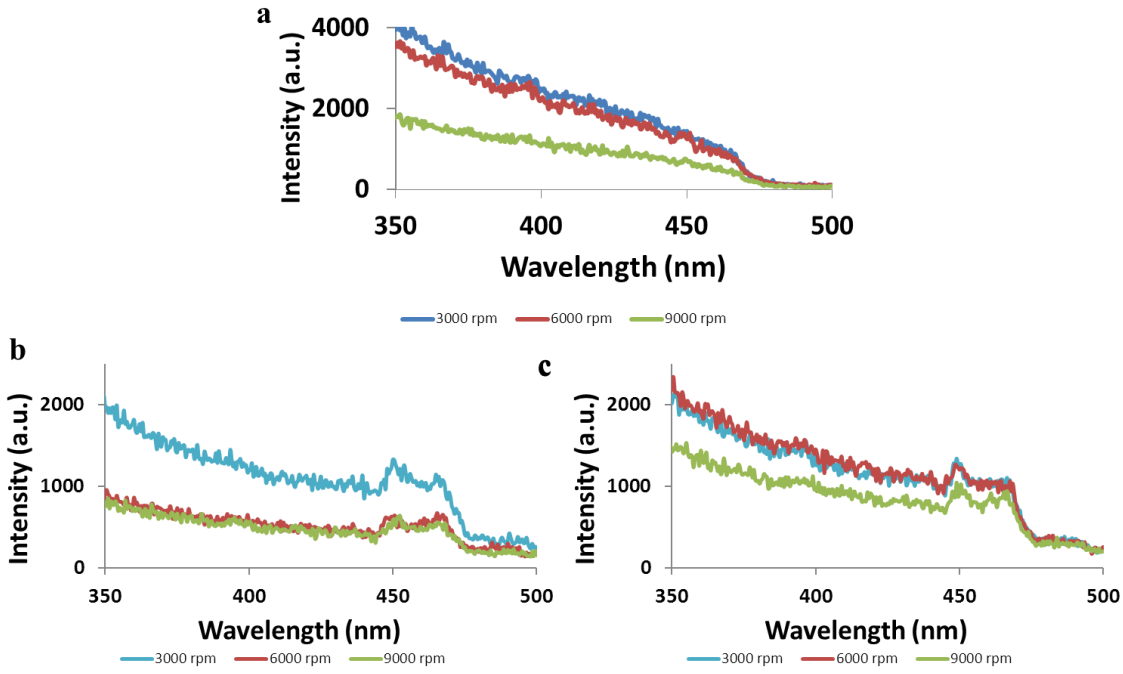

Figure 5.18. Excitation spectra collected at λ_{em} = 620 nm for (a) PS-CdS control films, (b) 30/70 and (c) 50/50 blend films prepared at 3000, 6000 and 9000 rpm spin rates.

The shoulder that is observed for all cases at ~ 470 nm corresponds to the absorption of CdS QDs, as it resembles its absorption spectrum (Figure 5.8). The contribution of the SP absorption of the Ag NPs in the observed excitation spectra is the presence of the peak at ~ 450 nm, which was observed for all cases and is the result of coupling between the Ag NPs with QDs. This suggests that both mechanisms of enhanced excitation and emission are operative here. Increased intensity observed at around 450 nm, suggest the first mechanism because if the SPs only absorb the excitation light then the excitation spectrum should show a decrease whereas we are observing an increase due to the enhancement in the excitation field via coupling between the dipole mode of SP and the excitation field. The latter mechanism was suggested by the presence of ~ 450nm peak, which overlaps with the CdS peak demonstrating the coupling between the two NPs; this results in transfer of the energy from the QDs (in form of emitted photon) into dipole mode of SP.[13-14]

To better understand the operative mechanism, fluorescence decay profiles at λ_{em}= 620 nm were measured exciting the samples at λ_{ex}= 420 nm (~ maximum of SP absorption, Figure 5.8). Due to the apparent increased excitation of the Ag-containing films in the ~ 450 region (Figure 5.18), decay profiles were also collected exciting at λ_{ex}= 450 nm. An intermediate excitation wavelength of λ_{ex}= 435 nm was also considered. Decay profiles were also collected for the control PS-CdS films for comparison (sample profiles provided in Figure 5.19a and b for 30/70 and 50/50 blends, respectively). In all cases the best fit ($\chi^2 \leq 1.2$) was obtained with a double-exponential (equation 5.5) model:[71]

$$I(t) = \alpha_1 \exp(-t/\tau_1) + \alpha_2 \exp(-t/\tau_2) \quad (5.5)$$

$$\tau = (\alpha_1 \tau_1^2 + \alpha_2 \tau_2^2)/(\alpha_1 \tau_1 + \alpha_2 \tau_2) \quad (5.6)$$

For a broad distribution of states the lifetimes of actual states can be determined from averaging individual exponential lifetimes ($\tau_1, \tau_2,...$); therefore, the intensity-average lifetime (equation 5.6) was calculated for each decay profile and then was averaged between three runs for each film. The values for the blend films and the PS-CdS control films are listed in Table 5.2.

Table 5.2. Average lifetimes values

30/70 blend films	**Average lifetimes (μs)**		
	λ_{ex} = 420 nm	**λ_{ex} = 435 nm**	**λ_{ex} = 450 nm**
3000 rpm	*1.77 ± 0.09*	*1.90 ± 0.04*	*1.63 ± 0.09*
6000 rpm	*1.54 ± 0.04*	*1.76 ± 0.10*	*1.17 ± 0.04*
9000 rpm	*1.48 ± 0.05*	*1.10 ± 0.04*	*1.08 ± 0.06*
50/50 blend films	**Average lifetimes (μs)**		
	λ_{ex} = 420 nm	**λ_{ex} = 435 nm**	**λ_{ex} = 450 nm**
3000 rpm	*1.75 ± 0.07*	*2.38 ± 0.11*	*1.46 ± 0.09*
6000 rpm	*1.62 ± 0.05*	*1.88 ± 0.07*	*1.42 ± 0.05*
9000 rpm	*1.65 ± 0.11*	*1.15 ± 0.09*	*1.11 ± 0.10*
PS-CdS control	**Average lifetimes (μs)**		
	λ_{ex} = 420 nm	**λ_{ex} = 435 nm**	**λ_{ex} = 450 nm**

films			
3000 rpm	*1.20 ± 0.10*	*1.62 ± 0.08*	*1.47 ± 0.10*
6000 rpm	*1.23 ± 0.09*	*1.54 ± 0.10*	*1.55 ± 0.07*
9000 rpm	*1.07 ± 0.01*	*1.40 ± 0.07*	*1.48 ± 0.01*

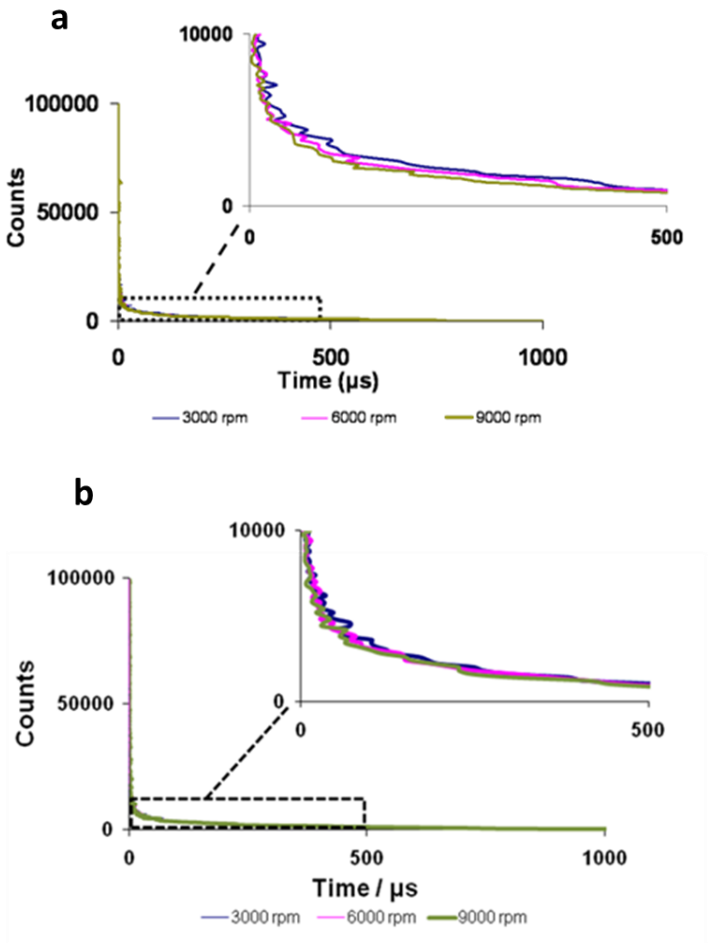

Figure 5.19. Sample decay profiles provided for (a) 30/70 and (b) 50/50 blends at different spin rates.

It was observed that lifetimes are generally longer for blend films than for the control PS-CdS films. Interestingly, the values demonstrate a decreasing trend by

increasing the spinning rate, as displayed in table 5.2, and shorter lifetimes were observed for the films with stronger PL enhancement. This is not the classical observation that the systems with enhanced PL have longer lifetime; however, this has been previously observed for some other systems of interacting luminescent and metallic nanostructures.[18,23,72,73] Shortening of lifetime can be attributed to inverse proportionality between the lifetime and the decay rate, which is composed of radiative and non-radiative recombination rates; increase in the radiative rate as the result of field enhancement decreases the lifetime. The trend in lifetimes as a function of excitation wavelength is illustrated in Figure 5.20a-c for films prepared at 3000, 6000 and 9000 rpm, respectively. Figure 5.21c, reveals a different trend in lifetimes of blend films prepared at 9000 rpm comapre with 3000 and 6000 rpm. For the 9000 rpm blend films, lifetime is decreasing by increasing the excitation wavelength, whereas for 3000 and 6000 rpm lifetime is first increases then decreases. For all three spin rates (Figure 5.20a-c) lifetime for the PS-CdS control films has a similar trend: it increases by increasing the excitation wavelength; the change in the lifetime can be attributed to the size distribution of QDs resulting in different lifetimes at different excitation wavelengths (red traces in Figure 5.20a-c).

Short life time, which accompanies the PL enhancement, can describe the blue shift that we observed earlier in the PL of PS-CdS/PMMA-Ag blend films relative to the PS-CdS control (Figure 5.10-5.12); short lifetimes do not allow excitons to diffuse to regions with lower excited states before they undergo radiative decay (they do not have enough time for the diffusion); therefore, they emit at a higher energy (regions with larger bandgap). A similar phenomenon of blue shifted- enhanced PL emission has been observed by another group[18] for a system of CdTe NWs in vicinity of gold NPs.

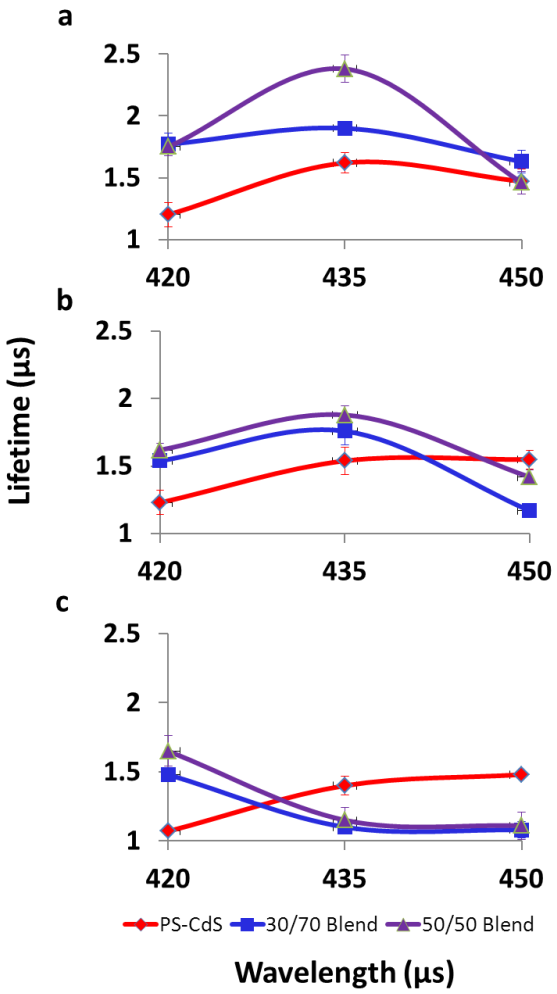

Figure 5.20. Life times measured at three excitation wavelengths of 420, 435 and 450 nm for blend films and PS-CdS control films prepared at (a) 3000, (b) 6000, and (c) 9000 rpm.

5.4. Conclusion

A comprehensive study of the optical properties of PS-CdS/PMMA-Ag NPs spin-coated blend films was presented in this work. It was demonstrated that the characteristic length of phase-separation *(d)* can be tuned by adjusting the spinning rate in order to increase the extent of interactions between "Ag-rich" and "CdS-rich" domains by increasing the interfacial area between the domains, and by decreasing the distance

between them which increases the number of particles that are within the operative distance of interaction from each other. Enhancement in the PL intensity of PS-CdS QDs in vicinity of Ag NPs was observed and enhancement factors were calculated after correcting the PL spectra for the differences between the thickness and relative QD content of the films; an enhancement factor as high as 36 times was calculated.

Excitation spectra of the films suggested two mechanisms for the PL enhancement: enhancement of the excitation field as the result of coupling between the SP and the excitation field, and the enhancement of the radiative rate by coupling between the emitted photon from QDs and SP of Ag NPs. Shortening of lifetime was also observed for PL-enhanced films, which is attributed to the increase in the radiative rate as a result of field enhancement.

5.5. References

(1) Schuck, P. J.; Fromm, D. P.; Sundaramurthy, A.; Kino, G. S.; Moerner, W. E., *Phys. Rev. Lett.***2005,** 94, 017402.

(2) Kuhn, S.; Akanson U. H.; Rogobete, L.; Sandoghdar, V., *Phys. Rev. Lett.***2006**, 97, 017402.

(3) Carminati, R.; Greffet, J.J.; Henkel, C.; Vigoureux, J.M., *Opt. Commun.***2006**, 261, 368.

(4) Rogobete, L.; Schniepp, H.; Sandoghdar, V.; Henkel, C., *Opt. Lett.***2003**, 28, 1736.

(5) Girard, C.; Martin, O. J. F.; Dereux, A., *Phys. Rev. Lett.***1995**, 75, 3098.

(6) Novotny, L., *Appl. Phys. Lett.***1996**, 69, 3806.

(7) Thomas, M.; Greffet, J.J.; Carminati, R.; Arias-Gonzalez, J. R., *Appl.Phys. Lett.***2004**, 85, 3863.

(8) Baffou, G.; Girard, C.; Dujardin, E.; des Francs, G. C.; Martin, O. J. F., *Phys. Rev. B* **2008**, 77, 121101(R).

(9) des Francs, G. C.; Girard, C.; Laroche, T.; Leveque, G.; Martin, O. J. F., *J. Chem. Phys.***2007**, 127, 034701.

(10) Yeh, D. M.; Huang, C. F.; Lu, Y. C.; Yang, C. C., *Appl. Phys. Lett.***2008**, 92, 091112.

(11) Tang, J.; Birkedal, H.; McFarland, E. W.; Stucky, G. D., *Chem. Commun.* **2003**, 2278-2279.

(12) Kulakovich, O.; Strekal, N.; Yaroshevich, A.; Maskevich, S.; Gaponenko, S.; Nabiev, I.; Woggon, U.; Artemyev, M., *Nano Lett.* **2002**, *2*, 1449.

(13) Neogi, A.; Lee, C. W.; Everitt, H. O.; Kuroda, T.; Tackeuchi, A.; Yablonovitch, E. *Phys. Rev. B* **2002**, *66*, 153305.

(14) Neogi, A.; Morkoc, H., *Nanotechnology* **2004**, *15*, 1252.

(15) Gontijo, I.; Boroditsky, M.; Yablonovitch, E.; Keller, S.; Mishra, U. K.; DenBaars, S. P., *Phys. Rev. B* **1999**, *60*, 11564.

(16) Kamat, P. V.; Shanghavi, B. *J., Phys. Chem. B* **1997**, *101*, 7675.

(17) Gryczynski, I.; Malicka, J.; Jiang, W.; Fischer, H.; Chan, W. C. W.; Gryczynski, Z.; Grudzinski, W.; Lakowicz, J. R. *J., Phys. Chem. B* **2005**, *109*, 1088.

(18) Lee, J.; Govorov, A. O.; Dulka, J.; Kotov, N. A., *Nano Lett.* **2004**, *4*, 2323.

(19) Okamoto, K.; Niki, I.; Shvartser, A.; Narukawa, Y.; Mukai, T.; Scherer, A., *Nature. Mater.* **2004**, *3*, 601.

(20) Shimizu, K. T.; Woo, W. K.; Fisher, B. R.; Eisler, H. J.; Bawendi, M. G. *Phys. Re*V. *Lett*. **2002**, *89*, 117404.

(21) Gueroui, Z.; Libchaber, A. *Phys. Re*V. *Lett.* **2004**, *93*, 166104.

(22) Hecker, N. E.; Hopfel, R. A.; Sawaki, N.; Maier, T.; Strasser, G., *Appl. Phys. Lett.* **1999**, *75*, 1577.

(23) Biteen, J. S.; Pacifici, D.; Lewis, N. S.; Atwater, H. A., *Nano Lett.* **2005**, *5*, 1768.

(24) Nien, S. Y.; Chiu, N. F.; Ho, Y. H.; Lee, J. H.; Lin, C. W.; Wu, K. C.; Lee, C. K.; Lin, J. R.; Wei, M. K.; Chiu, T. L., *Appl. Phys. Lett.***2009**, 94, 103304.

(25) Khurgin, J. B.; Sun, G.; Soref, R. A., *Appl. Phys. Lett.***2008**, 93, 021120.

(26) Sun, G.; Khurgin, J. B.; Soref, R. A., *J. Opt. Soc. Amer. B* **2008**, 25, 1748.

(27) Khurgin, J. B.; Sun, G.; Soref, R. A., *Appl. Phys. Lett.***2009**, 94, 071103.

(28) Sun, G.; Khurgin, J. B.; Soref, R.A., *Appl. Phys. Lett.***2009**, vol. 94, 101103.

(29) Sun, G.; Khurgin, J. B. Yang, C. C., *Appl. Phys. Lett.***2009**, vol. 95, 171103.

(30) Hutter, E.; Fendler, J. H., *Adv. Mater*. **2004**, 16, 1685.

(31) Haus, J. W.; Kalyaniwalla, N.; Inguva, R.; BowdenC. M., *J. appl. Phys.***1989**, 65, 1420.

(32) Novotny, L.; Bian, R. X.; Xie, X. S., Phys. Rev. lett. **1997**, 79, 645.

(33) Khurgin, J. B.; Sun, G.; Soref, R. F., *J. Opt. Soc. Am. B* **1968**, 24, 8.

(34) Krames, M. R.; Shchekin, O. B.; Mueller-Mach, R.; Mueller, G. O.; Zhou, L.; Harbers, G.; Craford, M. G., *J. Disp. Technol*. **2007**, 3, 160.

(35) Huang1, Z; Wang, J.; Liu, Z.; Xu, K.; Yang, H.; Cao, B.; Han, Q.; Zhang, G.; Wang, C., *Appl. Phys. Exp***2010,** 3, 072001.

(36) Nie, S.; Emory, S. R., *Science***1997**, 21, 275, 1102.

(37) Kneipp, K.; Wang, Y.; Kneipp, H.; Perelman, L. T.; Itzkan, I.; Dasari, R. R.; Feld, M. S., *Phys. Rev. Lett.***1997**, 78, 1667.

(38) Moskovitz, M., *Rev. Mod. Phys.***1985**, 57, 783.

(39) Moskovitz, M.; Tay, L. L.; Yang, J.; Haslett, T., *Top. Appl. Phys.***2002**, 82, 215.

(40) Michaels, A. M.; Nirmal, M.; Brus, L. E., *J. Amer. Chem. Soc.***1999**, 121, 9932.

(41) Pompa, P. P.; Martiradonna, L.; Della Torre, A.; Della Sala, F.; Manna, L.; ; De Vittorio, M.; Calabi, F.; Cingolani, R.; Rinaldi, R., *Nature Nanotechnology* **2006,** 1, 126.

(42) Jin, Y.; Gao, X., *Nature Nanotechnology***2009**, 4, 571.

(43) Song, J. H.; Atay, T.; Shi, S. F.; Urabe, H.; Nurmikko, A. V., *NanoLett.* **2005**, *5*, 1557.

(44) Chen, C. J.; Osgood, R. M., *Phys. Rev. Lett.***1983**, 50, 1705.

(45) Link, S.; El-Sayed, M.A., *Int. Rev. Phys. Chem.***2000**, 19, 409.

(46) Moores, A.; Goettmann, F., *New Journal of Chemistry* **2006,** 30, (8), 1121.

(47) Liz-Marza n, L. M.; Giersig, M.; Mulvaney, P., *Langmuir* **1996,** 12, (18), 4329.

(48) Maye, M. M.; Lim, I. I. S.; Luo, J.; Rab, Z.; Rabinovich, D.; Liu, T.; Zhong, C.-J., *JACS* **2005,** 127, (5), 1519.

(49) Tiggesbäumker, J.; Köller, L.; Lutz, H. O.; Meiwes-Broer, K. H., *Chemical Physics Letters* **1992,** 190, (1-2), 42.

(50) Link, S.; El-Sayed, M. A., *The Journal of Physical Chemistry B* **1999,** 103, (21), 4212.

(51) Chapman, R.; Mulvaney, P., *Chemical Physics Letters* **2001,** 349, (5-6), 358.

(52) Lica, G. C.; Zelakiewicz, B. S.; Constantinescu, M.; Tong, *The Journal of Physical Chemistry B* **2004,** 108, (52), 19896.

(53) Li, X.; Zhang, J.; Xu, W.; Jia, H.; Wang, X.; Yang, B.; Zhao, B.; Li, B.; Ozaki, Y., *Langmuir* **2003,** 19, (10), 4285.

(54) Jia, H.; Zeng, J.; Song, W.; An, J.; Zhao, B., *Thin Solid Films* **2006,** 496, (2), 281.

(55) Xie, Y.; Ye, R.; Liu, H., *Colloids and Surfaces A: Physicochemical and Engineering Aspects* **2006,** 279, (1-3), 175.

(56) Maillard, M.; Giorgio, S.; Pileni, M. P., *Advanced Materials* **2002,** 14, (15), 1084.

(57) Lei, Z.; Zhang, L.; Wei, X., *Journal of Colloid and Interface Science* **2008,** 324, (1-2), 216.

(58) Chaudhari, V. R.; Haram, S. K.; Kulshreshtha, S. K.; Bellare, J. R.; Hassan, P. A., *Colloids and Surfaces A: Physicochemical and Engineering Aspects* **2007,** 301, (1-3), 475.

(59) Zhu, J.-J.; Liao, X.-H.; Zhao, X.-N.; Chen, H.-Y., *Materials Letters* **2001,** 49, (2), 91.

(60) Liu, S.; Huang, W.; Chen, S.; Avivi, S.; Gedanken, A., *Journal of Non-Crystalline Solids* **2001,** 283, (1-3), 231.

(61) Cheyne, R. B.; Moffitt, M. G. *Langmuir* **2005**, *21*, 10297.

(62) Cheyne, R. B.; Moffitt, M. G. *Macromolecules* **2007**, *40*, 2046.

(63) Mayer, A. B. R., Polym. Adv. Technol. 2001, 12, 96.

(64) Zhang, F.; Guan, N.; Li, Y.; Zhang, X.; Chen, J.; Zeng, H., *Langmuir* **2003,** 19, (20), 8230.

(65) Hu, X.; Hu, C.; Qu, J., *Materials Research Bulletin* **2008,** 43, (11), 2986.

(66) P. Cyganik, A. B., U. Steiner, J. Rysz, A. Bernasik,; S. Walheim, Z. P. a. J. R., *Europhysics Letters* **2003,** 62.

(67) Raczkowska, J.; Cyganik, P.; Budkowski, A.; Bernasik, A.; Rysz, J.; Raptis, I.; Czuba, P.; Kowalski, K., *Macromolecules* **2005,** 38, (20), 8486.

(68) Jaczewska, J.; Budkowski, A.; Bernasik, A.; Raptis, I.; Moons, E.; Goustouridis, D.; Haberko, J.; Rysz, J., *Soft Matter*.**2009**, **5**, 234.

(69) Lawrence, C. J., *Phys. Fluids***1988,** 31, 2786.

(70) Atkins, P. W.; De Paula, J. *The Elements of Physical Chemistry*, Oxford University Press, **2005**, pg. 230.

(71) Wang, C.-W.; Moffitt, M. G. *Langmuir* **2004,** *20*, 11784.

(72) Jung, D.-R.; Kim, J.; Nam, S.; Nahm, C.; Choi, H. *Appl. Phys. Lett*. **2011**, 99, 041906.

(73) Ito, Y.; Matsuda, K.; Kanemitsu, Y. *Phys. Rev. B***2007,** 75, 033309.

(74) Brandrup, J.; Immergut, E. H.; Grulke, E. A.; *Polymer Handbook* **1999**, Wiley.

Chapter 6: SIMULTANEOUSLY ADDRESSING TWO DIFFERENT NANOPARTICLE TYPES TO SPECIFIC REGIONS OF A CHEMICALLY PATTERNED SUBSTRATE IN A SINGLE SPIN-COATING STEP

6.1. Introduction

Organizing nanoparticles (NPs) into micro- and nanoscale structures on surfaces has various applications in medical diagnosis,[1,2] sensing,[3,4] nano- and optoelectronic devices,[5,6] light emitting diodes,[7] and photovoltaics.[8] A variety of techniques have been reported on this matter including scanning probe-related patterning techniques,[8-14] the use of optical tweezers to position NPs on surfaces,[15,16] micro contact printing,[7,17-21], layer by layer assembly technique[22,23] and various lithographic approaches.[24-29]

The ability to fabricate patterned structures of multiple NP types with different functionalities (such as optical properties) opens up many new routes to design micro and nanodevices. Hua et.al.[30] employed a layer-by-layer assembly approach combined with lithography to obtain a pattern of two types of NPs, where each one is directed to the desired location on the surface to form striped pattern of NPs; although this technique results in high precision patterning, it is a labor-intensive and a multistep process. Jamshidi et.al.[31] developed an elaborate technique, called nanopen to pattern multiple NPs using optoelectronic tweezers to collect and immobilize them into patterned structures via electrokinetic forces. Vossmeyer et.al.[32] reported a selective deposition technique for patterning multiple NP types through selective deposition of each NP type onto chemically distinct interaction sites of a substrate, which is prepared by lithographic masking. However, there is still the need for a fast, simple and efficient approach to pattern structurally- and compositionally-complex NP film structures.

As demonstrated in previous chapters of this thesis, microcontact printing (μCP)[33-36] is a popular technique for patterning colloids, polymers and NPs; the objective of this chapter is to develop a versatile technique based on μCP for simultaneous

patterning of multiple NP types in discrete surface locations using a facile single step spin-coating process. Our method is based on directed patterning of PS/PMMA blend films via spin-coating onto pre-patterned OTS glass, as developed in Chapter 4.[37-49] In that chapter, this methodology was extended to patterning of CdS QDs, by replacing PS homopolymer wihtin the spin-coated blend solution with PS-coated (PS-stabilized QDs); the QDs possessed identical surface energy to the PS homopolymer and therefore, localized selectively above the OTS lines. In this chapter, this technology is further extended to include the simultaneous patterning of PS-coated CdS QDs, which should be directed to the lower-surface energy OTS lines of the substrate and PMMA-coated Ag NPs, which should be directed to the higher-surface energy regions between the OTS lines. The specific interest in polymer-supported patterns of Ag NPs and CdS QDs is to provide a suitable proof-of-concept system for simultaneous multi-NP patterning. However, this system also has some interesting optical behaviour as a result of QD-surface plasmon interactions, as discussed in Chapter 5.

6.2. Experimental

6.2.1. Materials

The polystyrene-coated CdS QDs (PS-CdS) used in this work is similar to the sample used in chapter 5 (refer to 5.2.3.1). In summary, QDs were synthesized via templated growth of CdS in the cores of reverse micelles consisting of polystyrene-*block*-poly (acrylic acid) copolymer PS(226)-*b*-PAA(22), where numbers in brackets indicate number-average degrees of polymerization for each block. Each PS-CdS has a core of a

~ 5 nm CdS nanoparticle (determined from UV-vis and using Henglein's empirical relationship), with a poly (cadmium acrylate) (PACd) layer at the CdS surface, covalently-attached to a solubilized external PS brush layer.

Poly(methyl methacrylaye)-coated silver NPs (PMMA-Ag), prepared as described in chapter 5 (refer to 5.2.1) by templated growth of Ag in the micelles cores of poly(methyl methacrylate)-*block*-poly(acrylic acid) copolymer PMMA(170)-*b*-PAA(28), purchased from Polymer Source Inc. In summary, the size of PMMA-Ag NPs is ~ 15 nm in average (determined from TEM imaging) with a PAA layer at the surface, covalently-attached to the PMMA corona. The hydrodynamic radius (R_h) determined from DLS is 35.4 nm and the aggregation number of 44.9.

Three different PS homopolymer samples with molecular weights (M_w) of 131 000 g/mol (previously synthesized in our group by anionic polymerization), 33 000 g/mol (Polymer Source Ltd.) and 6 000 g/mol (Polymer Source Ltd) were used for mixing with NPs blend; they are denoted in the text as PS 131k, 33k and 6k, respectively. PMMA homopolymer with M_w=120 000 g/mol (denoted as PMMA 120k, Aldrich) was also used.

6.2.2. Preparation of Polydimethylsiloxane (PDMS) Stamps for Microcontact Printing

Masters with microscale periodic stripe patterns were obtained using commercial compact discs (CDs). Top layers on a CD were removed revealing the underlying polycarbonate layer with the desired topographic features. The polycarbonate was used as the master and prepolymer and curing agent for polydimethylsiloxane (PDMS) (Dow Corning: Sylgard 184 DC-184 A and DC 184-B) were mixed in a 10:1 (v:v) ratio, then

poured over a polycarbonate master, followed by 4 h curing at 80˚C. The topology of resulting PDMS stamp consisted of periodic raised stripes corresponding to the troughs of the polycarbonate masters. The PDMS stamps were sonicated in a 1 : 2 (v : v) solution of ethanol/deionized water immediately prior to use. Detailed procedure for PDMS preparation is provided in chapter 2 (section 2.2.1).

6.2.3. Microcontact Printing Glass Substrates with Octadecyltrichlorosilane (OTS)

Glass cover slips (VWR scientific, 18 x 18 mm) were cleaned by sonication for 10 min in 95% ethanol, followed by 10 min sonication in deionized water. To introduce a layer of hydroxyl groups on the glass surface, the cover slips were submerged in a piranha solution at 70˚C for 30 min. The resulting hydrophilic glass substrates were cleaned from excess piranha using the same procedure described in chapter3 (refer to 3.2.3) followed by drying with a UHP N_2 (g) stream prior to immediate use for microcontact printing (μCP). The ink for μCP was prepared by dissolving octadecytrichlorosilane (OTS, Aldrich) in anhydrous hexane (≥99%, Aldrich) under UHP N_2 (g) to obtain a 5 mM solution. For inking the PDMS stamp, a non-patterned smooth block of PDMS was used as an ink pad similar to chapter 4 (refer to 4.2.3 for more details). One drop of the ink solution was spin-coated on the pad at 3000 rpm for 30 s followed by 20 s drying by a stream of UHP N_2 (g). Then a patterned PDMS was brought into contact with the inked pad for 10 s. The inked PDMS stamp was then used to transfer the OTS molecules to the surface of a hydrophilic glass cover slip by a conformal

contact for 30 s under a 200-g weight. OTS-patterned glass substrates were used immediately for spin-coating NPs blends on them.

6.2.4. PS-CdS/ PMMA-Ag Blend Solutions Preparation

Solutions of 0.5, 1.0, 2.0 and 4.0 wt% of PS-CdS and PMMA-Ag were prepared separately in spectro grade toluene (Aldrich) and stirred for 4 h then left overnight to equilibrate. The 30/70 and 50/50 (w/w) PS-CdS/ PMMA-Ag blend solutions were each prepared by gravimetrically mixing the appropriate amounts of two solutions (PS-CdS and PMMA-Ag) into a clean vial and stirring it for 4h then let it equilibrate overnight.

In order to increase the characteristic length scale of the phase-separation in NPs blend films, homopolymers were added to the blends. Solutions of 0.5, 1.0 and 2.0 wt% PS-CdS, PMMA-Ag, PS, and PMMA were prepared separately in spectro grade toluene (Aldrich) and stirred for 4 h then left overnight to equilibrate. The 30/60/10 PS-CdS/PMMA-Ag/PMMA, 20/10/70 PS-CdS/PS/PMMA-Ag, 10/20/50/20 and 20/10/60/10 PS-CdS/PS/PMMA-Ag/PMMA blend solutions (all weight fractions) were each prepared by mixing the appropriate amounts of two solutions into a clean vial and stirring it for 4h then let it equilibrate overnight.

6.2.5. Preparation of Spin-coated Films

One drop of the blend solution was spin-coated on the patterned or non-patterned glass substrate for 30 or 60 s at different spinning rates of 3000, 6000 and 9000 rpm. The drop was applied after the substrate reached a rate of 9000 rpm and it was deposited onto the centre of the spinning substrate using a microsyringe. Spin-coated film looks

uniformly clear and it was dried overnight under vacuum prior to characterization and then they were stored covered in dark.

For each condition, three copies were prepared for complete characterization. Non-patterned glass substrates were cleaned prior to spin-coating by sonication in methanol, chloroform, toluene and acetone each for 10 min.

6.2.6. Blend Film Characterization

6.2.6.1. Atmoic Force Microscopy (AFM)

AFM in contact modewas performed on a MFP-3D atomic force microscope from Asylum Research with non-conductive silicon nitride cantilevers from Veeco (model: NP-10). The cantilevers are 0.4 - 0.7 μm thick and their resonance frequency ranges from 12-75 kHz and spring constants ranging from 0.06-0.58 N/m. For each sample, at least three images at different locations on the substrate were obtained to determine the regularity of the film structure. All images presented in this paper were scanned over a 10 μm x 10 μm area at a scan rate of 0.5 Hz and they represent typical features observed for each film.

6.2.6.2. Laser Scanning Confocal Fluorescence Microscopy (LSCFM)

LSCFM measurements of patterned 1.0 wt% PS-CdS/PS/PMMA-Ag/PMMA 10/20/50/20 blend film were carried out on a Zeiss LSM 700 with diode laser. Films were

excited at λ_{ex} = 480 nm, and emitted light above 520 nm was directed to the PMT detector by a variable dichroic filter. A Zeiss Plane-Aprochromat 63x oil-immersion objective lens (NA=1.3) was used for imaging. The pinhole diameter was set to 33 µm. To prepare samples for LSCFM measurements, spin-coated blend film on a glass coverslip was taped to a glass microscope slide, such that the film was sandwiched between the slide and coverslip. Zeiss Immersionsoel 518 C oil was deposited between the objective and the coverslip in order to provide a constant-refractive index media between the objective and the glass.

6.2.6.3. Transferring the Patterned Films to TEM Grids by Removal of the Glass Substrate

Patterned films were released from the glass coverslips by selective etching of the glass using hydrofluoric acid (HF). HF (48%, EMD) was diluted to a 10% concentration using deionized water (18 MΩ/cm, Barnstead NANOpure® DIamond™). A sample was immersed in a solution of 10% HF in a plastic petri dish (Fisher-Scientific). After the glass substrate was etched away the film floated on the solution. The thin film was then quickly collected onto a 400 mesh copper TEM grid (ProSciTech, Catalogue number: GCU1C4C). To remove residual HF, the prepared samples on TEM grids were washed twice with deionized water and then dried under active vacuum in a desiccator prior to TEM analysis.

6.2.6.4. Transmission Electron Microscopy (TEM)

Bright field transmission electron microscopy analysis was conducted on a Hitachi 8000 STEM and a Tecnai G2 F20 STEM operating a 200 kV. Energy dispersive X-ray spectroscopy (EDS) experiments were carried out on the Tecnai G2 F20 STEM. Beryllium sample holders were used for this in order to avoid high X-ray background signals.

6.2.6.5. Scanning Electron Microscopy (SEM) and Energy Dispersive X-ray Spectroscopy (EDS)

SEM and EDS analysis were performed on a Hitachi S-4800 FESEM (field emission SEM) at 7 kv accelerating voltage. The instrument has a Bruker Quantax EDS system for X-ray spectroscopy. Since the patterned NPs films on glass are not conductive enough for SEM analysis, the films were first carbon-coated. To do this, samples were mounted onto SEM pin mounts (EMS, Catalogue number: 75183) and were transferred to a home-built carbon evaporator where a 2 nm-thick layer of carbon was evaporated onto the film surface. The carbon evaporation was conducted at 10^{-6} torr with 100 A of current passing through the two graphite electrodes (EMS, Catalogue number: 70200).

6.2.6.6. Focused Ion Beam (FIB) Micro-Sampling for TEM imaging

Hitachi FB-2100 focused ion beam system is utilized for FIB micro-sampling; this technique was employed to lift out a portion of the 1.0 wt% PS-CdS/PS/PMMA-Ag/PMMA 10/20/50/20 blend film for TEM imaging. The region of interest (few

micrometer in dimensions) was coated by tungsten (W), the protection layer, and then was cut from the sample by FIB milling; first the front side then the back followed by both right and left sides of the region of interest were deep trenched leaving a micro-bridge at the upper left corner. The bridge was cut off at the micro-sample completely removed from the bulk-sample (the procedure for cutting is illustrated in Figure 6.1. The micro-sample was then mounted on a FIB/TEM (STEM) compatible specimen holder using a special carrier.[52]

The procedure can be described as: first thinning the edges of the micro-sample by FIB milling to remove the portion and mount it on to an edge of the carrier. After securing the micro-sample on the carrier, it was rotated so that the surface of the micro-sample is parallel to the incident ion beam then thinning of the micro-sample is carried out from the substrate in order to obtain a plan-view TEM specimen from the surface.

The milling was performed at an accelerating voltage of 40 kV. The beam currents of 60 and 3.5 nA used in these operations.

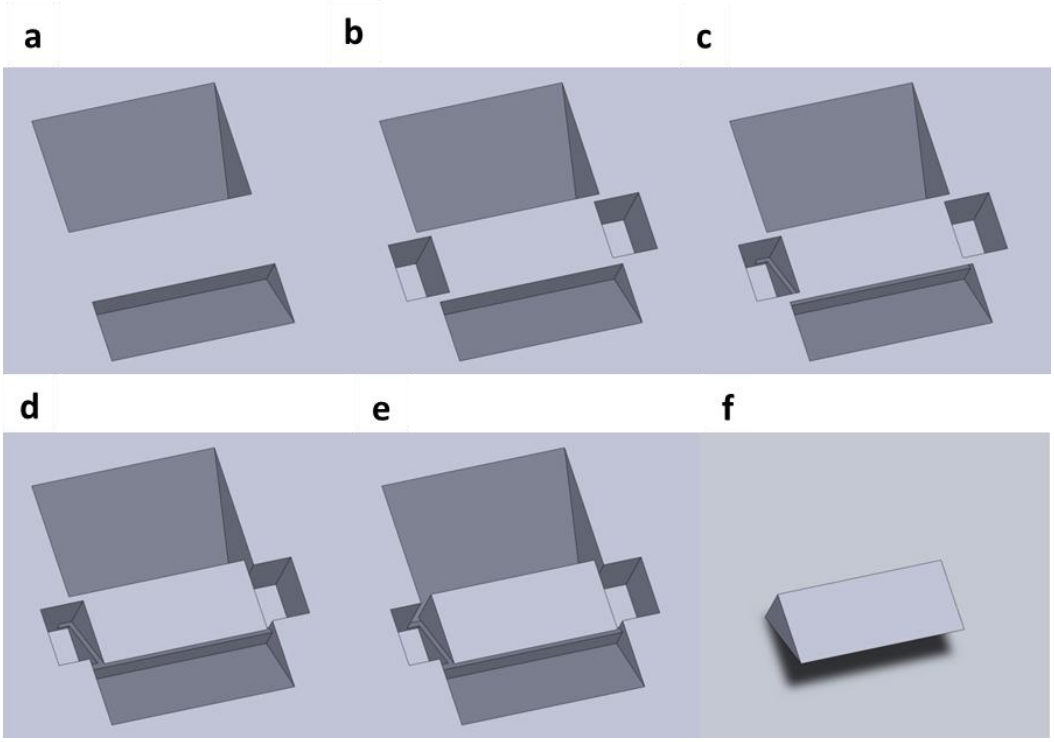

Figure 6.1. (a) Plan-view cut at 40 kV and 60 nA (angled cuts), (b) Plan-view cut at 40 kV and 3.5 nA, (c) Tilt sample to 40° for bottom cut at 40 kV and 3.5 nA, (d) Plan-view cut at 40 kV and 3.5 nA, (e) Bringing in the microsampler probe, welding to upper right corner of the wedge and then plan-view cut at 40 kV, 3.5 nA, (f) resulting sample.[50]

6.3. Results and Discussion

To study the effect of a patterned surface on the structure of a blend film, first we investigated the morphology of the same blend on a homogenous glass surface without patterned surface energies. First, the morphologies of the PS-CdS/PMMA-Ag NP blend films, which were previously discussed in Chapter 5 in connection with photoluminescence studies, were investigated. As described in Chapter 5, these films were prepared via spin-coating the blend solutions of c_p = 4.0 wt % 30/70 and 50/50 (w/w) PS-CdS/PMMA-Ag in toluene onto a non-patterned clean glass surface at three different spin rates of 3000, 6000 and 9000 rpm. Interestingly, and in contrast to PS/PMMA homopolymer blends described in Chapter 4, AFM images of the PS-CdS and

PMMA-Ag blend films (Figure 6.2), reveal relatively featureless topologies without developed PS/PMMA domain structures for all spin rates and both compositions. The rare surface features that are observed in these images are probably dust or other impurities. The absence of microscale domain features on the surface of the blend films cannot be a result of insufficient interfacial tension between blend components, since the PS/PMMA and PS-CdS/PMMA-Ag pairs should have very similar interaction energies. Rather, as discussed below, we attribute this absence of phase-separation in the NP blends to the difference in structure between homopolymers and polymer-coated NPs. This absence of phase-separated structure on the micron scale in the spin-coated PS-CdS/PMMA-Ag blends precludes their patterning on microcontact printed surfaces and therefore must now be addressed.

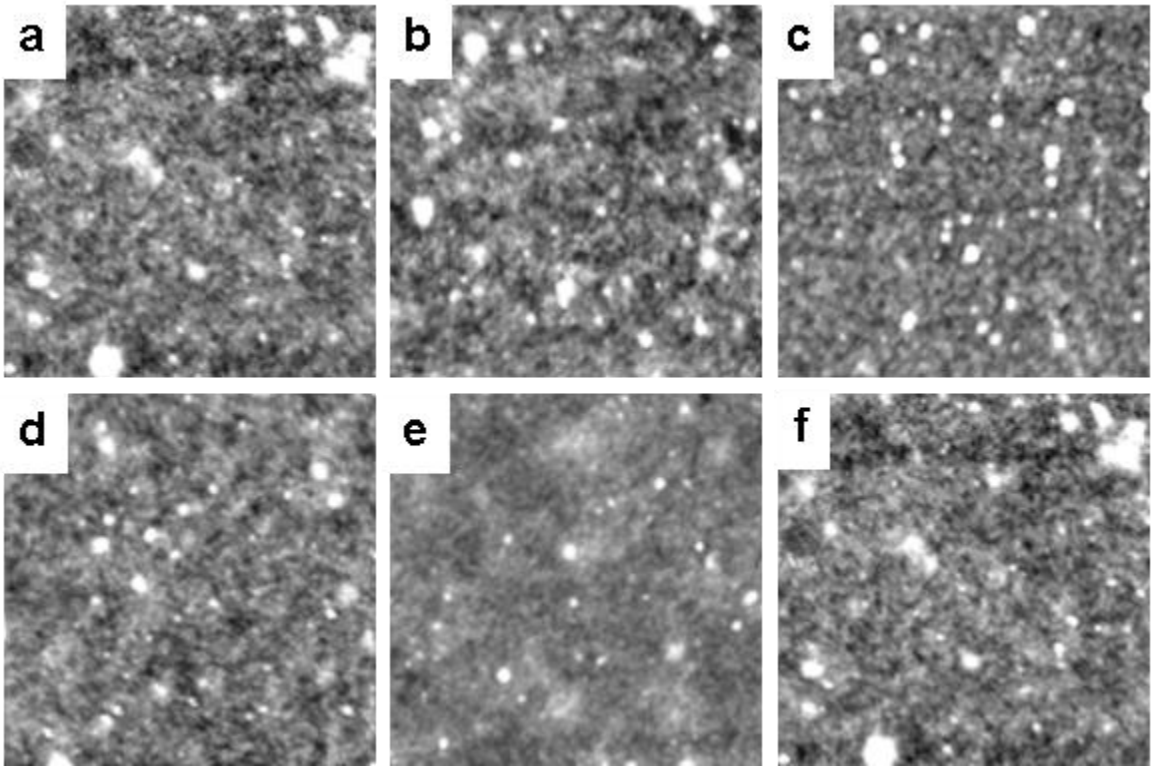

Figure 6.2. 10-10 μm AFM images of 4.0 wt% 30/70 (a-c) and 50/50 (d-f) PS-CdS/PMMA-Ag samples spin-coated at (a, d) 3000, (b, e) 6000 and (c, f) 9000 rpm on quartz slide.

To understand the absence of phase-separated structure in these blends, we must first consider what happens to PS-CdS/PMMA-Ag pairs as the solvent evaporates. As described in Chapter 5, both NPs can be described as spherical polymer brushes, with PS or PMMA chains attached at one end to a relatively small and compact NP core, resulting in a relatively large extended and highly solvent-swollen corona. The interactions between spherical polymer brushes, in the form of reverse block copolymer micelles in organic solvents, have been described in detail by Gast and coworkers.[58,59] At micelle volume fractions above the critical overlap concentration, it was found that steric repulsion between overlapping coronal chains of approaching micelles effected repulsive

"soft-sphere" intermicellar interactions, leading to micelle odering into a body-centred cubic lattice. This ordering resulted in gel formation with a dramatic increase in vicosity and extremely limited particle mobility.[58,59] We believe similar gelation of PS-CdS/PMMA-Ag NPs as the solvent evaporates during spin-coating leads to their highly restricted mobility, providing a strong kinetic constraint on phase-separtion despite the thermodynamic driving force. Effectively, once the PS-CdS and PMMA-Ag NPs are "frozen" into a gel, they have very limited translational mobility and cannot therefore segregate into microscale phase domains before the solvent is completely depleted and the polymer blend becomes vitrified.

In order to prevent gelation of the PS-CdS and PMMA-Ag NPs, we decided to add PS, PMMA, or a mixture of PS/PMMA homopolymers to the blend solutions prior to spin-coating. The idea is to increase the free volume and to prevent the overlap of approaching NP brushes and the resulting soft-sphere ordering during solvent evaporation by adding homopolymer to the spaces in between the brushes. To investigate the effect of added homopolymer on the phase-separation, we first added PS homopolymer with three different M_w values of 6k, 33k and 131k g.mol^{-1}, each at 10 wt% relative to the total polymer composition, while maintaining PS (PS + PS-CdS)/PMMA (PMMA-Ag) ratio of 30/70 (w/w). The three resulting blends are therefore, described as PS (6k, 33k, or 131k)/PS-CdS/PMMA-Ag 10/20/70 (w/w/w). All blends were spin-coated at a polymer concentration of c_p = 1.0 wt %. Since Figure 6.2 shows PS-CdS/PMMA-Ag blends spin-coated at 4.0 wt %, we also carried out the control experiment at c_p = 1.0 wt % for the blend without added PS.

AFM of the resulting blends on clean glass (Figure 6.3, a to c) show that the addition of PS homopolymer increases the extent of phase-separation and that the size of the resulting phase domains increases as the M_w of the added homopolymer increases. Specifically, very fine but difficult to measure domains were observed in the PS(6k) blend, whereas the measured average domain sizes increased to 0.2 ± 0.1 μm and then to 0.4 ± 0.1 μm in the PS(33k) and PS(131k) blends, respectively. The observed trends suggest that higher M_w homopolymer increase the particle mobility (by impeding gelation) to a greater extent than lower M_w homopolymer. This is explained by the relative tendency of different sized homopolymers to intercolate into the solvent-swollen brushes of the NPs. It is found that when the homopolymer is on the same order or greater than the size of the brush chains then there is a tendency for the chains to be excluded from the brush and occupy the interparticle spaces; this is referred to as the "dry brush" case. [61-64] Conversely, when the M_w of added homopolymer is smaller than that of the similar polymer brush, the homopolymer gets included in the brush, this is referred to as the "wet brush" case.[61-64] In our system, the NP mobility should be increased to a greater extent when most of the homopolymer is localized between the NPs rather than within the brushes, in order to prevent interparticle overlap and ordering. This explains the relative increase in phase-separation which is observed in Figure 6.3 a-c. Schematic describing the gelation and also the effect of added low and high M_w homopolymer to the NPs blend are illustrated in Figure 6.4 a-c, respectively.

Figure 6.3 d-f illustrates the film morphologies of PS-CdS/PS/PMMA-Ag on OTS-patterned surfaces. For added 6k and 33k PS, the polymer surface topology did not reveal the underlying surface pattern, because *d* is still not large enough; however, for the

blend with added 131k PS, which has the largest *d* in this series, patterned lines were observed but no separate phases meaning that both phases are present in the regions in between the OTS lines and further phase-separation between them result in the formation of small domain phases in these regions (Figure 6.3f).

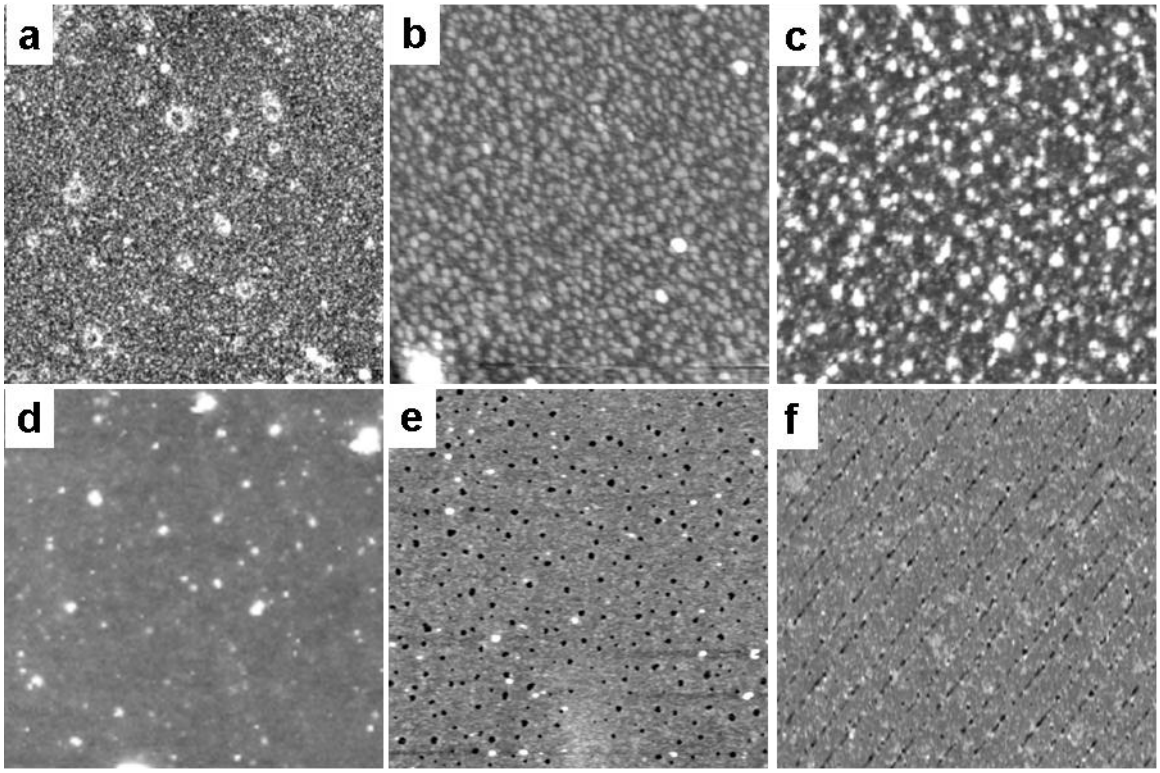

Figure 6.3. 10-10 µm AFM images of 1.0 wt% 20/10/70 (w/w/w) PS-CdS/PS/PMMA-Ag films prepared using (a, d) 6 k, (b, e) 33 k and (c, f) 131 k PS homopolymer. Films spin-coated at 6000 rpm from toluene on non-patterned (a-c) and OTS-patterned substrates (d-f).

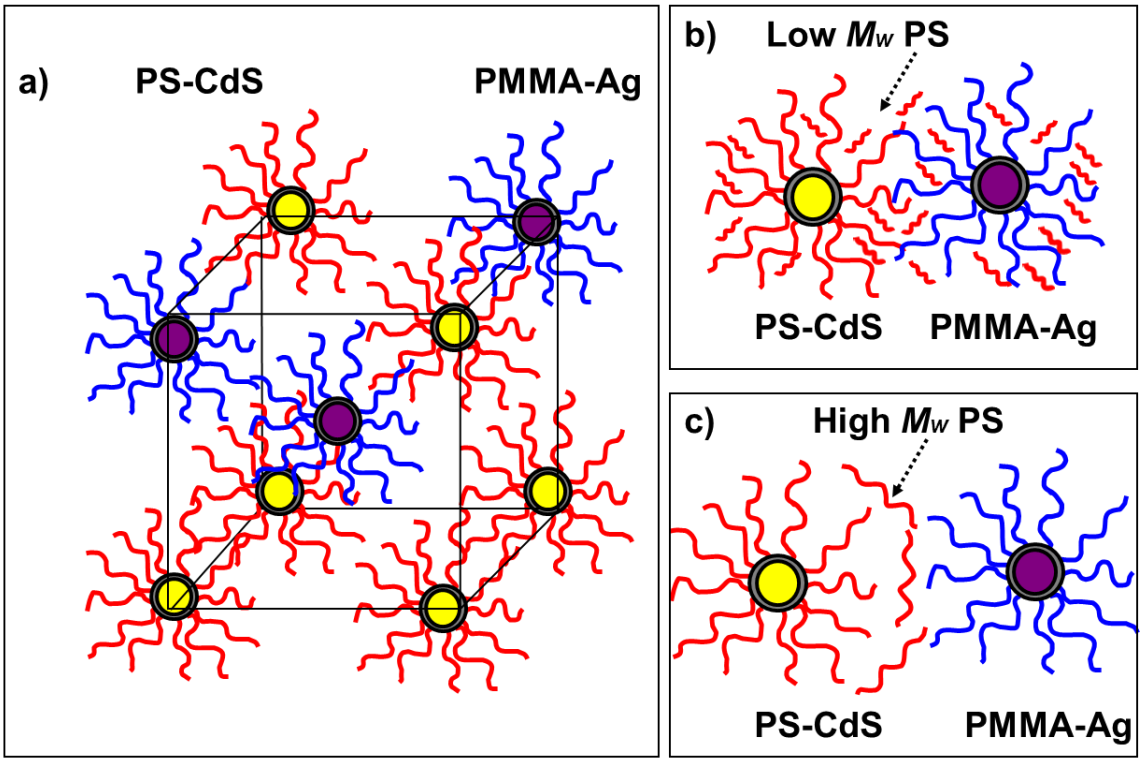

Figure 6.4. Schematic describing (a) NPs blend forming ordered body-centred cubic lattice, (b) addition of Low M_w PS to the NPs blend forming a "wet-brush" blend, and (c) addition of high M_w PS to the NPs blend forming a "wet-brush" blend.

The effect of added homopolymer is also demonstrate for the NPs blend with added 10% (w) of PMMA with M_w = 120k homopolymer. Films were prepared using 1.0 wt% 30/60/10 (w/w/w) PS-CdS/PMMA-Ag/PMMA on non-patterned and OTS-patterned substrates (Figure 6.5 a and b, respectively). Similar to the case of added high M_w PS, d has increased (d = 0.4 ± 0.1 µm) and the pattern lines were observed in the blend film when spin-coated on the patterned substrate. The similar results observed for high M_w PS and high M_w PMMA suggest that the chemical nature of added homopolymer is relatively not important since both PS and PMMA are compatibilized by solvent swelling.

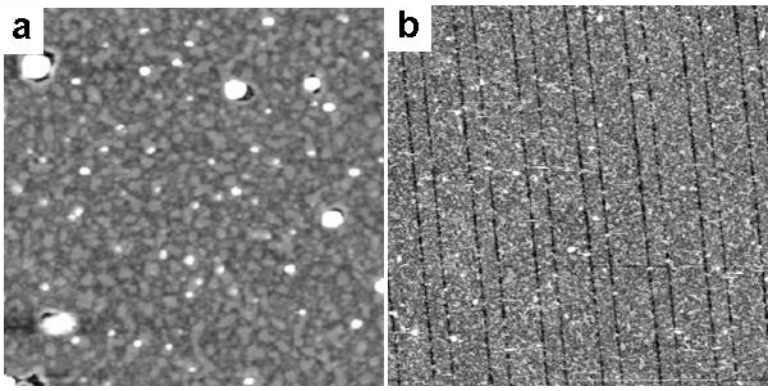

Figure 6.5. 10-10 µm AFM images of c_p = 1.0 wt% 30/60/10 (w/w/w) PS-CdS /PMMA-Ag/PMMA films prepared using 120 k PMMA. Films spin-coated at 6000 rpm from toluene on (a) non-patterned and (b) OTS-patterned substrates.

As described in chapter 4 (4.3.1), d can be adjusted by fine-tuning the c_p of the blend and the spinning rate, at which the films are prepared. Therefore, we studied the morphology of the blend films with added 10% of either 133k PS or 120k PMMA on OTS-patterned substrates for three different solution concentrations of 0.5, 1.0 and 2.0 wt% and three different spin rates of 3000, 6000 and 9000 rpm. For all cases either polymer surface topology did not reveal the underlying surface pattern or similar morphology to the ones shown in Figures 6.3 f and 6.5 b were obtained. This implies that the blend has to be modified furthermore; so, we pursued this by adding 10% of PS and 10% of PMMA to further increase the free volume and to further prevent the interparicle overlaps. AFM images of the blend of 20/10/60/10 (w/w/w/w) PS-CdS/PS/PMMA-Ag/PMMA are shown in Figure 6.6 for c_p = 0.5, 1.0 and 2.0 wt% and spin rates of 3000, 6000 and 9000 rpm.

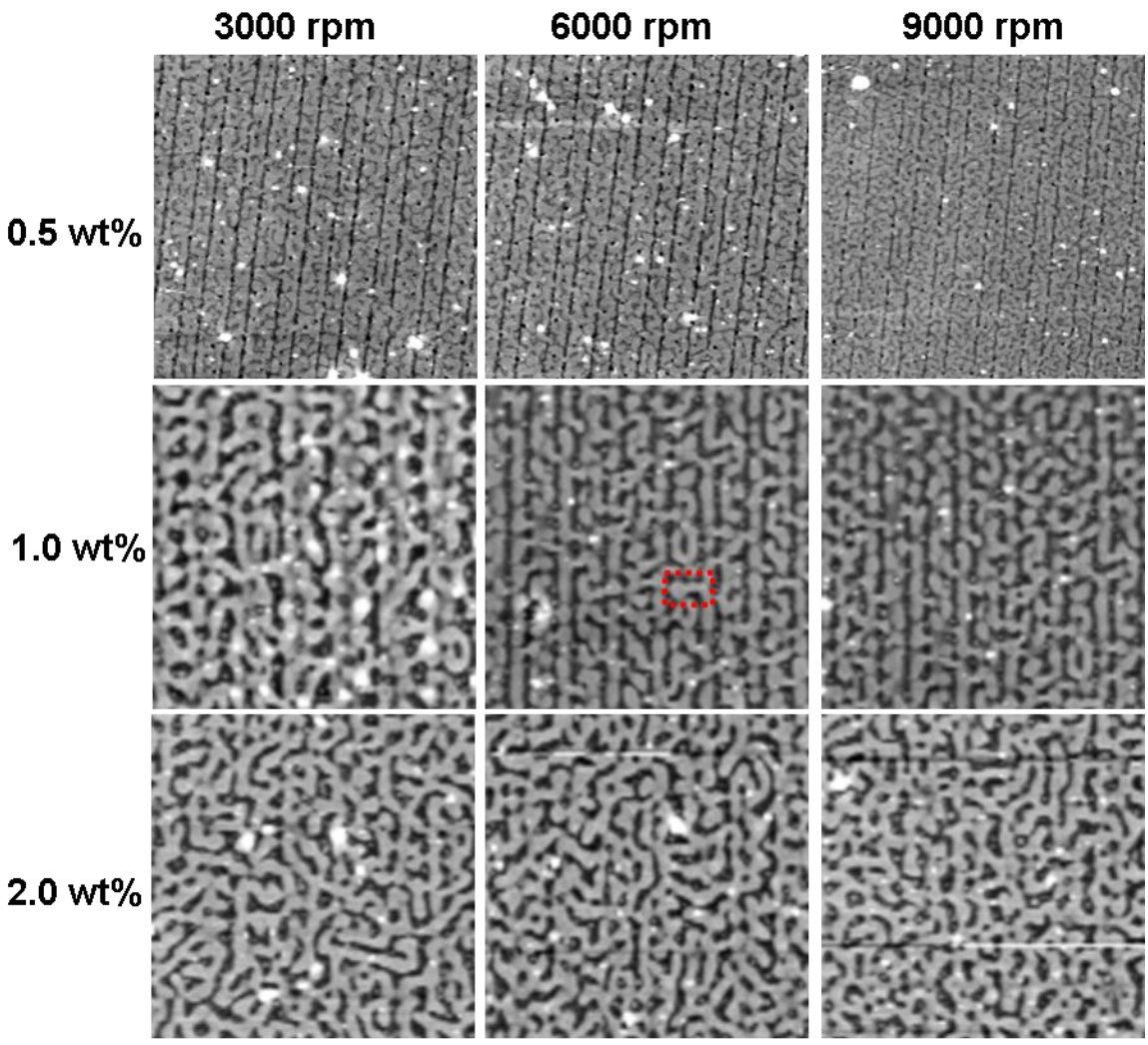

Figure 6.6. 10-10 μm AFM images of c_p = 0.5, 1.0 and 2.0 wt% of 20/10/60/10 PS-CdS/PS/PMMA-Ag/PMMA (w/w/w/w/) films spin-coated at 3000, 6000 and 9000 rpm from toluene on OTS- patterned substrates. The bridging between the raised domains is highlighted on the AFM image for 6000 rpm and 1.0 wt%.

The addition of both types of homopolymers at once results in the phase-separated NP domains that are considerably larger than in previous cases. Average measured *d* for c_p = 0.5, 1.0 and 2.0 wt% blend films spin-coated at 6000 rpm are 0.2 ± 0.1, 0.5 ± 0.1, and 0.7 ± 0.1 μm respectively. For c_p = 0.5 wt%, small phase domains of both PS and PMMA are observed in the regions in between the OTS lines for all three

spin rate cases. For c_p = 1.0 wt% raised PMMA domains are elongated along the pattern direction connected by some bridges (as the one highlighted in Figure 6.6) that span the OTS lines of the underlying substrate. For c_p = 2.0 wt%, domain shapes are mostly irregular with little elongation along the pattern direction. The best pattern replication in this series is obtained for the c_p = 1.0 wt% blend at high spin rates (6000 and 9000 rpm). however, even for these cases, the raised domains are not discrete and they are connected through bridges; thus, to improve the patterned structures, the amount of added homopolymers were increased from 10 to 20 % (w); the reason for adding more homopolymer to the NPs blend is to increase the amount of homopolymers that localize in between NPs polymer brushes preventing the intermicellar interactions and therefore, improving the mobility of the particles so they can form discrete domains on the specific regions of the substrate. For the blend of 10/20/50/20 PS-CdS/PS/PMMA-Ag/PMMA (w/w/w/w) pattern replication was obtained for both c_p = 0.5 and 1.0 wt% blends. Low magnification AFM images (50-50μm, shown in Figure 6.7) demonstrate the long-range patterning of these blends. The improvement is more obvious for the 1.0 wt% case, which shows the least amount of bridging defect in the patterned domains.

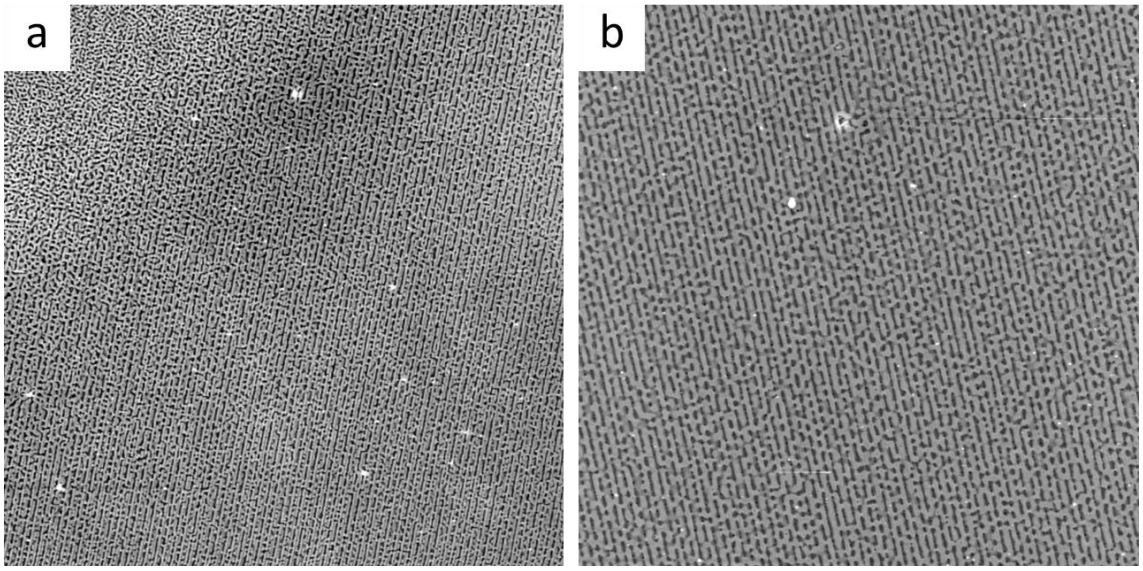

Figure 6.7. 50-50 µm AFM images of (a) c_p = 0.5 and (b) c_p = 1 wt% of 10/20/50/20 PS-CdS/PS/PMMA-Ag/PMMA (w/w/w/w) films spin-coated at 6000 rpm from toluene on OTS patterned substrates.

To identify the domains, LSCFM imaging was performed to probe the PL of the QDs from the regions to where they are directed. The excitation and emission filters for LSCFM were selected according to the PL properties of the constituent PS-CdS QDs, as shown in chapter 3 (Figure 3.8b). LSCFM image of the film (Figure 6.8 b) shows localized CdS emission from the photoluminescent striped pattern. The periodicity of bright and dark stripes are similar to that of the OTS underlying pattern; comparing the spacing between the pattern lines in the LSCFM image (Figure 6.8 b) and in the underlying OTS pattern (portrayed in 6.8a), suggests the registration of CdS-containing PS domains to the OTS lines. Based on this, we propose the lateral distribution of the domains as depicted in Figure 6.8 a. Regions in between the bright stripes in the LSCFM image (presumably Ag-containing PMMA domains) are dark, demonstrating the localization of QDs only above OTS stripes.

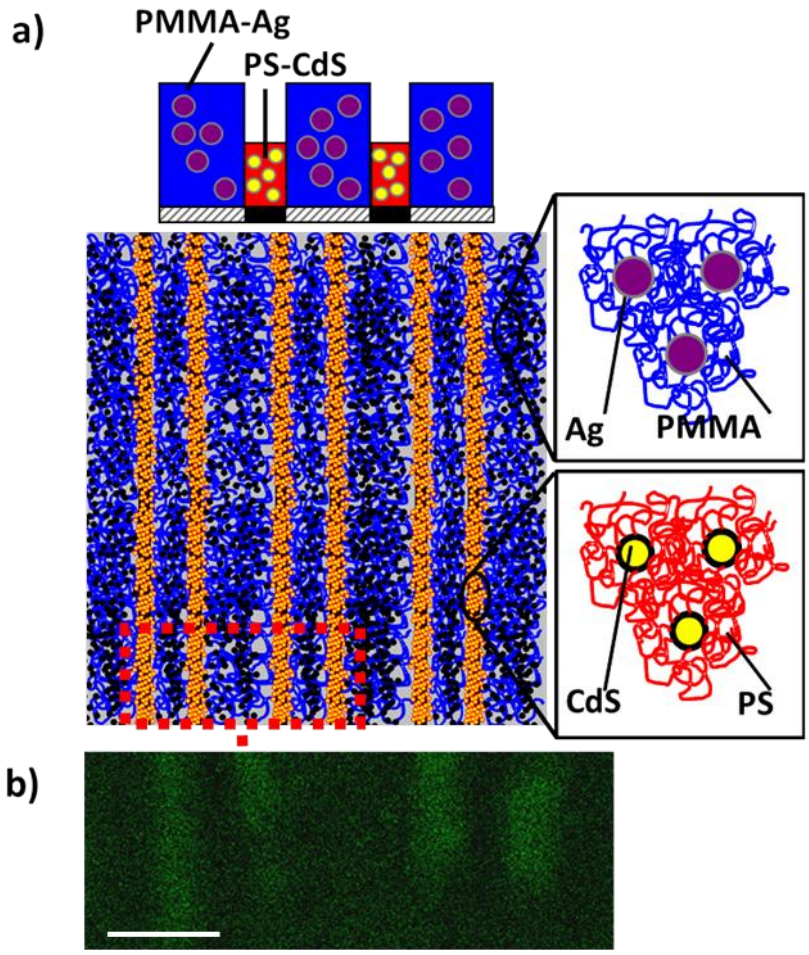

Figure 6.8. (a) Lateral distribution of PS-CdS within the PS phase and the PMMA-Ag within the PMMA phase forming the patterned morphology observed in top-view of the film, and (b) LSCFM image of the c_p = 1.0 wt% 10/20/50/20 PS-CdS/PS/PMMA-Ag/PMMA (w/w/w/w) patterned film. Scale bar is showing 1 μm.

LSCFM imaging does not resolve the distribution of individual CdS within the PS domains due to resolution limitations and therefore, in order to resolve the distribution of individual NPs within the polymer phases and also to confirm the location of Ag NPs, other imaging techniques such as TEM and SEM were utilized. Both these methods are equipped with EDS allowing elemental analysis and mapping of the components.

For TEM imaging the challenge is in transferring the NPs blend film from the OTS-patterned glass substrate to a TEM grid; since the films are too thin (~ 30 nm) physical lifting of the film from the glass was not successful; for this, we tried to scratch the edges of the film using a scalpel and let the detached film float on a surface of DI water. After this unsuccessful attempt, we tried another method: detaching the film by dissolving the glass substrate in aqueous HF and then transferring the free-standing film from the HF solution to a TEM grid. Using this method we were able to transfer the film to a TEM grid but TEM imaging showed the distortion of the patterned structure. Two sample images at high and low magnification are illustrated in Figure 6.9 that show disappearance of the pattern; this is perhaps due to some migration of PS and PMMA during the lifting process as well as growth of Ag NPs aggregates in the aqueous media that result in formation of the large features observed in TEM images.

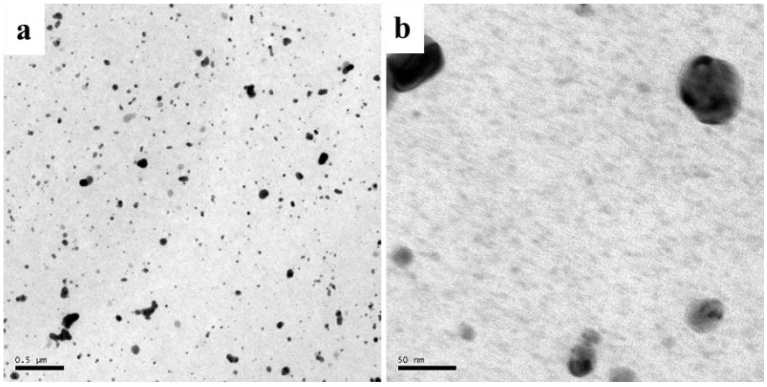

Figure 6.9. (a) low and (b) high-magnification TEM images of the c_p = 1.0 wt% 10/20/50/20 (w/w/w/w) PS-CdS/PS/PMMA-Ag/PMMA patterned film removed from glass substrate using a HF solution and transferred to a TEM grid. Scale bar in (a) shows 0.5 µm and in (b) shows 50 nm.

We also tried SEM imaging, the challenge we confronted was due to the non-conductivity of our samples; for SEM imaging samples should be conductive to prevent the accumulation of electrostatic charges at the surface. To improve the conductivity of our sample, blend films were carbon-coated prior to imaging but still the conductivity was quite low not allowing us to focus the scope; therefore, EDS analysis did not show accurate elemental mapping. Figure 6.10a and b demonstrate the map obtained for Cd and Ag elements on the film, respectively; the maps display a uniform distribution of both Cd and Ag throughout the film, which is contradicting with the localized PL we observed from CdS QDs by LSCFM imaging.

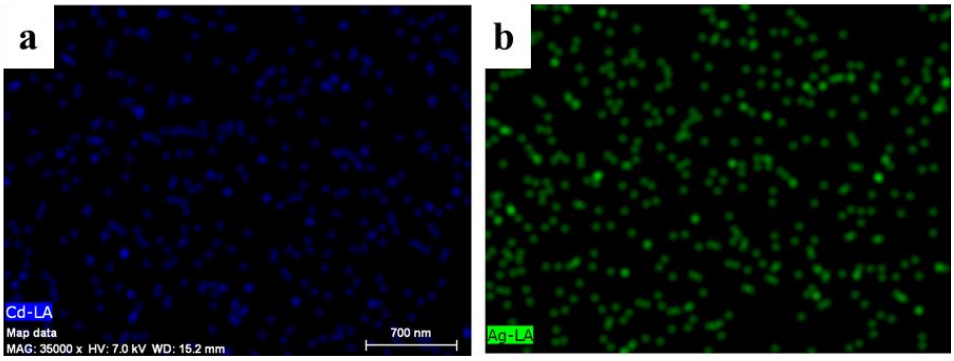

Figure 6.10. SEM-EDS mapping of (a) Cd and (b) Ag of the carbon-coated c_p = 1.0 wt% 10/20/50/20 (w/w/w/w) PS-CdS/PS/PMMA-Ag/PMMA patterned film; images do not reveal any localization of elements.

Next, we utilized FIB to obtain a micro-sample for TEM imaging by removing a portion of the sample by FIB milling and mounting it on a FIB/TEM (STEM) compatible specimen holder for TEM imaging. FIB thinning for cutting the micro-sample is still undergoing and we are hoping to obtain TEM images of the microsample to resolve the position of NPs on the patterned substrate.

6.4. Conclusion

In this work we developed a fast, inexpensive, and single-step methodology to simultaneously pattern two types of polymer-coated NPs by facile method of spin-coating onto chemically-patterned substrates, which are obtained by μCP OTS on hydrophilic glass. This process is based on surface energy heterogeneity of the patterned substrate that directs the NPs according to their surface energies.

The first challenge we tackled in this work was the gelation occurring in the NPs blend films as the solvent evaporates and intermicellar overlaps leads to highly restricted particle mobility, providing a strong kinetic constraint on their phase-separtion. Therefore, PS-CdS and PMMA-Ag NPs cannot segregate into microscale phase domains before the solvent is completely depleted. We managed to increase the domain sizes by adding PS, PMMA or PS/PMMA homopolymers to the NPs blends in order to obtain a dry brush blend, where homopolymers localize in between the polymer brushes of NPs inhibiting the intermicellar overlaps and thus, improving the mobility of particles. The film morphologies of NPs and homopolymer blends were then fine-tuned by changing variables such as solution concentration and spinning rate to obtain domains that can be directed by the underlying OTS-patterned substrate.

Patterned structure of c_p = 1.0 wt% 10/20/50/20 (w/w/w/w) PS-CdS/PS/PMMA-Ag/PMMA patterned film was characterized by LSCFM imaging, which revealed the photoluminescent arrays confirming the surface-directed positioning of QDs on the patterned surface. However, our efforts to obtain SEM or TEM images remained unsuccessful and, therefore, it is difficult to come to a definite conclusion without images that show precise positions of the individual NPs. We could not directly demonstrate the

alternating Ag- and CdS-containing stripes but LSCFM imaging shows alternating stripes of bright (CdS-containing) and dark (presumably Ag-containing) regions which is an indirect indication for surface-directed patterning of NPs.

The methodology presented in this chapter is flexible and it can be used for patterning different types of NPs into variety of device-oriented structures making this method a strong tool in fabricating micro- and nanoscale devices.

6.5. References

(1) Brown, P. O.; Botstein, D. *Nat. Genet.* **1999**, *21*, 33.

(2) Schena, M.; Shalon, D.; Davis, R. W.; Brown, P. O. *Science* **1995**, *270*, 467.

(3) Anker, J. N.; Hall, W. P.; Lyandres, O.; Shah, N. C.; Zhao, J.; Van Duyne, R. P. *Nat. Mater.* **2008**, *7*, 442.

(4) Hoa, X. D.; Martin, M.; Jimienez, A.; Beauvis, J.; Charette, P.; Kirk, A.; Tabrizian, M., *Biosensors and Bioelectronics***2008**, 24, 970.

(5) Huang, M. H.; Mao, S.; Feick, H.; Yan, H.; Wu, Y.; Kind, H.; Weber, E.; Russo, R.; Yang, P. *Science* **2001**, *292*, 1897.

(6) Javey, A.; Guo, J.; Wang, Q.; Lundstrom, M.; Dai, H. *Nature* **2003**, *424*, 654.

(7) Rizzo, A.; Mazzeo, M.; Palumbo, M.; Lerario, G.; D'Amone, S.; Cingolani, R.; Gigli, G., *Adv. Mater*.**2008**, 20, 1886.

(8) Schubert, U. S.; Wouters, D. *Angew. Chem. Int. Ed*.**2004**, 43, 2480.

(9) Piner, R. D.; Zhu, J.; Xu, F.; Hong, S.; Mirkin, C. A. *Science* **1999**, *283*, 661.

(10) Salaita, K.; Wang, Y.; Mirkin, C. A. *Nat. Nanotechnol.* **2007**, *145*, 145.

(11) Basnar, B.; Willner, I. *Small* **2009**, *5*, 28.

(12) Ginger, D. S.; Zhang, H.; Mirkin, C. A. *Angew. Chem., Int. Ed.* **2004**, *43*, 30.

(13) Li, B.; Goh, C. F.; Zhou, X.; Lu, G.; Tantang, H.; Chen, Y.; Xue, C.; Boey, F. Y. C.; Zhang, H. *Ad*V. *Mater.* **2008**, *20*, 4873.

(14) Wang, H. T.; Nafday, O. A.; Haaheim, J. R.; Tevaarwerk, E.; Amro, N. A.; Sanedrin, R. G.; Chang, C. Y.; Ren, F.; Pearton, S. J. *Appl.Phys. Lett.* **2008**, *93*, 143105.

(15) Hoogenboom, J. P.; Vossen, D. L. J.; Faivre-Moskalenko, C.; Dogterom, M.; van Blaaderenb, A., *Appl. Phys. Lett.***2002**, 80, 4828.

(16) Grigorenko1, A. N.; Roberts1, N. W.; Dickinson1 M. R.; Zhang,Y. *Nature Photonics***2008,** 2, 365.

(17) Xia, Y.; Whitesides, G. M. *Annu. Re*V. *Mater. Sci.* **1998**, *28*, 153.

(18) Fan, Z.; Ho, J. C.; Jacobson, Z. A.; Yerushalmi, R.; Alley, R. L.; Razavi, H.; Javey, A. *Nano Lett.* **2008**, *8*, 20.

(19) He, H. X.; Li, Q. G.; Zhou, Z. Y.; Zhang, H.; Huang, W.; Li, S. F. Y.; Liu, Z. F. *Langmuir* **2000**, *16*, 9683.

(20) Ahn, J. H.; Kim, H. S.; Lee, K. J.; Jeon, S.; Kang, S. J.; Sun, Y.; Nuzzo, R. G.; Rogers, J. A. *Science* **2006**, *314*, 1754.

(21) Minelli, C.; Geissbuehler, I.; Eckert, R.; Vogel, H.; Heinzelmann, H.; Liley, M. *Colloid Polym. Sci.* **2004,** 282, 1274.

(22) Gao, M.; Sun, J.; Dulkeith, E.; Gaponik, N.; Lemmer, U.; Feldmann, J., *Langmuir* 2002, 18, 4098.

(23) Park, J.;Fouche, L. D.; Hammond,P. T. Adv. Mater. 2005, 17, 2575.

(24) Xia, D.; Brueck, S. R. J. Nano Letters, 2004, 4 (7), 1295.

(25) Hung, A. M.; Micheel, C. M.; Bozano, L.D.; Osterbur, L.W.; Wallraff, G. M; Cha, J. N. *Nature Nano.***2010**,5, 121.

(26) Hua, F.; Cui, T.; Lvov, Y. *Langmuir***2002**, 18 (17), 6712. 21, 22

(27) Werts, M. H. V.; Lambert, M.; Bourgoin, J.-P.; Brust, M.*Nano Letters***2002**, 2 (1), 43.

(28) Gotschy, W.; Vonmetz, K.; Leitner, A.; Aussenegg,F. R., *Appl. Phys. B***1996**, 63, 381.

(29) Werts, M. H. V. ; Lambert, M. ; Bourgoin, J. P. ; Brust, M., *Nano Lett.***2002**, *2*, 43.

(30) Hua, **F**.; Shi, J.; Lvov, Y.; Cui, T., *Nano Lett.***2002**, 2, 1219.

(31) Jamshidi, A.; Neale, S. I.; Yu, K.; Pauzauski, P. J.; Schuck, J.; Valley, J. K.; Hsu, H. Y.; Ohta, A. T.; Wu, M.C., *Nano lett.***2009**, 9, 2921.

(32) Vossmeyer, T.; Jia, S.; DeIonno, E.; Diehl, M.; Kim, S. H., *J. Appl. Phys*. **1998**, 84, 3664.

(33) Wilbur, J. L.; Kumar, A.; Kim, E.; Whitesides, G. M., *Adv. Mater*. **1994**, 6, 600.

(34) Xia, Y.; Mrksich, M.; Kim, E.; Whitesides, G.M. *J. Am. Chem. Soc*. **1995**, 117, 9576.

(35) Xia, Y.; Whitesides, G. M., *Langmuir***1997**, 13, 2059.

(36) Mrksicha, M.; Whitesides, G. M. *TIBTECH* **1995**, 13, 228.

(37) Walheim, S.; Ramstein, M.; Steiner, U. *Langmuir***1999**, 15, 4828.

(38) Zong, Q.; Li, Z.; Xie, X., *Macromolecular Chemistry and Physics***2004**, 205, (8), 1116.

(39) Heriot, S. Y.; Jones, R. A. L., *Nat. Mater*. **2005**, 4, (10), 782.

(40) Walheim, S.; Boltau, M.; Mlynek, J.; Krausch, G.; Steiner, U. *Macromolecules* **1997**, 30, 4995.

(41) Raczkowska, J.; Cyganik, P.; Budkowski, A.; Bernasik, A.; Rysz, J.; Raptis, I.; Czuba, P.; Kowalski, K. *Macromolecules***2005**, 38, 8486.

(42) Park, L. Y.; Munro, A. M.; Ginger, D. S. *J. Am. Chem. Soc*. **2008**, 130, 15916.

(43) Jaczewska, J.; Budkowski, A.; Bernasik, A.; Raptis, I.; Moons, E.; Goustouridis, D.; Haberko, J.; Rysz, J. *Soft Matter***2009**, 5, 234.

(44) Sehgal, A.; Ferreiro, V.; Douglas, J. F.; Amis, E. J.; Karim, A. *Langmuir***2002**, 18, 7041.

(45) Andrew, P.; Huck, W. T. S., *Soft Matter*, **2007**, 3, 230.

(46) Fukunaga, K.; Elbs H.; Krausch, G., *Langmuir***2000**, 16, 3474.

(47) Rockford, L.; Liu, Y.; Mansky, P.; Russell, T. P., *Phys. Rev. Lett*. **1999**, 82:2602.

(48) Krausch, G.; Kramer, E. J.; Bates, F. S., *Phys. Rev. Lett*. **1993**, 71, 3669.

(49) kielhorn, L.; Muthukumar M., *J. Chem. Phys*. **1999**, 111, 2259.

(50) Adam Schuetze, Advanced Microscopy Facility, University of Victoria, Victoria, 2011.

(51) Kamino, T.; Yaguchi, T.; Hashimoto, T.; Ohnishi, T.; Umemura, K. *Introduction to Focused Ion Beams*, Chapter11, Springer, **2005**, New York.

(52) Takeno, H.; Iwata, M.; Takenaka, M.; Hashimoto, T. *Macromolecules***2000**, 33, 9657.

(53) Wang, W.; Shiwaku, T.; Hashimoto, T. *Macromolecules***2003**, 36, 8088.

(54) Bruder F.; Brenn, R. *Phys. Rev. Lett*. **1992**, 69, 624.

(55) Heier, J.; Kramer, E. J.; Revesz, P.; Battistig, G.; Bates, F. S. *Macromolecules* **1999**, 32, 3758.

(56) Wang, H.; Composto, R. J. *Europhys. Lett*.**2000**, 50 (5), 622.

(57) Chung, H.-J.; Wang, H.; Composto, R. J. *Macromolecules*, **2006**, 39, 153.

(58) Gast, A.P. *Langmuir* **1996,** *12*, 4060.

(59) McConnell, G.A.; Lin, E.K.; Gast, A.P.; Huang, J.S.; Lin, M.Y.; Smith, S.D. *Faraday Discussion* **1994**, 98, 121.

(60) Lide, D. R. *CRC Handbook of chemistry and physics*, 90th ed., Taylor and Francis, **2009.**

(61) Chen, H.-L.; Lin, S.-Y.; Huang, Y.-Y.; Chiu, F.-C.; Liou, W.; Lin,J. S. *Macromolecules* **2002**, *35*, 9434.

(62) Higuchi, T.; Tajima, A.; Yabub, H.; Shimomura, M. *Soft Matter*, **2008**, 4, 1302.

(63) Chen, Y.; Gohr, K.; Schaertl, W.; Schmidt, M.; Yezek, L. *Progr.Colloid.Polym.Sci.*,**2002**, 121, 28.

(64) Gao, Y.; Liu, H. *J. Appl. Polym. Sci*. **2007**, 106, 2718.

Chapter 7. CONCLUSION AND CONTRIBUTIONS TO ORIGINAL KNOWLEDGE

7.1. Conclusions and Contributions to Original Knowledge

In this chapter a summary of the notable findings discussed in the thesis, and the contributions of this work to original knowledge is provided. Our effort in this thesis is to develop new methodologies to combine facile top-down patterning with efficient bottom-up self-assembly of polymers and NPs, in order to increase the complexity and ordering of hierarchical polymers/NPs architectures.

Microcontact printing (μCP) was utilized as the top-down patterning technique. In chapter 2, we demonstrated a general experimental protocol to produce hydrophilic/hydrophobic arrays with microscale periodicities, consisting of octadecyltrichlorosilane (OTS) stripes patterned onto glass surfaces by μCP. The procedure involves transfer of OTS to a piranha-treated glass substrate using a PDMS stamp with patterned topology. We showed the effect of parameters such as OTS solution concentration and printing time on the amount of transferred OTS to the glass surface, and consequently on the uniformity of the resultant pattern, which was characterized by optical microscopy (OM) and atomic force microscopy (AFM). Contact angle and OM monitoring of a drying DI water droplet confirmed the chemical heterogeneity of patterned OTS films.

The transparent patterned substrates were then used to direct bottom-up assemblies of polymer/NPs. We demonstrated two strategies for this and therefore, the rest of this chapter is divided in two sections to individually describe each strategy: first section reviews the first approach developed for polymer/NP patterning by surface-directed assemblies via Langmuir-Blodgett (LB) transfer to chemically-patterned substrates. In the next section our second strategy is summarized, which is polymer/NP

patterning via polymer/polymer phase-separation on chemically-patterned surfaces. Thus, section 7.1.1 reviews chapter 3, and section 7.1.2 discusses chapter 4-6.

7.1.1. Patterning block copolymer aggregates via Langmuir-Blodgett transfer to microcontact-printed substrates

In chapter 3, a methodology has been demonstrated which combines nanoscale self-assembly of amphiphilic block copolymers at the air-water interface with microscale templated assembly of the resulting aggregates via LB transfer to chemically-patterned surfaces, which were produced by μCP. Two copolymer samples of poly (styrene)-*block*-poly (ethylene oxide) (PS-*b*-PEO, with M_n = 141 k and 185 k) were used. We showed that dewetting of the subphase during the slow vertical withdrawal of the substrate through the water surface during LB transfer, results in selective positioning of copolymer aggregates in the hydrophilic stripes of a hydrophilic/hydrophobic patterned film. The importance of surface energy heterogeneities along the subphase-substrate contact line on the surface-directed patterning of aggregates was demonstrated by comparing LB transfer of PS-*b*-PEO aggregates when stripes of the patterned substrate are oriented perpendicular and parallel to the air-water interface, which resulted in selective positioning of aggregates only for the perpendicular orientation. The effect of surface pressure on LB patterning was also investigated, revealing that when the monolayer is compressed to high surface densities, packing constraints prevent the formation of patterned LB films. The method was also utilized for patterning of hierarchical photoluminescent strands formed via self-assembly of polymer-stabilized cadmium sulfide (CdS) quantum dots (QDs) and an amphiphilic block copolymer at the

air-water interface. Laser scanning confocal fluorescence microscopy (LSCFM) confirm the localized CdS emission from the microscale photoluminescent stripe array, formed via transfer of the PS-CdS QDs and PS-*b*-PEO aggregates to a chemically-patterned surface.

The major contribution of this work is to provide a versatile approach for fabricating hierarchical polymer and polymer/NP architectures with combination of the fast and inexpensive top-down technique of μCP with efficient bottom-up assembly of block copolymer at the air-water interface. The method can be used for variety of amphiphilic block copolymers and functional NPs to obtain patterned structures with different functionalities.

7.1.2. Patterning polymer/nanoparticle assemblies via polymer/polymer phase-separation on microcontact-printed substrates

Chapter 4 demonstrated another example for combining the top-down and bottom-up assemblies. In this part, OTS-patterned substrates were used to direct a different self-assembly process, which is the polymer/polymer phase-separation. Patterned structures were obtained by spin-coating polymer blends onto chemically heterogeneous pre-patterned substrates, possessing regions of various surface energies that direct the polymer domains.

We demonstrated the directed phase-separation of poly (styrene)/ poly (methyl methacrylate) (PS/PMMA) blends based on their surface energies on chemically-patterned surfaces with alternating low surface energy OTS stripes (hydrophobic) and high energy glass (hydrophilic). We proposed the lateral distribution of the polymer

domains with respect to the underlying pattern based on an AFM study on the morphologies and the feature dimensions of the blend films before and after selective removal of the components. The important effect of length scale commensuration between the characteristic length scale of phase-separation (d), and the pattern periodicity (λ) was demonstrated. It was observed that pattern replication occurs when d is in the same order as λ, and no pattern was obtained in polymer film when $d > \lambda$. For $d < \lambda$ the arrangement of polymers is surface-directed at the substrate but since domain sizes are small both domains exist in the regions in between the OTS lines. Studying the blend films of different composition demonstrated that when the composition does not match the area fraction of the underlying patterned surface, the composition mismatch increases the extent of defects such as bridging between the raised domains. The effect of solvent was also considered and it was shown that when solvent has high vapour pressure, the high rate of evaporation does not allow polymer domains in the spin-coated films to selectively wet their energetically-preferred regions. This study provided us with valuable information on the behaviour of PS/PMMA blends at the OTS-patterned substrate. In the last part of chapter 4 we extended this method to organize domains of PS-CdS QDs and PMMA polymer into the striped pattern. LSCFM imaging displays the luminescent arrays of patterned films due to the embedded QDs, which are addressed to underlying OTS stripes because of the preferential wetting of PS at those regions.

This achievement motivated us to utilize this methodology for patterning multi-NP types. For this, we prepared another type of NPs that are PMMA-stabilized in order to employ the same approach of PS/PMMA patterning and to simultaneously pattern PS-stabilized/PMMA-stabilized NPs. A metal NP was chosen to be used with our CdS

sample, because of the interesting interactions between the surface plasmon (SP) of metallic NPs and photoluminescence (PL) of QDs.

A sample of PMMA-stabilized silver (PMMA-Ag) NP was synthesized via templated growth of Ag in the micelle core of poly (methyl methacrylate)-*block*-poly (acrylic acid). The synthesis and characterization of Ag NPs was presented in the first part of Chapter 5 followed by a comprehensive study of the optical properties of PS-CdS/PMMA-Ag spin-coated films. It was demonstrated that *d* can be tuned by adjusting the spinning rate in order to increase the extent of interactions between "Ag-rich" and "CdS-rich" domains by increasing the interfacial area between the domains, and also by decreasing the distance between the interacting NPs, which increases the number of particles that are within the operative distance of interaction from each other. Enhancement in the PL intensity of PS-CdS QDs in vicinity of Ag NPs was observed and enhancement factors were calculated after correcting the PL spectra for the differences between the thickness and relative QD content of the films; an enhancement factor as high as 36 times was calculated. Excitation spectra of the films were also investigated; spectra suggested that two mechanisms are in operation for the PL enhancement in these blend films: enhancement of the excitation field as the result of coupling between the SP and the electromagnetic field of the excitation radiation, and the enhancement of the emission by coupling between the emitted photon from a radiative decay of QDs and SP of Ag. Shortening of lifetime was also observed for PL-enhanced films, which is attributed to the increase in the radiative rate of recombination as a result of field enhancement.

Finally, in chapter 6, our methodology was extended to patterning multi-NP types. Our strategy is based on surface-directed polymer/polymer phase-separation, similar to chapter 4 but here polymers are not free chains; they are the brushes attached to the surface of NPs. Optically-interacting NPs blend of chapter 5 (PS-CdS and PMMA-Ag) were used for this work. The process is based on directing NPs to different regions of an energetically-heterogeneous patterned surface via surface energies of NPs.

The first challenge in this work was the gelation occurring in the NPs blend films as the solvent evaporates that prevents the phase-separation. We managed to overcome this by adding homopolymers similar to the ones used as the polymer brushes to the blends to obtain a dry brush blend, where homopolymers localize in between the NPs inhibiting the intermicellar interactions in the blend and therefore, improving the mobility of particles to phase-separate. The film morphologies of NPs and homopolymer blends were then fine-tuned by changing variables such as solution concentration and spinning rate to obtain domains that can be directed by the underlying-OTS film. Patterned structures of these blends were characterized by LSCFM imaging that revealed luminescent arrays of the patterned blend films confirming the surface-directed positioning of QDs on the patterned surface but our efforts to obtain SEM or TEM images remained unsuccessful and therefore, it is difficult to conclude the lateral distribution of NPs without images that show precise positions of the individual NPs. However, LSCFM imaging showed alternating stripes of bright (CdS-containing) and dark (presumably Ag-containing) regions, which is an indirect indication for surface-directed patterning of NPs.

The main contribution of this part of the work to original knowledge is that we developed a fast, inexpensive, and single-step methodology to simultaneously pattern two types of polymer-stabilized NPs by spin-coating their blends onto chemically-patterned substrates. This methodology is versatile and flexible; it can be used for patterning different types of NPs into variety of device-oriented structures making the technique a strong tool in fabricating micro- and nanoscale devices, where specific organizations of multi-NP types is required.

7.2. Suggested Research on Surface-Directed Patterning of Polymer/Nanoparticle Assemblies

The methodologies that we developed in this work are both versatile and flexible. Therefore, the methodology can be applied for patterning various polymer/ NP assemblies into micro and nanoscale device-oriented structures. Polymers and NPs can be chosen depending on the optical, electronic, and mechanical desired properties of the final structure. The important parameters affecting the pattern replication were all investigated in this work with their effects; hence, for new blends the established parameters only have to be optimized because the characteristic length scale of phase-separation differ for various polymers or NP blends.

The choice of patterns are also wide open; beside microcontact printing there are also other techniques recently developed to prepare elaborate patterns with few nanometer features. Using such patterned substrates the blends can be patterned into many functional and device-oriented structures. For new patterns the procedure has to be

optimized based on the parameters we established in this work in order to obtain commensuration between the length scale of the pattern periodicity and the domain sizes.

For patterning polymers/NPs assemblies into more elaborate patterns with smaller features, the blends have to be modified in order to achieve a high level of registration between the blend components and the energy-matching regions of the substrate. To do that, one idea is to add a component to the blend that segregate into the interface between the main blend components and increases the level of separation between the domains.

In general, our methodologies are flexible to be tailored for fabrication of different structures based on the required function of the structure and its field of application.